REPORT DOCUMENTATION PAGE

The public reporting burden for this collection of information is estimated to average 1 hour per response, including the time for reviewing instructions, searching existing data sources, gathering and maintaining the data needed, and completing and reviewing the collection of information. Send comments regarding this burden estimate or any other aspect of this collection of information, including suggestions for reducing the burden, to Department of Defense, Washington Headquarters Services, Directorate for Information Operations and Reports (0704-0188), 1215 Jefferson Davis Highway, Suite 1204, Arlington, VA 22202-4302. Respondents should be aware that notwithstanding any other provision of law, no person shall be subject to any penalty for failing to comply with a collection of information if it does not display a currently valid OMB control number.
PLEASE DO NOT RETURN YOUR FORM TO THE ABOVE ADDRESS.

1. REPORT DATE *(DD-MM-YYYY)*	2. REPORT TYPE		3. DATES COVERED *(From - To)*
19/Feb/2002	DISSERTATION		

4. TITLE AND SUBTITLE
INITIALIZATION OF CLUDS IN THE PSU/NCAR MESOSCALE MODEL USING THE AIR FORCE'S REAL TIME NEPHANALYSIS

5a. CONTRACT NUMBER

5b. GRANT NUMBER

5c. PROGRAM ELEMENT NUMBER

6. AUTHOR(S)
CAPT CANTRELL LOUIS E JR

5d. PROJECT NUMBER

5e. TASK NUMBER

5f. WORK UNIT NUMBER

7. PERFORMING ORGANIZATION NAME(S) AND ADDRESS(ES)
TEXAS A&M UNIVERSITY

8. PERFORMING ORGANIZATION REPORT NUMBER
CI02-18

9. SPONSORING/MONITORING AGENCY NAME(S) AND ADDRESS(ES)
THE DEPARTMENT OF THE AIR FORCE
AFIT/CIA, BLDG 125
2950 P STREET
WPAFB OH 45433

10. SPONSOR/MONITOR'S ACRONYM(S)

11. SPONSOR/MONITOR'S REPORT NUMBER(S)

12. DISTRIBUTION/AVAILABILITY STATEMENT
Unlimited distribution
In Accordance With AFI 35-205/AFIT Sup 1

DISTRIBUTION STATEMENT A
Approved for Public Release
Distribution Unlimited

13. SUPPLEMENTARY NOTES

14. ABSTRACT

20020305 164

15. SUBJECT TERMS

16. SECURITY CLASSIFICATION OF:			17. LIMITATION OF ABSTRACT	18. NUMBER OF PAGES	19a. NAME OF RESPONSIBLE PERSON
a. REPORT	b. ABSTRACT	c. THIS PAGE		252	19b. TELEPHONE NUMBER *(Include area code)*

INITIALIZATION OF CLOUDS

IN THE PSU/NCAR MESOSCALE MODEL

USING THE AIR FORCE'S REAL-TIME NEPHANALYSIS

A Dissertation

by

LOUIS EDWARD CANTRELL, JR.

Submitted to the Office of Graduate Studies of
Texas A&M University
in partial fulfillment of the requirements for the degree of

DOCTOR OF PHILOSOPHY

May 2002

Major Subject: Meteorology

ABSTRACT

Initialization of Clouds in the PSU/NCAR Mesoscale Model
Using the Air Force's Real-Time Nephanalysis. (May 2002)
Louis Edward Cantrell, Jr.
B.S., Texas A&M University; M.S., Texas A&M University
Chair of Advisory Committee: Dr. John W. Nielsen-Gammon

Modern operational mesoscale numerical weather prediction models have the potential to forecast cloud structure and distribution more accurately through cloud physical initialization than through simple cloud cover estimation with synoptic-scale data or through dynamic initialization. In an attempt to produce a better cloud forecast and to reduce model spin-up time, a technique is developed that converts the Air Force's Real-Time Nephanalysis (RTNEPH) into cloud species mixing ratios that are used to initialize the PSU/NCAR Fifth-Generation Mesoscale Model (MM5). The cloud analysis and the model are chosen to simulate the operational modeling environment at Air Force Weather Agency (AFWA). MM5 is used to forecast clouds evolving around a stationary front along the Texas coast of the Gulf of Mexico from 13 September 2000 through 15 September 2000.

A cloud physical parameterization scheme currently in use in the Eta model provides the framework for converting RTNEPH clouds to data that can be used to initialize MM5. Modifications to this scheme make it purely diagnostic and account for the higher resolution grid to which it is applied. The technique used to initialize clouds is called the Cloud Initialization Scheme (CIS). Cloud variables analyzed by CIS are used to examine how sensitive MM5 forecast cloud distributions are to the initial distribution of clouds. Analyzed cloud is also compared to MM5 forecast clouds to determine if cloud forecasts are improved using this technique, and to determine if model spin-up is reduced.

Results indicate dramatic improvement in reducing spin-up time but only slight improvement in forecast accuracy. Large differences exist between the distribution characteristics of the analysis and of the forecast. MM5's response to cloud insertion indicates cloud-scale vertical winds must be assimilated, clouds diagnosed in regions of synoptic-scale descent must be permitted to persist, and diffusion of cloud variables must be reduced to maintain the discrete characteristics of real clouds. Although this work was inconclusive in producing a better cloud forecast, it has demonstrated that improving cloud forecast accuracy is within reach by including cloud updrafts, by correctly assimilating the synoptic wind analysis with the nephanalysis, and by adjusting the model's cloud diffusion technique.

INITIALIZATION OF CLOUDS

IN THE PSU/NCAR MESOSCALE MODEL

USING THE AIR FORCE'S REAL-TIME NEPHANALYSIS
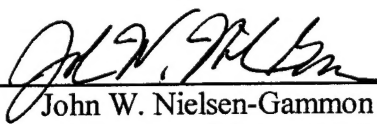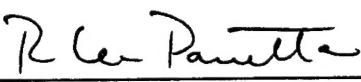
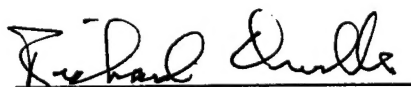A Dissertation

by

LOUIS EDWARD CANTRELL, JUNIOR

Submitted to Texas A&M University
in partial fulfillment of the requirements
for the degree of
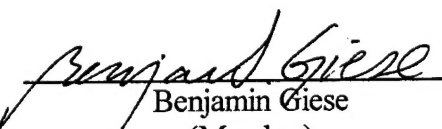
DOCTOR OF PHILOSOPHY
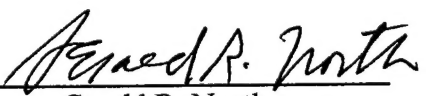
Approved as to style and content by:

John W. Nielsen-Gammon	Lee Panetta
(Chairman of Committee)	(Member)
Richard Orville	Benjamin Giese
(Member)	(Member)

Gerald R. North
(Head of Department)

May 2002

Major Subject: Meteorology

TABLE OF CONTENTS

LIST OF TABLES

LIST OF FIGURES

CHAPTER I

INTRODUCTION

1.1. Cloud Forecasting with NWP Models

Cloud forecasts have been a part of numerical weather prediction (NWP) in the Air Force for 40 years (Jensen 1962, Jensen 1963). A great deal of progress has been made during this period in improving forecasts of large-scale continuous fields such as pressure, temperature, and wind. However, forecasts of discrete fields such as clouds and precipitation have not had the same levels of improvement. In NWP, convective cloud processes should be parameterized when model grid spacing exceeds 10 km (Molinari and Dudek 1992). Some operational forecast models now routinely produce data at such resolution or finer (Doran 1999, Hamill and Colucci 1997). Cloud forecasting, however, has not improved even though continuous data fields are being output at higher resolution and accuracy.

Norquist (1999) assessed the cloud predictive skill of the Pennsylvania State University / National Center for Atmospheric Research Fifth Generation Mesoscale Model (PSU/NCAR MM5: Grell et al. 1994). The best statistical cloud predictions derived from MM5 forecast products were compared against a cloud analysis produced by the Air Force's Real Time Nephanalysis (RTNEPH: Hamill et al. 1992). The percentages of correct categorical cloud amounts are presented in Table 1.1.

Table 1.1. Percentage of correct categorical cloud amounts statistically diagnosed from MM5 forecast data against RTNEPH data. Adapted from table 5, Norquist 1999. Best value from either multiple linear regression (MLR) method or multiple discriminate analysis (MDA) method.

	6-h	12-h	18-h	24-h	30-h	36-h
High						
Best	86.4	77.6	87.0	83.7	86.1	83.4
Persistence	82.6	78.6	80.6	78.6	79.7	76.9
Middle						
Best	61.7	69.5	60.1	70.2	57.5	69.0
Persistence	67.8	71.9	64.2	71.3	61.5	68.3
Low						
Best	43.3	47.6	41.5	44.5	36.1	40.8
Persistence	53.2	51.6	46.6	50.4	42.0	42.6
Total						
Best	46.5	47.0	44.0	43.0	38.4	41.3
Persistence	52.7	48.2	46.4	46.2	40.3	40.5

This dissertation follows the style and format of the *Journal of the Atmospheric Sciences*.

These data do not indicate skill significantly better than persistence. Generally, the best predictors were only able to show slightly better skill than persistence for cloud forecasts at high levels. The best predictors for low-level and middle-level clouds performed poorly. Norquist reported that the best predictors were also inconsistent in that prominent predictors at one forecast time would not appear at later forecast times.

1.2. What Is a Cloud?

In very broad terms, the underlying reason cloud forecasting is so difficult is because we cannot consistently and objectively define what a cloud is. Unlike temperature, pressure, or water vapor mixing ratio, we cannot define a "cloud" state variable that is differentiable in space and time and has well-defined statistical behavior. A cloud can be defined variously according to the different observing systems. Human observers identify clouds by appearance (type) and cloud base altitude. Instruments make insitu measurements of clouds by sensing time averages of relative humidity, water or ice particle concentration, or by measuring the attenuation or scatter of radiation. Clouds could be defined as a radiance extinction coefficient, or as the analog voltage indicated by the measuring instrument. Satellite observations define clouds by infrared or microwave brightness temperatures, or by visual gray-shades, or by retrieved quantities from spectral radiance analysis. Mesoscale and synoptic scale forecast models sometimes define clouds as a saturation pressure deficit (SPD; e.g. Meso-Eta Model, Janjic 1994) or condensation pressure spread (CPS; Air Force cloud forecast models such as ADVCLD, Kopp et al. 1997). CPS and SPD are the change in pressure a parcel must experience before all the water vapor in the parcel becomes saturated. Other synoptic scale forecast models define clouds as functions of relative humidity and possibly some turbulence parameter, which is itself a function of temperature gradient, wind shear, heat flux, and static stability. The RTNEPH cloud analysis model defines cloud as a coverage amount, type, base height, and top height using a mixture of definitions from satellites, observations, and subjective analysis. Even in cloud resolving models, clouds are defined using mixing ratios of water vapor, cloud liquid water, cloud ice, graupel, rain, and snow (e.g. MM5). Clouds are generally defined using a threshold value of one or more of the above quantities. Although clouds cannot be resolved in general circulation models, their effects are parameterized in terms of idealized cloud shape, composition, albedo, radiative properties, distribution, and depth. Even cloud distribution is modeled using probability density functions, random placement, or even fractal distributions.

The definition of a cloud, as it is used by the Air Force and other military planners, is an obscuration from either above, below, or within a region of space. The ability to identify targets or to elude detection from any of these vantage points is obviously important to the military. Clouds are also a source of contamination to airborne systems. An example is the extreme sensitivity airborne intelligence gathering cameras have to scratching of the lens from cloud drops. Clouds are also an important reactant within chemical plumes of military interest. In a more generalized way, clouds are

markers of other processes important to those engaged in military operations. Those markers may be contrails, regions of precipitation affecting ground movement, or regions of air turbulence or icing affecting flight operations. In all the myriad definitions, "cloud" must be translated to the military application in order to be useful. The general categories of translation methods include parameterizations, rules, functions of state, and statistical methods such as using multiple discriminate analysis or multiple linear regression.

The cloud initialization scheme (CIS) presented herein is a multi-level translation of the definition of "cloud". Initially, the RTNEPH translates surface and synoptic upper-air observations, satellite observations, rules, and "bogusing" (subjective human adjustments) to cloud coverage amounts, cloud types, bases, and tops. Next, CIS translates this definition of "cloud" by using parameterizations and rules to produce mixing ratios of cloud variables. The cloud variable mixing ratios are then used to initialize the mesoscale model to produce a forecast of those cloud variable mixing ratios. Finally, once the forecast is produced, those mixing ratios must be translated to a new definition of cloud useful for a particular military application. Clouds are generally discrete unlike the continuous variables of temperature, water vapor, pressure, and wind used to describe the state of the atmosphere. The definition of a cloud is quite flexible but it is as subjective and as nebulous as the name implies.

1.3. Cloud Forecasts Must Improve

Knowledge of the location, amount, and physical properties of near-future cloud cover are crucial in United States Air Force mission planning. Piloting, surveillance, reconnaissance, targeting, battle damage assessments, and other mission types depend on the ability to anticipate and exploit cloud conditions day or night. The Air Force has relied on NWP to forecast clouds at increasingly finer resolution to meet increasing demands for cloud information. Coincident with the need for increased resolution, increases in forecast accuracy are also required because advances in technology place narrow operating conditions for various weapons or reconnaissance systems (Lewis 1998, Norquist 1999). It is imperative that the accuracy of cloud prediction keeps pace with evolving technology.

The improvement of cloud forecasts has been a problem due to the paradoxically discrete nature of clouds and their dependence on large-scale continuous variables such as temperature, pressure, moisture, and vertical motion. The treatment of clouds in NWP is also not easy because the transformations and interactions between the various water phases are quite complicated. Initial data accuracy and assimilation are obvious culprits to problems in NWP as well. Assimilating observations is an important problem encountered in NWP particularly when using models with horizontal resolutions finer than that from the available observations (Talagrand and Courtier 1987). It has been demonstrated frequently that an accurate representation of the initial atmospheric state is essential to obtaining accurate numerical forecasts. Associated with the problem of initial data accuracy is the so-called model "spin-up" problem. Mesoscale models initialized with only synoptic-scale distributions of

water vapor underestimate the potential energy of the initial environmental state and thus lead to errors in computing the kinetic energy of an evolving system. A potential energy thought experiment that demonstrates this principle is presented in Appendix C. These problems are discussed in more detail in Chapter II.

NWP still offers the best hope for achieving accurate cloud forecasts by resolving the scales at which discrete cloud processes occur. Within the last decade, computing resources have become available to operational forecast agencies to routinely generate cloud resolving forecasts and thus have the potential of producing accurate cloud forecasts (Cortinas and Stensrud 1995, Stensrud et al. 1997). The solution explored here is to initialize a mesoscale model with a cloud analysis to obtain a better cloud forecast.

1.4. Research Goals

The succeeding research goals are three-fold. The first goal is to develop a method to diagnose distributions of cloud variables from a high-resolution cloud analysis. This data is used to initialize clouds in a mesoscale model. The second goal of this study is to assess the importance of cloud-scale processes at model initialization time to cloud forecast accuracy. Cloud forecasts are generated using a mesoscale model for a variety of initial conditions. Results are compared to baseline model runs in which cloud data are not used at initialization. Results from tests with and without cloud initialization are evaluated against cloud analysis data as a performance reference. The third goal of this study is to determine if initializing a mesoscale model with cloud information can reduce or eliminate model spin-up time.

Chapter II describes the problems encountered in attempts to improve cloud forecast accuracy. How cloud initialization may be the key to improved forecast accuracy is also explored. Chapter III presents an overview of a new cloud initialization methodology. Chapter IV presents a method to horizontally and vertically distribute a cloud analysis to a mesoscale model grid. A detailed mathematical description of the cloud initialization scheme, which converts a cloud analysis to water species mixing ratios, is given in Chapter V. Chapter VI presents initial results after tuning the cloud initialization scheme using idealized cloud profiles. A description of the mesoscale model experiments and a weather analysis for two case studies are given in Chapter VII. During the research, incompatibilities between data sources used to initialize the mesoscale model were discovered. These are examined in Chapters VIII and Appendix E. Chapters IX and X outline the methods used to evaluate the mesoscale model's performance in cloud forecasting for the case studies. Results are summarized in a large-scale analysis and in a local-scale analysis. Chapter XI presents a discussion of the model's response to cloud initialization. An objective measure of model spin-up time is also developed. A summary, conclusions, and proposed future work are given in Chapter XII.

CHAPTER II

CLOUDS IN NWP MODELS

2.1. Treatment of Clouds

The treatment of clouds poses the greatest difficulty in NWP models. Clouds are discrete, and their scales can vary from 1 km to 1000 km (Lovejoy 1982). Cloud fields are typically observed to be extremely irregular and fragmented at all scales (Cahalan and Joseph 1989). In fact, their spatial distribution is fractal (Lovejoy 1982) with fractal dimensions differing for various cloud processes and cloud types (Carvalho and Silva Dias 1998). Clouds arise when water vapor changes phase to the liquid or ice phases. Several properties of a volume of air containing water vary substantially when these phase changes take place. Precipitation processes occur, radiative properties of the air volume change dramatically, and the attendant responses to these changes alter the evolution of weather.

Approaches to improve cloud forecasting are highly varied. One approach is to improve data assimilation methodologies and NWP initialization techniques. Efforts to decrease uncertainty in analysis data may also increase assimilation accuracy. The availability of new data types with higher spatial and temporal resolutions from satellite-based instruments provides more information on the state of the initial environment. These data also provide more information that can be used in the validation of model output to identify model weaknesses. New methods are continuously being developed to translate information from these data types into variables that can be assimilated by NWP models. Stochastic approaches have sought improvements in implicit prediction through statistical methodologies using model output statistics (MOS), conditional climatologies, multiple-linear-regression (MLR), and multiple-discriminate analysis (MDA). Another approach is to increase the sophistication of NWP models. This is achieved through the development of more sophisticated parameterization schemes to represent the in-cloud microphysical processes, cloud radiative feedbacks, and planetary boundary layer processes important in predicting low level moisture. Finally, the development of more powerful computer systems can make routine operational production of high-resolution cloud forecasts feasible. The approach taken in this study is to consider only the assimilation of clouds from discrete cloud observations.

The assimilation of discrete cloud observations to initialize a NWP model is difficult when a model's grid size is larger than the scale of the cloud. Assimilation of discrete cloud variables on model grids can be approximated through methods such as bulk parameterization (Rutledge and Hobbs 1983, Pielke 1984), which represent the aggregate effects of clouds. The presence of water in various phases within mesoscale systems necessitates that equations governing the evolution of water must be included in mesoscale models. Coincident with evolving water substance, the heat transferred during phase changes must be modeled as well. Processes that affect the mixing ratios of water substance and the quantity of heat transferred during phase changes occur at scales smaller than the cloud. Mesoscale

models must therefore parameterize for their influence. This is accomplished via bulk representation of the microphysics. In the simplest of mixed phase bulk parameterization schemes, liquid water and ice are categorized into four classes: cloud liquid water, cloud ice, rain, and snow. This classification method is based on the simple principle that cloud liquid water and cloud ice do not have appreciable fall velocities whereas rain and snow do (Pielke 1984).

In climate models, there has been success in assimilating clouds by estimating their distribution with idealized spectral distributions (e.g. Sengupta et al. 1990). This method is performed by fitting observations to probability density functions (PDF), such as Weibull, gamma, or lognormal PDF's, then finding the coefficients of these functions. Variational assimilation methods demand to know the error covariances of the observations. PDF's used in idealized spectral distributions have known statistical characteristics that make variational assimilation easier to accomplish.

Discrete clouds can also be assimilated through optimal interpolation methods (Daley 1991), which convert point measurements to a continuous field so that one can compare spatial distribution with the distribution of other continuous variables. Daley (1991) presents a comprehensive review of assimilation methods.

The evolution of mesoscale circulations, especially those associated with moist convection, is sensitive to the initial distribution of water in the atmosphere. For example, the timing and persistence of clouds are sensitive to the distribution of low-level water vapor (Hong et al. 1995). Surface outflow dynamics associated with supercells are sensitive to moisture content in the midtroposphere (Gilmore and Wicker 1998). It has been further demonstrated that storm strength is more sensitive to the variability in moisture than in temperature (Crook 1996). Complex cloud microphysical processes can produce perturbations in the distribution of moisture that alter the dynamical evolution of storms (Park, 1999). Storm predictability is strongly affected by such evolutionary changes in the distribution of moisture. When air parcels become saturated on ascent (cloudy), their potential energy increases due to the release of latent heat on further lifting. The potential energy of an atmospheric column is therefore sensitive to the amount and phase of the water existing in the column. A thought experiment demonstrating this principle is presented in Appendix C.

Radiative responses from clouds are also important. Clouds reduce surface insolation, decreasing near-surface daytime air temperatures. The contrast between cloudy and clear regions can produce boundary layer baroclinic zones and mesoscale circulations (e.g. Segal et al. 1986, Markowski et al. 1998). Betts and Boers (1990) assert that if rawinsonde data with low horizontal resolution is used in mesoscale modeling, the placement of cloud edges will be inaccurate and produce large errors in the local surface energy radiation budget. Conventional surface observations are not dense enough to adequately resolve cloud-shading contrasts important in circulations generated by differential cloud shading (Ruggiero et al. 1999).

2.2. Model Spin-Up

Model spin-up degrades cloud forecast accuracy during the first few hours of model integration. There is no standardized definition of model spin-up; however, the general quality of spin-up as it is described in the literature is consistent. Kristjansson (1992) defined model spin-up time as the time it takes for domain averaged precipitation and cloud cover to reach a semi-steady state. The spin-up period is characterized by unrealistically small amounts of cloud coverage and precipitation. It arises because of deficiencies in observations, analysis techniques, and initialization procedures. Lee and Krishnamurti (1995) similarly defined model spin-up as low equilibrium of the humidity field. The definition given by Mohanty et al. (1986) focuses on energy aspects by defining it as the persistence of deficient latent heating during the first few hours of model integration. Spin-up arises from inconsistencies of the initial fields with the dynamics and physical parameterizations of the model (Heckley 1985, Krishnamurti et al. 1991). Model spin-up can degrade the accuracy in predicting where clouds will form (e.g. Lejenas 1979, Mohanty et al. 1986). Model spin-up is sensitive to the initial analysis of the humidity field (Hammarstrand 1987). Further, enhancing initial relative humidity fields can reduce model spin-up times (Perkey 1976, Danard 1985, and Turpeinen et al. 1990).

Mesoscale NWP models are generally initialized with synoptic-scale analyses of continuous state variables (pressure, relative humidity, temperature, and horizontal winds). Synoptic-scale relative humidity fields do not contain saturated columns of water (clouds). In fact, bulk parameterization methods typically designate some threshold relative humidity far less than 100% to infer the existence of clouds. In mesoscale models, cloud-scale saturation generally occurs only after sufficient moisture convergence or vertical lifting during spin-up. In NWP, the potential energy of a modeled system is converted to kinetic energy through temporal integration of the model's governing equations. By not including observed cloud distribution data on model initialization, variables such as water vapor, cloud liquid water, cloud ice, rain, and snow are under-represented and result in underestimating the initial state's available potential energy. In most studies that use mesoscale models to simulate the evolution of observed weather phenomena, model spin-up has been considered unavoidable.

2.3. Initial Data Quality

Models produce better forecasts when initial data quality is improved. One objective in NWP is to determine as accurately as possible the state of the atmosphere in order to determine the values of the dependent variables required to begin integrating the model equations (Pielke 1984). A way to improve initial data quality is to simply assimilate as many observations as possible as long as those observations are either physically or dynamically linked to the model's dependent variables. Talagrand (1997) defined assimilation as a process in which observations distributed in time are merged together with a dynamical numerical model of the flow. Assimilation can be used for model initialization. One category of initialization methodology is called objective analysis. Objective analysis extrapolates

observed dependent variables to a model grid using a variety of techniques including least squares distances, optimal interpolation, and other variational analysis procedures (Pielke 1984). Another subset of objective analysis is physical initialization, which converts data retrieved from satellites and radar to model dependent variables before gridding. Assimilation of observations can be accomplished either by direct insertion or by variational assimilation. Direct insertion simply replaces background model values, generated from a previous forecast or initialization, with observed values of the dependent variables. Variational assimilation attempts to simultaneously minimize the variance between the observations and the analysis and between the background model values and the analysis.

It is important to include mesoscale features on initialization if mesoscale models are to forecast convective weather events better. Stensrud and Fritsch (1994) performed model simulations of weakly forced mesoscale convective systems using conventional initialization techniques and using techniques that initialize the model with mesoscale convective features. It was found that a mesoscale model was capable of producing a useful simulation of convective weather events but only when mesoscale convective features were included at the model's initial time. Fritsch and Chappell (1981) found that even large-scale models are sensitive to the specific initial locations of deep convection.

Tiedtke (1993) asserted that an effective way to improve cloud forecasts is to enhance the initial representation of clouds in the models. Assimilation of cloud data produces better predictions of mesoscale circulations. Lipton (1993) retrieved cloud radiative characteristics from geostationary satellite data and assimilated the data into a mesoscale model. For case studies over the Texas panhandle, both Lipton (1993) and McNider et al. (1995) found that assimilating cloud data produced better predictions of mesoscale circulations. Estimates of initial water vapor distributions over tropical regions are degraded by the scarcity of conventional observations and benefit from physical initialization (Mather et al. 1992, Krishnamurti et al. 1994). Using a physical initialization method in the Florida State University Global Spectral Model, Lee and Krishnamurti (1995) demonstrated that cloud forecast quality is improved and that model spin-up of clouds is considerably reduced. Forecast rain rates were compared to rain rates retrieved from satellite-based outgoing longwave radiation, special sensor microwave imager (OLR SSM/I), and raingauge data. The physical initialization method they used improved initial cloud amount and forecast cloud amounts over the tropics, reduced cloud amount spin-up time, improved predictive skill out to day four, and improved the balance between cloud shortwave forcing and longwave forcing.

A fundamental principle of initialization in NWP is that models initialized with mesoscale data have the potential to forecast mesoscale structure better than those initialized with synoptic-scale data. In other words, NWP models are sensitive to initial conditions (Lorenz 1963). Following this principle, mesoscale models initialized with cloud-scale cloud information have the potential to forecast cloud structure and distribution better than by initializing them with cloud information from only synoptic-scale data.

This chapter has reviewed work that supports the hypothesis that assimilation of cloud data at initialization could lead to an increase in the accuracy of a cloud forecast. The next chapter presents an overview of a new cloud initialization technique to further test this hypothesis.

CHAPTER III

CLOUD INITIALIZATION METHODOLOGY

3.1. Research Objectives

The hypothesis presented in the previous chapter posits that the evolution of weather is sensitive to initial cloud distribution, and that the assimilation of cloud-scale cloud data at initialization can lead to an increase in cloud forecast accuracy. To test this hypothesis, this research has three objectives. The first objective is to develop a technique to initialize a mesoscale NWP model with discrete cloud observations. The second objective is to determine if mesoscale NWP models with discrete cloud initialization have lower spin-up time. The third objective is to test whether a mesoscale NWP model can forecast cloud structure and distribution more accurately through discrete cloud initialization instead of relying wholly on model spin-up of clouds. This is accomplished by comparing analyzed clouds to clouds forecasted from a mesoscale NWP model with and without discrete cloud initialization.

3.2. Nephanalysis

The independent variable in this study is the cloud analysis. Satellite remote sensing offers the best source of cloud data. These data complement surface observations because they are homogeneous (with respect to collection from a single spacecraft) and spatially continuous as compared to point observations, data collection is frequent, and collection is at relatively low cost (Harris, 1987). Kärner and Keevallik (1993) suggested there are three methodical approaches to estimate cloud amount above a target area: visual ground-based observations, satellite nephanalysis, and satellite radiation measurements. The satellite nephanalysis method infers cloud properties primarily from visual satellite imagery at resolution and areal coverage far greater than can be achieved from direct visual observation. The first nephanalysis was based on early satellite television pictures (Arking 1964, Clapp 1964). The introduction of radiation measurement satellites in the late 1960's made it possible to extract even more cloud coverage information, particularly the altitude of cloud tops. These methods were merged by the U. S. Air Force into the three-dimensional nephanalysis model (3DNEPH, Coburn 1970) and later the Real-Time Nephanalysis model (RTNEPH, Fye 1978, Kiess and Cox 1988, Hamil et al. 1992). RTNEPH is part of the Cloud Depiction and Forecast System-I (CDFS-I), which consists of a system of computer processors, a centralized database, a data distribution network, and a set of meteorological models. RTNEPH, the cloud analysis portion of the CDFS-I suite of models, has been in operation since 1978. The RTNEPH today is a premier source of global cloud information including cloud type, coverage amount and layer depths. RTNEPH will be upgraded by 2002 to include geostationary satellite data sources as part of CDFS-II at Air Force Weather Agency (AFWA), Offutt Air Force Base, Nebraska (Sterling Software 1998).

The RTNEPH database is archived at Air Force Combat Climatology Center (AFCCC), Asheville, North Carolina (Zamiska and Giese 1986). It consists of cloud information merged from polar orbiting Defense Meteorological Satellite Program (DMSP) and National Oceanic and Atmospheric Administration (NOAA) weather satellites, and ground-based and sea-based hourly and special observations. Data is located to an 8th mesh grid (Hoke et al. 1979). The 8th mesh grid is composed of 512 x 512 horizontal data points on a Northern or Southern Hemisphere polar stereographic projection. Grid spacing provides a resolution of approximately 48-km at 60 degrees North and South latitudes. The database is updated within minutes following receipt of each quarter orbit from DMSP spacecraft in a 101-minute, sun-synchronous orbit. NOAA spacecraft data are used to update the database at three-hour intervals. Each RTNEPH grid point contains up to four 'floating' layers of cloud data. The archived database is available on synoptic hours (00, 03, 06, 09, 12, 15, 18, and 21 UTC). The primary elements of the database are listed in Table 3.1. A complete description of how RTNEPH data is used in this research is provided in Chapter IV.

Table 3.1. Some useful cloud data elements contained in the AFCCC RTNEPH database.

For each cloud layer (up to 4)
• Percent cloud coverage
• Cloud type
• Cloud base height
• Cloud top height
Total cloud coverage amount for all layers combined
Present weather (if available from surface station)
Visibility (if available from surface station)
Flags for presence of surface fog
Source parameters such as spacecraft identifier and data valid time

3.3. Cloud Initialization Scheme

Cloud data from RTNEPH must be translated to cloud variables that can be processed by a mesoscale NWP model. It is therefore necessary to convert RTNEPH data into mixing ratios of water vapor, cloud liquid water, cloud ice, rain, and snow. A cloud initialization scheme has been developed to accomplish this task. The scheme is fundamentally based on the work of Zhao (1993) and Zhao and Carr (1997); however, some important changes and additions have been made to their scheme to adapt it to the cloud analysis used in this research. The Zhao and Carr scheme is prognostic while this one is diagnostic. In addition, this scheme has been adapted to make use of explicit cloud scale information provided by RTNEPH and to work at higher resolution. The scheme is a sequence of four steps: 1) infer distributions of cloud variables from the RTNEPH data, 2) determine water phase and mixing ratios in the cloudy layers, 3) compute rain and snow mixing ratios, then 4) interpolate the data to the mesoscale NWP model grid.

The first step will input and distribute RTNEPH data to a very high-resolution three-dimensional grid (6 km - 18 km horizontal, 30 m - 300 m vertical grid spacing). The grid domain depends on the domain selected for a particular model simulation. In distributing the cloud coverage amounts, each layer in a column is tagged either cloudy (saturated) or clear (unsaturated). Surface temperature data is provided by the Air Force's surface temperature model (SFCTEMP) database (Kopp 1995, Westphal 1986) archived at AFCCC in 3-hourly increments on the 8th mesh grid. Temperature, pressure, and water vapor profiles will be used from a coincident Navy Operational Global and Regional Atmospheric Prediction Systems analysis (NOGAPS, Baylor and Lewit 1992). NOGAPS data is provided for each vertical column in the domain. The resulting columns of data will contain cloud type, cloud base, and cloud top for up to four layers of clouds, temperature, pressure, relative humidity, and horizontal wind vector components. The second step in the scheme will diagnose the phase of water in the cloud depending on cloud top temperature and level temperature. Once the phase of the water is determined at each level, adiabatic cloud liquid water and cloud ice concentrations will be computed. The third and most complex step of the scheme will diagnose precipitation rates for rain and snow. Evaporation and sublimation, coagulation and accumulation, and various melting processes that could occur in the cloud are estimated using bulk parameterizations. Mixing ratios of each cloud variable will be integrated from the top of the column downward so that precipitation falling from a higher level and evaporation between cloudy layers influences mixing ratios below. Using suitable raindrop and snow size distributions, rain and snow mixing ratios will then be diagnosed. The fourth step of the scheme will transform the vertical distribution of cloud liquid water, cloud ice, rain, and snow mixing ratios to the vertical coordinates matching the mesoscale NWP model grid. A detailed mathematical description of the cloud initialization scheme is given in Chapter V.

3.4. Mesoscale NWP Model

The primary dependent variables to be monitored in this research are mixing ratios of water vapor, cloud liquid water, cloud ice, rain, and snow. These variables are forecast by a mesoscale NWP model. The model selected for this study is the Pennsylvania State University / National Center for Atmospheric Research Fifth-Generation Mesoscale Model (PSU/NCAR MM5), version 3.3 (Grell et al. 1994). It is the mesoscale NWP model of greatest interest to the United States Air Force today (Doran et al. 1999) and has been in operational use at Air Force Weather Agency (AFWA) since 1998. It serves as part of the technological foundation of the Air Force Weather Director's weather support reengineering initiative (Lewis 1998). Under this initiative, MM5 is intended to enhance military regional forecast centers' ability to provide tailored, high-resolution cloud forecasts to their military customers. MM5 is also the model of choice of the U.S. Army Test and Evaluation Command (ATEC) (Swerdlin et al. 2001).

Up until January 2001, AFWA initialized MM5 using the Local Analysis and Prediction System (LAPS: McGinley et al. 1991) developed by the Forecast Systems Laboratory (FSL). New improvements to LAPS have added the capability to analyze cloud species, which can be used to initialize MM5 (McGinley and Smart 2001). However, LAPS was replaced in January 2001 by the Mesoscale Data Assimilation System / Multivariate Optimal Interpolation (MDAS/MVOI: Ritz et al. 2001). The MDAS/MVOI system replaced LAPS to increase the "relocatability" of the mesoscale model window, to increase assimilation processing speed, and to utilize observational data that varied greatly in quality and quantity from one operational area to another. MDAS/MVOI is not currently capable of assimilating clouds and precipitation.

Without the new version of LAPS, the ability to initialize clouds and precipitation is limited. There are currently only two techniques with which to incorporate cloud information when initializing MM5 at AFWA. The first is to use forecast cloud data from a previous model run through dynamic initialization. Dynamic initialization is commonly used at AFWA as a first guess initialization for temperatures, winds, and cloud variables. Without dynamic initialization, all cloud variables in the initialization file except water vapor are set to zero on initialization. Integration of the model equations then spins up cloud variables. MM5 has a four-dimensional data assimilation (FDDA, Grell et al. 1994) capability, but this method of initialization does not currently assimilate cloud variables other than water vapor. The second technique is to manually augment an input data file called MMINPUT_DOMAINn (Dudhia et al. 1999). This file contains all of MM5's gridded input fields including cloud variables. Manual input of clouds into this file is termed "direct insertion". A description of MM5's configuration and initialization is given in Chapter VII.

3.5. Analysis Method

In all modeling experiments conducted in this research, MM5 uses three nested domains centered over the Houston Ship Channel in Southeast Texas. The smallest grid spacing is set to 6 km in order to extract the greatest amount of information available from the cloud analysis. The smallest domain covers an area roughly 400 x 400 km^2. The largest domain covers most of the continental United States. Boundary and initial conditions are derived from coincident NOGAPS analyses. Starting at forecast hour -06, MM5 uses FDDA to "nudge" winds, temperatures, and water vapor distributions to analyses valid at forecast hours -03 and +00. Two pairs of experiments are conducted in this research. The first pair of experiments forecast clouds over the period 13 September 2000, 00-UTC (universal time coordinates) through 14 September 2000, 06-UTC (forecast hours -06 to +24). The next pair of experiments forecasts clouds over the period 14 September 2000, 12-UTC through 15 September 2000, 18-UTC (forecast hours -06 to +24). Each pair of experiments consists of a model initialized with clouds and one not initialized with clouds. For those models initialized with clouds, the cloud analysis is directly inserted to the model grid (replacing any spin-up cloud) at forecast times -06 and +00. Cloud

variables forecast by the model are then compared to the cloud analysis at three-hour intervals from forecast hours +03 to +24. A description of the synoptic situation for the two periods listed above is given in Chapter VII. Chapters IX and X detail the results of the experiments.

3.6. Research Environment and Challenges

RTNEPH, SFCTEMP, and NOGAPS analyses are provided by AFCCC in ASCII format. The MM5 model was run on SGI (Silicon Graphics, Inc.) Unix workstations using the IRIX operating system within the Professor Nielsen-Gammon working group in the Department of Atmospheric Sciences at Texas A&M University, College Station, Texas. High-speed computing resources are not required for this investigation but would be necessary for operational implementation of the technique. MM5 version 3.3 source code is made available by the National Centers for Atmospheric Research Mesoscale and Microscale Meteorology (NCAR MMM) Division. Analysis of the output data archives is conducted with FORTRAN-90 and IDL (Interactive Data Language: Research Systems, Inc.) visualization programs written specifically for this research.

The research conducted here is not without pitfalls. The diagnostic cloud physical parameterization used to convert RTNEPH clouds to mixing ratios of cloud variables cannot be used in reverse. Once mixing ratios are computed, there is no suitable method to "de-parameterize" the variables back to cloud amount, cloud layer depth, cloud type, etc. Additionally, statistical methods such as those employed by Norquist (1999) have so far proven unsatisfactory. Because of this barrier, MM5 output is not compared directly with RTNEPH but rather with variables parameterized from RTNEPH.

Another important problem is that MM5 uses a prognostic cloud physics scheme to produce mixing ratios of cloud liquid water, cloud ice, rain, and snow, while on the other hand, the cloud parameterization from the RTNEPH cloud analysis is diagnostic. The distributions and concentrations of cloud variables produced by these two methods may depart significantly. It was nevertheless expected that the fraction of the error vectors attributed to these differences would produce a consistent bias that could be measured and filtered during analysis of the model's performance.

A final problem involves previous results. In preliminary modeling tests at Air Force Weather Agency in 1999, initializing MM5 with high-resolution cloud information produced unexpectedly poor results (McAtee 1999). When a cloud-resolving grid is initialized with clouds and precipitation, clouds are not dynamically balanced with the large-scale environment without an initial distribution of vertical velocities on a similar scale. In that case, most of the clouds used in initialization dissipated rapidly resulting in almost no contribution to the evolving weather patterns forecast by the model. Similar results were found by Cram et al. (1995) when LAPS was used to initialize clouds in a mesoscale forecast model without a balance between the initial cloud vertical winds and large-scale horizontal momentum fields. In this study, no effort has been made to define a vertical velocity pattern matching RTNEPH clouds. Because this research hints at improvement through cloud parameterization on

initialization, the most logical succeeding step in future research would use a coincidentally high-resolution vertical velocity distribution matching the cloud analysis and balanced with the initial momentum field.

The following two chapters present the heart of the technique, which converts the RTNEPH analysis to variables that can be used to initialize MM5. Chapter IV presents the method used to distribute RTNEPH clouds to the model's grid, and Chapter V presents the method used to convert RTNEPH clouds to cloud variable mixing ratios.

CHAPTER IV

DISTRIBUTION OF RTNEPH

4.1. Vertical Distribution

Distributing RTNEPH cloud data to a cloud-resolving grid is problematic because the cloud coverage amounts are at 48-km resolution (8th mesh) -- too coarse for explicit precipitation schemes. (See Figures 4.1 and 4.2. Also, see Hoke et al. 1979 for a detailed description of the RTNEPH data grid.) The RTNEPH data does however contain "implied" cloud coverage information at much higher resolution. Cloud amounts are given in percent for up to four floating layers. These cloud layers are formulated to overlap following the assumption that the unobscured fraction of cloud at lower levels represents the total fractional coverage for that layer.
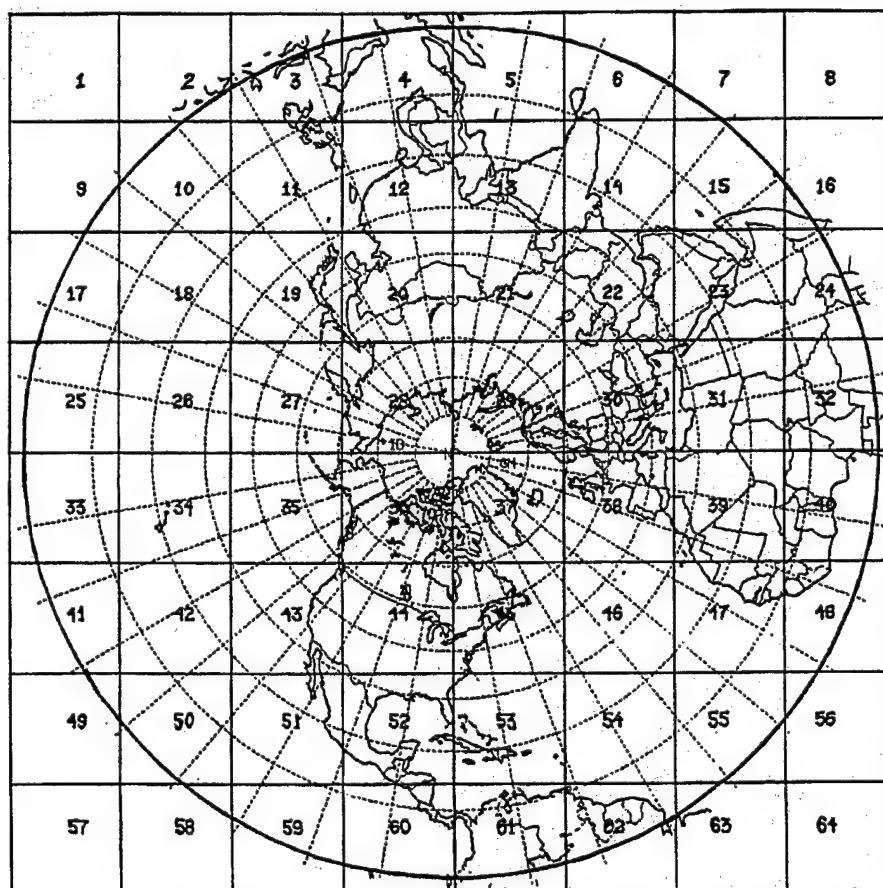
Figure 4.1. Northern Hemisphere RTNEPH grid over a polar-stereographic projection. Each square partition is an RTNEPH box (1600 nm on a side). Corner boxes are not used. Reproduced from Figure 2.1, pg. 4 of Kiess and Cox (1988) with permission.
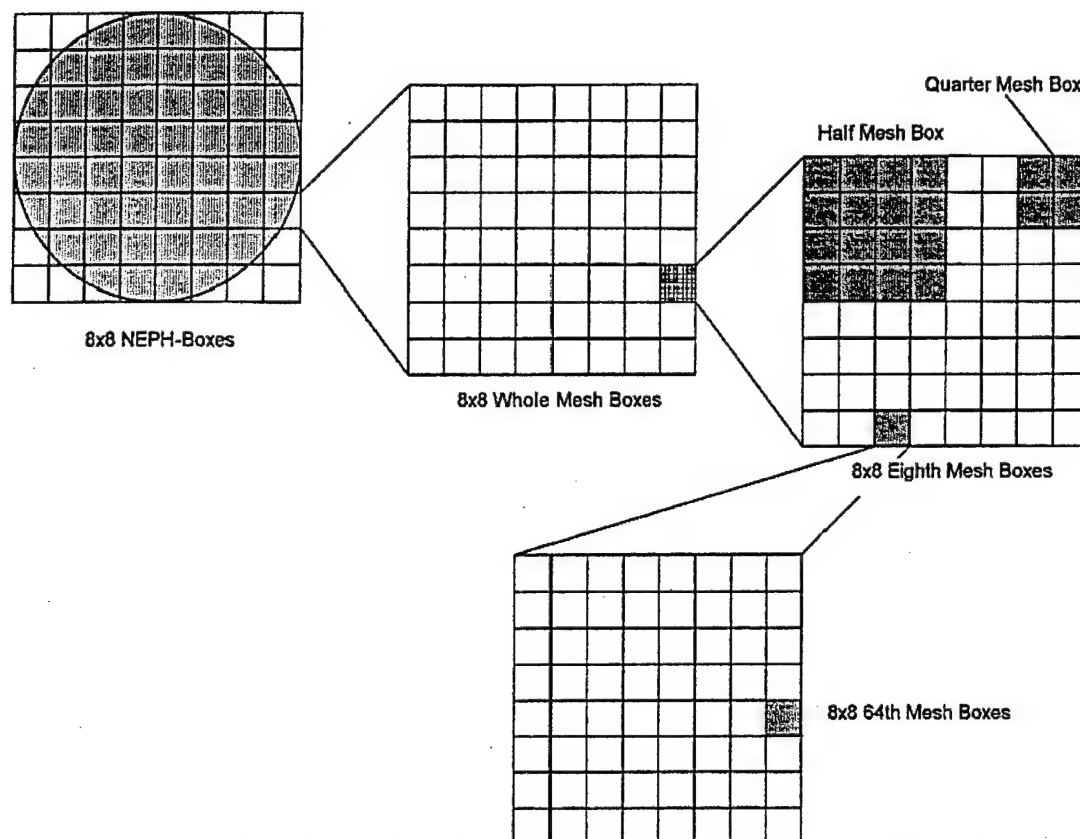
Figure 4.2. Mesh division from a Neph-Box grid on a hemispheric polar-stereographic projection down to 64th mesh (6 km or resolution of a cloud pixel). RTNEPH analysis data is archived at 8th mesh (48 km) resolution.

A problem arises in how precipitation is calculated within the 8th mesh volume. The precipitation scheme (described in Chapter V) integrates downward various cloud properties including the mixing ratios of water vapor, cloud liquid water, and cloud ice. Within a single 8th mesh volume, the vertical profiles of these mixing ratios can take several simultaneous forms. Imagine a stone dropped from the highest level of an 8th mesh volume containing one cloud layer. If the cloud amount is less than 100%, the stone can take two possible paths. It can fall entirely through unsaturated, cloud-free air or it can fall through a layer of cloudy, saturated air. It becomes more complicated as cloud layers are added. Two layers for instance could result in the precipitation integration (path of a falling-stone) only through cloud-free air, only through layer-1, only through layer-2, or through layers 1 and 2. Thus for the two cloud layer volume, a precipitation path could be calculated for up to four possible vertical profiles of cloud. Figure 4.3 illustrates a typical 2-layer case. In this case, three possible precipitation profiles must be computed. 40% of an 8th mesh area is rain free, 40% is under layer-1 only precipitation, 10% is under layer-2 only precipitation, and 10% is under layer-1 and layer-2 precipitation. The cloud-free profile would undoubtedly produce no precipitation. However, the

remaining three profiles would produce different precipitation rates depending on the depth, altitude and composition of each cloud layer, and on the amount of seeding from layers above. The result is a group of precipitation rates for the 8th mesh volume, each precipitation rate applying to a particular fraction of the 8th mesh volume.

The problem that must be solved here is how a group of 8th mesh volume precipitation rates will be distributed to a cloud-resolving model grid. The devised method must spatially distribute the precipitation rates among the model grid points to adequately represent precipitation and latent heating occurring over the entire 8th mesh volume. Using a maximum or average precipitation rate to represent the entire 8th mesh volume is unacceptable. An 8th mesh volume initialized with the strongest precipitation rate would introduce too much precipitation and diabatic heating potential. An average profile applied equally to all the cloud resolving grid points within the 8th mesh volume would not adequately represent variation among cloud resolving profiles of diabatic heating implied by the data. The objective here is to develop a method that will initialize a cloud-resolving grid with all of the cloud profiles implied within the 8th mesh volume.
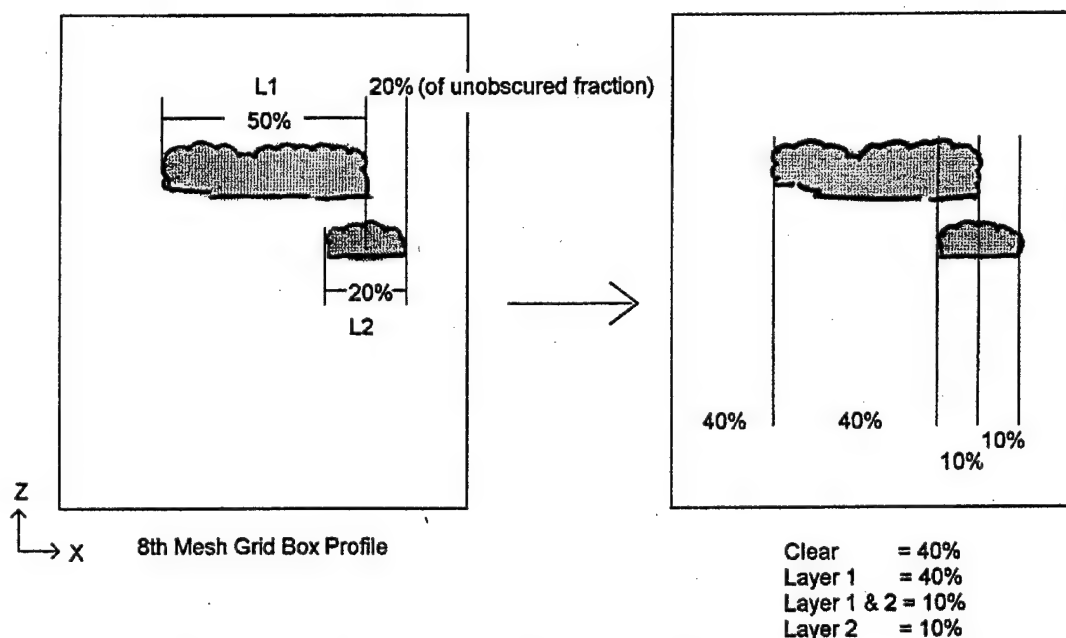
Figure 4.3. A typical 2-layer case with 50% coverage for the highest layer and 20% cloud amount for the bottom layer. Total cloud amount is 60%.

The following distribution algorithm is used to determine how many cloud layers are contained within the 8th mesh volume and what fraction of the 8th mesh volume each cloud profile occupies. Table 4.1 indicates that there are up to 2^n cloud profiles possible depending on the number of cloud layers

observed, n. The profiles are listed in order of decreasing potential for precipitation. Distributing cloud coverage amount to a finite number of grid points introduces rounding errors. For instance, a 70% cloud coverage amount distributed to 64 grid points results in a rounding error of about half a percent. While not significant, rounding errors could cumulatively eliminate consideration of some profiles that occupy only a small fraction of the 8th mesh volume. Therefore, those profiles most likely to produce precipitation are preferred over others under the assumption that it is better to over-represent precipitation than to under-represent it. Profiles with adjacent cloud layers are preferred over those with larger distances between layers. Profiles with layers only near the surface are preferred over profiles with only high layers.

Table 4.1. Possible cloud layers included in a cloud profile within an 8th mesh volume containing no layers, one layer, two layers, three layers or four layers. Possible profiles are listed in order of preference to maximize precipitation potential for a given profile. Layer-1 is the highest layer.

0 Layers	1 Layer	2 Layers	3 Layers	4 Layers
0	1	1,2	1,2,3	1,2,3,4
	0	2	2,3	2,3,4
		1	1,2	1,2,3
		0	1,3	1,3,4
			3	1,2,4
			2	3,4
			1	2,3
			0	1,2
				2,4
				1,3
				1,4
				4
				3
				2
				1
				0

The fraction of the 8th mesh volume that each cloud profile occupies may be diagnosed from the cloud coverage amounts at each layer. In formulating cloud coverage amounts for multiple layers, RTNEPH makes spreading assumptions about clouds obscured by higher layers. The basic assumption is that the fraction of the total area unobscured by upper layer clouds that contains lower layer clouds is equal to the fraction lower layer obscured by cloud.

Deconstruction of the cloud layer amounts into obscured and unobscured fractions can be solved from a simple system of 45 equations. Construction of the cloud profiles follows a simple top-down procedure. Layer-1 cloud coverage amount is first distributed to the cloud resolving grid points within the 8th mesh volume. Designate this unobscured cloud coverage amount as $_1U$. The left subscript 1 indicates layer-1. A 50% cloud coverage amount is illustrated in the top layer of Figure 4.4. The fraction of the 8th mesh volume covered by layer-1 clouds is given by the fraction $_1f_1$, and the fraction of

the 8th mesh volume that is cloud free at layer-1 is given by the fraction $_1f_0$. The subscript on the left indicates layer of interest, and the subscript on the right indicates which layers above the point are obscuring the point. If layer-1 cloud coverage amount from the RTNEPH data is designated L_1 then $_1f_1$ and $_1f_0$ are computed following equation 4.1:

$$\left.\begin{array}{l} _1U = L_1 \\ _1f_1 = _1U \\ _1f_0 = 1 - _1U \end{array}\right\} Layer \quad 1 \tag{4.1}$$
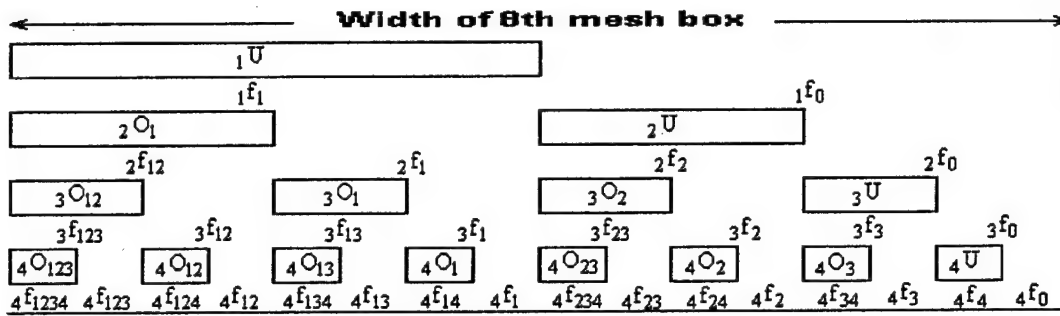
Figure 4.4. Illustration of assumed horizontal cloud distribution for four cloud layers having 50% cloud coverage amount on each layer.

Next, the fraction of layer-2 cloud coverage amount obscured by layer one ($_2O_1$) is placed beneath the appropriate fraction of layer-1 cloudy points. The unobscured fraction of the layer-2 cloud coverage amount (U_2) is distributed to grid points not obscured by layer-1. When distributing the obscured fraction of the layer-3 cloud coverage amounts ($_3O_{12}$, $_3O_1$, and $_3O_2$) beneath layer-2, preference is given according to Table 4.1. This ensures a maximum precipitation distribution. When the entire obscured fraction of layer-3 cloud coverage amount has been distributed, the remaining unobscured fraction of the layer-3 cloud coverage amount (U_3) is distributed to any point not obscured by either layer-1 or layer-2. When distributing the obscured fraction of layer-4 cloud coverage amounts ($_4O_{123}$, $_4O_{12}$, $_4O_{13}$, $_4O_1$, $_4O_{23}$, $_4O_2$, and $_4O_3$) beneath layer-3, preference is similarly given first to points obscured by all layers then by lower adjoining layers. When the entire obscured fraction of the layer-4 cloud coverage amount has been distributed, the remaining unobscured fraction of the layer-4 cloud coverage amount (U_4) is distributed to any point unobscured by cloud from above. The full 45-equation set used to compute the fractions of the 8th mesh volume obscured by the various cloud profiles is given in Appendix F.

For each profile created, the cloud coverage amount at each layer is assumed either 0% (cloud-free) or 100% (cloudy) for integration purposes. The cloud profiles (vertical distributions of mixing ratios of

cloud liquid water, precipitation, snow, etc.) are diagnosed following the scheme outlined in Chapter V. As mentioned previously, the cloud profile is assigned to an appropriate fraction of cloud resolving model grid points contained in the 8th mesh volume. Now that the fraction of an 8th mesh area has been determined for each possible cloud profile, it is necessary to determine how that profile will be horizontally distributed.

4.2. Horizontal Distribution

In the atmosphere, cloud distribution depends on dynamic and thermodynamic factors interacting on several scales (Carvalho and Silva-Dias 1998). Betts and Ridgway (1988) determined that different cloud parameterizations influence surface energy budgets differently and consequently affect the evolution of precipitation systems. Weger et al. (1992) noted that several cloud distribution studies find some cloud fields clustered or regular. Varying geometric complexity in clouds also influences cloud radiative properties (Davies 1984). Thus, changes in cloud distribution alone can change the evolution of weather (Han and Ellingson 1999).

a. Distribution definition

Distribution is composed of two elements: cloud dimension and cloud separation distance. The distribution method must parameterize these two elements. The complexity in the spatial distribution of clouds is believed to be due to variations in topography, surface features, boundary layer processes, or even data sources. There are three general methods to parameterize cloud distribution, all of which are used in various general circulation models (GCM). These three methods are patterned, random, and fractal. Because mesoscale models have supposed cloud resolving resolution and explicit cloud and precipitation schemes, there has traditionally been no need to parameterize cloud distribution.

b. Patterned distributions

A patterned distribution method is defined here as a method that calculates a probability distribution function for cloud separation distance based on an analytic function. Examples of the most popular distribution functions are the Wiebull distribution, the log-normal distribution, the power-law distribution, and the gamma distribution (Sengupta et al. 1990). In comparing these distributions against high-resolution satellite imagery, Sengupta et al. found that the Wiebull distribution best represented cumulus clumping behavior, while the log-normal distribution best represented nearest-neighbor spacing. Han and Ellingson (1999) found that size distribution has a significant impact in influencing radiative fluxes in GCM's when the cloud fraction is between 0.2 and 0.8, but is insensitive for cloud fractions less than 0.2 or aspect ratios less than 0.5. [Han and Ellingson defined cloud aspect ratio $\beta = 2h/D$, where h is thickness, and D is side length.] Because the methodology of Han and Ellingson was to calculate the probability of a clear line of sight through the clouds, they found that all

of the above analytic expressions produced similar probabilities. It appears that the choice of distribution function was not that important in their results. However, it was found that different distributions best match different observations in terms of nearest neighbor distances or "clumpiness" behavior.

c. Random distributions

Random cloud distributions of clouds are examined with models designed by Ellingson (1982), Harshvardhan and Weinman (1982), and Naber and Weinman (1984). It was found that compared to a regular cloud field, a random cloud field allows more visible cloud sides and thus gives larger equivalent cloud fractions. In other words, random cloud fields produce higher radiative fluxes than patterned cloud fields. In analyzing Landsat, Advanced Very High Resolution Radiometer (AVHRR), and Skylab imagery, Zhu et al. (1992) drew the following conclusions about real cloud distributions:

- Cloud fields tend toward clustering when small clouds are included.
- Cloud distribution appears random when clouds less than 250 m in diameter are eliminated from a sample.
- Clouds with diameters larger than 500 m have a strong signal or regularity in statistical analysis.
- Clouds less than 1 km in diameter have an average spacing that is 3 to7 cloud diameters.
- The ratio of cloud spacing to cloud diameter (one possible measure of fractal dimension) increases sharply with increasing diameter.

Zhu et al. asserts that clouds organize because of physical processes: Clouds mutually suppress circulations; eddies and gravity waves organize clouds, etc. This suggests that a patterned distribution may be superior to a random distribution for clouds with diameters greater than 500 m.

d. Fractal distributions

The final distribution method considered here is the fractal distribution method. Before describing what a fractal distribution could contribute to cloud modeling, it is instructive to first define fractals. Fractals are shapes with structure at all scales but with no characteristic length (Mandelbrot 1982). Fractal means "fractional dimension". Fractals have the property of self-similarity at various scales, and they are modeled by continuous but not differentiable functions. Fractal dimension gives the degree of complexity of a fractal surface. It quantifies the static geometry of an object. Fractal dimension has other names such as box dimension, or more rigorously defined as the capacity dimension, or Hausdorff dimension (Eckman and Ruelle 1985).

The fractal dimension may be defined simply as:

$$D = - \lim_{\varepsilon \to 0^+} \frac{\log N(\varepsilon)}{\log \varepsilon} \tag{4.2}$$

where　D　Fractal dimension,

　　　　ε　Upper limit for the radius of a ball

　　　　$N(\varepsilon)$　Fewest number of balls of radius $\leq \varepsilon$ needed to cover compact subset S of metric space.

Fractal dimension can be defined mathematically with a varying degree of rigor. Sometimes, simple methods of computing fractal dimension are limited -- for instance, a more robust definition for the fractal dimension is required because equation 4.2 is undefined if $\varepsilon = 1$. From the above mathematical expression, the fractal dimension may be represented by the power law slope formula:

$$\lim_{\varepsilon \to 0^+} N(\varepsilon) = \varepsilon^{-D} \tag{4.3}$$

Box dimension is a simplified definition that assumes stackable squares or cubes of side length ε instead of balls or circles with radii ε. This method lends itself well to computation such as that performed in Gotoh and Fujii (1998).

Apart from the idealized definition, fractals in nature are the geometric shapes arising from physical processes at various scales. Fractal geometry provides a model to investigate complex cloud shape and distribution. Self-similarity at several scales in clouds has been found from satellite and radar imagery. Lovejoy (1982) asserted that shapes in cloud and rain regions are fractals because they have no discernable characteristic length scale between one kilometer and planetary scale. Using an area-perimeter relation, Lovejoy analyzed tropical cloud and radar echo patterns and found their fractal dimension is roughly 4/3. Lovejoy is frequently sited as a foundation for studies involving the fractal dimension of clouds.

Clouds also exhibit the property of being "multi-fractal" in that subsets of observed clouds associated with unique mesoscale physical processes have different fractal dimensions. Rys and Waldvogel (1986) found the fractal dimension of mid-latitude hail clouds changes abruptly above a threshold cloud diameter. Cahalan and Joseph (1989) found different fractal dimensions for different cloud types and maturity within the subtropical boundary layer. Gotoh and Fujii (1998) found the fractal dimension of cumulus clouds changed when cloud area and cloud base height exceeded certain thresholds. Carvalho and Silva-Dias (1998) also found fractal dimension varied with cloud-scene coverage amount and with cloud distribution. In these studies, the changes in fractal dimension are attributed to differently scaled physical processes that contribute to cloud formation. The continuing discovery of the multifractal nature of clouds and cloud systems could lead to the development of ways to perform automated identification of certain mesoscale features mentioned here (Gotoh and Fujii 1998).

e. Distribution selection

Apparently, the literature suggests that in formulating a cloud parameterization, cloud type, cloud amount, and mesoscale cloud structure must be considered to optimally identify a fractal dimension with which to parameterize cloud distribution. The limitations of the model grid and the source data must be considered though. The RTNEPH data is based on pixels at 6-km resolution. The distribution of clouds can only be considered independently for each 8th mesh box. Distribution is therefore limited to scaling information from cloud sizes ranging from only 6 km (the size of a cloud pixel) to 48 km (the

size of an 8th mesh grid box). Cloud coverage may be part of a feature scaled larger than 48 km so it is not realistic to utilize fractal dimensions applicable only to the 6 km to 48 km range. Another shortfall of using fractals to distribut clouds is that fractal dimension addresses horizontal size distribution but does not address inter-cloud distance distributions. A patterned or random distribution of inter-cloud distances is therefore left for consideration. Recalling the results of Han and Ellingson (1999), a distribution pattern matching clouds with one degree of clumpiness will not necessarily match clouds with another degree of clumpiness. A determination of clumpiness is not possible from the RTNEPH data except at scales larger than 8th mesh so no best distribution pattern can be selected. In this scheme, cloud profiles will therefore be randomly horizontally distributed within the 8th mesh area at 6-km and 18-km resolution. Each 8th mesh box contains (8 x 8) 6-km profiles or (3 x 3) 18-km profiles.

Figure 4.5 illustrates how RTNEPH clouds are horizontally distributed. These figures are created by shading the temperature of the highest cloud top for each cloud column (similar to an infrared or IR satellite image -- lighter for high clouds and darker for low clouds).

In summary, RTNEPH cloud variables are first deconstructed to 2^n possible profiles explicitly defining the occurrence of cloud at various levels. The horizontal fraction of the 8th mesh box containing any given profile is also computed to the nearest 6-km and 18-km increments. These profiles are then randomly distributed within the 8th mesh box. The following chapter presents a detailed mathematical description of how these cloudy/cloud-free layers are converted to mixing ratios of cloud variables suitable for initializing MM5.
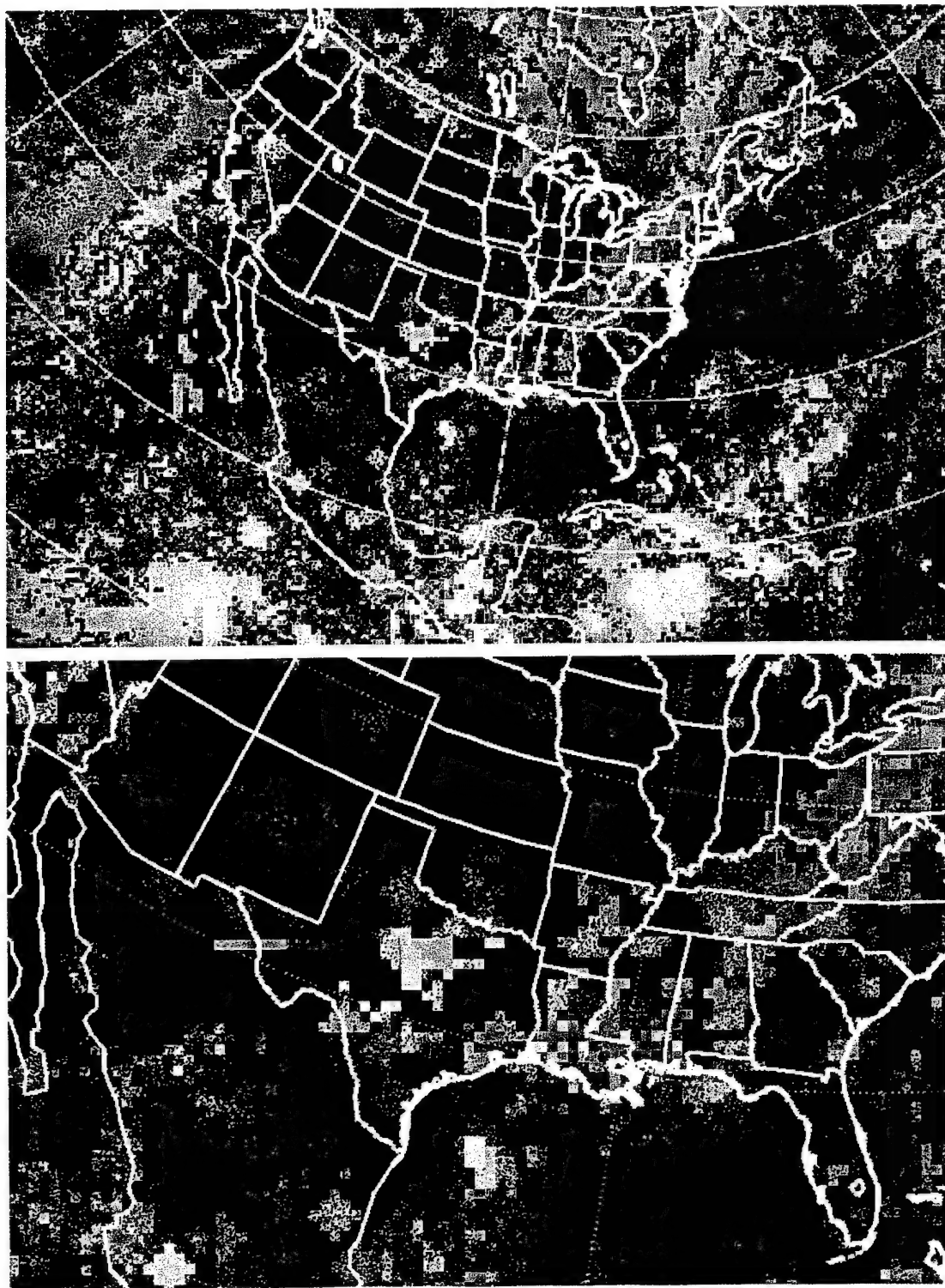
Figure 4.5. Pseudo-IR image of RTNEPH cloud coverage randomly distributed to an 18-km grid (top), and to a 6-km grid (bottom). Both images are valid on 13 September 2000, 00-UTC.

CHAPTER V
CLOUD INITIALIZATION SCHEME (CIS)

5.1. Introduction

The challenges to calculating mixing ratios of rain and snow arise from the precipitation formation process that involves complicated interactions among precipitation particles of different sizes, shapes, and phases. The proposed scheme must account for limitations to computing resources available for operational NWP models, and for the unavailability of observations of particle size, shape, phase, and distribution. The bulk parameterization method introduced by Kessler (1969) is used here to reduce the computational power necessary to estimate mixing ratios of rain and snow and to make up for the lack of detailed microphysical observations.

The cloud initialization scheme (CIS) has five steps. In the first step, RTNEPH clouds are distributed horizontally and vertically. The method used to perform this step was presented in Chapter IV. In the second step, NOGAPS analyzed temperature profiles are used to estimate the liquid water content of the cloud at various levels in the cloud. Bulk parameterizations are used to determine the fraction of the liquid water content that will be in ice phase while conserving liquid water and ice contents. Liquid water and ice contents are then converted to mixing ratios. After liquid water and ice mixing ratios have been determined, the third step employs several bulk parameterizations for the principal microphysical processes associated with the formation of rain and snow to compute precipitation release rates. The greatest strength of this method is that precipitation release rates are diagnostically calculated directly from the cloud liquid water and cloud ice mixing ratios. In the fourth step, precipitation rates are found by vertically integrating the precipitation release rates downward from the top of the cloud column. The fifth and final step computes rain and snow mixing ratios, which are solved from idealized size distributions that are functions of rain and snow rate. This eliminates the requirement of computing terminal velocities of precipitation particles, which would require greater computing resources. The following sections describe in great mathematical detail how mixing ratios of cloud liquid water, cloud ice, rain, and snow are computed using RTNEPH clouds and NOGAPS temperatures, dewpoints, pressures, and geopotential heights. This chapter presents steps two through five. The reader is referred to Appendix B for variable definitions if they are not defined within the text.

5.2. Water Phase and Concentration

Bulk parameters such as vertical velocity, cloud age, cloud condensation nuclei concentration, etc., are not available from the RTNEPH cloud analysis, therefore no ratios of supercooled water to ice at a given level can be directly inferred. Two methods, which estimate phase of cloud water, were considered. The Zhao and Carr (1997) scheme, which is used in the Meso-Eta model, uses a very

simplistic approach. At a particular level in the cloud, cloud particles may be either liquid, supercooled liquid, or ice -- ice is not analyzed in a layer containing cloud liquid water. When the Reisner et al. (1998) mixed phase physics scheme is used in MM5, ice can occur at all levels above the melting line in the presence of cloud liquid water. Later, in the experimental portion of the research, MM5's forecast of cloud ice and cloud liquid water is compared to mixing ratios produced by CIS. To increase the compatibility of the CIS mixing ratio analysis to the MM5 mixing ratio forecast, the method used to determine the ice cloud fraction must follow that used in MM5. If CIS is to be designed for the Meso-Eta model, the method proposed in Zhao and Carr (1997) should be used. CIS must be compatible to the mesoscale model. In fact, wherever possible, the same or similar diagnostic bulk parameterizations used in MM5 are used in CIS. The principle of the scheme is to adopt as much of the cloud physics used by the model as possible.

At the outset, it must be stated that this scheme does introduce severe limitations on the types of processes that can be modeled to estimate rain and snow. Graupel growth mechanisms are ignored. Snow crystals and graupel can grow by riming and contact freezing. Supercooled droplets can freeze and splinter. The release of latent heat of fusion after supercooled droplets collide with an ice crystal could warm the ice crystal and vary its diffusional growth rate or cause wet growth. They can accumulate on graupel to form a slushy state as well. These changes can influence the melting rate of snow and graupel after passing downward through the melting level. These complex processes are nevertheless ignored in CIS.

a. Adiabatic liquid and ice water contents

Estimates of the mixing ratios of water vapor, cloud liquid water, and cloud ice must be found first. Clouds are assumed to be saturated water vapor layers containing condensed droplets or ice crystals. Water vapor concentration within the cloud is assumed saturated (100% relative humidity, RH) with respect to the phase of the cloud particles and to the temperature and pressure at the given level. There is no water vapor super-saturation used in this scheme.

Cloud liquid water structure is approximated using parcel theory. Saturated parcels rising adiabatically through a specified vertical distance produce a known quantity of liquid water, the adiabatic liquid water content, which can be integrated through the depth of the parcel ascent to yield the integrated adiabatic liquid water content. The depth of parcel ascent is determined by the RTNEPH analyzed cloud base and cloud top heights. During a typical cloud's growth, rising moist air becomes saturated at the cloud's base then undergoes adiabatic ascent upward to the cloud's top. The adiabatic liquid water content represents the theoretical upper bound on cloud liquid water condensed for a rising parcel. Following Rogers and Yau (1989), adiabatic changes in temperature are related to changes in water vapor mixing ratio at constant pressure.

$$c_p dT = -L_c dw \left[\left(\frac{1}{1+w} \right) \left(\frac{1}{1+0.9w} \right) \right] \tag{5.1}$$

The correction factor in brackets takes into account the difference in specific heats for moist air and dry air. This correction factor is near unity and is often ignored to facilitate easy integration of water vapor mixing ratio. Temperature (T), specific heat of dry air at constant pressure (c_p), latent heat of condensation (L_c), and water vapor mixing ratio (w) are then related by the simplified expression:

$$c_p dT = -L_c dw \tag{5.2}$$

At saturation, this expression becomes:

$$\frac{c_p dT}{L_c} = -dw_s \tag{5.3}$$

Once a rising parcel of moist air becomes saturated at cloud base, further lifting causes the parcel to expand pseudo-adiabatically and condense or deposit the water vapor onto liquid droplets. The saturation mixing ratio, w_s, decreases by the amount dw_s. The amount of water that must be deposited to keep the parcel exactly saturated is denoted $d\chi$.

$$d\chi = -dw_s = \frac{c_p dT}{L_c} \tag{5.4}$$

In equation 5.4, dT represents the difference between the incremental change in temperature and the change that would occur if the parcel were cooling dry adiabatically. To compute the adiabatic water content between a cloud's top and base, simply solve the following integral relationship from cloud base, C_b, to cloud top, C_t:

$$\int_{C_b}^{C_t} d\chi = c_p \int_{C_b}^{C_t} \frac{dT}{L_c} = c_p \int_{C_b}^{C_t} \frac{\Gamma_d - \Gamma_m}{L_c} dz \tag{5.5}$$

The terms Γ_d and Γ_m represent the dry adiabatic and saturated (moist) adiabatic temperature lapse rates with height. The latent heat associated with the process is assumed invariant with height but is kept within the integral to represent the appropriate value depending on the phase change that is to take place. The saturated adiabatic lapse rate is computed as follows:

$$\Gamma_d = \frac{g}{c_p} \tag{5.6}$$

$$q_{sw} = \frac{\varepsilon e_{sw}}{p - e_{sw}} \tag{5.7}$$

$$q_{si} = \frac{\varepsilon e_{si}}{p - e_{si}} \tag{5.8}$$

$$\Gamma_m = \Gamma_d \left(1 + \frac{L_c q_{sw}}{R_d T} \right) \Bigg/ \left(1 + \frac{L_c^2 \varepsilon q_{sw}}{R_d c_p T^2} \right) \tag{5.9}$$

$$e_{sw} = 611.2 \exp\left[17.67\left(\frac{T-T_0}{T-29.65}\right)\right] \tag{5.10}$$

$$e_{si} = 611.0 \exp\left[22.514 - \frac{6150}{T}\right] \tag{5.11}$$

Γ_m Moist lapse rate [K m^{-1}]
Γ_d Dry adiabatic lapse rate [K m^{-1}]
L_c Latent heat of condensation = 2.5 x 10^6 J kg^{-1}
g Acceleration of gravity = 9.8 m s^{-2}
T Temperature [K]
T_0 Reference melting temperature = 273.15 K
p Pressure [Pa]
c_p Specific heat of dry air at constant pressure = 1004 J K^{-1} kg^{-1}
R_d Gas constant for dry air = 287 J K^{-1} kg^{-1}
q_{sw} Saturation mixing ratio with respect to liquid water [kg kg^{-1}]
q_{si} Saturation mixing ratio with respect to ice [kg kg^{-1}]
e_{sw} Saturation vapor pressure with respect to liquid water [Pa]
e_{si} Saturation vapor pressure with respect to ice [Pa]
ε Ratio of molecular weights water to dry air = 0.622

The saturation vapor pressure used in the calculation at this point in the scheme is only with respect to the liquid water phase of the cloud particle. Using simple parcel theory, mixing ratios are computed upward from the base of the cloud using the temperature and pressure at the cloud's base. The maximum adiabatic cloud liquid water content and cloud liquid water mixing ratio at a given level within the cloud are computed as follows:

$$\chi(\sigma) = \int_{\sigma=C_b}^{\sigma=\sigma} d\chi \tag{5.12}$$

$$q'_c(\sigma) = f\chi(\sigma)/\rho(\sigma) \tag{5.13}$$

$\chi(\sigma)$ Adiabatic liquid water content [kg m^{-3}] at level σ
$q'_c(\sigma)$ Cloud liquid water mixing ratio [kg kg^{-1}] at level σ
f Fraction of adiabatic liquid water content retained as a function of cloud type
$\rho(\sigma)$ Air density [kg m^{-3}] at level σ

To account for processes such as entrainment and accumulation by precipitation particles in the cloudy column, only a fraction of these mixing ratios is retained. Rogers and Yau (1989) found that observations of cloud liquid water are only about half of their adiabatic value. This is due to conversion to precipitation particles, and to evaporation processes from mixing of environmental air through the cloud sides, and from penetrative downdrafts from the cloud top. Adiabatic cores are sometimes observed in large convective systems but these are not parameterized in this scheme. Observations of cumuliform and stratiform clouds reveal that both cloud types exhibit less than adiabatic liquid water contents. Generally, stratiform clouds have higher liquid water contents than cumuliform clouds. In this scheme, the resulting mixing ratios of cloud liquid water and cloud ice are set according to cloud type (Table 5.1). These values are selected based on tuning experiments (some of which are presented in Chapter VI) to produce reasonable cloud species mixing ratio profiles. Cloud type specific fractions are necessary because RTNEPH employs default cloud thickness as a function of cloud type in regions

of sparse surface observations. Without adjusting the fraction of adiabatic cloud liquid water retained, some cloud types produced too much cloud liquid water and resulted in over-production of precipitation.

Table 5.1. Fraction of adiabatic liquid and ice content retained for each cloud type.

Cb: 10%	St: 40%	Sc: 20%	Cu: 10%	As: 20%
Ns: 80%	Ac: 20%	Cs: 10%	Cc: 20%	Ci: 10%

b. Ice parameterization

In MM5, water species mixing ratios can change due to horizontal advection, divergence, vertical advection, diffusion, and conversion from one phase to another. The following equation, used to forecast cloud ice, is adapted from Grell, et al. (1994; chapters 2 and 5).

$$
\frac{\partial p^* q_i}{\partial t} = -m^2 \left[\frac{\partial p^* u q_i / m}{\partial x} + \frac{\partial p^* u q_i / m}{\partial x} \right] \quad \text{horizontal advection and divergence term}
$$

$$
- \frac{\partial p^* q_i \dot{\sigma}}{\partial \sigma} \quad \text{vertical advection term}
$$

$$
+ q_i DIV \quad \text{non - hydrostatic divergence term}
$$

$$
+ p^* \left(P_{II} + P_{IC} - P_{ID} \right) \quad \text{phase conversion process term}
$$

$$
+ D_{q_i} \quad \text{diffusion and vertical mixing term}
$$

(5.14)

q_i	Cloud ice mixing ratio
p^*	Difference between surface pressure and model lid pressure
m	Map scale factor
u, v	Components of horizontal wind
$\dot{\sigma}$	Vertical velocity in sigma coordinates
DIV	Non-hydrostatic divergence equation
D_{qc}	Diffusion and vertical mixing equations
P_{IC}	Release rate for heterogeneous freezing of cloud water to cloud ice [s^{-1}]
P_{ID}	Release rate for deposition of water vapor onto ice particles [s^{-1}]
P_{II}	release rate for cloud ice initiation [s^{-1}]

The phase conversion process term is subdivided into three terms commonly called release rates (e.g. Sundqvist et al. 1989), which are the rates at which the mass of a water constituent per unit mass of moist air is converted from one phase to another.

At this point in the scheme, the only cloud constituents in the cloudy column are saturated water vapor and cloud liquid water. The next step is to diagnose cloud ice by estimating four processes:

- Rate of ice initiation,
- Rate of deposition of water vapor onto ice crystals,
- Rate of Heterogeneous freezing, and
- Homogeneous freezing

A cloud ice mixing ratio is estimated from these four processes and the cloud liquid water content is adjusted to account for the transfer of liquid mass to the ice phase. The release rate for cloud ice initiation follows Grell et al. (1994) and is given by the formula,

$$P_{II} = \max\left[(M_0 n_c - q_c)/\Delta t, \; 0\right]$$ (5.15)

P_{II} release rate for cloud ice initiation [s⁻¹]
q_c Cloud liquid water mixing ratio [kg kg⁻¹]
M_0 Mass of smallest ice particle = 10^{-12} kg
n_c Number concentration of ice nuclei [m⁻³]
Δt Characteristic time step [s]

Fletcher's (1962) formula provides an estimate for the number concentration of ice nuclei (n_c),

$$n_c = 10^{-2} \exp\left[0.6(T_0 - T)\right]/\rho$$ (5.16)

n_c Number concentration [kg⁻¹]
ρ Air density [kg m⁻³]
T Temperature [K]
T_0 Reference melting temperature = 273.15 K

Following Reisner et al. (1998), the T-value has been limited to 246 K for temperatures colder than 246 K because the Fletcher curve produces erroneously high concentrations of ice particles at very cold temperatures. The product ($M_0 n_c$) represents the critical ice nuclei mixing ratio necessary before ice nucleation is considered efficient. The Δt term in equation 5.15 is a function of grid spacing, where $\Delta t = 3\Delta x/1000$ (the horizontal grid spacing, Δx, has units [m]). It is assumed that sufficient supersaturation over ice exists within the cloud.

In cloud regions where the temperature is colder than -40 °C, all cloud liquid water is converted to cloud ice via homogeneous freezing. The release rate for the heterogeneous freezing of cloud water to cloud ice follows Bigg (1953),

$$P_{IC} = B'\left\{\exp\left[A'(T_0 - T)\right] - 1\right\}\frac{\rho q_c^2}{\rho_w N_c}$$ (5.17)

P_{IC} Release rate for heterogeneous freezing of cloud water to cloud ice [s⁻¹]
A' Coefficient = 0.66 K⁻¹
B' Coefficient = 100 m⁻³ s⁻¹
N_c Number of cloud droplets per unit volume of air = 10^8 m⁻³
ρ_w Density of water = 1000 kg m⁻³

The release rate for the deposition of water vapor onto ice particles is found following Grell et al. (1994).

$$P_{ID} = \frac{4D_i(S_i - 1)n_c}{A_i + B_i}$$ (5.18)

where D_i is estimated from the mass-diameter relation for hexagonal plates from Rutledge and Hobbs (1983).

$$D_i = 16.3 M_i^{1/2}, \quad M_i = \frac{q_c}{n_c \rho}$$ (5.19)

$$S_i = q'_v / q_{si}$$ (5.20)

$$A_i = \frac{L_s^2 \rho}{K_a R_v T^2}, \quad B_i = \frac{1}{q_{si}\chi} \tag{5.21}$$

P_{ID} Release rate for deposition of water vapor onto ice particles [s^{-1}]
D_i Mean diameter of ice crystals [m]
M_i Mean mass of ice crystals [kg]
L_s Latent heat of sublimation = 2.833 x 10^6 J kg^{-1}
S_i Saturation ratio with respect to ice
q'_v Saturation vapor pressure with respect to water in the cloud region [kg kg^{-1}]
χ Diffusivity of vapor in air [m^2 s^{-1}]
R_v Gas constant for water vapor = 461 J K^{-1} kg^{-1}
K_a Thermal conductivity of air [J m^{-1} s^{-1} K^{-1}]

The diffusivity of water vapor in air for the temperature range between -40 °C and 40 °C is from Pruppacher and Klett (1997, pg. 503).

$$\chi = 2.138x10^{-5}\left(\frac{T}{T_0}\right)^{1.94}\left(\frac{p_0}{p}\right) \tag{5.22}$$

p_0 Reference pressure = 101325.0 Pa

The thermal conductivity of air is from Pruppacher and Klett (1997, pg. 508).

$$K_a = 2.38x10^{-2} + 7.12x10^{-5}\left(T - T_0\right) \tag{5.23}$$

Finally, the transfer of mass from the liquid phase to the ice phase is conserved by adjusting the cloud liquid water mixing ratio. The time step selected in equation 5.24 is the same as that used in equation 5.15 because the resulting domain aggregate profile of cloud ice mass is similar to the vertical distribution of cloud ice mass in MM5 simulations.

$$q_i = \begin{cases} (P_{II} + P_{IC} + P_{ID})\Delta t, & T \geq -40°\text{C} \\ q'_c, & T < -40°\text{C} \end{cases} \tag{5.24}$$

$$q_c = q'_c - q_i \tag{5.25}$$

q_i Cloud ice mixing ratio [kg kg^{-1}]
q_c Cloud liquid water mixing ratio adjusted for ice [kg kg^{-1}]
q'_c Initial cloud liquid water mixing ratio [kg kg^{-1}]

All clouds are assumed buoyantly stable -- in other words, they have the same temperature profile as the large-scale environment at every level of the cloud. This is to create a static cloud layer. Water vapor mixing ratios, however, are redefined to saturation with respect to liquid water and to the environmental temperature profile throughout the cloudy column. The preceding section has described how to determine mixing ratios of cloud liquid water, cloud ice, and water vapor. The following section now uses these mixing ratios to estimate the rain and snow release rates at each level in the cloudy column.

5.3. Precipitation Parameterization

The diagnostic parameterization of precipitation release is collectively based on the Zhao and Carr (1997) scheme and on the cloud precipitation physics scheme employed in MM5 (Grell et al. 1994).

The Zhao and Carr (1997) scheme was recently introduced into the National Centers for Environmental Prediction (NCEP) Eta model, which resulted in significant improvements to the model's precipitation forecasts. Their scheme was also placed into the global spectral, medium-range forecast model (MRF) at NCEP (Zhao et al. 1995). These two schemes are selected as the foundation for this scheme because they compute release rates that are diagnostic and rely primarily on knowing only the concentrations of water vapor, cloud liquid water, and cloud ice. Prognostic precipitation schemes by their very nature require model spin-up or the use of forecasted data fields. This scheme offers an alternative initialization technique that can be based on analyzed cloud data. Table 5.2 lists precipitation processes modeled in this scheme.

Table 5.2. Phase conversion processes modeled in CIS.

Cloud Liquid Water and Cloud Ice
Condensation of vapor into cloud liquid water
Initiation of ice (transfer of water from liquid cloud droplet to ice particle)
Deposition of vapor onto ice particles in clouds
Heterogeneous freezing of cloud liquid water when $T \geq -40^{\circ}C$
Homogeneous freezing of cloud liquid water when $T < -40^{\circ}C$
Rain and Snow
Autoconversion of cloud liquid water to rain
Collection of cloud liquid water by rain
Autoconversion of cloud ice to snow
Collection of cloud ice by snow
Collection of cloud liquid water by snow
Collection of snow by rain
Collection of rain by snow
Melting of snow due to increasing temperature
Melting of snow due to collection of cloud liquid water
Evaporation of rain
Evaporation of melting snow
Sublimation of snow
Deposition of water vapor onto snow

There are several important adaptations made in this scheme. The primary difference between CIS and the scheme used in the Eta, MRF, and MM5 models is that cloud coverage amount and cloud type are known and do not require parameterization from the relative humidity fields. Cloud liquid water and ice contents are diagnosed directly from the RTNEPH cloud analysis. This scheme will also be applied at higher vertical resolution than these models. Finally, this scheme goes one step further by diagnosing rain and snow mixing ratios at each level of the cloudy column.

a. Rain release rate parameterization

The dominant processes considered in rain production or reductions are autoconversion, accumulation of cloud liquid water, accumulation by and of snow, evaporation, and melting snow.

Sundqvist (1995) defines autoconversion as a process in which cloud droplets (ice particles) occasionally collide and coalesce (aggregate) due to the random motions of the particles. The autoconversion process is simply a function of the cloud particle mixing ratio present. Intuitively, the autoconversion process should be more efficient as particle sizes (and thus terminal velocity) decrease, as number concentration increases, and as turbulence within the cloud increases. However, these parameters are not contained in the RTNEPH data, therefore they must be estimated. The rate of release of precipitation is given by the Kessler parameterization following Grell et al. (1994),

$$P_{raut} = \max[k_1(q_c - q_{critical}), \quad 0]$$ (5.26)

P_{raut} Release rate of rain due to autoconversion of cloud liquid water [s^{-1}]
k_1 Coefficient [s^{-1}]
$q_{critical}$ Critical cloud liquid water mixing ratio [kg kg^{-1}]

The inverse of the constant k_1 represents the characteristic time that cloud droplets are converted into raindrops. The empirical constant $q_{critical}$ is the mixing ratio that q_c must exceed before the release of precipitation is considered efficient.

As stated above, turbulence should increase the autoconversion rate. The only way to parameterize this effect is to adjust the threshold mixing ratios based on cloud type (available in the RTNEPH data). The coefficients for stratiform and convective cases recommended by Sundqvist et al. (1989) are given in Table 5.3.

Table 5.3. Coefficients for autoconversion of rain.

Convective	Stratiform
$k_1 = 1.0 \times 10^{-3}$ s^{-1}	$k_1 = 1.0 \times 10^{-4}$ s^{-1}
$q_{critical} = 5.0 \times 10^{-4}$ kg kg^{-1}	$q_{critical} = 3.0 \times 10^{-4}$ kg kg^{-1}

Sundqvist et al. (1989) distinguishes the autoconversion process from the collection (coalescence or aggregation) process by precipitation (rain or snow). Collection effectiveness in this case is not simply a function of the cloud particle mixing ratios but is a function of the precipitating particle amounts as well. The release rate for the accumulation of cloud liquid water by falling rain follows Grell et al. (1994).

$$P_{racw} = \frac{\pi}{4} a_r c_r q_c E_r N_{0r} \frac{\Gamma(3+b_r)}{\lambda_r^{3+b_r}}$$ (5.27)

$$\lambda_r = \left(\frac{\pi N_{0r} \rho_w}{\rho q_r}\right)^{\frac{1}{4}}$$ (5.28)

P_{racw} Release rate of rain due to accumulation of cloud liquid water [s^{-1}]
Γ Gamma function
a_r Rain coefficient = 842 m^{1-br} s^{-1}
b_r Rain coefficient = 0.8
c_r Rain coefficient = 0.35

E_r Collection efficiency for rain = 1
N_{0r} Raindrop size distribution intercept parameter [m^{-4}]
λ_r,   Raindrop size distribution slope parameter [m^{-1}]
q_r Rain water mixing ratio [kg kg^{-1}]

Constants a_r and b_r are associated with the assumed droplet fall speed from the relationship

$$V(D) = a_r D^{b_r} \tag{5.29}$$

V Droplet fall speed [m s^{-1}]
D Droplet diameter [m]

When using the constant intercept parameter as in Reisner et al. (1998), the modeled rainfall rates are too high in deep cumulus clouds. Sekhon and Srivastava (1971) found a relationship for the raindrop size distribution intercept parameter of the form:

$$N_{0r}\left(m^{-4}\right) = 1.87x10^9 R_r^{0.37} \tag{5.30}$$

where R_r is the rainfall rate [m s^{-1}]. Just as Reisner et al. (1998) derived an expression for the snow size intercept parameter as a function of snow mixing ratio, the rain size intercept parameter can be similarly derived as a function of rain mixing ratio. First, R_r [m s^{-1}] is written as

$$R_r = \frac{\rho q_r U_{dr}}{\rho_w} \tag{5.31}$$

where U_{dr} is the mass weighted terminal velocity for rain [m s^{-1}]. Using an exponential size distribution, (following Grell et al. 1994, equation 5.3.1.1.15) we can write:

$$U_{dr} = \frac{a_r \Gamma(4 + b_r)}{6\lambda_r^{b_r}} \tag{5.32}$$

Combining equations 5.28, and 5.30 through 5.32 yields equation 5.33. Computation of q_r is presented in a later section.

$$N_{0r} = \left[1.87x10^9 \left(\rho q_r \alpha \left(\frac{\pi \rho_w}{\rho q_r}\right)^{\frac{-b_r}{4}}\right)^{0.37}\right]^{\frac{4}{4+0.37b_r}} \tag{5.33}$$

$$\alpha = \frac{a_r \Gamma(4 + b_r)}{6\rho_w}$$

b. Snow release rate parameterization

The dominant processes considered in snow production or snow reduction are autoconversion, aggregation, sublimation, melting, accumulation by and of rain, and evaporation of melting snow. The release rate due to autoconversion of cloud ice to snow in MM5 is formulated similar to that for P_{II}, the initiation of ice.

$$P_{saut} = \max\left[\left(q_i - \frac{M_{max}n_c}{\rho}\right)\bigg/(10\varDelta t), \quad 0\right] \tag{5.34}$$

P_{saut} Release rate of snow due to autoconversion of cloud ice [s⁻¹]

M_{max} Coefficient = 9.4 x 10^{-10} kg

In this case, the product of $(M_{max} \, n_c \, / \, \rho)$ represents the critical cloud ice mixing ratio that must be present before snow production is considered efficient.

Following Reisner et al. (1998), the collection of cloud ice by falling snow is modeled using an expression similar to that used for the accumulation of cloud liquid water by rain.

$$P_{saci} = \frac{\pi}{4} a_s q_i E_s N_{0s} \frac{\Gamma(3+b_s)}{\lambda_s^{3+b_s}} \tag{5.35}$$

A similar expression is introduced to simulate the collection of cloud liquid water by falling snow.

$$P_{sacw} = \frac{\pi}{4} a_s c_s q_c E_s N_{0s} \frac{\Gamma(3+b_s)}{\lambda_s^{3+b_s}} \tag{5.36}$$

$$\lambda_s = \left(\frac{\pi N_{0s} \rho_{ws}}{\rho q_s} \right)^{\frac{1}{4}} \tag{5.37}$$

P_{saci} Release rate of snow due to accumulation of cloud ice [s⁻¹]

P_{sacw} Release rate of snow due to accumulation of cloud liquid water [s⁻¹]

Γ Gamma function

E_s Collection efficiency for snow = 0.1

N_{0s} Sekhon-Srivastava snow size distribution intercept parameter [m⁻⁴]

a_s Snow coefficient = 11.72 $m^{1-br} \, s^{-1}$

b_s Snow coefficient = 0.41 $m^{1-br} \, s^{-1}$

c_s Snow coefficient = 0.24

λ_s,   Sekhon-Srivastava snow size distribution slope parameter [m⁻¹]

ρ_{ws} Mean density of snow particles = 100 kg m⁻³

q_s Snow mixing ratio [kg kg⁻¹]

Sekhon and Srivastava (1970) recommend a modified Marshall-Palmer intercept parameter N_{0s} for the size distribution using the expression

$$N_{0s} = 1.72 P_s^{-0.94} \tag{5.38}$$

where P_s (m s⁻¹) is the snowfall rate. Grell et al. (1994, equation 5.3.1.2.4) expressed this intercept in terms of snow mixing ratio, q_s, as

$$N_{0s} = \left\{ 1.72 \left[\frac{1}{\rho q_s \alpha} \left(\frac{\pi \rho_{ws}}{\rho q_s} \right)^{\frac{b_s}{4}} \right]^{0.94} \right\}^{\frac{4}{0.94 b_s + 4}}, \quad \alpha^{-1} = \frac{6 \rho_w}{a_s \Gamma(4 + b_s)} \tag{5.39}$$

c. Precipitation release rate reduction parameterization

After autoconversion and collection processes have defined the snow and rain release rates, their depletion rates are computed following Grell et al. (1994). The snow release rate is reduced by five mechanisms while rain is reduced by two.

P_{sm1} Melting due to increasing temperature,

P_{sm2}	Melting due to collection of cloud liquid water,
P_{racs}	Collection of snow by rain,
E_{rs}	Sublimation of snow,
E_{rsm}	Evaporation of melting snow,
P_{sacr}	Collection of rain by snow, and
E_{rr}	Evaporation of rain.

In this scheme, snowmelt can occur above the melting level, and it does not occur immediately after falling through the melting level. Processes that warm snow above the melting level, such as the release of latent heat of fusion during riming collisions, are not considered. This scheme is constructed so that some regions at the ground may experience a mixture of rain and snow. In order to model snow reduction processes, separate expressions are used to estimate the release rates for each process.

The following expression for the release rate of melting snow due to increasing temperature is based on the work of Rutledge and Hobbs (1983).

$$P_{sm1} = -\frac{2\pi N_{0s}}{L_f} K_a (T - T_0) \left[\frac{f_1}{\lambda_s^2} + f_2 \left(\frac{a_s \rho}{\mu} \right)^{1/2} \frac{\Gamma(5/2 + b_s/2)}{\lambda_s^{5/2 + b_s/2}} \right] \tag{5.40}$$

The term in brackets represents a distribution-integrated ventilation factor,

$$F = f_1 + f_2 S_c^{1/3} Re^{1/2} \tag{5.41}$$

with the Schmidt number, Reynolds number, and dynamic viscosity of air given by the functions

$$S_c = \mu / \rho \chi \tag{5.42}$$

$$Re = V(D) D \rho / \mu \tag{5.43}$$

P_{sm1}	Release rate of snow melt due to increasing temperature [s^{-1}]
S_c	Schmidt number
Re	Reynolds number
F	Ventilation factor
L_f	Latent heat of fusion = 3.33 x 10^5 J kg^{-1}
μ	Dynamic viscosity of air [kg m^{-1} s^{-1}]
f_1	Coefficient = 0.65
f_2	Coefficient = 0.44

The expression for the dynamic viscosity of air comes from Pruppacher and Klett (1997, pg. 417).

$$\mu = [1.718 + 0.0049(T - T_0)]x10^{-5}, \quad T \geq T_0$$
$$\mu = [1.718 + 0.0049(T - T_0) - 1.2x10^{-5}(T - T_0)^2]x10^{-5}, \quad T < T_0 \tag{5.44}$$

When snow melts, the resulting liquid water contributes to rain. P_{sm1} therefore contributes to the rain release rate while it decreases the snow release rate.

Snow melts at a rate proportional to the rate at which it accumulates cloud liquid water. This melted snow also contributes to the rain release rate as it decreases the snow release rate.

$$P_{sm2} = C_{ws} P_{sacw} \tag{5.45}$$

Zhao and Carr (1997) estimate snow release rate by taking into account the probable average difference in temperature between the cloud liquid water and the snow crystals over the depth of the melting layer.

$$C_{ws} = \frac{C_w \Delta \overline{T}}{L_f} \tag{5.46}$$

Because this expression is used in a high-resolution model, C_{ws} is computed as a function of temperature instead of using an average temperature difference.

$$C_{ws} = \frac{C_w(T - T_0)}{L_f} \tag{5.47}$$

Combining equations 5.45 through 5.47, the contribution to the rain release rate resulting from snowmelt by accumulating cloud water is given by the following expression.

$$P_{sm2} = \frac{C_w(T - T_0)}{L_f} P_{sacw} \tag{5.48}$$

P_{sm2} Release rate of snowmelt due to accumulation of cloud liquid water [s^{-1}]
C_w Specific heat of liquid water = 4218 J K^{-1} kg^{-1}
C_{ws} Snowmelt rate factor [s^{-1}]

Snowmelt in this case will not occur above the melting line with the assumption that the cloud liquid water and snow are both at ambient air temperature. Below the melting level, snow is assumed to have temperature T_0, and cloud liquid water is assumed to be at ambient air temperature.

The release rate for the evaporation of rain as it falls through an unsaturated layer was formally developed by Rutledge and Hobbs (1983). Evaporation does not take place within any cloud layer.

$$E_{rr} = \frac{2\pi N_{0r}(S_w - 1)}{A_w + B_w} \left[\frac{f_1}{\lambda_r^2} + f_2 \left(\frac{a_r \rho}{\mu} \right)^{1/2} \frac{\Gamma(5/2 + b_r/2)}{\lambda_r^{5/2 + b_r/2}} \right] \tag{5.49}$$

$$S_w = q_v / q_{sw} \tag{5.50}$$

$$A_w = \frac{L_v^2 \rho}{K_a R_v T^2}, \quad B_w = \frac{1}{q_{sw} \chi} \tag{5.51}$$

E_{rr} Release rate for evaporation of rain [s^{-1}]
S_w Supersaturation with respect to liquid water
q_v Environmental water vapor mixing ratio [kg kg^{-1}]
f_1 Coefficient = 0.78
f_2 Coefficient = 0.31

In this scheme, the evaporation release rate is computed only to diminish the precipitation rate, not to enhance water vapor in sub-cloud regions which otherwise could lead to saturation and alter the analyzed cloud base altitude.

The release rate for the sublimation of snow above the melting level is computed similarly but only outside clouds.

$$E_{rs} = -\frac{4N_{0s}(S_i - 1)}{A_i + B_i} \left[\frac{f_1}{\lambda_s^2} + f_2 \left(\frac{a_s \rho}{\mu} \right)^{1/2} \frac{\Gamma(5/2 + b_s/2)}{\lambda_s^{5/2 + b_s/2}} \right] \tag{5.52}$$

E_{rs} Release rate for sublimation of snow [s^{-1}]
f_1 Coefficient = 0.65
f_2 Coefficient = 0.44

Within a cloud layer that is above the melting line, snow is permitted to grow via vapor deposition. The release rate for vapor deposition on snow is given by

$$D_{rs} = \frac{4N_{0s}(S_i - 1)}{A_i + B_i}\left[\frac{f_1}{\lambda_s^2} + f_2\left(\frac{a_s\rho}{\mu}\right)^{1/2}\frac{\Gamma(5/2 + b_s/2)}{\lambda_s^{5/2+b_s/2}}\right]$$

(5.53)

$S_i = q'_v / q_{si}$

D_{rs} Release rate for deposition of water vapor onto snow within a cloud [s^{-1}]
f_1 Coefficient = 0.65
f_2 Coefficient = 0.44

Below the melting level, snow is assumed to have a thin shell of liquid water that prevents sublimation. The release rate due to evaporation of the liquid water shell on snow below the melting level, E_{rsm}, simply replaces A_i and B_i with A_w and B_w.

$$E_{rsm} = -\frac{4N_{0s}(S_i - 1)}{A_w + B_w}\left[\frac{f_1}{\lambda_s^2} + f_2\left(\frac{a_s\rho}{\mu}\right)^{1/2}\frac{\Gamma(5/2 + b_s/2)}{\lambda_s^{5/2+b_s/2}}\right]$$

(5.54)

E_{rsm} Release rate for evaporation of melting snow [s^{-1}]
f_1 Coefficient = 0.65
f_2 Coefficient = 0.44

The release rates for the collection of rain by snow (P_{racs}) and for the collection of snow by rain (P_{sacr}) are presented in a later section. The method of system closure must be discussed beforehand.

5.4. System Closure

a. Rainfall rate and snowfall rate parameterization

The rates of rainfall and snowfall must be calculated to close this series of equations. Starting at the top of the cloud let superscript n denote the level being evaluated. The rainfall and snowfall rates are computed by integrating the total release rates of rain and snow at each level. The total release rates for rain and snow are the sum of all processes affecting their release rates.

$$P_{rain-total} = P_{raut} + P_{racw} + P_{racs} + P_{sm1} + P_{sm2} - P_{sacr} - E_{rr}$$
$$P_{snow-total} = P_{saut} + P_{saci} + P_{sacw} + P_{sacr} - P_{racs} - P_{sm1} - P_{sm2} + D_{rs} - E_{rs} - E_{rsm}$$

(5.55)

The rainfall and snowfall rates are computed by integrating these total release rates from the top of the cloudy column to the sigma level of interest.

$$P_r = \frac{p_{sfc} - p_{top}}{g}\int_{\sigma_{top}}^{\sigma} P_{rain-total}\,d\sigma$$

(5.56)

$$P_s = \frac{p_{sfc} - p_{top}}{g}\int_{\sigma_{top}}^{\sigma} P_{snow-total}\,d\sigma$$

In linear form, the previous equations are computed stepwise from the top of the highest cloud in the column downward to the surface. The level (n) represents the sigma level of interest and the level (n-1) represents the level immediately above it.

$$P_r^n = P_r^{n-1} + \left[\frac{p_{sfc} - p_{top}}{g}\right](P_{rain-total})^{(n)} \Delta\sigma$$

$$P_s^n = P_s^{n-1} + \left[\frac{p_{sfc} - p_{top}}{g}\right](P_{snow-total})^{(n)} \Delta\sigma$$

(5.57)

Precipitation rates at the top of the highest cloud in the column are zero. Snowfall rate is computed only if ice crystals are present in the column. Total snow and rain release rates ($P_{rain-total}$ and $P_{snow-total}$) can be either positive or negative, but snowfall and rainfall rates below cloud layers are restricted to positive values only. Once the rainfall and snowfall rates are calculated over each vertical interval, the mixing ratios are computed using appropriate raindrop and snow size distributions.

b. Rain and snow mixing ratio parameterization

The mixing ratios of rain and snow are diagnosed by assuming continuous raindrop and snow size distributions. The classical Marshall-Palmer raindrop size distribution (Marshall and Palmer, 1948) is a simplified gamma distribution of the following form.

$$n(D_{r0}) = n_{r0} \exp(-\Lambda_r D_{r0})$$

(5.58)

Sekhon and Srivastava (1971) found that the Marshall-Palmer intercept and slope parameters (n_{r0}, Λ_r) underestimate the mean volume diameter, which decreases at high rainfall rates. They instead recommend that the intercept parameter is not constant but rather a function of the rainfall rate. Their modified intercept and slope parameters have been selected for this scheme. Both parameters are functions of the rainfall rate in units of millimeters per hour.

$$\Lambda_r = 3.8 R^{-0.14} mm^{-1}$$

$$n_{r0} = 7.0x10^3 R^{0.37} m^{-3} mm^{-1}$$

(5.59)

The rainfall rate, R, in this case is reduced to the ground level. P_r has units [kg m^{-2} s^{-1}].

$$R = \left(3.6x10^6\right)\frac{P_r}{\rho_w}\left(\frac{\rho_\sigma}{\rho_0}\right)^{0.4} mmhr^{-1}$$

(5.60)

One problem with the Sekhon and Srivastava (1971) formulation concerns the pressure reduction component given in equation 5.60. Rainfall rate is pressure reduced because the number distribution is based on surface observations. The problem with this pressure reduction component arises when the only rain-forming process is melting snow. Suppose there is a special case in which the base of a deep ice cloud coincides with the melting line. Suppose further that the air beneath this cloud is saturated with respect to water vapor to eliminate consideration of evaporation/sublimation processes. Below the ice cloud, snow will melt to rain. If there are no clouds between the ice cloud and the surface, there

should be no additional liquid water contributing to forming rainfall rate. Precipitation rate should be conserved from the base of the ice cloud all the way to the surface. To achieve this constraint, equation 5.60 is simplified. A closer look at this behavior of the model is given in a subsequent section detailing five model-tuning cases in Chapter VI.

$$R = 3.6x10^6 \frac{P_r}{\rho_w} mmhr^{-1} \tag{5.61}$$

Sekhon and Srivastava (1970) proposed a size distribution for snow analogous to the raindrop size distribution. In this formulation, the mean diameter, D_{s0}, is the mean equivalent diameter of the water drop from the melted snow crystal in mm units. The precipitation rate given is the snow's equivalent water precipitation rate. P_r has units [kg m^{-2} s^{-1}], and ρ_w has units [kg m^{-3}].

$$n(D_{s0}) = n_{s0} \exp(-\Lambda_s D_{s0}) \tag{5.62}$$

$$\Lambda_s = 2.29 \left(3.6x10^6 \frac{P_s}{\rho_w} \right)^{-0.45} mm^{-1}$$

$$n_{s0} = 2.5x10^3 \left(3.6x10^6 \frac{P_s}{\rho_w} \right)^{-0.94} m^{-3} mm^{-1} \tag{5.63}$$

Once the raindrop and snow size distributions are selected, the liquid water contents are found following Pruppacher and Klett (1997).

$$lwc_r = 10^{-3} \int_0^\infty \underbrace{\frac{\pi}{6} \rho_w D_{r0}^3}_{raindrop-mass} n(D_{r0})dD_{r0}$$

$$lwc_s = 10^{-3} \int_0^\infty \underbrace{\frac{\pi}{6} \rho_w D_{s0}^3}_{snow-mass} n(D_{s0})dD_{s0} \qquad \text{units [g m}^{-3}] \tag{5.64}$$

Substituting the number distributions into the above integral then solving using straightforward integration by parts yields the following simple formulas for the mixing ratios of rain and snow.

$$lwc_r = \frac{10^{-3}\pi\rho_w n_{r0}}{\Lambda_r^4}, \quad lwc_s = \frac{10^{-3}\pi\rho_w n_{s0}}{\Lambda_s^4} \quad \text{units [g m}^{-3}] \tag{5.65}$$

The final mixing ratios, which are later used to initialize the mesoscale model, are computed from the liquid water contents. Air density has units [kg m^{-3}].

$$q_r = \frac{lwc_r}{\rho_a}, \quad q_s = \frac{lwc_s}{\rho_a} \quad \text{units [g kg}^{-1}] \tag{5.66}$$

c. Collection of snow by rain and collection of rain by snow

The release rates due to the collection of snow by rain and due to the collection of rain by snow are computed differently here than in MM5. The formulas for these processes presented by Reisner et al. (1998, equations A.47 and A.48) were too unstable for this diagnostic procedure. The release rate due

to the collection of snow by rain is developed by taking into account the differences in fall speed and total cross-sectional area between snow and rain. We begin with the mass of a raindrop, which is the product of its density and spherical volume.

$$m = \rho_w \frac{\pi D_r^3}{6} \qquad (5.67)$$

ρ_w Density of liquid water = 1000 kg m^{-3}

The same equivalent liquid water mass for a snowflake is the product of its density and an assumed plate volume with diameter D_s and depth h.

$$m = \rho_s \frac{\pi D_s^2 h}{4} \qquad (5.68)$$

ρ_s Bulk density of snow = 100 kg m^{-3}

If the diameter-to-height ratio (D_s/h) is assumed for plates to be 6:1, then the mass of the snowflake becomes:

$$m = \rho_s \frac{2}{3} \pi D_s^3 \qquad (5.69)$$

Solve for D_s as a function of D_r:

$$D_s = \left(\frac{1}{4} \frac{\rho_w}{\rho_s} \right)^{\frac{1}{3}} D_r \qquad (5.70)$$

The cross-sectional area of a falling raindrop with mass m is given by:

$$a_{\perp r} = \frac{\pi D_r^2}{4} \qquad (5.71)$$

The cross-sectional area a falling snowflake with the same mass m is therefore given by:

$$a_{\perp s} = \frac{\pi D_s^2}{4} = \left(\frac{1}{4} \frac{\rho_w}{\rho_s} \right)^{\frac{2}{3}} \frac{\pi D_r^2}{4} \qquad (5.72)$$

where D_r here is the diameter of an equivalent liquid water droplet from the snowflake. A function relating the cross-sectional areas of rain and snow is therefore:

$$a_{\perp s} = \beta_s a_{\perp r} \qquad (5.73)$$

$$\beta_s = \left(\frac{1}{4} \frac{\rho_w}{\rho_s} \right)^{\frac{2}{3}} \qquad (5.74)$$

where $a_{\perp r}$ is the equivalent liquid water cross-sectional area for a snowflake, and β_s is the constant of proportionality which takes density and shape differences into account.

The fraction (F) of snow equivalent liquid water content removed by rain is proportional to the mass-weighted mean cross-sectional area of the rain ($A_{\perp r}$) per unit volume, and inversely proportional to the mass-weighted mean cross-sectional area of the equivalent liquid water content of the snow ($A_{\perp s}$) per unit volume (only equivalent liquid water contents of snow are known).

$$F = \frac{\alpha A_{\perp r}}{\beta_s A_{\perp s}} \qquad (5.75)$$

The density and shape corrected total cross-sectional area of snow is given by the denominator, $\beta_s A_{\perp s}$. The fraction F is also proportional to the ratio α, which is the fraction of a falling volume of snow that is overtaken by a falling volume of rain per unit time.

$$\alpha = \frac{U_r - U_s}{U_s}, \quad U_r = \frac{P'_r}{lwc'_r}, \quad U_s = \frac{P'_s}{lwc'_s} \qquad (5.76)$$

α Ratio indicating rate at which rain overtakes snow [unitless]
U_r Mass-weighted mean velocity of rain [m s^{-1}]
U_s Mass-weighted mean velocity of snow [m s^{-1}]
P'_r Rainfall rate [kg m^{-2} s^{-1}] (before collection of snow by rain)
P'_s Snowfall rate [kg m^{-2} s^{-1}] (before collection of snow by rain)
lwc'_r Liquid water content of rain [kg m^{-3}] (before collection of snow by rain)
lwc'_s Liquid water content of snow [kg m^{-3}] (before collection of snow by rain)

The total cross-sectional area of the rain per unit volume is found from the following functional development. Pruppacher and Klett (1997) provide an equation for the liquid water content in terms of the number of drops per cubic meter of air per mm size interval:

$$lcw_r = 10^{-6} \int_0^\infty \rho_w \underbrace{\frac{\pi}{6} D_{0r}^3}_{\substack{\text{volume} \\ \text{mass}}} \underbrace{n(D_{0r}) dD_{0r}}_{\text{per unit volume}}, \quad n(D_{0r}) = n_{0r} \exp(-\Lambda_{0r} D_{0r}) \qquad (5.77)$$

lwc_r Liquid water content of rain [kg m^{-3}]
$n(D_{0r})$ Number of raindrops per unit volume per diameter [m^{-3} mm^{-1}]
D_{0r} Diameter of raindrop [mm]
n_{0r} Raindrop size distribution intercept parameter [m^{-3} mm^{-1}]
Λ_{0r} Raindrop size distribution slope parameter [mm^{-1}]
ρ_w Density of liquid water = 1000 kg m^{-3}

The total cross-sectional area per unit volume of the raindrop distribution providing this liquid water content is then:

$$A_{\perp r} = 10^{-6} \int_0^\infty \underbrace{\frac{\pi}{4} D_{0r}^2}_{\substack{\text{cross} \\ \text{sectional} \\ \text{area}}} \underbrace{n(D_{0r}) dD_{0r}}_{\text{per unit volume}}, \quad n(D_{0r}) = n_{0r} \exp(-\Lambda_{0r} D_{0r}) \qquad (5.78)$$

$A_{\perp r}$ Total cross-sectional area of rain per unit volume [m^2 m^{-3}]

Substitute the modified gamma function for the number distribution and solve the integral.

$$A_{\perp r} = 10^{-6} \int_0^\infty \frac{\pi}{4} D_{0r}^2 n_{0r} \exp(-\Lambda_{0r} D_{0r}) dD_{0r} \qquad (5.79)$$

This equation may be solved by using the identity:

$$\int_0^\infty X^2 e^{aX} dX = e^{aX} \left(\frac{X^2}{a} - \frac{2X}{a^2} + \frac{2}{a^3} \right) \Bigg|_{X=0}^{X=\infty} \qquad (5.80)$$

$$A_{\perp r} = 10^{-6} \frac{\pi}{4} n_{0r} \left[e^{-A_{0r}D_{0r}} \left(\frac{D_{0r}^2}{-A_{0r}} - \frac{2D_{0r}}{(-A_{0r})^2} + \frac{2}{(-A_{0r})^3} \right) \right]_{D_{0r}=0}^{D_{0r}=\infty}$$

$$A_{\perp r} = 10^{-6} \frac{\pi}{4} n_{0r} \left[e^{-\infty} \left(-\frac{\infty^2}{A_{0r}} - \frac{2\infty}{A_{0r}^2} - \frac{2}{A_{0r}^3} \right) - e^{-0} \left(-\frac{0^2}{A_{0r}} - \frac{2 \cdot 0}{A_{0r}^2} - \frac{2}{A_{0r}^3} \right) \right]$$

$$A_{\perp r} = \frac{10^{-6} \pi n_{0r}}{4} \left[0 - 1 \left(0 - 0 - \frac{2}{A_{0r}^3} \right) \right] = \frac{\pi n_{0r}}{2x10^6 A_{0r}^3} \tag{5.81}$$

Similarly, the total cross-sectional area per unit volume of the equivalent liquid water for snow is:

$$A_{\perp s} = \frac{\pi n_{0s}}{2x10^6 A_{0s}^3} . \tag{5.82}$$

$A_{\perp s}$ Total cross-sectional area of snow equivalent liquid water per unit volume [$m^2\ m^{-3}$]
$n(D_{0s})$ Number of snowflakes per unit volume per diameter [$m^{-3}\ mm^{-1}$]
D_{0s} Diameter of equivalent liquid water from snowflake [mm]
n_{0s} Snowflake size distribution intercept parameter [$m^{-3}\ mm^{-1}$]
A_{0s} Snowflake size distribution slope parameter [mm^{-1}]

Substitution of parameters from equations 5.59 and 5.60 into equation 5.81 yields:

$$A_{\perp r} = \frac{7.0x10^3 \pi \left(3.6x10^6 \frac{P'_r}{\rho_w} \left(\frac{\rho_\sigma}{\rho_0} \right)^{0.4} \right)^{0.79}}{1.09744x10^8} \tag{5.83}$$

P'_r Rainfall rate [$kg\ m^{-2}\ s^{-1}$] (before collection of snow by rain)

Substitution of parameters from equation 5.63 into equation 5.82 yields:

$$A_{\perp s} = \frac{2.5x10^3 \pi \left(3.6x10^6 \frac{P_s}{\rho_w} \right)^{0.41}}{2.4017978x10^7}$$

P'_s Snowfall rate [$kg\ m^{-2}\ s^{-1}$] (before collection of snow by rain)

The reduction fraction, F, is used to adjust the equivalent liquid water content of snow, lwc_s, at the given sigma level. To make the adjustment, it is necessary to compute an intermediate snow liquid water content using equation 5.65 taking into account only $P_{saut} + P_{saci} + P_{sacw}$ release rates and the snowfall rate from the level immediately above. Snow equations 5.55-5.57, and 5.62-5.65 with this modification are used to obtain lwc'_s. The intermediate liquid water content is then reduced by rain accumulation.

$$lwc_s = lwc'_s - F \cdot lwc'_s \tag{5.84}$$

With the new liquid water content, lwc_s, equations 5.55-5.57 and 5.62-5.66 are inverted to solve for $P_{snow-total}$. Finally, P_{racs} is found from $P_{snow-total} = P_{saut} + P_{saci} + P_{sacw} - P_{racs}$.

If the ratio α is less than 1, it indicates that snow is overtaking rain. In that case, P_{sacr}, the release rate due to the collection of rain by snow is computed similarly. The intermediate rain liquid water

content, lwc'_r, is found from $P_{rain\text{-}total} = P_{raut} + P_{racw}$ using equation 5.55. Then the fraction F is computed using

$$F = \frac{\beta_s A_{\perp s}}{\alpha A_{\perp r}}, \quad \alpha = \frac{U_s - U_r}{U_r} \tag{5.85}$$

$$lwc_r = lwc'_r - F \cdot lwc'_r \tag{5.86}$$

With the new liquid water content, lwc_r, equations 5.55-5.57 and 5.62-5.65 are inverted to solve for $P_{rain\text{-}total}$. Finally, P_{sacr} is found from $P_{rain\text{-}total} = P_{raut} + P_{racw} - P_{sacr}$.

The cloud initialization scheme just presented uses RTNEPH clouds to estimate mixing ratios of cloud liquid water, cloud ice, rain, and snow. These fields are used to initialize MM5. Other fields are used to initialize MM5 as well including NOGAPS and the Air Force's surface temperature analysis (SFCTEMP). Before they are used to initialize the model, Chapter VI next presents the cloud initialization scheme tuning results using idealized cloud profiles typical of those found in RTNEPH.

CHAPTER VI

CLOUD INITIALIZATION SCHEME (CIS) TUNING

6.1. Introduction

Six idealized cases are used to tune the cloud analysis algorithm called the Cloud Initialization Scheme (CIS). The first two cases illustrate the properties of precipitating cloud types. Case **A** has separate nimbostratus (Ns) and stratus (St) layers and produces a moderate amount of rain that reaches the surface. Case **B** involves a cumulonimbus (Cb) with a capping cirrostratus (Cs) layer immediately above. This cloud pattern produces a large amount of rain that reaches the surface. The third and fourth cases are examples of non-precipitating clouds. Case **C** is used to examine the fair weather instances of a thin stratus (St) layer. Case **D** depicts a cumulus (Cu) cloud layer below an altostratus deck. Case **E** is a deep, snow-producing cloud designed to verify that liquid water content is conserved as snow changes phase to rain. Case **F** is a null-cloud case used to verify that there are no false mixing ratios analyzed where there is no cloud. No figures are produced for case **F** in this chapter. Table 6.1 describes the cloud type, top and base altitudes of each layer for the first five cases. The cloud depths selected are the default RTNEPH cloud depths for each cloud type used. The following section describes the idealized atmospheric profiles of temperature and dewpoint used to tune CIS. Section 6.3 presents the results of the tuning experiments.

Table 6.1. Cloud column properties for each case.

	Case A: Ns/St	Case B: Cb/Cs	Case C: St	Case D: Cu/As	Case E: Cb
Layer 1 Type	St	Cs	St	As	Cb
Layer 1 Base/Top	2700 m - 3000 m	7500 m - 9300 m	600 m - 900 m	3480 m - 4500 m	2310 m - 7200 m
Layer 2 Type	Ns	Cb	-	Cu	-
Layer 2 Base/Top	600 m - 2610 m	600 m - 7500 m	-	1020 m - 3000 m	-

6.2. Idealized Atmospheric Profiles

CIS requires a background atmosphere to compute a few, but important, state variables. For example, to compute the adiabatic cloud liquid water mixing ratio, it is insufficient to know only the cloud base and cloud top altitudes. The temperature profile between the cloud base and cloud top are needed to determine the magnitude of supersaturation for a parcel, which is saturated at cloud base, and which vertically traverses the cloud's thickness. A temperature lapse rate conducive for examining a typical cloud profile must therefore be greater than moist-adiabatic. Lapse rates greater than dry adiabatic may over-estimate cloud liquid water mixing ratios because such profiles rarely contain water vapor sufficient for producing clouds else they become highly unstable and likely to mix out. A background value for relative humidity is also desirable to examine the evaporation of precipitation that falls below cloud layers. The temperature profile must also have a melting line sufficiently high in

order to examine snow-melting processes as snow falls below cloud yet sufficiently low to allow the formation of snow in higher or deeper clouds. A standard atmosphere temperature lapse rate with a maximum dewpoint depression of 30 °C above the boundary layer is therefore selected as the background. The surface temperature, and therefore the height of the melting line, varies with the cloud case being examined.

For cases **B** through **E**, the temperature profile and surface temperatures are defined by the standard atmosphere. For case **A**, the surface temperature and standard atmosphere are decreased by 10 degrees Kelvin. Cases **A** through **D** assume a surface elevation of 100 m. Case **E** assumes a surface elevation of 86.63 m. The surface relative humidity is defined for each case in Table 6.2.

Table 6.2. Surface temperature and relative humidity for each case.

	Case A: Ns/St	Case B: Cb/Cs	Case C: St	Case D: Cu/As	Case E: Cb
Sfc Temp	277.5 K	287.5 K	287.5 K	287.5 K	287.5
Sfc RH	95%	95%	80%	70 %	100%

The dew point temperature depression at the surface is computed from the surface temperature and relative humidity using equations 6.1 through 6.3.

$$es = \exp\left(\frac{16.78 T_{sfc} - 116.9}{T_{sfc} + 237.3}\right) \tag{6.1}$$

$$e = es \frac{RH_{sfc}}{100} \tag{6.2}$$

$$T_d = \frac{116.9 + 237.3 \ln(e)}{16.78 - \ln(e)}, \quad T_{dd} = T - T_d \tag{6.3}$$

The units of RH_{sfc} are in %, es and e are in kPa, and T_{sfc}, T_d, and T_{dd} are in °C. The saturation vapor pressure (equation 6.1) is from Murray (1967), who reports it is within 0.1 percent of values in the Smithsonian Meteorological Tables for temperatures in the range from zero to 50 °C.

For cases **A** through **D**, the dew point temperature depressions are kept constant to 1000 m. Above this height, the dew point temperature depressions increase at eight times the lapse rate of the temperature profile with a maximum depression of 30 °C. Once the dew point depressions have been defined, the water vapor mixing ratio is computed using equations 6.4 through 6.7.

$$T_d = T - T_{dd} \tag{6.4}$$

$$e_\sigma = \exp\left(\frac{16.78 T_d - 116.9}{T_d + 237.3}\right) \tag{6.5}$$

$$w = 0.622 \frac{e_\sigma}{p - e_\sigma} \tag{6.6}$$

$$q = \frac{w}{1 + w} \tag{6.7}$$

Case **E** differs from the other four cases in that the dew point depression between the surface and the base of the ice cloud is zero. In CIS, saturation below cloud base prevents rain evaporation and melting snow evaporation. The cloud base in this case also coincides with the melting line to prevent snow sublimation, snow accumulation of cloud liquid water, or any rain production mechanisms that are independent of snowmelt. The different surface elevation was selected so that the cloud base occurs at a specific sigma level. Under such constraints, it is possible to determine if computed precipitation rates are conserved as snow melts to rain. In all cloudy layers, the dewpoint temperature is assumed to be at saturation (equal to the temperature). Tables detailing the temperature and specific humidity inputs to CIS for each case are given in Appendix D.

6.3. Results

a. Test environment profile

The cloud analysis algorithm, CIS, was applied to each of the six cases. The temperature/dew point profiles for all but the null case are given in Figures 6.1a through 6.1e. The cloud type is labeled at the top edge of each cloud layer in the column. If the cloud layer is above the melting line, it is depicted with light gray. Darker gray indicates the cloud layer is composed of only liquid water. A thick horizontal line indicates the altitude of the melting level. Supercooled rain and cloud liquid water may be present between the melting line and the -40 °C isotherm. The solid and dashed lines trace the profiles of temperature and dewpoint respectively.
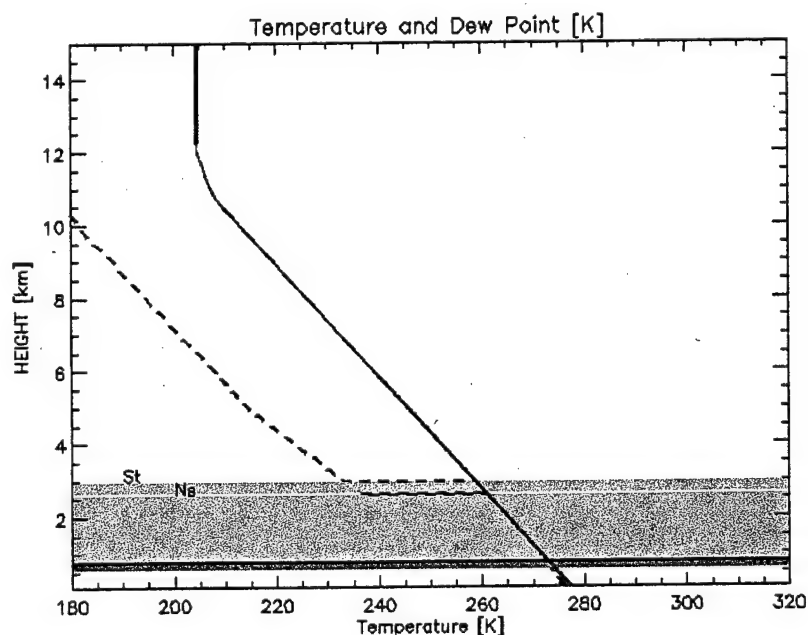
Figure 6.1a. Temperature and dew point profile for case **A**. Surface RH = 95%.
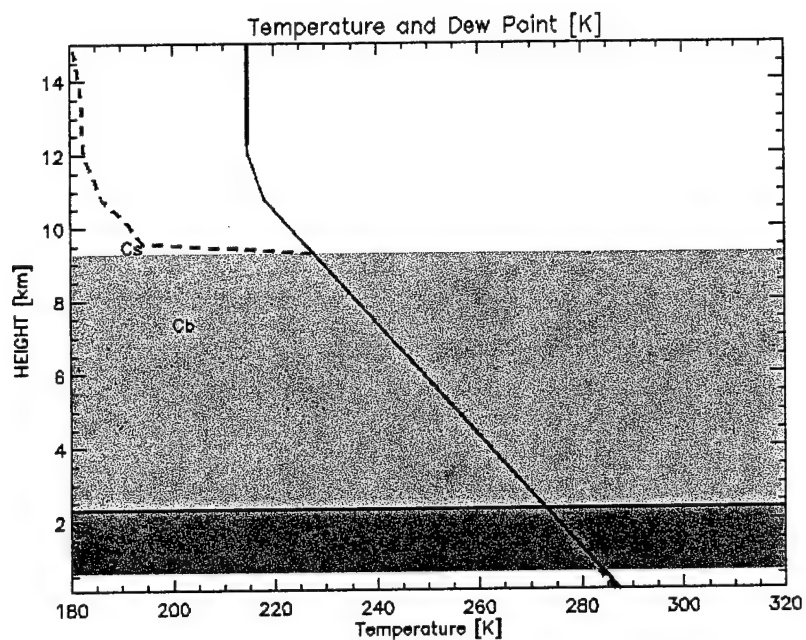
Figure 6.1b. Temperature and dew point profile for case **B**. Surface RH = 95%.
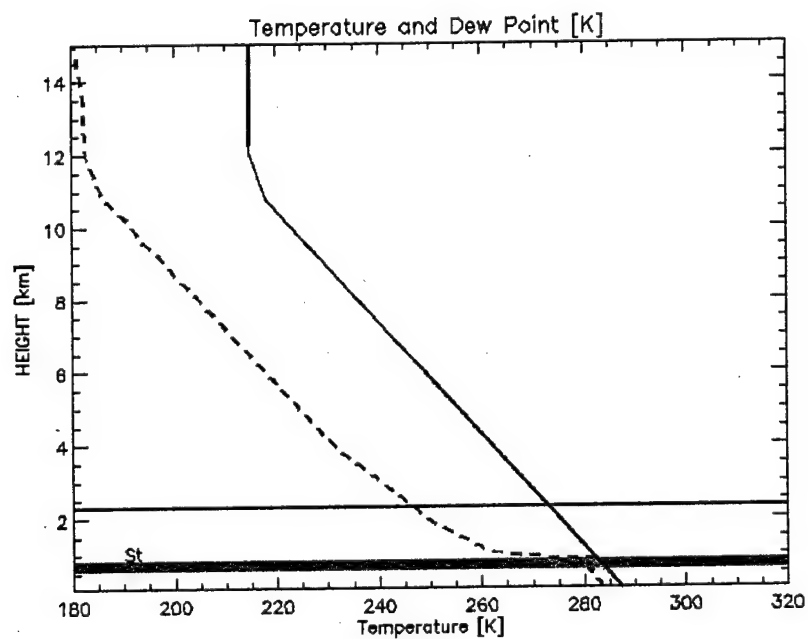
Figure 6.1c. Temperature and dew point profile for case **C**. Surface RH = 80%.
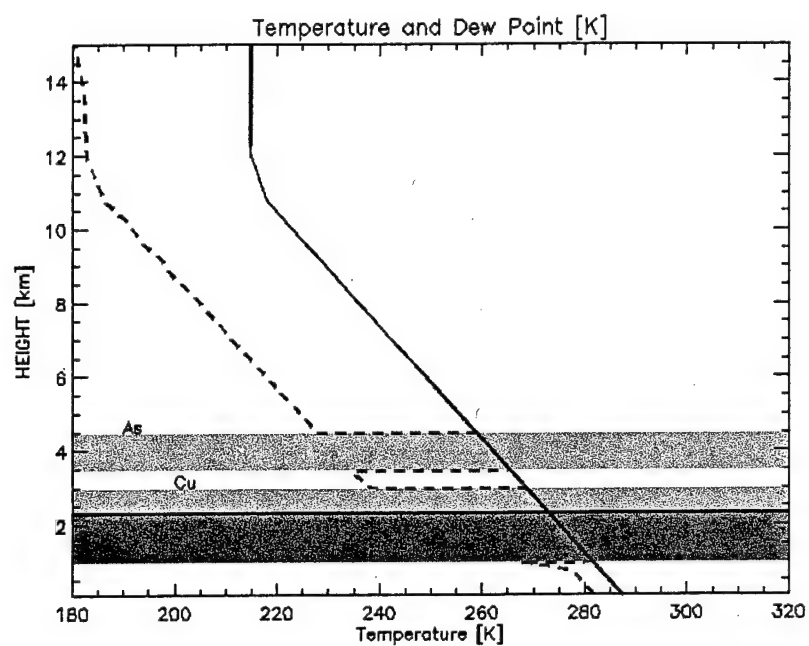
Figure 6.1d. Temperature and dew point profile for case **D**. Surface RH = 70%.
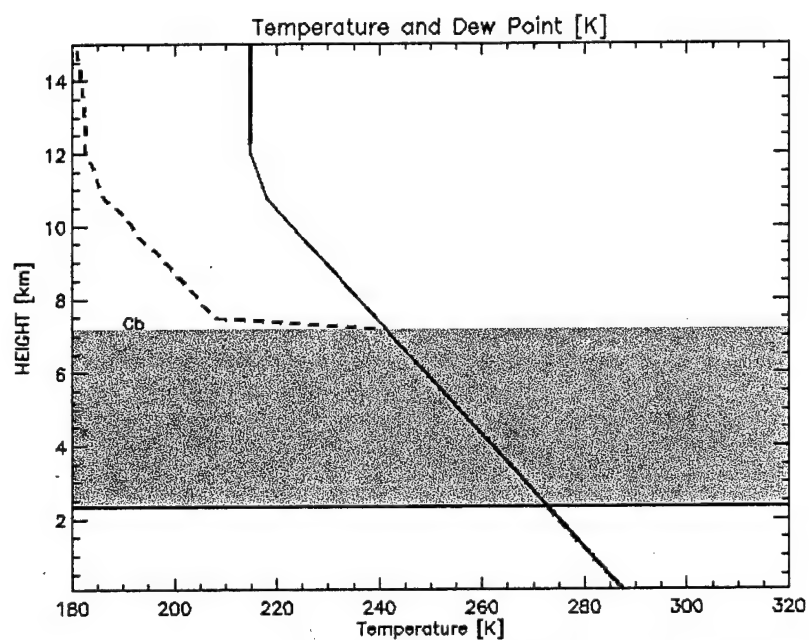
Figure 6.1e. Temperature and dew point profile for case **E**. Surface RH = 100%.

b. Profiles of cloud liquid water and cloud ice mixing ratio

Profiles of cloud liquid water (CLW) and cloud ice (ICE) mixing ratios for each case are shown in Figures 6.2a through 6.2e. Cloud liquid water is computed adiabatically. The cloud liquid water

mixing ratio is zero at cloud base, and it increases with height. If more than one cloud layer is immediately stacked with no cloud free layer between, the mixing ratio is computed from the bottom of the lowest layer to the top of the highest layer (e.g. Figure 6.2b). Otherwise, the mixing ratio is computed separately for each layer (e.g. Figure 6.2a). Cloud ice is then diagnosed from the adiabatic cloud liquid water using bulk parameterizations for four ice forming processes:

- Cloud ice initiation,
- Cloud ice depositional growth,
- Heterogeneous freezing, and
- Homogeneous freezing when the temperature is < -40 °C.

In the nimbostratus/stratus clouds (case **A**, Figure 6.2a), the maximum cloud liquid water mixing ratios are 0.15 g kg^{-1} at the top of the stratus layer and 2.37 g kg^{-1} at the top of the nimbostratus layer. There is no appreciable cloud ice in either of these cloud layers. Both clouds are primarily composed of supercooled droplets.

The cumulonimbus cloud (case **B**, Figure 6.2b) shows a maximum cloud ice mixing ratio of 1.04 g kg^{-1} at the top of the cloud. Above the melting line, cloud water is in mixed phase. Because there is no cloud free region between the two cloud layers, the adiabatic water content is computed continuously from the base of the cumulonimbus to the top of the cirrostratus cloud. The maximum cloud liquid water mixing ratio, 0.75 g kg^{-1}, occurs at 5.25 km. Although the cloud is deeper than the nimbostratus case, its maximum value is less. This is because more of the water has been converted to ice phase, and because the retained fraction of adiabatic liquid water is a function of cloud type (see Table 5.1). Ice and cloud liquid water mixing ratios are equivalent at the -25 °C temperature level; ice dominates above this level, liquid water dominates below.

The thin, near-surface stratus cloud (case **C**, Figure 6.2c) shows a maximum cloud liquid water mixing ratio of about 0.31 g kg^{-1} at cloud top, about twice that of the stratus layer in case **A** even though they are the same depth and cloud type. This is due to the greater temperature, and therefore higher water capacity, of the low-level stratus.

The cumulus/altocumulus clouds (case **D**, Figure 6.2d) shows a maximum cloud liquid water mixing ratio of about 0.40 g kg^{-1} at the top of the cumulus cloud. This isn't much more than the stratus case even though it is several times thicker than the stratus layer at nearly the same elevation and temperature profile. This reflects the assumption that cloud water contents are closer to adiabatic in stratiform clouds than in cumuliform clouds. In the Altostratus (As) layer, the maximum cloud liquid water mixing ratio is about 0.29 g kg^{-1} at its top, and it is computed separately because there is a cloud free layer between the cloudy layers. Both cloud layers are primarily composed of supercooled droplets.

The special cumulonimbus cloud (case **E**, Figure 6.2e) shows a maximum cloud ice mixing ratio of about 0.59 g kg^{-1} at the top of the cloud, and a maximum cloud liquid water mixing ratio of about 0.40 g

kg^{-1} at 5 km. Similar to case **B**, ice and cloud liquid water mixing ratios are equivalent at the -25 °C temperature level; ice dominates above this level, liquid water dominates below. In both cases **B** and **E**, cloud water is most pronounced in mixed phase between 4 and 7 km.
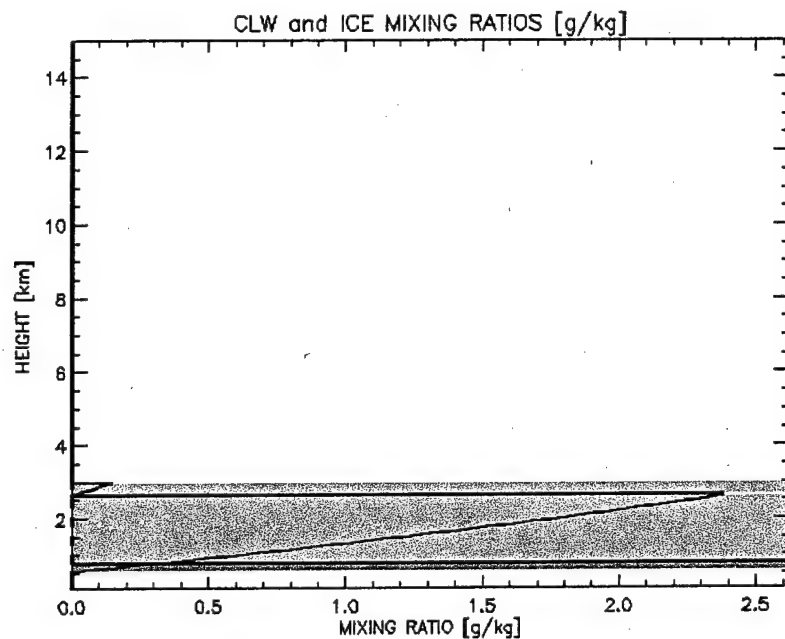
Figure 6.2a. Cloud liquid water (solid) and cloud ice (dashed) mixing ratio for case **A**.
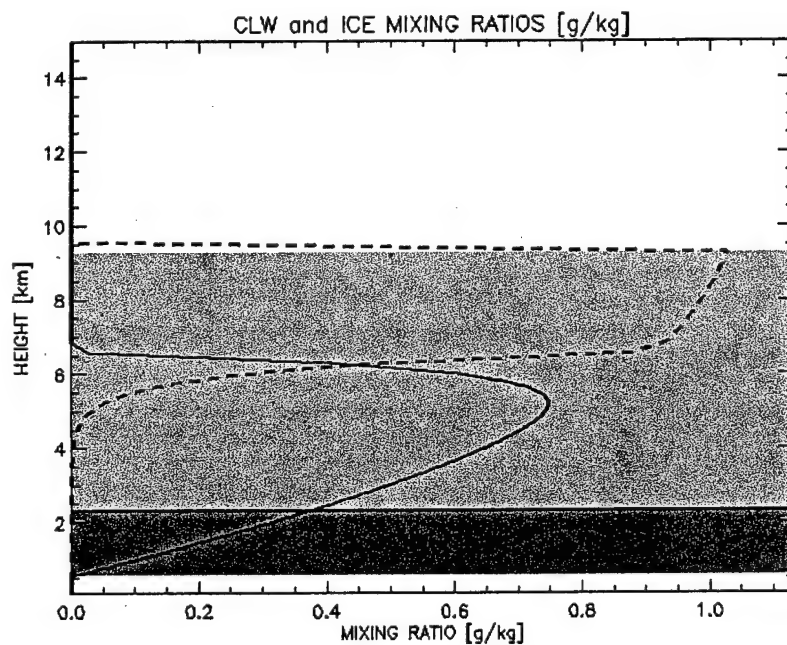
Figure 6.2b. Cloud liquid water (solid) and cloud ice (dashed) mixing ratio for case **B**.
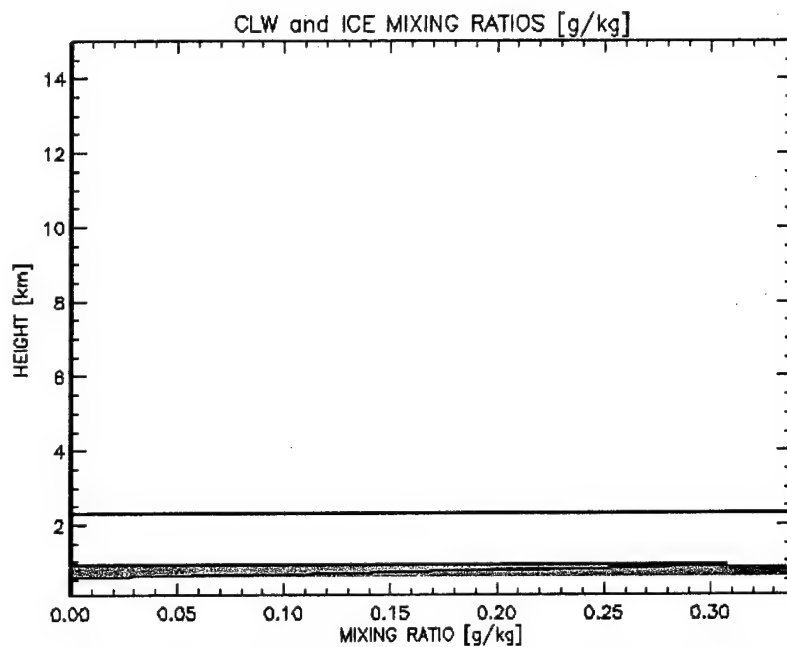
Figure 6.2c. Cloud liquid water (solid) and cloud ice (dashed) mixing ratio for case **C**.
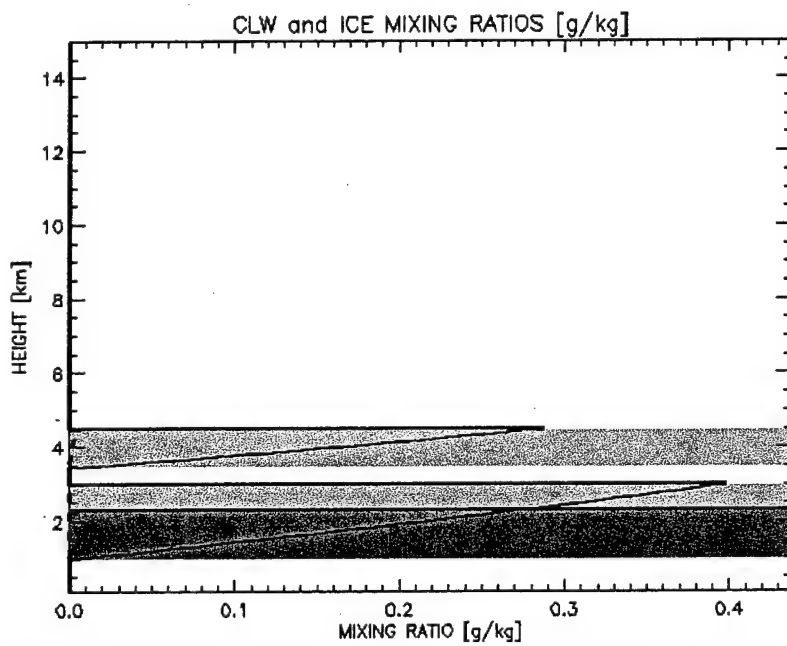
Figure 6.2d. Cloud liquid water (solid) and cloud ice (dashed) mixing ratio for case **D**.
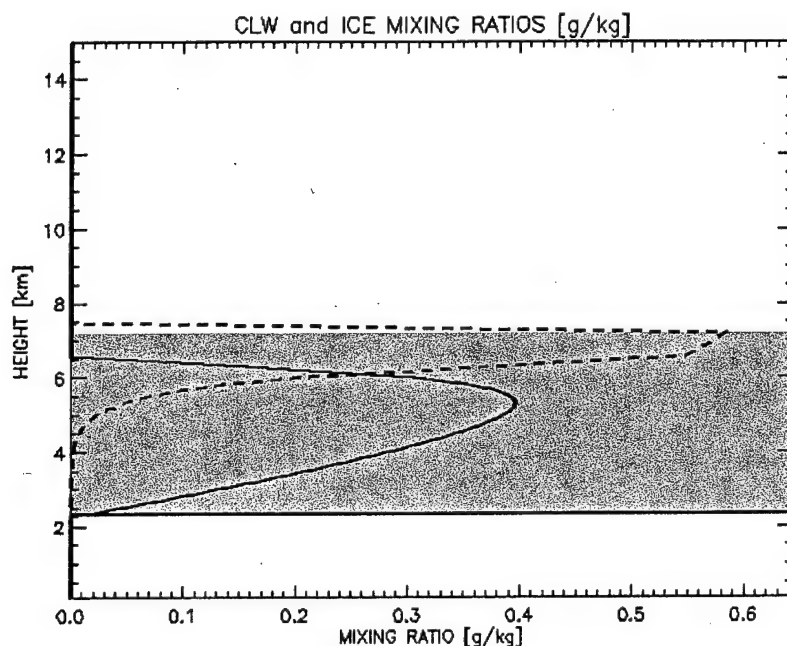
Figure 6.2e. Cloud liquid water (solid) and cloud ice (dashed) mixing ratio for case **E**.

c. Profiles of rain and snow release rate

Several bulk parameterizations are used to compute release rates of precipitation. A breakdown of release rates for autoconversion, collection, and evaporation of rain and snow are given in Figures 6.3a through 6.3e. Component release rate profiles [s^{-1}] are given above the total rain (solid) and total snow release rate profiles (dashed). Components are identified according to Table 6.3. The vertical coordinate of the profiles of release rate components is in km.

Table 6.3. Release rate components used in Figures 6.3a through 6.3e.

PRACW	accumulation of cloud liquid water by rain in clouds
PRAUT	autoconversion of cloud liquid water to rain in clouds
PSAUT	autoconversion of cloud ice to snow in clouds above melting line
PSACI	accumulation of cloud ice by snow in clouds above melting line
PSACW	accumulation of cloud liquid water by snow in clouds above melting line
PSM1	snowmelt due to increasing temperature below melting line
PSM2	snowmelt due to accumulation of cloud liquid water in clouds
PSM3	snowmelt due to accumulation by rain (negative to indicate accumulation of rain by snow)
DRS	deposition of vapor onto snow in clouds
ERR	evaporation of rain below clouds
ERS	sublimation of snow below clouds above the melting line
ERSM	evaporation of wet snow below clouds below the melting level
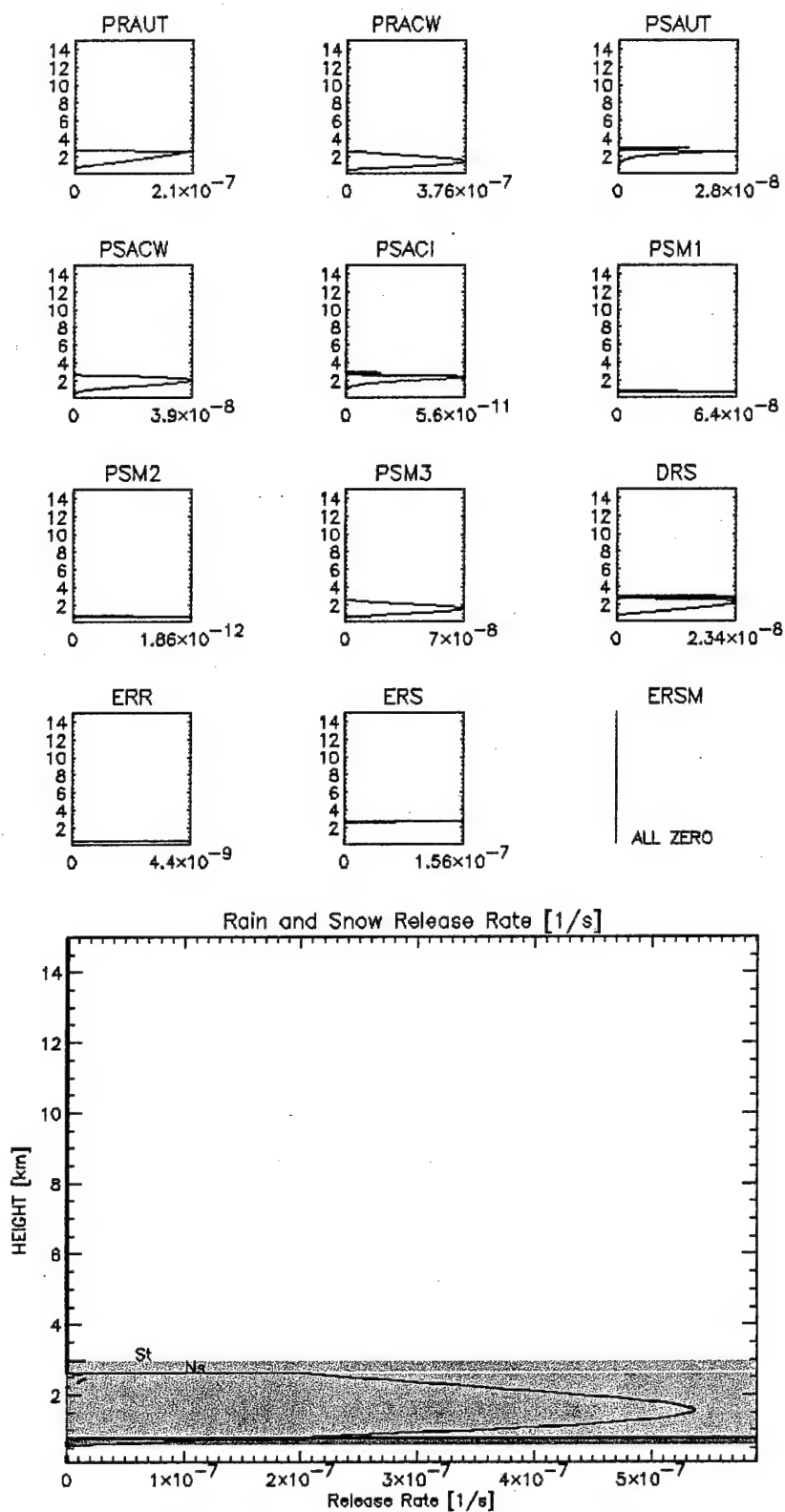
Figure 6.3a. Profiles of release rate components (small profiles above) and total release rate profile (lower plot) for case **A**. Solid line for rain, dashed line for snow.
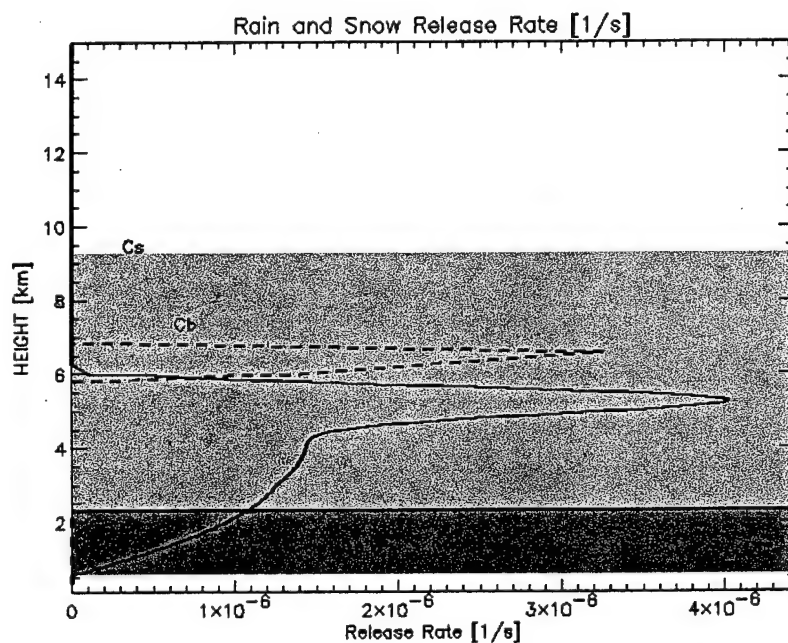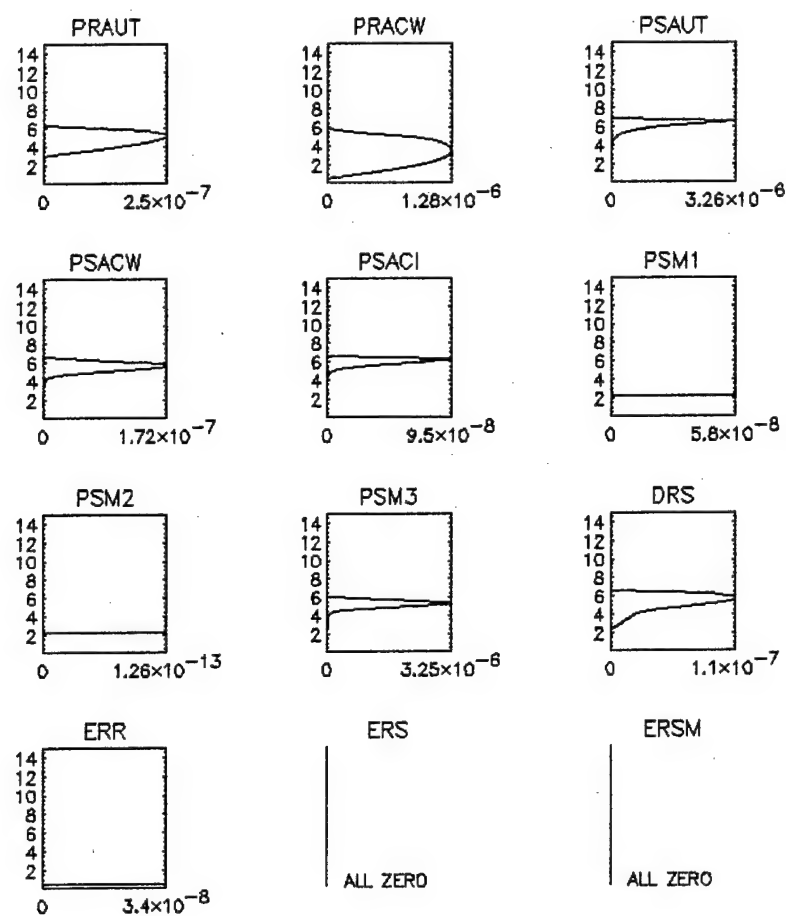
Figure 6.3b. Profiles of release rate components (small profiles above) and total release rate profile (lower plot) for case **B**. Solid line for rain, dashed line for snow.
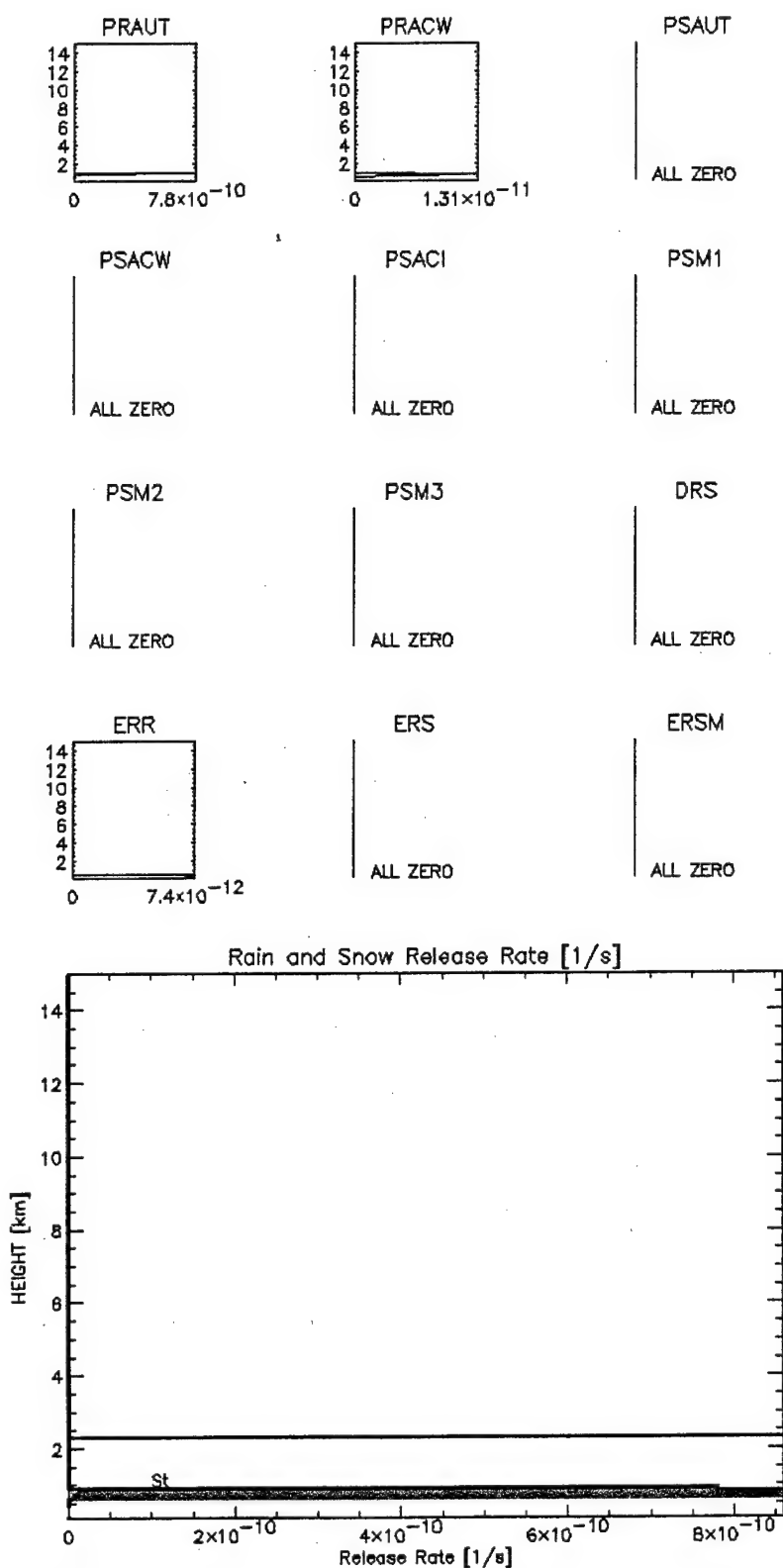
Figure 6.3c. Profiles of release rate components (small profiles above) and total release rate profile (lower plot) for case **C**. Solid line for rain, dashed line for snow.
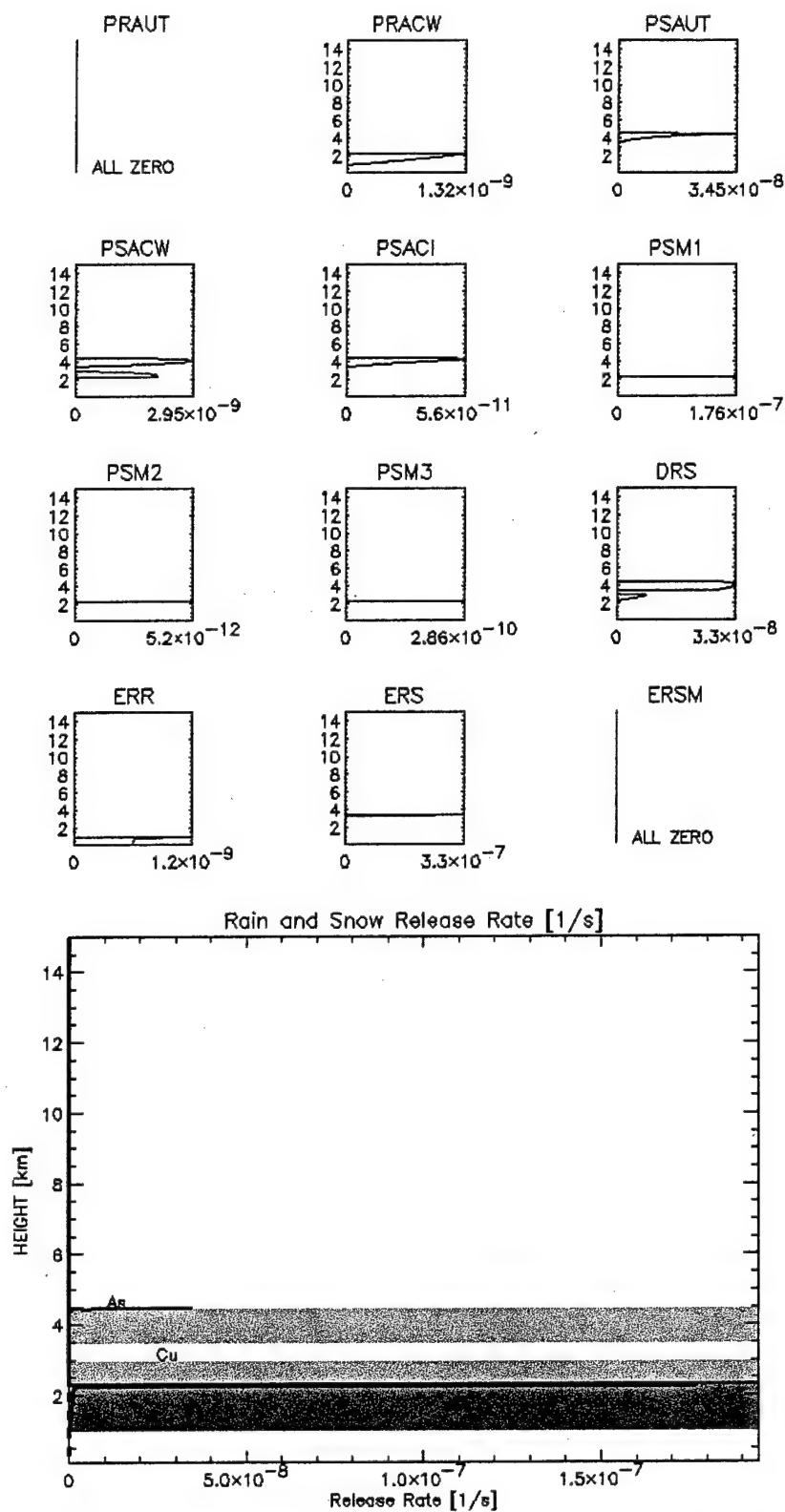
Figure 6.3d. Profiles of release rate components (small profiles above) and total release rate profile (lower plot) for case **D**. Solid line for rain, dashed line for snow.
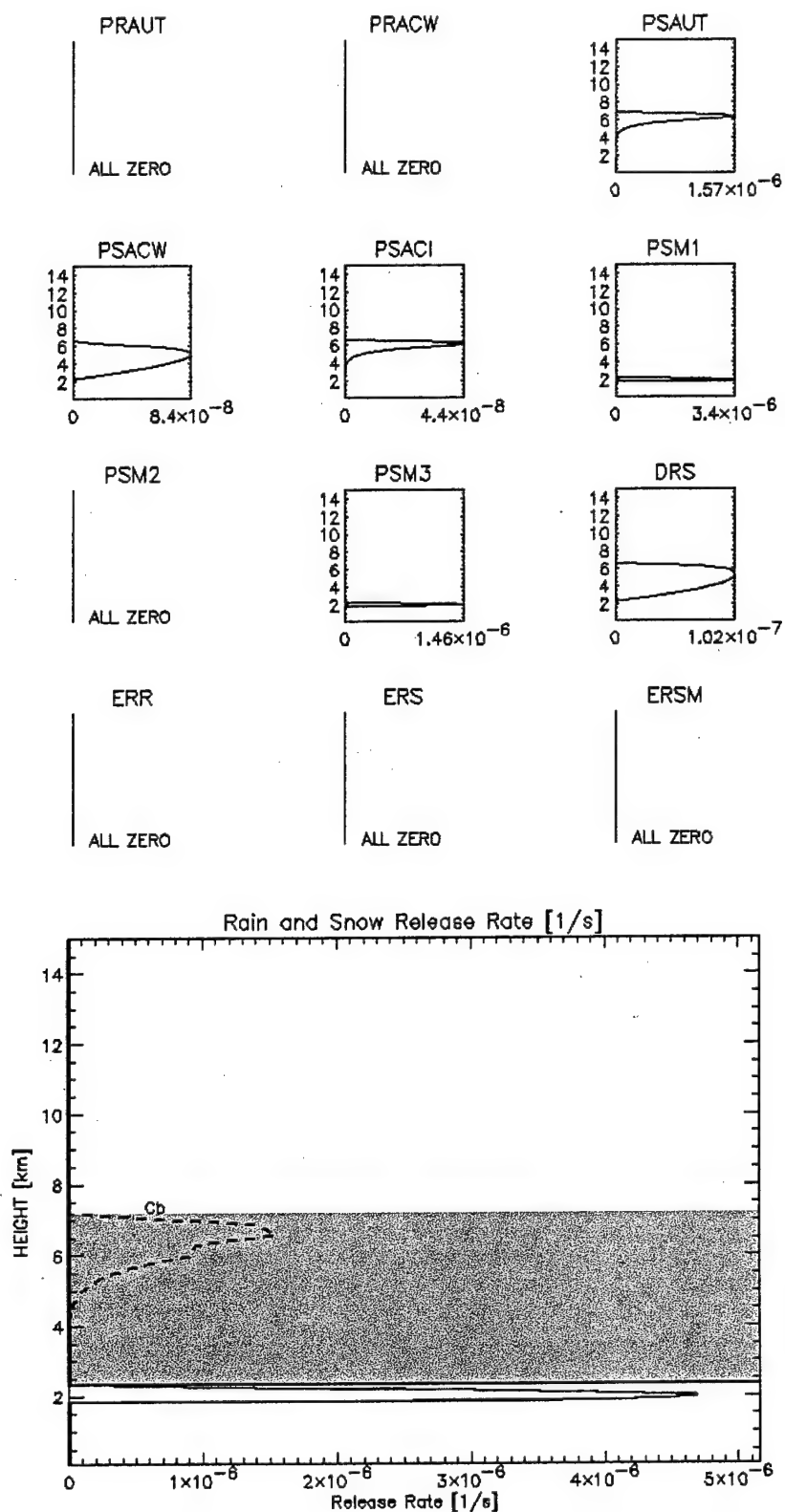
Figure 6.3e. Profiles of release rate components (small profiles above) and total release rate profile (lower plot) for case **E**. Solid line for rain, dashed line for snow.

d. Profiles of rain and snow precipitation rate

Cloud liquid water and cloud ice mixing ratio is computed adiabatically from cloud base to cloud top, but only a fraction of the cloud liquid water is retained for use in the analysis of rain and snow mixing ratio. The coefficients used in the bulk parameterizations for the various cloud processes included in CIS were developed primarily for models with larger grid spacing than that used here (6 km horizontal spacing). Therefore, nearly full saturation values result in overestimating rain and snow mixing ratios.

One step in the CIS algorithm toward computing rain and snow mixing ratios is to compute rainfall rates and snowfall rates. Figure 6.4a is a plot of precipitation rate in mm hr^{-1} units versus height for the nimbostratus/stratus clouds (case **A**). No precipitation rate is detected on this graph for the stratus cloud layer; however, the nimbostratus cloud layer produces a maximum rainfall rate of 3 mm hr^{-1} at the base of the cloud. This rate is slightly reduced by the time it reaches the surface due to evaporation. Rain and snowfall rates increase downward from the top of the nimbostratus cloud. A maximum snowfall rate of about 0.15 mm hr^{-1} occurs just below 2 km. Below this level, snow is removed because of collection by rain.

The plot of rainfall and snowfall rate for the cumulonimbus cloud (case **B**) is given in Figure 6.4b. The snowfall rate (dashed line) reaches a maximum of 6 mm hr^{-1} at about 6 km altitude. Below this level, snow is removed because of collection by rain. The maximum rainfall rate of 24.5 mm hr^{-1} occurs at cloud base. Evaporation slightly reduces this rate by the time it reaches the surface.

Case **B** was particularly useful in tuning the time scale used in the bulk parameterizations for ice (see equation 5.23). The CIS algorithm showed marked sensitivity to the value selected for the time scale, *dt*. In the algorithm, *dt* is set to 18 seconds. When the time scale was increased by a factor of five, cloud ice amounts increased by a factor of five up to the maximum available cloud liquid water. However, rain rates increased by a factor of more than ten when the time scale was set to the higher value. For this cumulonimbus case, the resulting rain rate was more than 300 mm hr^{-1}.

The stratus cloud (case **C**, Figure 6.4c) produces a maximum rainfall rate on the order of 10^{-4} mm hr^{-1} at cloud base. This very small rainfall rate is not extinguished before reaching the surface because near-surface relative humidity is 75% in this profile. The bulk parameterization function for the evaporation of rainwater (equation 5.48) is also continuous and asymptotic to zero. The small rainfall rate is never the less is negligible.

In the cumulus/altocumulus clouds (case **D**, Figure 6.4d), a maximum snowfall rate of 0.14 mm hr^{-1} occurs at the altostratus cloud base. Between the altostratus and cumulus cloud layers, all of the snow either melts or sublimes. Snowfall rate increases downward from the top of the cumulus cloud to the melting line. Rain is not activated above the melting line because it cannot be activated when cloud liquid water mixing ratios are below the thresholds stated in Table 5.3 (also see equation 5.25). Snow, on the other hand, will be activated when any non-zero value of cloud ice mixing ratio is present (see

equation 5.34). Below the melting line, the snow quickly changes phase to rain. The rainfall rate increases downward to a maximum at cloud base. Below cloud base, the rain rate is slightly reduced by evaporation. In this case, negligible precipitation reaches the surface (about 0.02 mm hr^{-1}).

In the special cumulonimbus cloud (case **E**, Figure 6.4e), snowfall reaches a maximum of 5.6 mm hr^{-1} at cloud base. Rain does not occur because the cloud liquid water mixing ratio is never high enough to activate bulk autoconversion of cloud liquid water to rain and subsequent accumulation processes. Because the sub-cloud region is saturated in this case, only two melting processes are at work converting the snow to rain; melting due to increased temperature, and melting due to being swept out by rain forming above. All of the snow has melted by the time it reaches the 1.8 km altitude level, about 500 m below the melting line and cloud base. The resulting rainfall after all the snow has melted is conserved. Total precipitation rate is conserved in this case because there are no formation or reduction processes altering the liquid water content, only a phase change from snow to rain. Once all of the snow has melted, the rainfall rate remains constant to the surface.
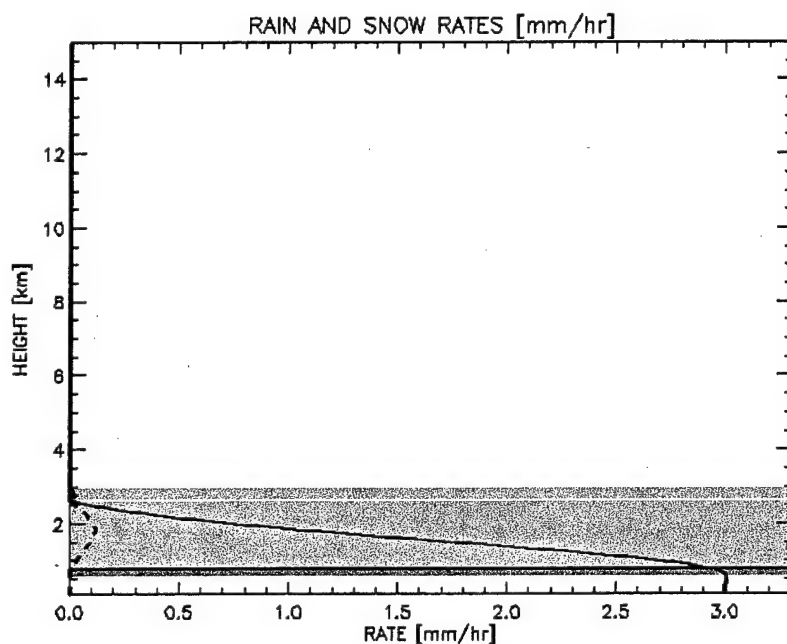
Figure 6.4a. Rain rate (solid) and snow rate (dashed) for case **A**.
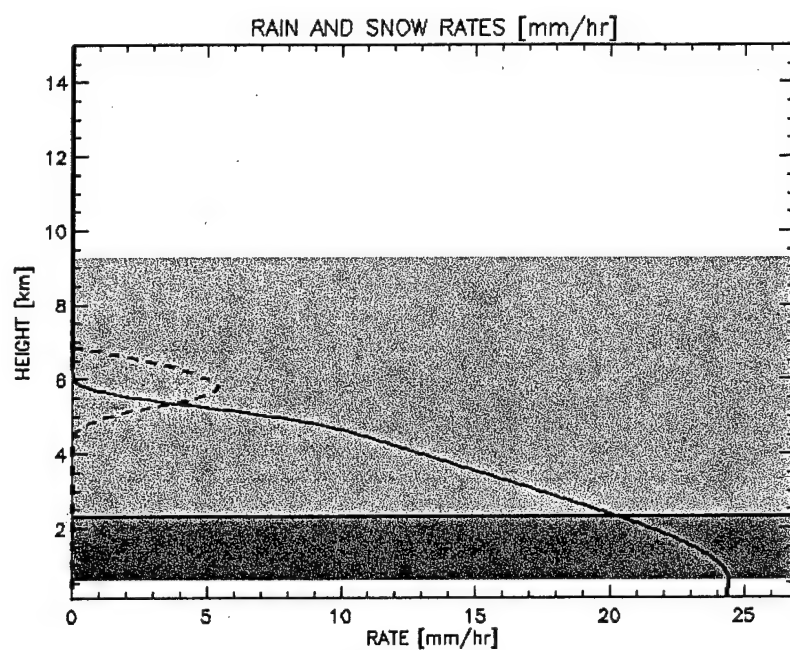
Figure 6.4b. Rain rate (solid) and snow rate (dashed) for case **B**.
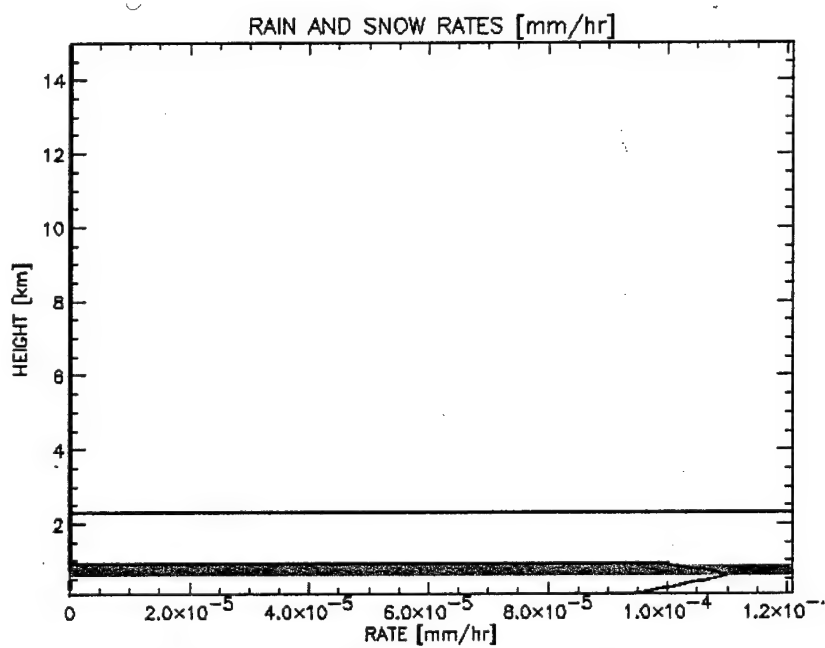
Figure 6.4c. Rain rate (solid) and snow rate (dashed) for case **C**.

RAIN AND SNOW RATES [mm/hr]
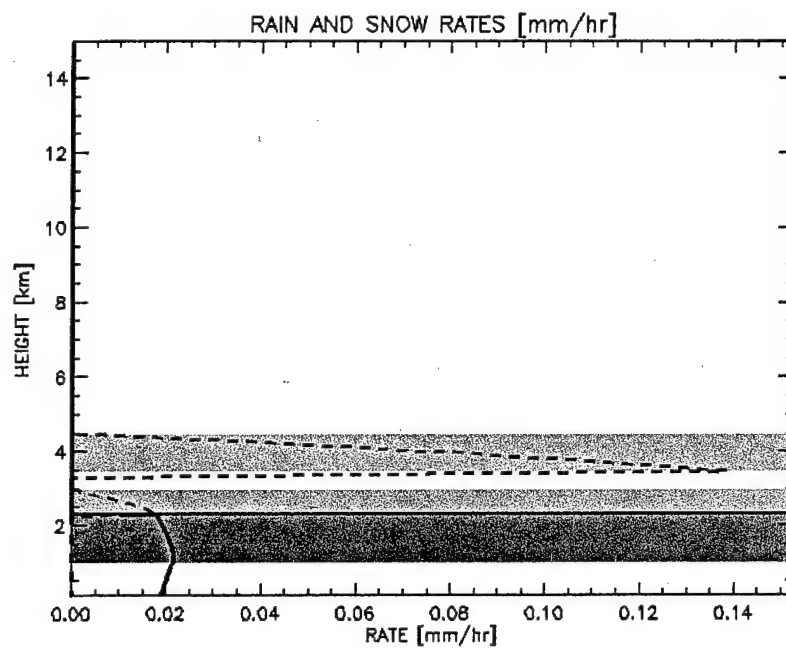
Figure 6.4d. Rain rate (solid) and snow rate (dashed) for case **D**.

RAIN AND SNOW RATES [mm/hr]
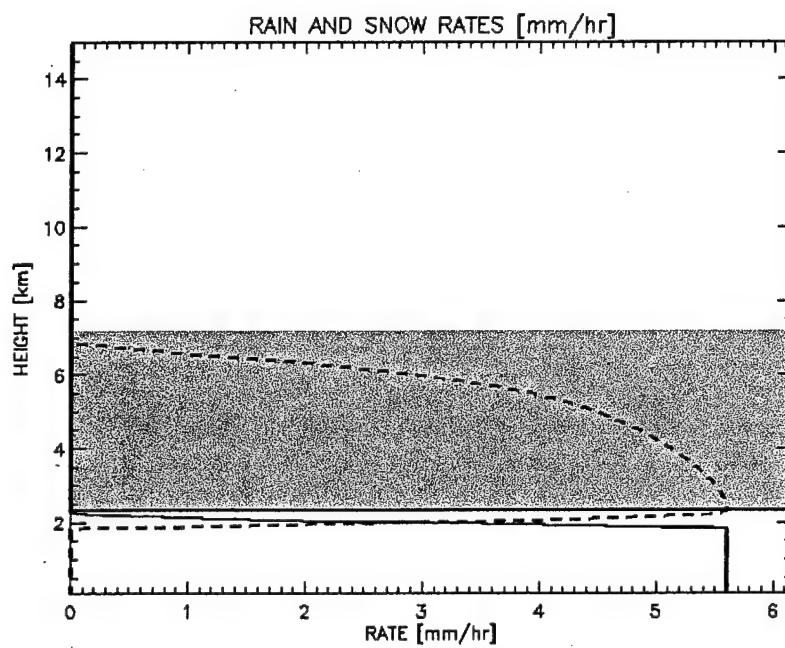
Figure 6.4e. Rain rate (solid) and snow rate (dashed) for case **E**.

e. Profiles of rain and snow content

Rainfall and snowfall rate is independent of the depth over which the precipitation falls in a unit time; however, liquid water content is dependent on the depth the precipitation falls in a unit time. Rain falls at a faster rate than snow and thus will spread the mass of melting snow over a greater depth. The result is lower liquid water content for rain than for snow (see Figure 6.5). The equivalent liquid water content for snow reaches a maximum of 1.25 g m^{-3} at cloud base. The liquid water content for rain reaches a maximum of only 0.53 g m^{-3}. Figure 6.6 illustrates how liquid water content changes with precipitation rate for both snowfall and rainfall in CIS. Rainfall liquid water content is roughly half of the snow liquid water content for the same precipitation rate.

The mass-weighted mean terminal velocity can be computed by finding the ratio of precipitation rate to liquid water content.

$$V_t = \frac{P}{lwc} \tag{6.8}$$

lwc   liquid water content of either rain or snow [kg m^{-3}]
P   precipitation rate for either rain or snow [kg m^{-2} s^{-1}]
V$_t$ Average terminal velocity for either rain or snow [m s^{-1}]

Figure 6.7 shows how average terminal velocity varies with precipitation rate. Using equation (6.8), the average terminal velocity for rain is roughly twice that of snow for a given precipitation rate. A higher terminal velocity for rain results in distributing rain mass over a greater depth and therefore reducing the liquid water content at a given level.
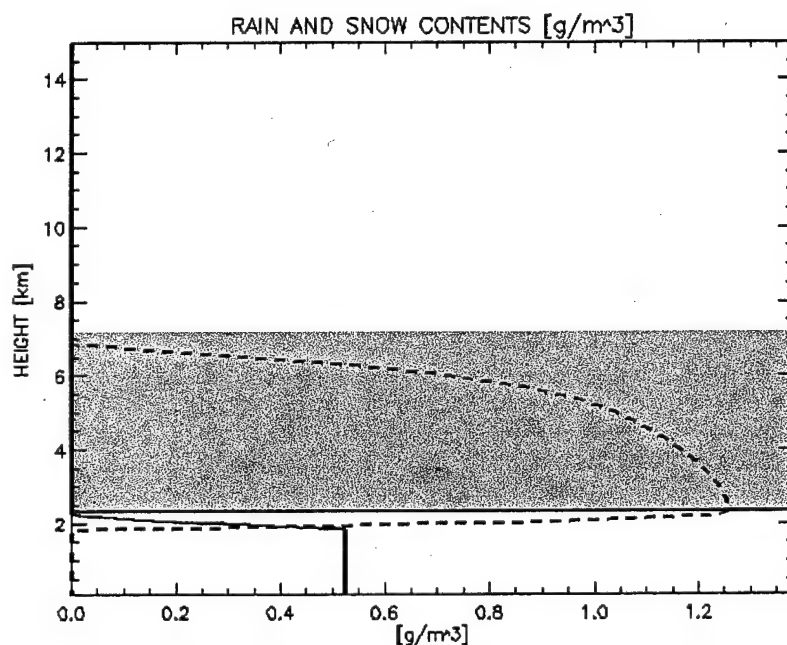
Figure 6.5. Rain (solid) and snow (dashed) equivalent liquid water contents for case **E**.
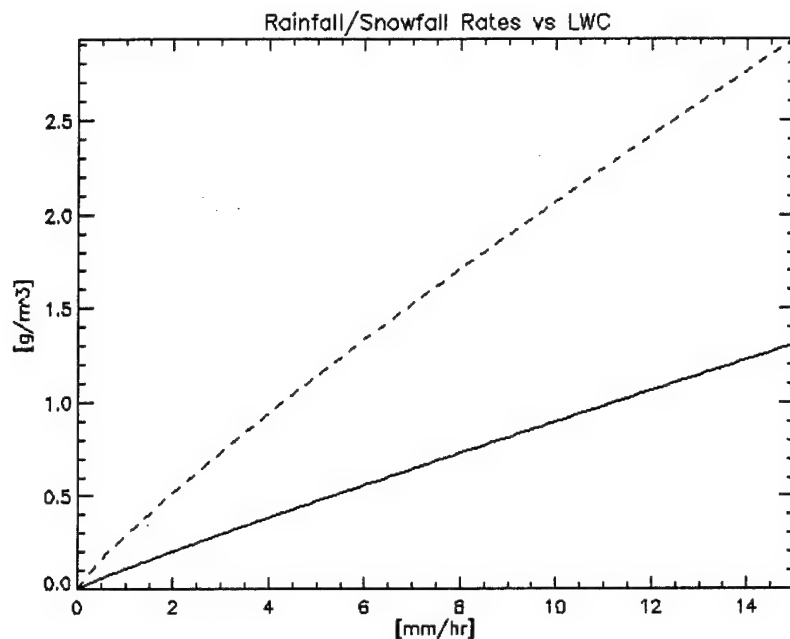
Figure 6.6. Liquid water content as a function of rainfall (solid) / snowfall (dashed) rate.
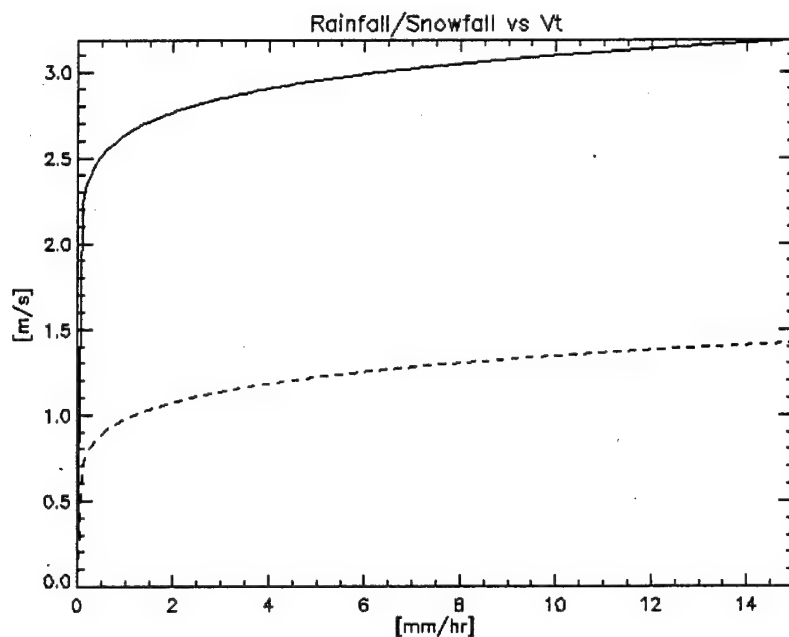
Figure 6.7. Terminal velocity as a function of rainfall (solid) / snowfall (dashed) rate.

f. Profiles of rain and snow mixing ratio

Profiles of rain and snow mixing ratio computed from the rainfall and snowfall rates for each case are presented in Figures 6.8a through 6.8e. These mixing ratios are later used to initialize a mesoscale

model. CIS computes mixing ratios from liquid water contents that are in turn generated from the rainfall and snowfall rates. Keep in mind that liquid water content has units of mass per unit volume, whereas mixing ratio is density dependent with units of mass per unit mass. Mixing ratio profiles will not generally parallel rainfall and snowfall rates, which have their maximum at cloud base. All five cases show a maximum mixing ratio above the cloud base. This is because air density is increasing downward at a rate faster than rainfall rate is increasing downward. To see this characteristic difference between mixing ratio and liquid water content, compare Figures 6.5 and 6.8e for case **E**. Figure 6.8e shows the profile of mixing ratio and Figure 6.5 shows the same case's profile of liquid water content. In Figure 6.8e, the maximum mixing ratio occurs about 1 km above cloud base. In Figure 6.5, the maximum equivalent liquid water for snow occurs at cloud base, and the maximum liquid water content for rain occurs at the level where all the snow has melted to form rain. This value for liquid water content is lower because the average terminal velocity for rain is higher. Because there is no evaporation, the rain content is conserved down to the surface.
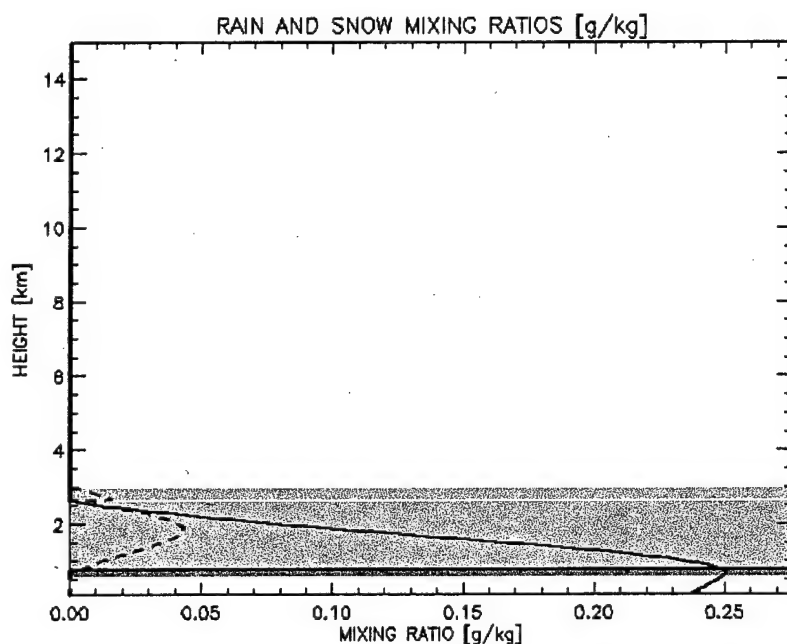
Figure 6.8a. Rain (solid) and snow (dashed) mixing ratio for case **A**.

RAIN AND SNOW MIXING RATIOS [g/kg]
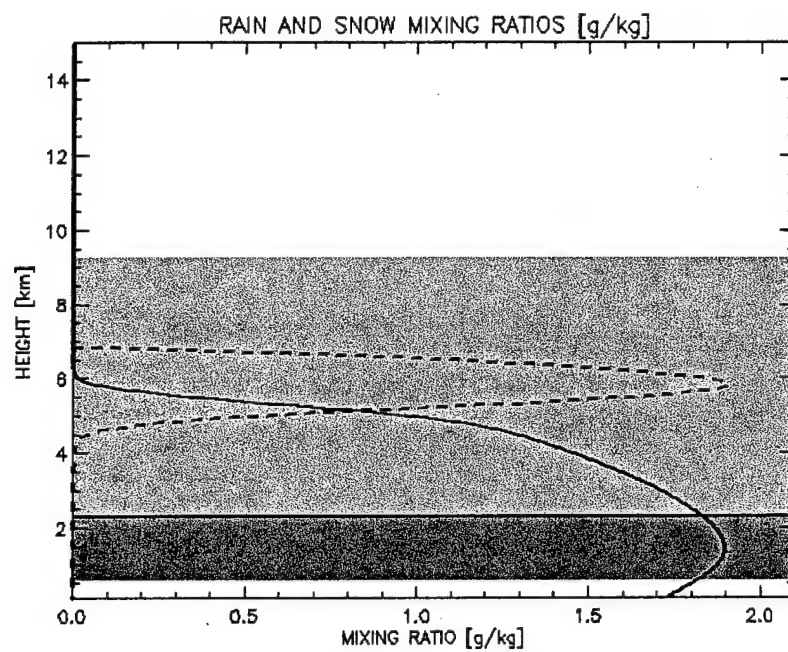
Figure 6.8b. Rain (solid) and snow (dashed) mixing ratio for case **B**.

RAIN AND SNOW MIXING RATIOS [g/kg]
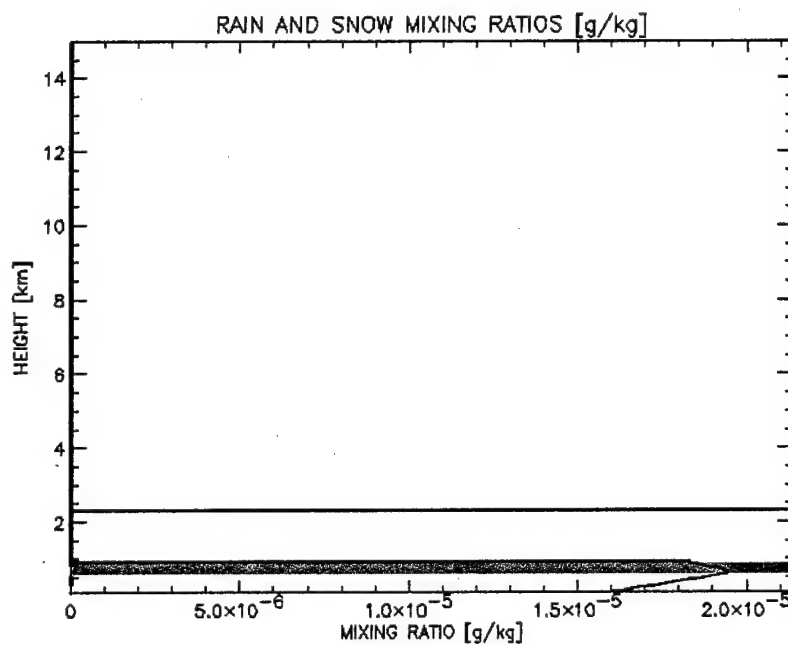
Figure 6.8c. Rain (solid) and snow (dashed) mixing ratio for case **C**.

RAIN AND SNOW MIXING RATIOS [g/kg]
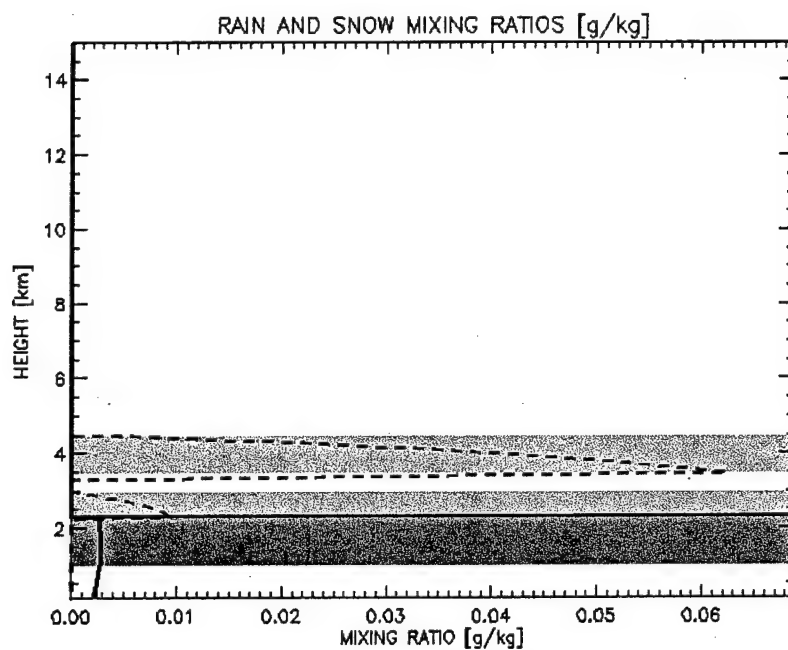
Figure 6.8d. Rain (solid) and snow (dashed) mixing ratio for case **D**.

RAIN AND SNOW MIXING RATIOS [g/kg]
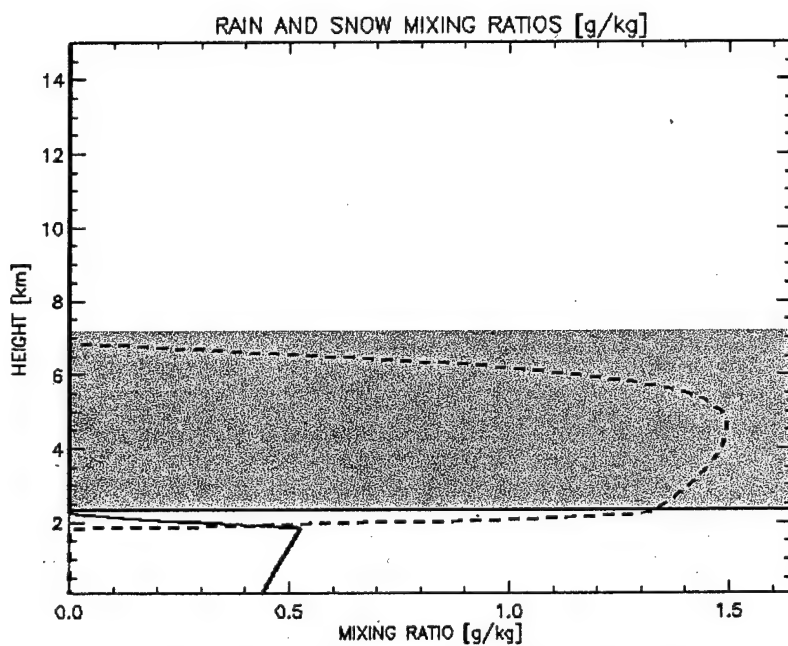
Figure 6.8e. Rain (solid) and snow (dashed) mixing ratio for case **E**.

g. Estimation of maximum column reflectivity

One final gross tuning parameter used in this study is the maximum column reflectivity. This is found using simple Z-R relationships borrowed from Sekhon and Srivastava (1970) for the snowfall rate and from Sekhon and Srivastava (1971) for the rainfall rate. Table 6.4 lists the maximum analyzed reflectivity based on the rainfall and snowfall rates in the cloud column. When applied to a real cloud analysis, the intensity and distribution of reflectivity values can identify where CIS is generating unrealistic rainfall rates, which are later used to compute the mixing ratios of rain and snow.

Table 6.4. Maximum analyzed reflectivity for each case.

Case 1: Ns/St	Case 2: Cb/Cs	Case 3: St	Case 4: Cu/As	Case 5: Cb
31.14 dBZ	48.70 dBZ	0.00 dBZ	13.54 dBZ	49.05 dBZ

h. Comparison of PSACR/PRACS parameterization between CIS and Reisner schemes

It was mentioned in Chapter V that the release rates due to the collection of snow by rain and due to the collection of rain by snow are computed differently in CIS than in MM5's Reisner scheme. The formulas for these processes in MM5 (Reisner et al. 1998, equations A.47 and A.48) were too unstable for this diagnostic procedure. The equations for the release rates due to the collection of rain by snow (P_{SACR}) and due to the collection of snow by rain (P_{RACS}) are given below:

$$P_{SACR} = \pi^2 \sqrt{\left(\alpha \overline{U}_r - \beta \overline{U}_s\right)^2 + \gamma \overline{U}_r \overline{U}_s}\, \frac{\rho_w}{\rho} N_{o,r} N_{o,s} \left(\frac{5}{\lambda_r^6 \lambda_s} + \frac{2}{\lambda_r^5 \lambda_s^2} + \frac{0.5}{\lambda_r^4 \lambda_s^3} \right)$$

$$P_{RACS} = \pi^2 \sqrt{\left(\alpha \overline{U}_r - \beta \overline{U}_s\right)^2 + \gamma \overline{U}_r \overline{U}_s}\, \frac{\rho_s}{\rho} N_{o,r} N_{o,s} \left(\frac{5}{\lambda_s^6 \lambda_r} + \frac{2}{\lambda_s^5 \lambda_r^2} + \frac{0.5}{\lambda_s^4 \lambda_r^3} \right)$$

α coefficient = 1.2 for equation A.47 and 1.7 for equation A.48
β coefficient = 0.95 for equation A.47 and 0.3 for equation A.48
γ coefficient = 0.08
λ_r, λ_s slope parameter in rain and snow size distribution (m^{-1})
ρ air density (kg m^{-3})
ρ_w density of liquid water = 1000.0 kg m^{-3}
ρ_s density of snow = 100.0 kg m^{-3}
U_r, U_s mass weighted mean terminal velocity for rain and snow (m s^{-1})
$N_{o,r}, N_{o,s}$ slope intercept in rain and snow size distribution (m^{-4})

The following figures compare results using the canned-cloud case E (cloud base coincides with melting line, no evaporation or sublimation below cloud base). Profiles of precipitation rates, precipitation equivalent liquid water contents, and precipitation mixing ratios for case E are given in Figures 6.4e, 6.5, and 6.8e respectively. Those profiles are created using the new parameterizations for PSACR and PRACS in CIS. As a reminder, PSACR is the release rate of snow due to the accumulation of rain by snow. PRACS is the release rate of rain due to the accumulation of snow by rain. Figures 6.9

through 6.11 show the precipitation rates, precipitation equivalent liquid water contents, and precipitation mixing ratios respectively using the Reisner scheme equations for PSACR and for PRACS. These plots indicate instability between the snow and rain values. Both release rates are a function of rain and snow from levels above as they are applied in CIS. The Reisner scheme is very sensitive to small changes in mixing ratio when precipitation content is conserved as it changes phase between snow and rain. It is for this reason the parameterizations for PSACR and PRACS are reformulated from those used in the Reisner scheme.
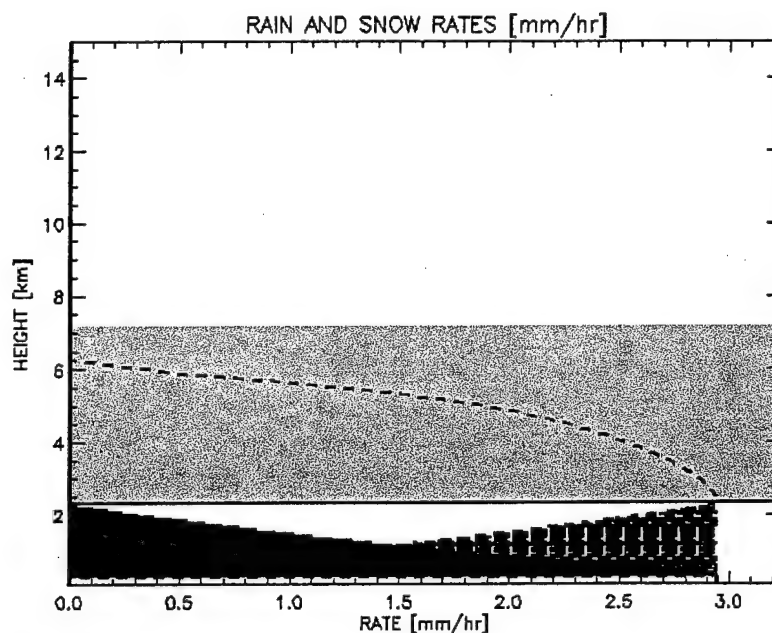
Figure 6.9. Rain (solid) and snow (dashed) rates for case **E** using the Reisner scheme parameterizations for PSACR and PRACS.
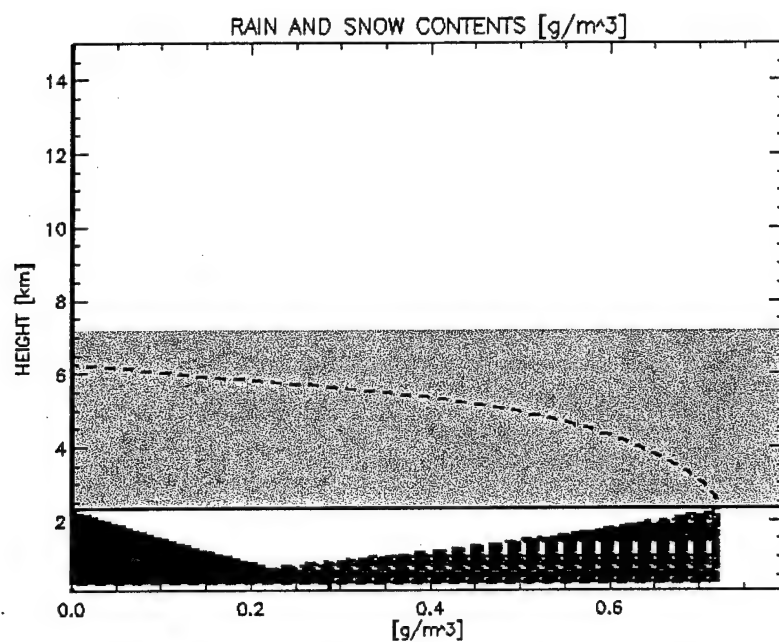
Figure 6.10. Rain (solid) and snow (dashed) equivalent liquid water contents for case **E** using the Reisner scheme parameterizations for PSACR and PRACS.
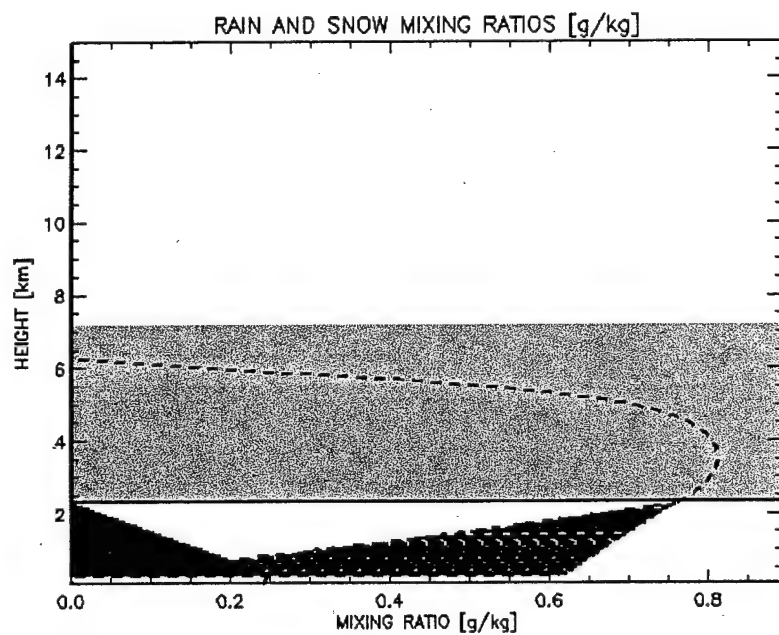
Figure 6.11. Rain (solid) and snow (dashed) mixing ratio for case **E** using the Reisner scheme parameterizations for PSACR and PRACS.

This chapter has presented the tuning results for the cloud initialization scheme using a few cloud profiles typical of those found in RTNEPH. The mixing ratio profiles of cloud liquid water, cloud ice, rain, and snow simulate well the vertical distribution of water species typical in clouds. Tuning showed highest sensitivity to the fraction of adiabatic cloud liquid water retained as a function of cloud type. Precipitation profiles within each cloud type were reasonable. Sub-cloud evaporation processes produced expected decreases in mixing ratio and water contents. The water content conserving feature of the scheme, which managed the mass of water species during its phase change from ice to liquid, also produced reasonable results. This scheme demonstrates that it can produce realistic mixing ratios and analyzed reflectivity values depending on the cloud profile to which it is applied. Chapter VII next presents details of the modeling experiments by outlining MM5's configuration, initialization, and application to two case studies.

CHAPTER VII

EXPERIMENT

7.1. Mesoscale Model

a. Model description

The NWP model selected for this study is the Pennsylvania State University/National Centers for Atmospheric Research Fifth-Generation Mesoscale Model (PSU/NCAR MM5), version 3.3 (Grell et al. 1994). Three nested domains are used with grid spacing 54 km (domain 1), 18 km (domain 2), and 6 km (domain 3). Domains 1 and 2 cover most of the southeastern United States. Domain 3 is roughly 400 km wide centered over the Houston Ship Channel. The three nested model domains are depicted in Figure 7.1.
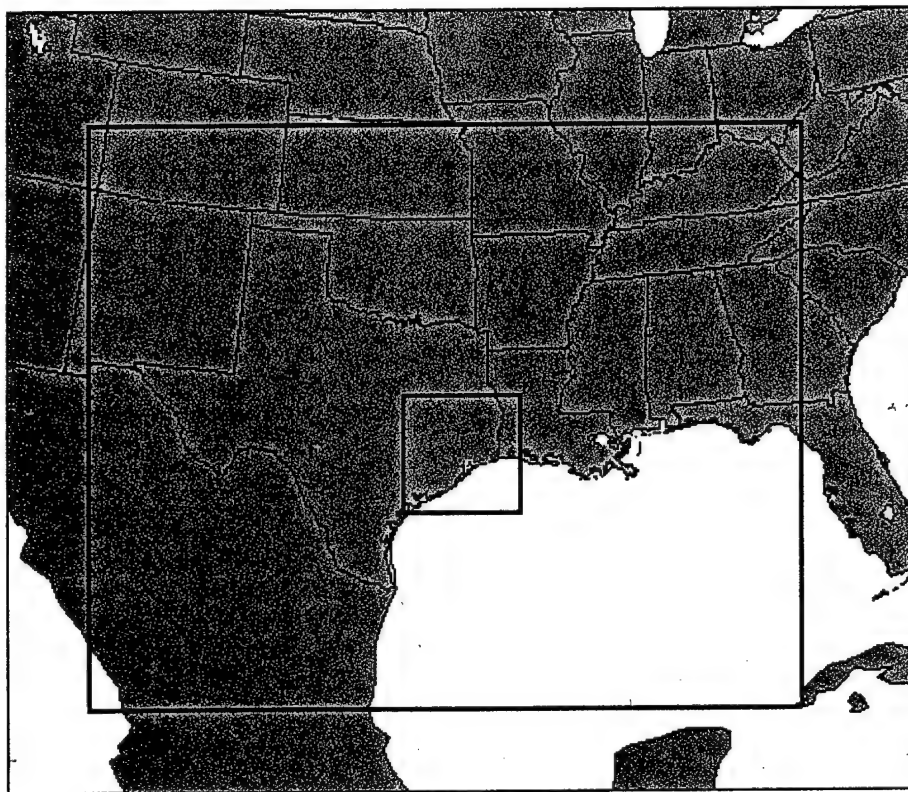
Figure 7.1. Model domains. Inner-most box contains domain 3.

Several physics packages, convection schemes, and boundary layer schemes are available in MM5. In this experiment, the Reisner mixed phase cloud physics scheme, which excludes graupel, is used. The Grell convection scheme is used on domains 1 and 2. No convection scheme is used on domain 3 because clouds are assumed explicitly defined at that resolution. The MRF boundary layer scheme is used on domain 1, and the Blackadar boundary layer scheme is used on domains 2 and 3. The model's four-dimensional data assimilation (FDDA) scheme is used to nudge initial temperatures and winds to analyzed temperatures and winds at forecast hours -6 and +0. MM5 is configured to employ full two-way nesting between domains.

b. *Source data*

MM5 is initialized with temperatures, pressures, winds, and cloud variables primarily from three different databases: the Navy Operational Global and Regional Atmospheric Prediction System (NOGAPS) analysis, the Air Force's Surface Temperature analysis (SFCTEMP), and the Air Force's Real Time Nephanalysis (RTNEPH). NOGAPS data includes temperature, dew point temperature, and geopotential height at standard pressure levels at 2.5-degree latitude/longitude resolution over the region of interest. NOGAPS is available in 6-hourly intervals. SFCTEMP provides surface temperature data only at the surface and is available at 8th-mesh (approximately 48 km) resolution. SFCTEMP data is available in 3-hourly intervals. A non-linear vertical interpolation scheme is applied to NOGAPS temperatures that intersect the surface to make NOGAPS data compatible with SFCTMP data (see Appendix E). RTNEPH data includes cloud amount, cloud type, cloud base and cloud top altitudes for up to four floating layers of clouds at 8th-mesh horizontal resolution. RTNEPH is available in 3-hourly intervals from the archive, however when used in real-time mode, updates are available at approximately 16-minute intervals over varying regions of the globe.

NOGAPS, SFCTEMP, and RTNEPH are also used as input in the cloud initialization scheme (CIS) to analyze cloud species mixing ratios of saturated water vapor, cloud liquid water, cloud ice, rain, and snow (see Chapters IV and V). CIS cloud variables are analyzed at 18-km resolution and at 6-km resolution at 3-hourly intervals. In direct-insertion simulations, CIS cloud variables are also used to initialize MM5. These data are obtained from the Air Force Combat Climatology Center (AFCCC; their mailing address is provided in the References). Data is provided for the North American region over the period 13 September 2000, 00-UTC, through 15 September 2000, 18-UTC.

c. *Experiment protocol*

A cloud variable analysis is produced using CIS at 3-hourly intervals. This analysis is compared to mesoscale model simulation output of the same variables. Some of the model simulations use CIS to initialize cloud variables. Because the mesoscale model does not output cloud type, cloud top, or cloud base information, no direct comparison with RTNEPH data can be made. The purpose of the

experiment is two-fold: to determine if model simulations initialized using CIS will spin-up faster than model simulations without initialization, and to determine if model simulations initialized using CIS will improve cloud variable forecasts over model simulations without cloud initialization.

Two forecast periods are examined:

- 13 September 2000, 00-UTC through 14 September 2000, 06-UTC (forecast hours -6 to +24)
- 14 September 2000, 12-UTC through 15 September 2000, 18-UTC (forecast hours -6 to +24)

Two types of simulations are run: without any cloud initialization and with CIS initialization. Assimilation of cloud data is performed using direct insertion of CIS analyzed cloud variables at forecast hours -6 and +0 into domains 2 and 3. Assimilation of clouds on domain 1 is performed using a Barnes analysis technique (described in the next section) that analyzes cloud variables from domain 2. Two special 1.5-hour simulations are also conducted for the 13 September, with-cloud initialization case. The first special simulation is crafted to directly insert cloud liquid water and cloud ice but excludes rain and snow. The second special simulation directly inserts cloud liquid water and cloud ice, excludes rain and snow, and sets all diffusion terms to zero.

d. Barnes' analysis of mixing ratios onto mother domain

Mixing ratios of water vapor, cloud liquid water, cloud ice, rain, and snow are directly inserted onto domains 2 and 3. In order to have these mixing ratios coherent on the mother domain, domain 1, a Barnes analysis technique is applied (Daley, 1991). The nested grid, domain 2, is assumed to contain regularly gridded observations of the mixing ratios. Mixing ratios on the mother grid (domain 1) are computed as follows:

$$f_A(\mathbf{r}_i) = \sum_{k=1}^{K_i} W(r_{ik}) f_O(\mathbf{r}_k) \tag{7.1}$$

$$W(r_{ik}) = \frac{w(r_{ik})}{\sum_{k=1}^{K_i} w(r_{ik})} \tag{7.2}$$

$$w(r_{ik}) = \exp\left(-\frac{r_{ik}^2}{2L^2}\right) \tag{7.3}$$

$f_A(\mathbf{r}_i)$ Analyzed mixing ratio on mother domain grid point $\mathbf{r}_i$.
$f_O(\mathbf{r}_k)$ Observed mixing ratio on nested domain grid point $\mathbf{r}_k$.
$W(r_{ik})$ Total weight function.
$w(r_{ik})$ Weight function.
L Weight parameter.
r_{ik} Absolute distance between observed and analyzed grid points in grid space.
K_i Total number of observed grid points considered for analysis grid point.
k Observation grid point.

The weight parameter L^2 is the number of observation grid points represented by a single analysis grid point. In this case, domain 2 and 1 grid spacing is 18 and 54 km respectively (factors of three times the smallest grid spacing), so $L^2 = 9$. Distances r_{ik} are calculated in grid space only.

e. Model output

Output for domain 1 includes complete model history files at 3-hour intervals from forecast hour -6 until termination. Output for domains 2 and 3 vary with simulation type. Both simulation types output complete model history files at 3-hour intervals from forecast hour -6 until termination. For the non-CIS simulations, output includes cloud variables, water vapor mixing ratio, temperature, vertical velocity, and pressure at 6-minute intervals between forecast hours -6 and +12. For the CIS-initialized simulations, output includes cloud variables and water vapor mixing ratio at 6-minute intervals between forecast hours -6 and +6.

7.2. Weather Analysis

a. Case selection

The period of study chosen to conduct two cloud forecast experiments was selected at random. The only criterion used in selecting a period of study was to choose a situation with great cloudiness. When the principal investigator asked his advisor to help him select a day for study, his advisor, Professor John Nielsen-Gammon, looked out the window from his 10th floor office in the Oceanography and Meteorology Building towering over the campus at Texas A&M University and simply replied, "Why not today"? That day was 13 September 2000. The data for the study was then collected after giving AFCCC sufficient time to archive three days of RTNEPH, NOGAPS, and SFCTEMP data. Two 24-hour forecast periods were chosen over the three-days between 13 - 16 September 2000. The first period examined is 13 September 2000, 00-UTC (forecast hour -6) to 14 September 2000, 06-UTC (forecast hour +24). The second period of the study is 14 September 2000, 12-UCT (forecast hour -6) to 15 September 2000, 18-UTC (forecast hour +24).

b. Synoptic situation

A stationary front producing persistent clouds over much of Southeast Texas dominates the weather situation. The series of satellite images given in Figure 7.2 shows the southern end of this front remains over Texas and Louisiana during the entire analysis period. At the initial time of the 13 September 2000 simulation (00-UTC), the satellite image in Figure 7.2 shows a wide swath of cloud along a front that extends eastward across Texas north of the 30-degree latitude line, then stretches northward along a line from southern Louisiana up through New York.
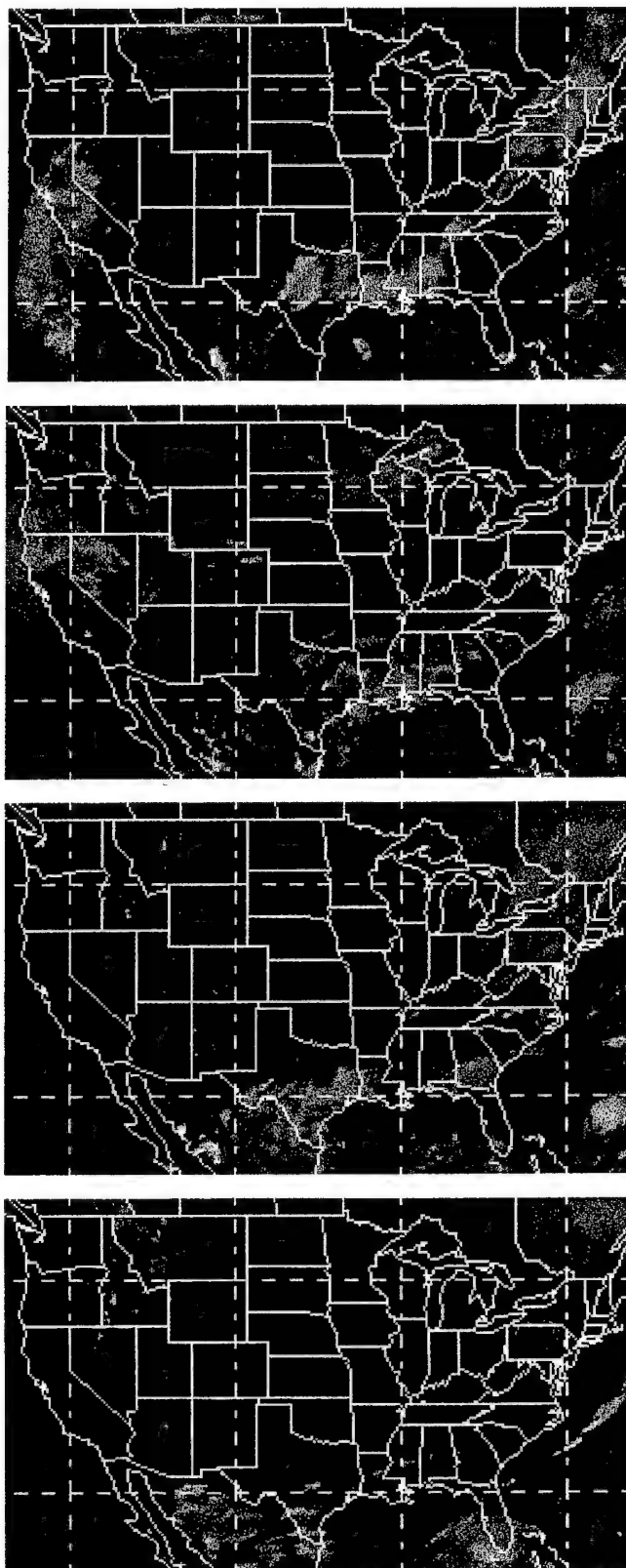
Figure 7.2. GOES satellite imagery, United States, 11μm IR channel, valid in 24-hour
increments (from top to bottom) at 2345-UTC, 13-15 September 2000.

Support for the front is depicted on NOGAPS analysis charts made for standard pressure levels at 850-mb, 700-mb, 500-mb, and 250-mb valid on 13 September 2000, 00-UTC. The 850-mb height and wind fields (Figures 7.3a and b) indicate the flow in the south-central and southeastern portions of the United States was under the influence of an anticyclone centered over Northeast Oklahoma and a weak trough that begins just east of the Great Lakes, runs along the Appalachian mountains, and terminates in a wind col over southern Louisiana. This trough does not appear to extend westward from the wind col into Texas at this level; however, air originating over the Gulf of Mexico flows into Texas from the southeast then turns cyclonically toward hot temperatures over Western Texas. This configuration produces cold air advection westward across all of Texas at this level. At 700-mb (Figures 7.4a and b), the northern portion of the trough tilts back toward the west and extends farther south along the Texas Gulf Coast. This indicates rapid movement of the northern portion of the trough eastward toward the Atlantic. Winds have backed with height to become northeasterly over Texas. Plenty of moisture for clouds is available along and east of the trough as indicated in Figure 7.4a. The main trough maintains its tilt with a 500-mb trough in eastern Texas (Figures 7.5) and at 250-mb trough in north-central Texas (Figure 7.6). High vorticity values clearly identify the trough at 500-mb with highest values centered over eastern Texas. East of the trough, an anticyclone centered over southern Nevada (not shown) is inducing northerly flow and weak cold-air advection over the remainder of Texas. All pressure levels up to 500-mb show cold-air advection over Texas; however, convection and instability induced by positive vorticity advection from the south and by diabatic heating from clouds predominates. Clouds are playing a very large role in the maintenance of instability over Texas. Isotachs drawn at 250-mb show the trough is supported by a weak branch of the polar jet stream. The northern part of the jet stream leads the trough indicating the trough over the Northeast United States will move rapidly eastward. The southern part of the jet stream over Texas and Louisiana lags or overlays the trough indicating the southern part of the trough will be stationary. The National Weather Service (NWS) mosaic radar reflectivity (Figure 7.7) for this time shows a line of frontal precipitation extending East-West from central Alabama through central Texas.
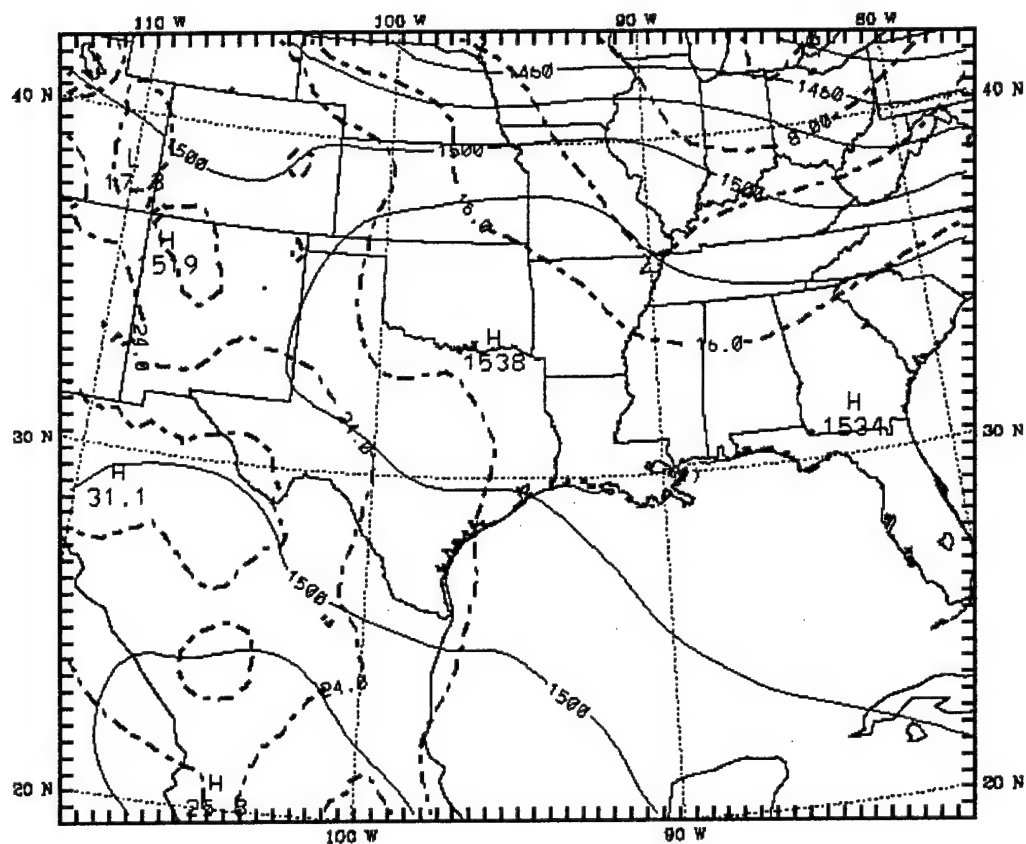
Figure 7.3a. 850-mb NOGAPS height (solid; m) and temperature (dashed; °C) analysis for 13 September 2000, 00-UTC.
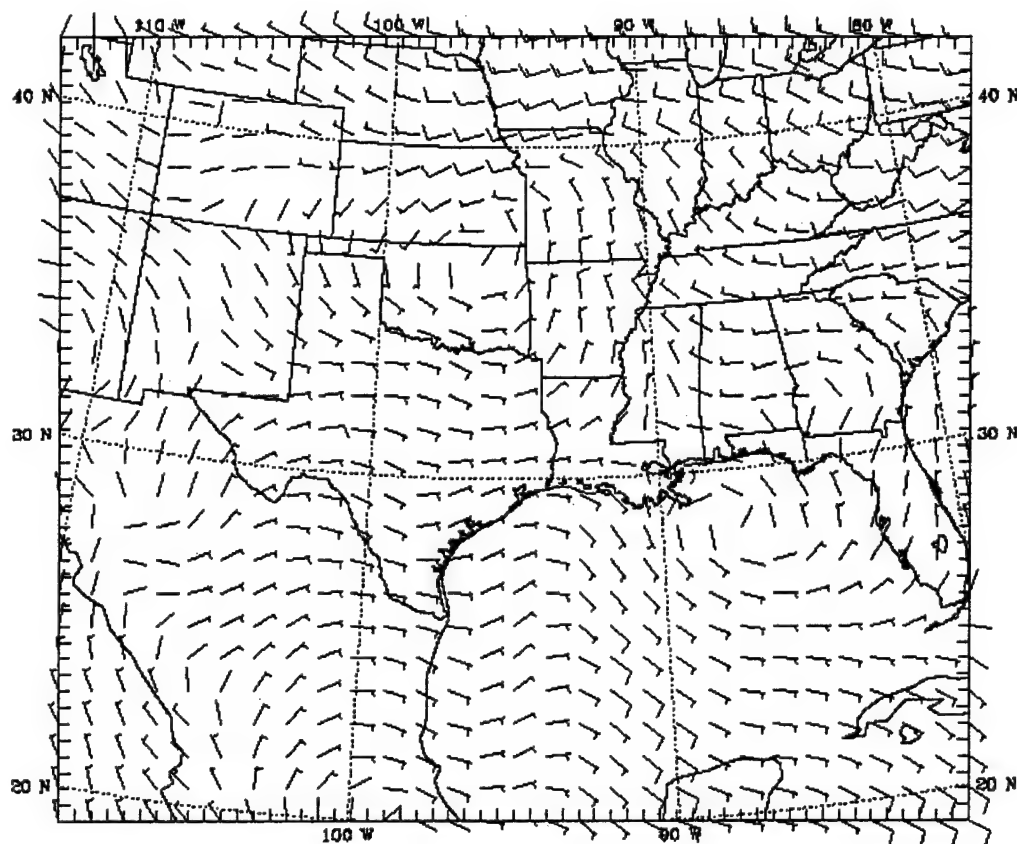
Figure 7.3b. 850-mb NOGAPS wind (kt) analysis for 13 September 2000, 00-UTC.
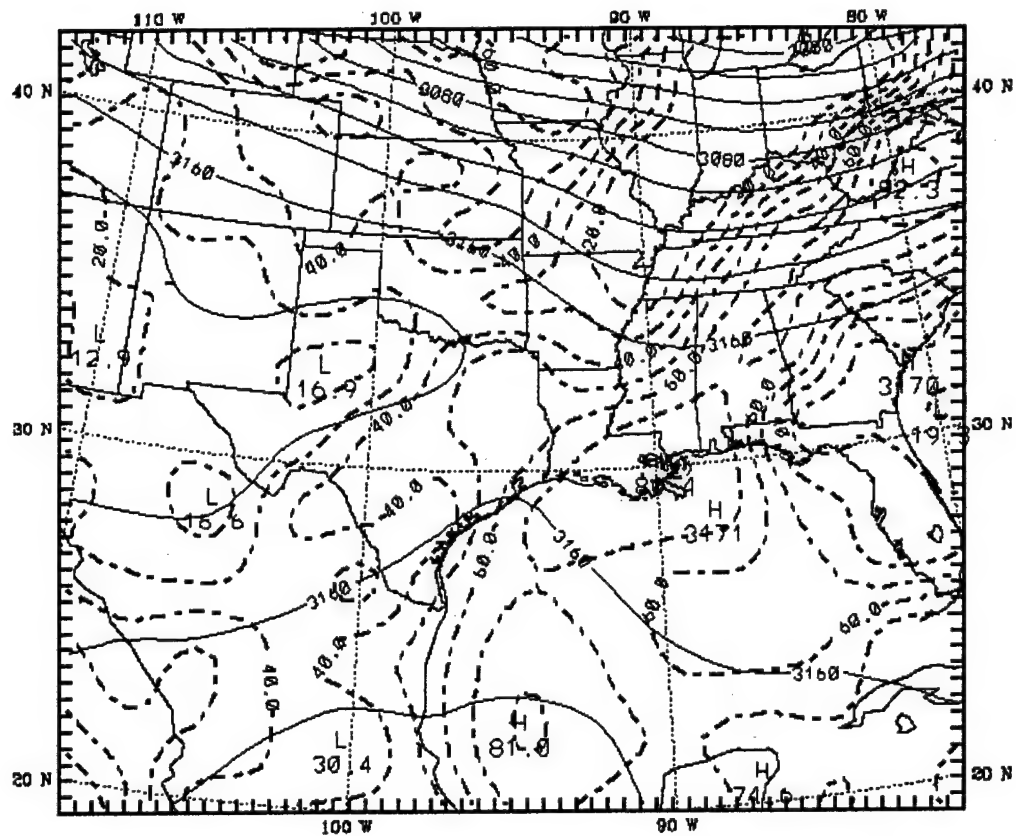
Figure 7.4a. 700-mb NOGAPS heights (solid; m) and relative humidity (dashed; %) analysis for 13 September 2000, 00-UTC.
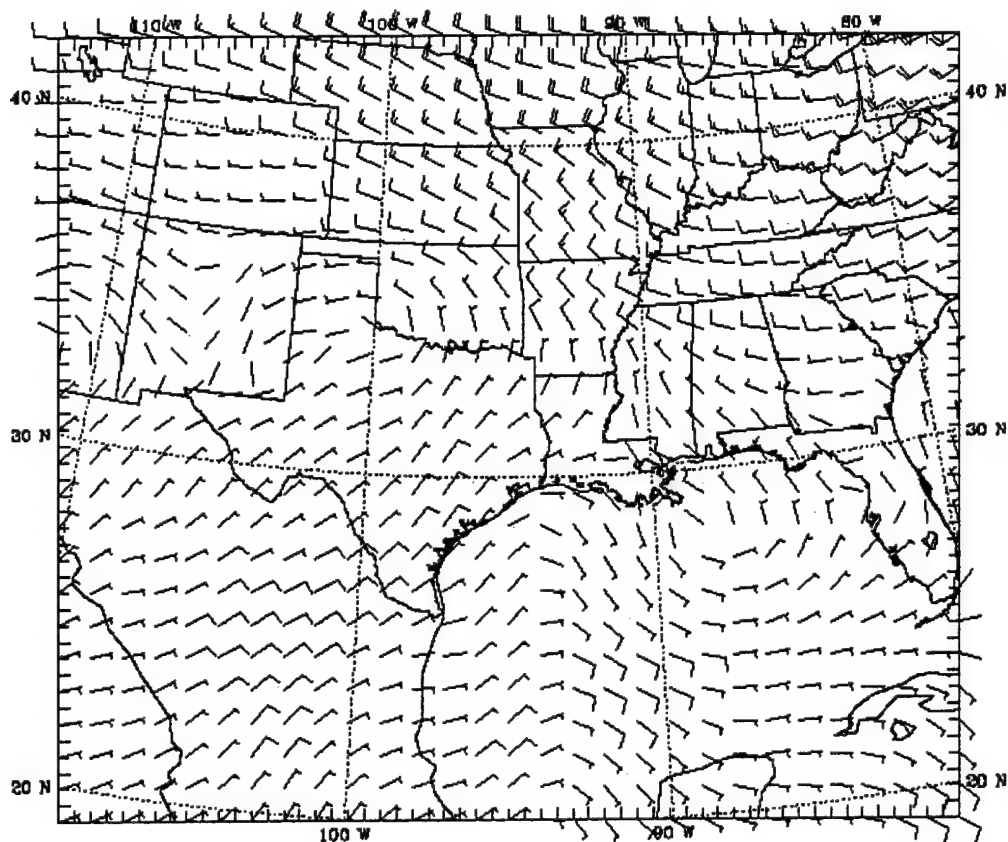
Figure 7.4b. 700-mb NOGAPS wind (kt) analysis for 13 September 2000, 00-UTC.
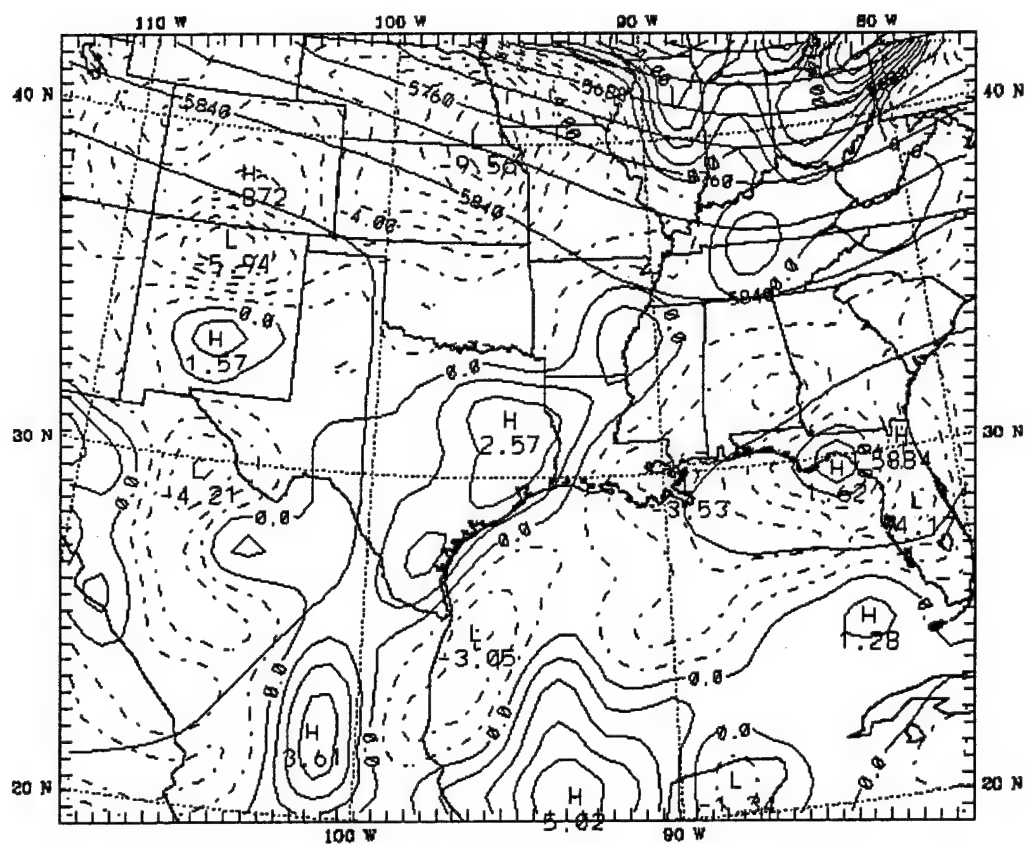
Figure 7.5. 500-mb NOGAPS heights (solid; m) and vorticity (dashed and solid; 10^{-5} s^{-1}) analysis for 13 September 2000, 00-UTC.
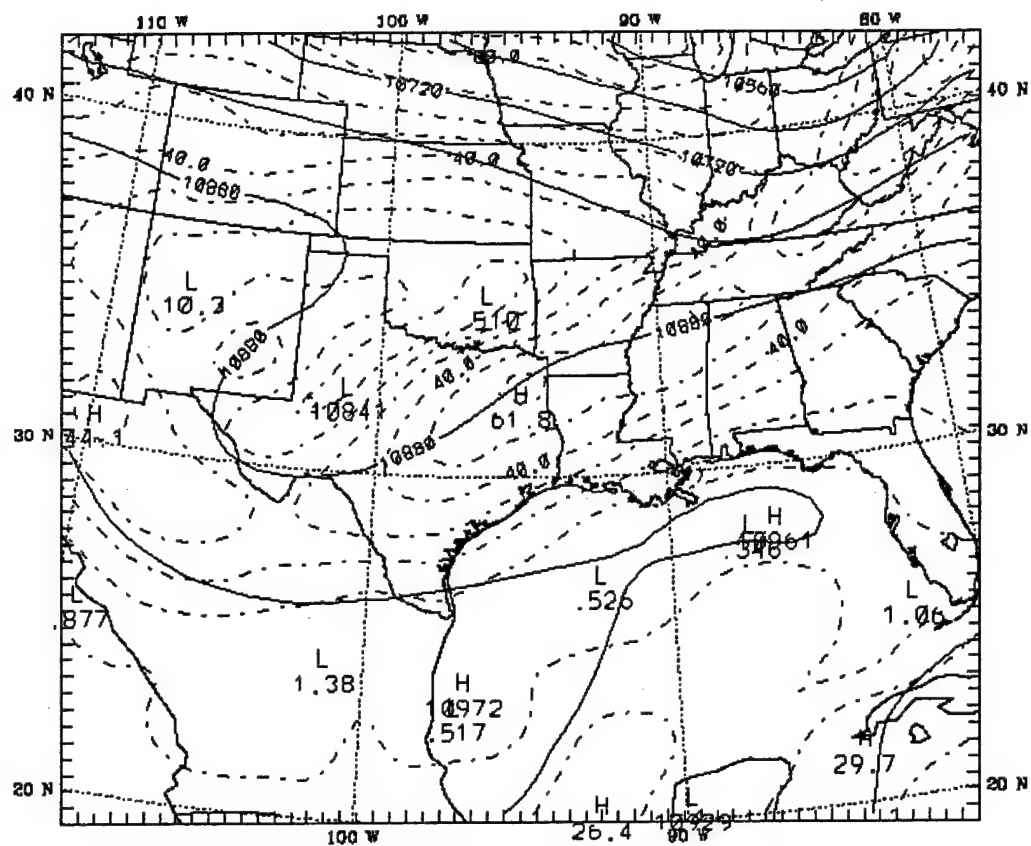
Figure 7.6. 250-mb NOGAPS heights (solid; m) and isotach (dashed; kt) analysis for 13 September 2000, 00-UTC.
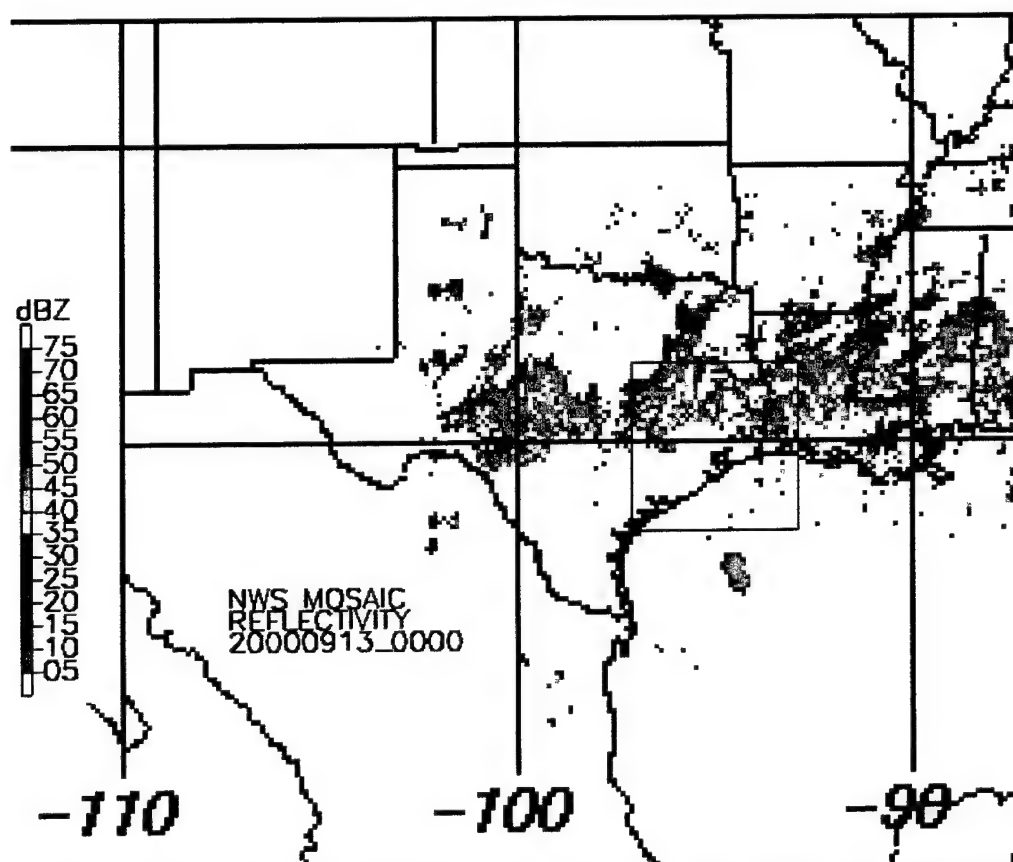
Figure 7.7. National Weather Service mosaic maximum radar reflectivity for 13 September 2000, 00-UTC. The box drawn over southeast Texas indicates innermost MM5 nest, domain 3.

By 00-UTC 14 September 2000, the southern portion of the trough has remained stationary while the northern portion of the trough has separated and swept out over the Atlantic. Clouds associated with the southern portion of the trough persist over the Gulf Coast states (see Figure 7.2b). A plot of 700-mb relative humidity (Figure 7.8a) shows moisture continues to be high along the Gulf Coast states. The line of high moisture has also become more zonally oriented. This low-level moisture largely controls the amount of potential buoyant energy available along the stationary front. Figure 7.8b shows drier air is advected from the north over the Southeast United States. Although it is difficult to see a well-defined trough over the Southeast United States at upper levels, a line of high vorticity depicted at 500-mb (Figure 7.9) shows that the front has become more zonally oriented. Horizontal wind shear from the 250-mb jet stream (Figure 7.10) is primarily responsible for dynamically maintaining convection over the Gulf Coast states because the jet axis is just north and parallel to the 500-mb ridge of vorticity; nearly all of the positive vorticity is shear-type vorticity induced by the jet.
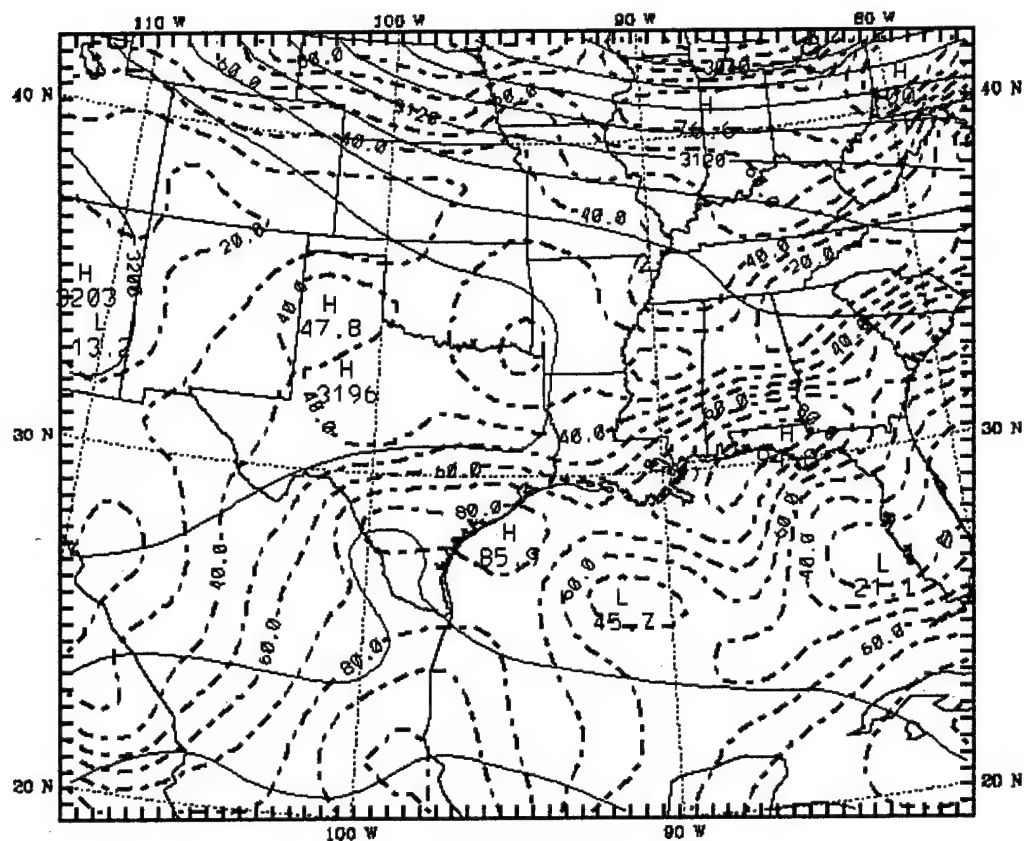
Figure 7.8a. 700-mb NOGAPS heights (solid; m) and relative humidity (dashed; %) analysis for 14 September 2000, 00-UTC.
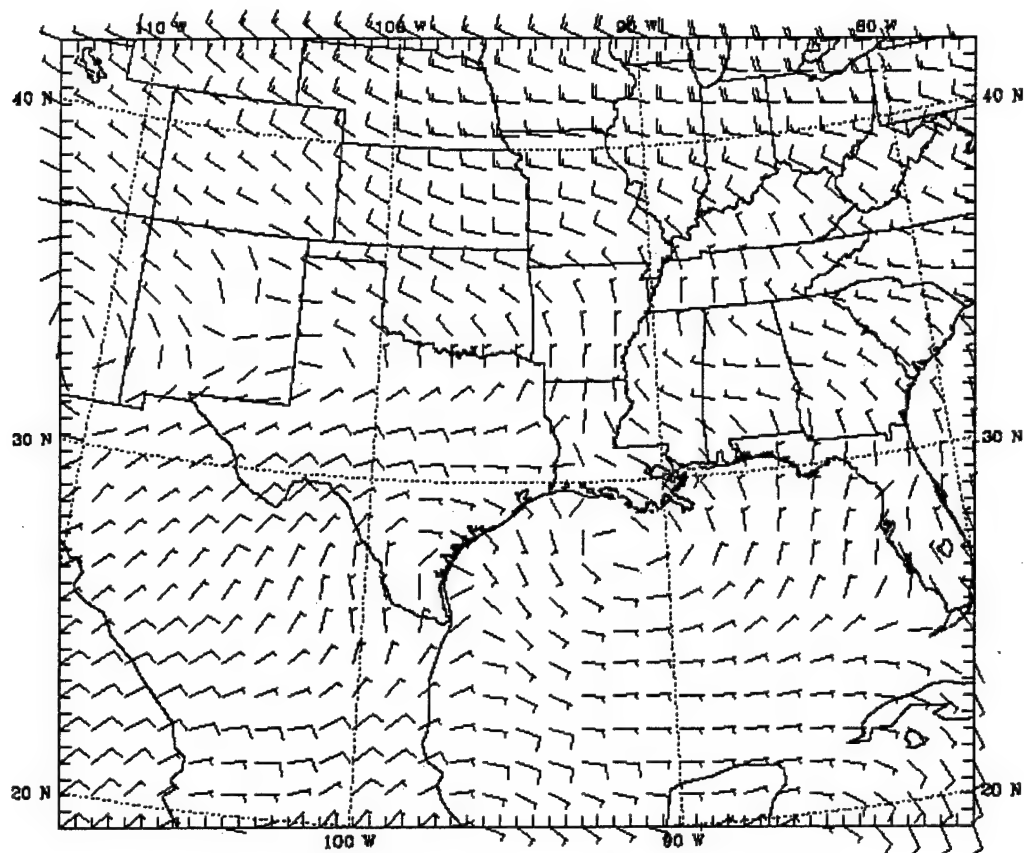
Figure 7.8b. 700-mb NOGAPS wind (kt) analysis for 14 September 2000, 00-UTC.
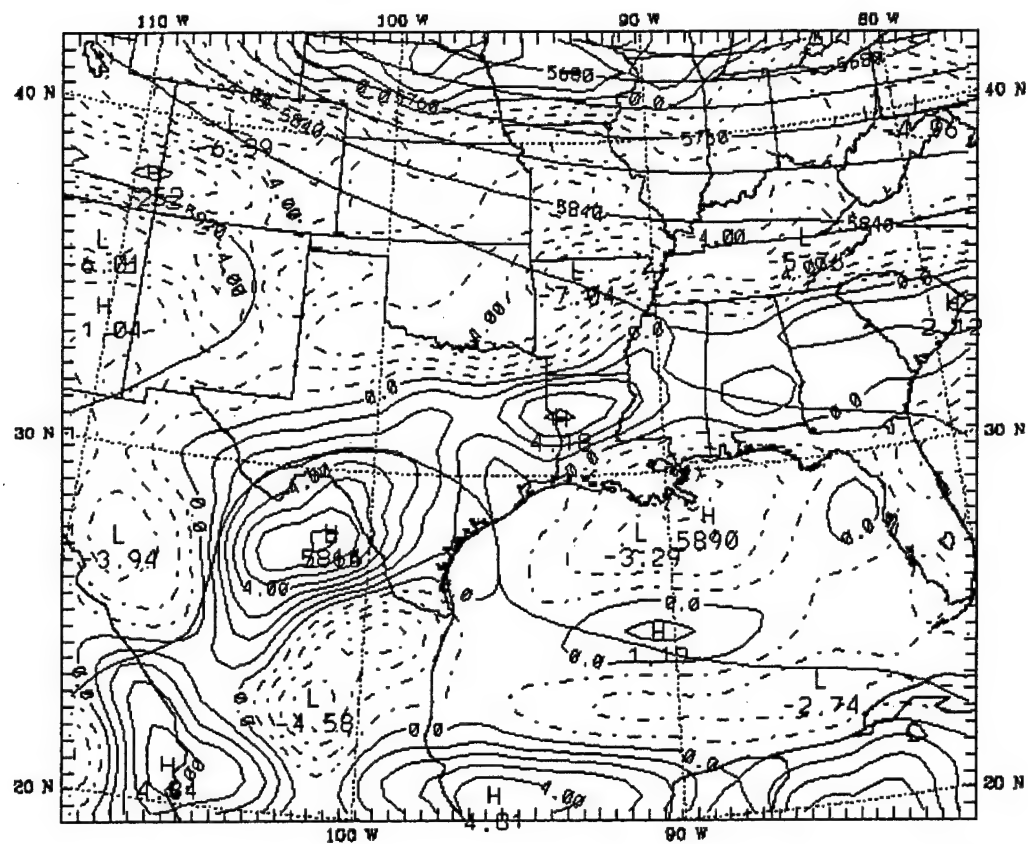
Figure 7.9. 500-mb NOGAPS heights (solid; m) and vorticity (dashed and solid; 10^{-5} s^{-1}) analysis for 14 September 2000, 00-UTC.
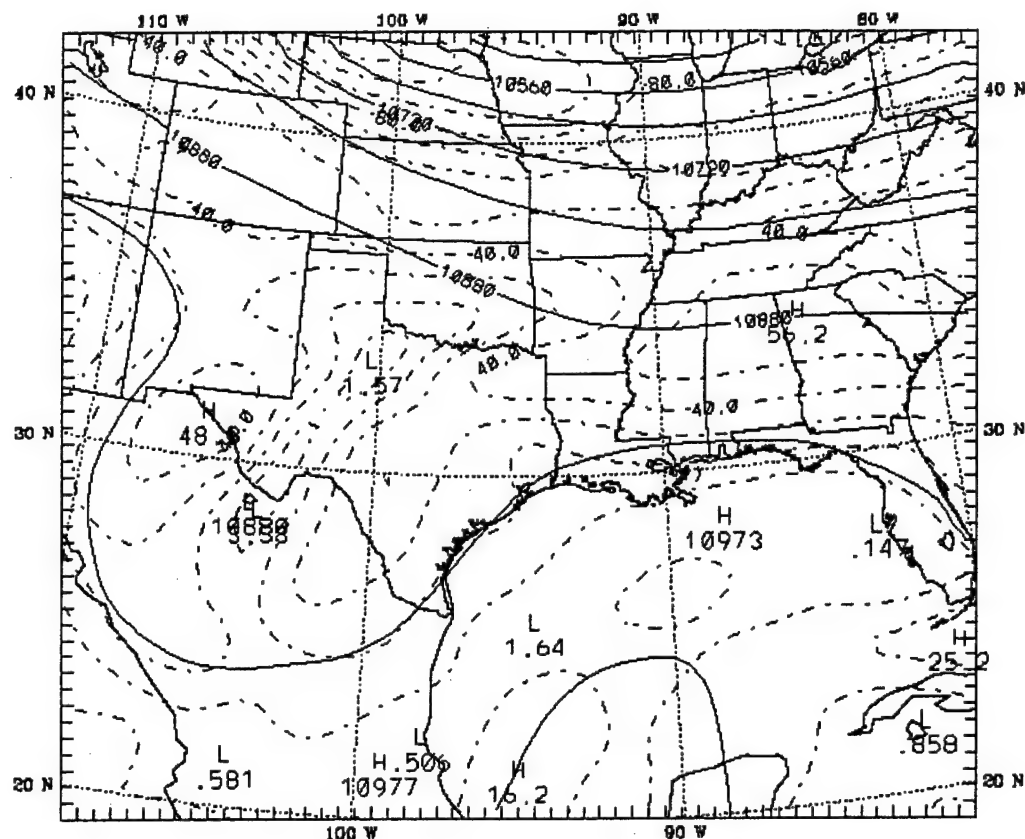
Figure 7.10. 250-mb NOGAPS heights (solid; m) and isotach (dashed; kt) analysis for 14 September 2000, 00-UTC.

Throughout the remainder of the analysis period, clouds and precipitation continue near dynamical support for convection over Texas and Louisiana. Figures 7.2c and 7.2d show clouds persisting over southern Texas and Louisiana. The line of maximum relative humidity on the 700-mb analysis (Figure 7.11a) valid for 15 September 2000, 00-UTC, is nearly stationary and parallel to the Gulf coast. On the 700-mb wind analysis (Figure 7.11b), an anticyclone centered on the Texas Panhandle is producing northerly flow over the entire southeastern United States. According to the wind and relative humidity analysis at this level, drier air is being advected southward over Texas. The 500-mb ridge of vorticity (Figure 7.12) and the 250-mb jet stream (Figure 7.13) also persist over southern Texas. Figures 7.14 and 7.15 show that scattered precipitation persists along the stationary front in Louisiana and Southeast Texas.

Air advected into a region of high vorticity will produce convection but not necessarily precipitation if there is insufficient moisture; however, active precipitation beneath the vorticity ridge may be enhanced by the mid-level advection of dry air, which increases the strength of downdrafts and maintains mesoscale circulations (e.g. Gilmore and Wicker 1998). The frontal event just presented is

instructive in a mesoscale cloud initialization study because it challenges the mesoscale NWP model to reproduce a synoptic situation that exists only because clouds and precipitation preexisted. A mesoscale modeling simulation that would advect drier, cooler, midlevel air into the region of a vorticity ridge would likely delay the onset of precipitation and cloud production if no clouds or precipitation were included on initialization. Before performing the MM5 simulations, some data incompatibilities are examined in Chapter VIII, specifically, incompatibility between vertical velocities diagnosed from NOGAPS and the occurrence of cloud in RTNEPH. Appendix E also looks at incompatibility between NOGAPS temperatures and the Air Force's surface temperature analysis.
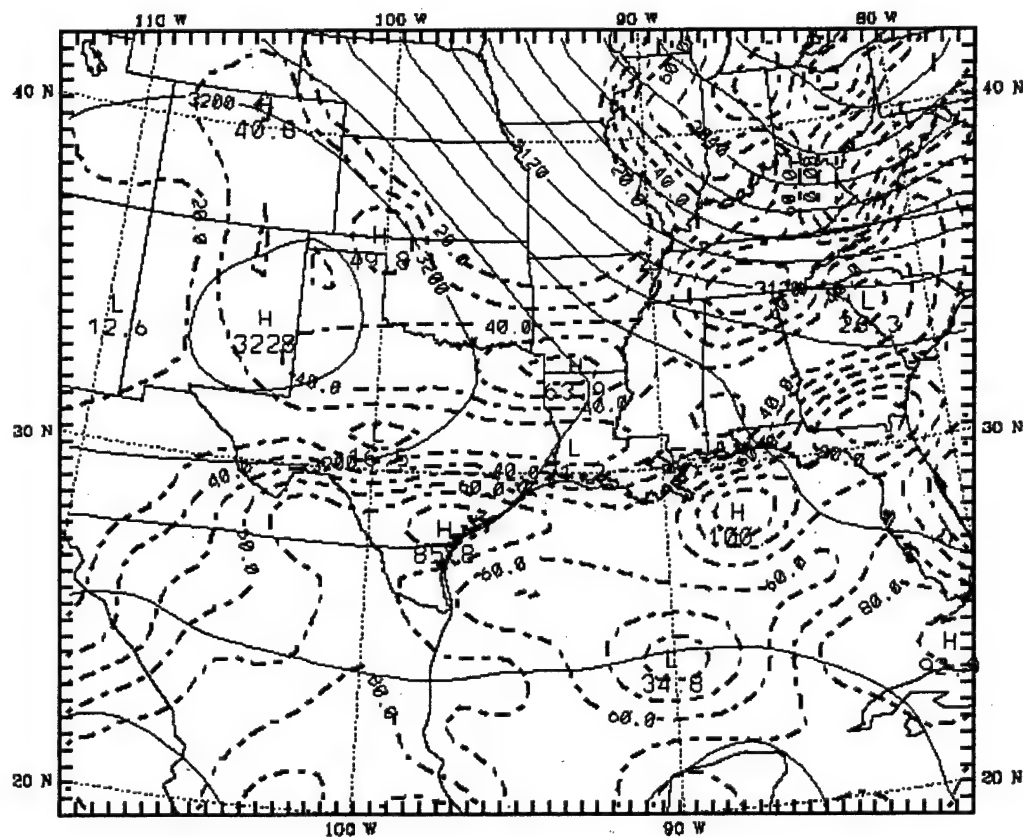
Figure 7.11a. 700-mb NOGAPS heights (solid; m) and relative humidity (dashed; %) analysis for 15 September 2000, 00-UTC.
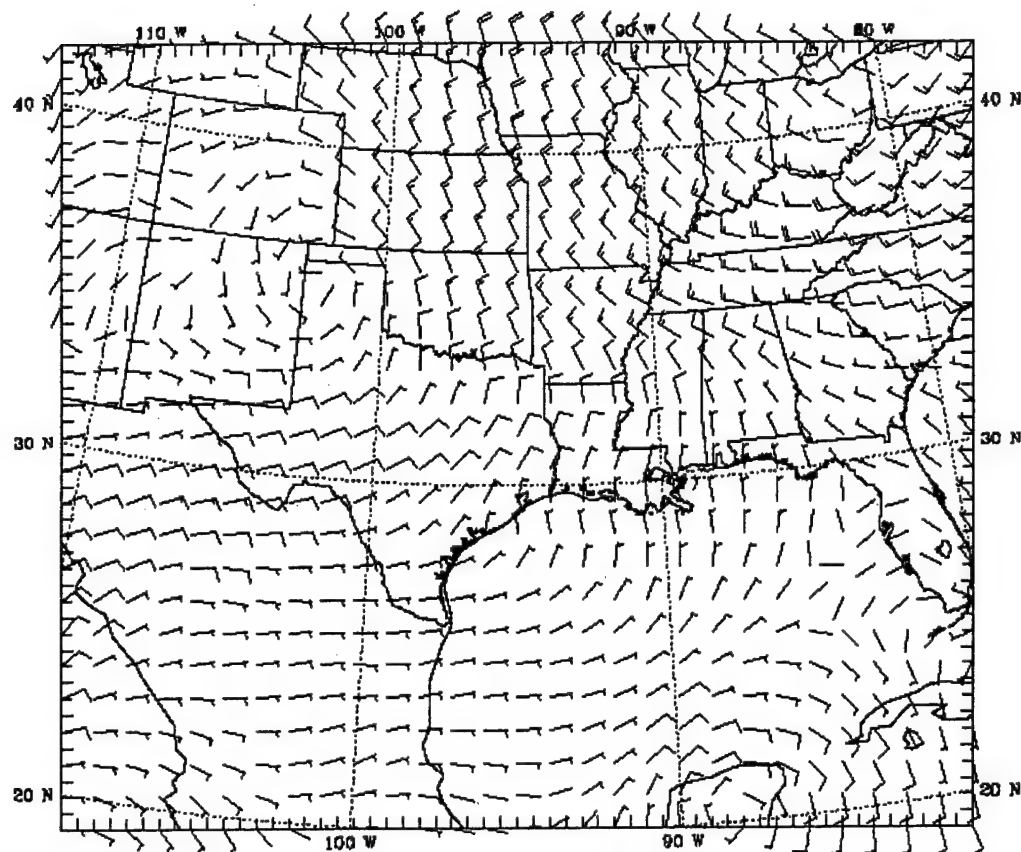
Figure 7.11b. 700-mb NOGAPS wind (kt) analysis for 15 September 2000,
00-UTC.

Figure 7.12. 500-mb NOGAPS heights (solid; m) and vorticity (dashed and solid; 10^{-5} s^{-1}) analysis for 15 September 2000, 00-UTC.

Figure 7.13. 250-mb NOGAPS heights (solid; m) and isotach (dashed; kt) analysis for 15 September 2000, 00-UTC.
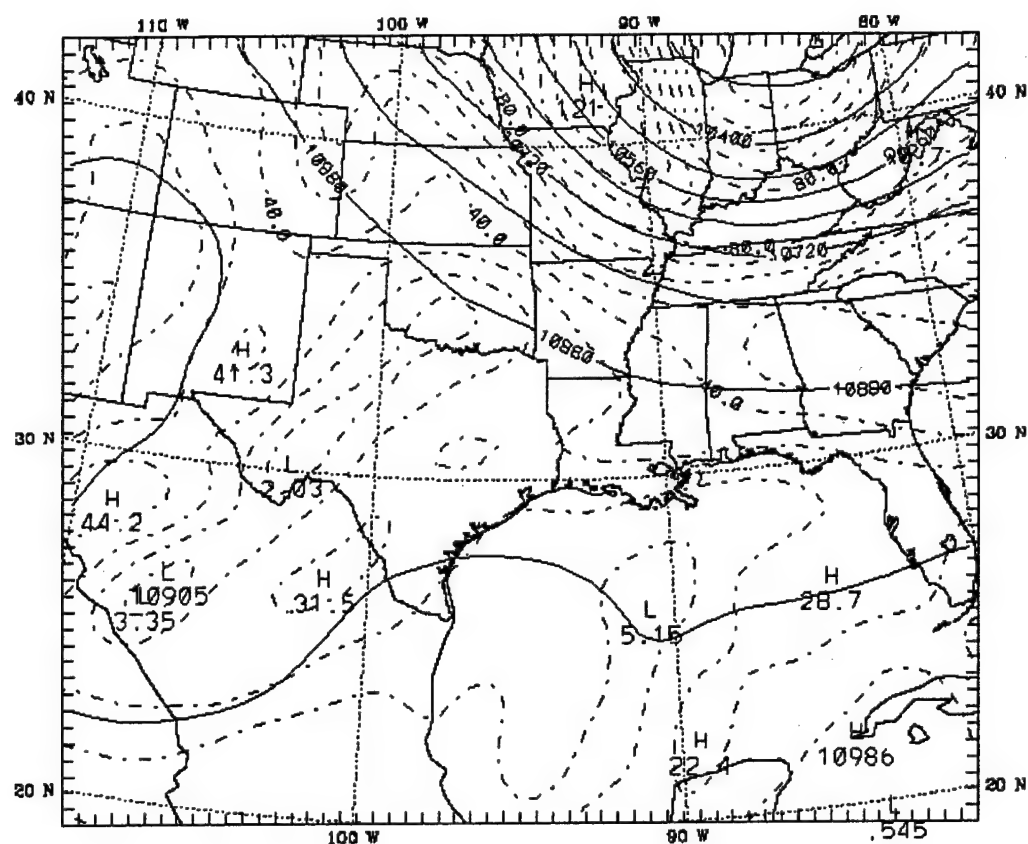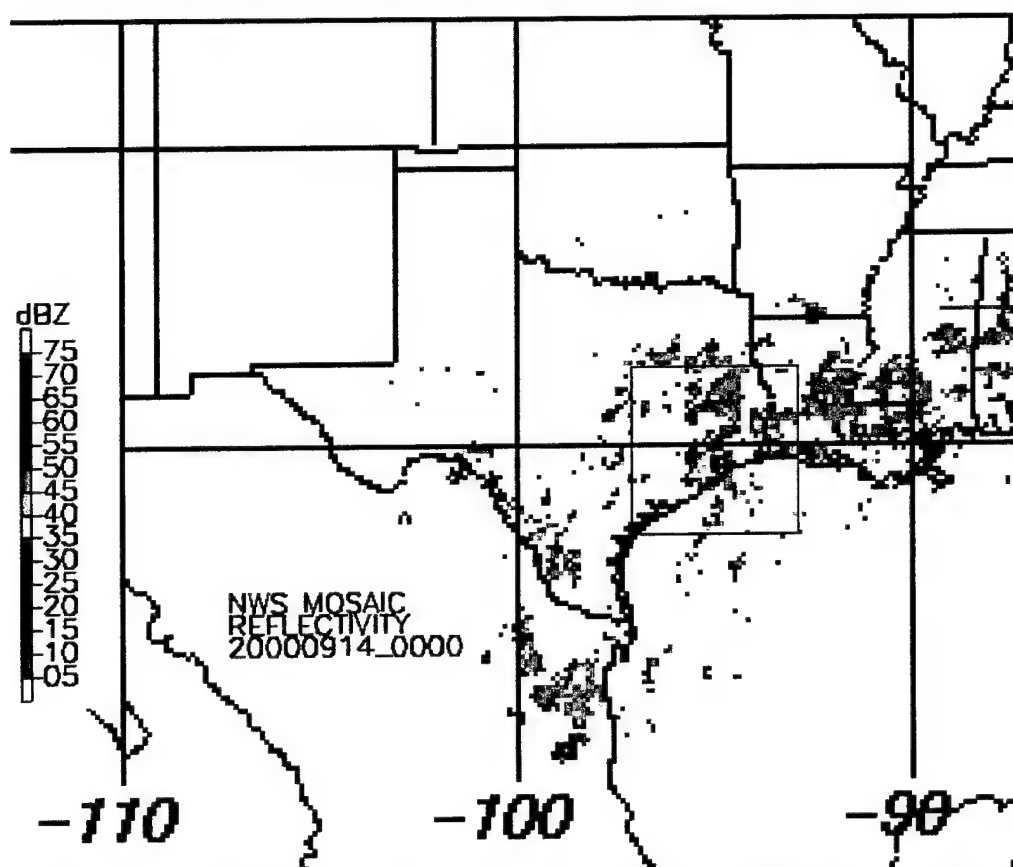
Figure 7.14. National Weather Service mosaic maximum radar reflectivity for 14 September 2000, 00-UTC. The box drawn over southeast Texas indicates innermost MM5 nest, domain 3.
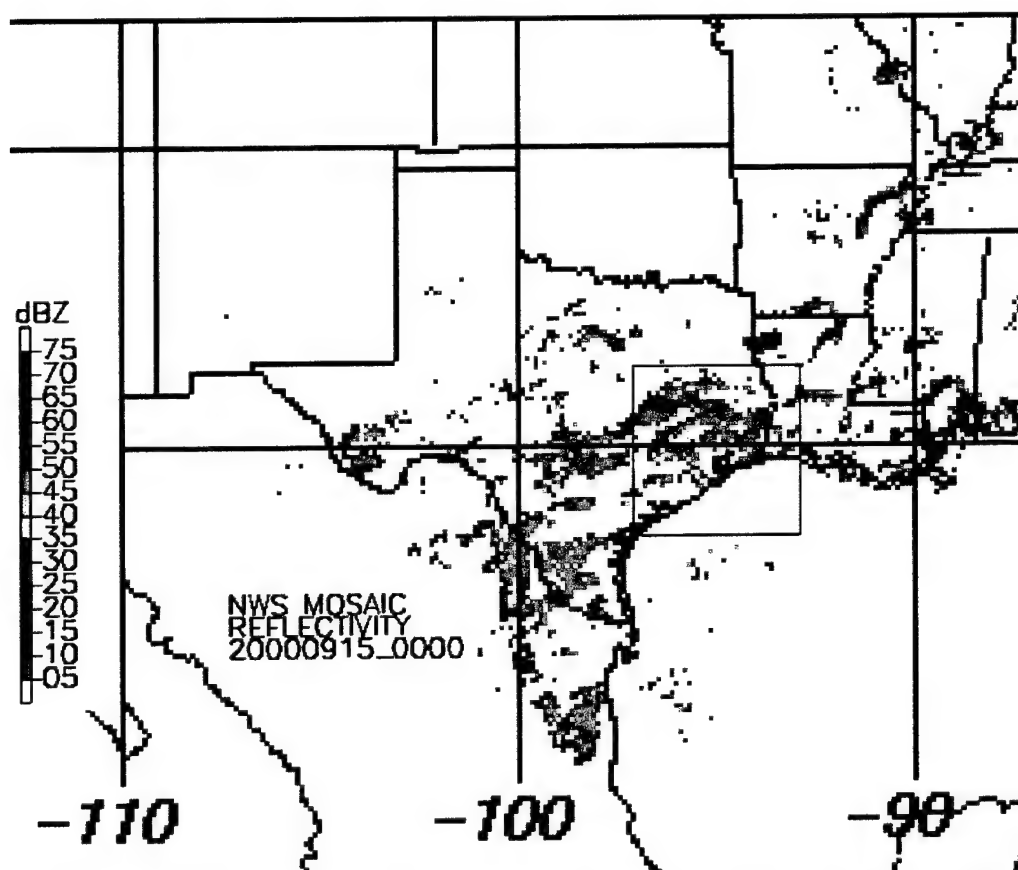
Figure 7.15. National Weather Service mosaic maximum radar reflectivity for 15 September 2000, 00-UTC. The box drawn over southeast Texas indicates innermost MM5 nest, domain 3.

CHAPTER VIII

INCOMPATIBILITY BETWEEN NOGAPS AND RTNEPH

8.1. Clouds in Subsidence Regions

Before using RTNEPH clouds to initialize MM5, it is important to assess whether those clouds are compatible with the NOGAPS wind analysis also used to initialize MM5. In other words, we ask whether RTNEPH clouds are compatible with NOGAPS diagnosed vertical velocities. The presence of cloud is generally associated with large-scale ascent or horizontal advection from regions of large-scale ascent to regions with little downward motion. Strong downward motion diagnosed from the initial wind field is generally incompatible with clouds analyzed at the same location.

In this study, NOGAPS winds are provided with a grid spacing of 2.5 degrees latitude and longitude, and RTNEPH clouds are provided with a grid spacing approximately 48 km. Granted, NOGAPS winds are analyzed on a much coarser grid than the RTNEPH; however, these winds are interpolated to the resolution of the MM5 model grid, as are the RTNEPH data. Incompatibility between the cloud and wind analyses could degrade the maintenance of the initial cloud field early in MM5's simulations. An estimate of the likelihood clouds will be prematurely dissipated can be made by measuring the incompatibility of RTNEPH clouds with NOGAPS diagnosed vertical velocities.

Section 8.2 discusses the method used to diagnose vertical velocity from the NOGAPS wind analysis. To assess compatibility, the diagnosed vertical motion is compared to the occurrence of RTNEPH clouds on those same levels in Section 8.3. If clouds are present and vertical motion is greater than or equal to zero, then the analyses are assumed compatible. If clouds are present and vertical motion is less than zero, then the analyses are assumed incompatible. If clouds are not present, compatibility cannot be assessed. The object is to determine three metrics: the fraction of model grid points containing cloud, the fraction of cloudy grid points compatible with diagnosed vertical velocities, and the fraction of cloudy grid points incompatible with diagnosed vertical velocities. In Section 8.4, a binomial distribution test for randomness is also performed to determine if RTNEPH clouds behave as clouds that are randomly distributed to grid points having an upward vertical velocity.

8.2. Computation of Vertical Velocity

To determine vertical velocity, the same continuity equations used by MM5 are used here. These equations are presented by Dudhia et al. (2001) in the MM5 Tutorial Class Notes and User's Guide (Version 3). The MM5 equation for divergence is given by equation 8.14 of the tutorial, page 8-4.

$$\nabla \cdot \mathbf{V} = \frac{\partial u}{\partial x} - \frac{\sigma}{p^*} \frac{\partial p^*}{\partial x} \frac{\partial u}{\partial \sigma} + \frac{\partial v}{\partial y} - \frac{\sigma}{p^*} \frac{\partial p^*}{\partial y} \frac{\partial v}{\partial \sigma} - \frac{\rho_0 g}{p^*} \frac{\partial w}{\partial \sigma} \tag{8.1}$$

Assuming hydrostatic mass continuity, this equation is reduced.

$$\nabla \bullet \mathbf{V} = 0$$

$$\frac{\partial w}{\partial \sigma} = \frac{p^*}{\rho_0 g}\left[\frac{\partial u}{\partial x} - \frac{\sigma}{p^*}\frac{\partial p^*}{\partial x}\frac{\partial u}{\partial \sigma} + \frac{\partial v}{\partial y} - \frac{\sigma}{p^*}\frac{\partial p^*}{\partial y}\frac{\partial v}{\partial \sigma}\right] \tag{8.2}$$

Values of w are computed on the full-sigma levels. Values of u, v, T, and p^* are computed on the half-sigma levels. The data are horizontally placed with Arakawa B-grid staggering. See Figures 8.1 and 8.2. Horizontal winds are placed on dot points, all other variables are placed on cross points.

Considering this configuration, w can be estimated using finite differences computed from the top-downward. The model lid vertical velocity is assumed zero. Sigma (σ) is computed according to equation 8.3.

$$\sigma = \left(p_0 - p_{top}\right)/\left(p_{0surface} - p_{top}\right) \tag{8.3}$$

p_0 reference pressure at a given level [Pa]
p_{top} specified constant top pressure (set to 10^4 Pa)
$p_{0surface}$ reference surface pressure [Pa]
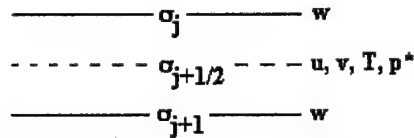
Figure 8.1. Vertical profile of state variables. Solid line represents full-sigma level, and dashed line represents half-sigma level.
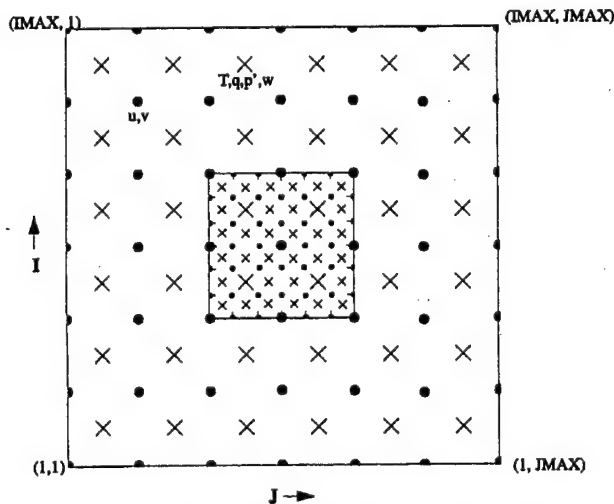
Figure 8.2. Horizontal distribution of state variables.

The reference temperature profile is computed as follows:

$$T_0 = T_{s0} + A \log_e (p_0 / p_{00})$$ (8.4)

T_0 reference temperature at reference pressure level p_0 [K]
T_{s0} reference temperature at sea level set at 275 K
p_0 reference pressure level [Pa]
p_{00} reference sea-level pressure constant set at 10^5 Pa
A   measure of lapse rate set at 50 K representing the temperature difference
     between p_{00} and p_{00}/e

The terrain height, Z_T, is a function of the surface reference pressure, $p_{0surface}$, according to equation 8.5.

$$Z_T = -\frac{RA}{2g}\left(\ln\frac{p_{0surface}}{p_{00}}\right)^2 - \frac{RT_{s0}}{g}\left(\ln\frac{p_{0surface}}{p_{00}}\right)$$ (8.5)

R   gas constant of dry air set at 287 J K^{-1} kg^{-1}
g   gravity set at 9.8 m s^{-1}
Z_T terrain height [m]

This quadratic can be solved for $p_{0surface}$.

$$\ln\left(\frac{p_{0surface}}{p_{00}}\right) = \frac{-\frac{RT_{s0}}{g} \pm \sqrt{\left(\frac{RT_{s0}}{g}\right)^2 - 4\frac{RA}{2g}Z_T}}{2\frac{RA}{2g}}$$ (8.6)

$$p_{0surface} = p_{00}EXP\left[\frac{-\frac{RT_{s0}}{g} \pm \sqrt{\left(\frac{RT_{s0}}{g}\right)^2 - 4\frac{RA}{2g}Z_T}}{2\frac{RA}{2g}}\right]$$ (8.7)

The difference between the reference surface pressure and the reference top pressure is defined as p*.

$$p^* = p_{0surface} - P_{top}$$ (8.8)

Equation 8.8 is substituted into equations 8.2 and 8.3. The equation for p_0 is a function of the height at the half-sigma levels using equation 8.7. The half-sigma level heights are known in the CIS algorithm because they have been computed using equation 8.5 in the REGRID preprocessor of MM5. REGRID analyzes input data fields to the horizontal MM5 grid. In CIS, RTNEPH cloud is flagged on the half-sigma level because that is where mixing ratios are computed in MM5.

$$p_0 = p_{00}EXP\left[\frac{-\frac{RT_{s0}}{g} \pm \sqrt{\left(\frac{RT_{s0}}{g}\right)^2 - 4\frac{RA}{2g}Z_\sigma}}{2\frac{RA}{2g}}\right]$$ (8.9)

Equation 8.9 is substituted into equations 8.2 and 8.3. One final component must be computed -- reference air density.

$$\rho_0 = \frac{p_0}{RT_0} \qquad\qquad (8.10)$$

Equations 8.3 through 8.10 are then substituted into equation 8.2 to solve for vertical velocity.

8.3. Compatibility Statistics

In order to initialize MM5, clouds are explicitly defined on the MM5 grid: a grid point is either clear or cloud-filled. The distribution of RTNEPH cloud to the MM5 grid is performed in the cloud initialization scheme (CIS) presented in Chapter IV and Chapter V. A few simple statistics are computed using NOGAPS and CIS analyses generated between 13 September 2000, 00-UTC, and 15 September 2000, 18-UTC, in 6-hr increments on MM5 model domain 3 (67 x 67 x 23 grid points) and domain 2 (133 x 109 x 23 grid points). CIS clouds and NOGAPS vertical winds are gridded to the MM5 coordinates before performing the compatibility analysis. Tables 8.1 and 8.2 list the fraction of each domain that is explicitly cloud filled and the fraction of those clouds coincident with a positive vertical velocity diagnosed from the NOGAPS horizontal winds. The most important fractions are those used to initialize MM5 (bold text). The total quantities on the right side of the tables give a better indication of how well RTNEPH and NOGAPS are compatible at these resolutions for any initial time chosen.

Table 8.1. Fraction of MM5 domain 3 containing explicit clouds and fraction of cloudy points with positive vertical velocities (nearest whole percent) diagnosed from NOGAPS winds. Data is sampled on MM5 domain 3 (6 km grid spacing) in 6-hour increments for the period 13 September 2000 (00-UTC) to 15 September 2000 (18-UTC). Dates in bold are used to initialize MM5.

Date/Time	13/00	13/06	13/12	13/18	Total
% Cloudy	9	4	35	7	9
% Match	33	44	41	26	35
% W ≥ 0	50	53	46	36	48
Date/Time	14/00	14/06	14/12	14/18	Range
% Cloudy	29	3	5	6	2-35
% Match	27	43	32	23	23-73
% W ≥ 0	44	53	45	38	38-57
Date/Time	15/00	15/06	15/12	15/18	
% Cloudy	3	3	3	2	
% Match	27	73	44	42	
% W ≥ 0	50	53	47	57	

Table 8.2. Fraction of MM5 domain 2 containing explicit clouds and fraction of cloudy points with positive vertical velocities (nearest whole percent) diagnosed from NOGAPS winds. Data is sampled on MM5 domain 2 (18 km grid spacing) in 6-hour increments for the period 13 September 2000 (00-UTC) to 15 September 2000 (18-UTC). Dates in bold are used to initialize MM5.

Date/Time	**13/00**	**13/06**	13/12	13/18	Total
% Cloudy	5	3	8	5	6
% Match	45	60	47	42	45
% W ≥ 0	54	55	53	51	54
Date/Time	14/00	14/06	**14/12**	**14/18**	Range
% Cloudy	8	5	6	6	3-8
% Match	44	55	43	45	37-60
% W ≥ 0	54	54	52	53	51-57
Date/Time	15/00	15/06	15/12	15/18	
% Cloudy	7	8	7	7	
% Match	37	47	44	44	
% W ≥ 0	53	55	54	57	

The number of grid points affected by cloud may be much larger because some mixing ratios of rain and snow below the cloud intersect non-cloudy sigma levels. Of the cloudy points identified in the domains used to initialize MM5, only 23% to 44% of them are associated with upward motion. The balance of 66% to 77% of clouds used to initialize MM5 will likely be dissipated by subsidence early on during model integration.

Within the twelve data sets examined above, the fraction of the model domain with cloud analyzed on the half-sigma cross points varies from as little at 2% up to 35% on domain 3 and from 3% to 8% on domain 2. The fraction of those cloudy points compatible with diagnosed vertical velocity varies from as little as 23% up to 73% on domain 2 and from 37% to 60% on domain 2. The average compatibility between RTNEPH clouds and NOGAPS diagnosed vertical velocities for all data sets in the study is 35% on domain 3 and 45% on domain 2.

To determine if sampling resolution was a factor, clouds are sampled at 8th mesh resolution (48-km resolution), which is the resolution of the original RTNEPH cloud analysis, over the region contained within domain 2. Those results are given in Table 8.3. Clouds are also sampled at 2.5-degree latitude/longitude resolution, which is the resolution of the original NOGAPS wind analysis, over the region contained within domain 2. Those results are given in Table 8.4. In the comparison against vertical velocity, a sample 8th-mesh region or 2.5-degree latitude/longitude region is considered cloudy if there is a horizontal cloud coverage amount of 25% or greater.

Table 8.3. Fraction of MM5 domain 2 containing RTNEPH resolution clouds and fraction of cloudy points with positive vertical velocities (nearest whole percent) diagnosed from NOGAPS winds. Data is sampled at 8th-mesh resolution (48 km grid spacing) with a threshold of 25% cloud coverage amount in 6-hour increments for the period 13 September 2000 (00-UTC) to 15 September 2000 (18-UTC). Dates in bold are used to initialize MM5.

Date/Time	**13/00**	**13/06**	13/12	13/18	Total
% Cloudy	7	6	11	7	9
% Match	45	60	47	42	45
% W ≥ 0	54	55	53	51	54
Date/Time	14/00	14/06	**14/12**	**14/18**	Range
% Cloudy	12	7	9	9	6-12
% Match	44	55	43	45	37-60
% W ≥ 0	54	54	52	53	51-57
Date/Time	15/00	15/06	15/12	15/18	
% Cloudy	10	12	11	11	
% Match	37	47	44	44	
% W ≥ 0	53	55	54	57	

Table 8.4. Fraction of MM5 domain 2 containing NOGAPS resolution clouds and fraction of cloudy points with positive vertical velocities (nearest whole percent) diagnosed from NOGAPS winds. Data is sampled at NOGAPS resolution (2.5-degree latitude/longitude grid spacing) with a threshold of 25% cloud coverage amount in 6-hour increments for the period 13 September 2000 (00-UTC) to 15 September 2000 (18-UTC). Dates in bold are used to initialize MM5.

Date/Time	**13/00**	**13/06**	13/12	13/18	Total
% Cloudy	4	3	12	5	9
% Match	38	68	45	36	44
% W ≥ 0	54	55	53	51	54
Date/Time	14/00	14/06	**14/12**	**14/18**	Range
% Cloudy	12	6	8	8	3-13
% Match	43	54	40	45	38-68
% W ≥ 0	54	54	52	53	51-57
Date/Time	15/00	15/06	15/12	15/18	
% Cloudy	10	13	12	11	
% Match	34	48	41	43	
% W ≥ 0	53	55	54	57	

Tables 8.3 and 8.4 do not vary substantially from Table 8.2 for the region contained by domain 2, indicating insensitivity to sampling resolution. This also indicates that if RTNEPH at any one time were used to initialize a mesoscale model using direct insertion of the cloud water, more than half of the clouds would likely be incompatible with the unadjusted NOGAPS wind field. To minimize this problem, the initial wind field would require some mass conserving modification to produce upward motion at the cloudy grid points. However, a technique to solve this problem is not addressed here.

8.4. Test for Randomness

Because RTNEPH clouds generally appear to occur roughly half the time at grid points with upward motion, another question arises, specifically is the distribution of RTNEPH cloud any different from random placement or noise? One way to answer this question is to treat the problem as a simple binomial distribution problem. If clouds are randomly assigned to a grid point, the probability of a success (assigning the cloud to a point with $W \geq 0$) on one trial is designated p. The probability of a failure (assigning the cloud to a point with $W < 0$) on one trial is designated q.

$$p = \frac{\text{number of points with } W \geq 0}{\text{total number of points}}$$
$$q = \frac{\text{number of points with } W < 0}{\text{total number of points}} \tag{8.11}$$

If there are n cloudy points in a sample, then for a normal noise distribution the theoretical mean number of successes and their standard deviation are given by the formulas (Naiman et al. 1972):

$$\mu_s = np$$
$$\sigma_s = \sqrt{npq} \tag{8.12}$$

A good rule of thumb that assures the binomial histogram is approximately normal is when both np and nq are greater than 5. The normal distribution is defined by a table of z scores and percentile ranks. For the sample above, the z score for achieving at least m successes is given by the formula:

$$z_m = \frac{m - \mu_s}{\sigma_s} \tag{8.13}$$

The null hypothesis in this case is that a cloud will be placed on a grid point with $W \geq 0$.

$$H_0 : p' = p \tag{8.14}$$

The motivated, or alternative, hypothesis is that cloud placement is not random and is more likely to be placed on a grid point with $W \geq 0$.

$$H_a : p' > p \tag{8.15}$$

The object now is to test whether the motivated hypothesis is correct or incorrect. To do this, the null hypothesis is tested at the 0.05 significance level (the probability of incorrectly claiming that the clouds are biased in being placed on a grid point with $W \geq 0$). The 0.05 significance level identifies the area under the normal curve as 0.025 on the left and 0.0975 on the right. The critical z scores are ± 1.96. The limits of success for the null hypothesis are then defined by the equation:

$$S_c = \mu + \sigma z_c \tag{8.16}$$

To illustrate, consider the 13 September 2000 (00-UTC) case with explicit cloud sampling on domain 3. There were 51454 points with $W \geq 0$, and 51793 points with $W < 0$. Of the 9240 cloudy points (n), 3070 of them occurred on a point with $W \geq 0$. Assuming the null hypothesis is true, the following computations are made:

$$p' = \frac{51454}{50291 + 51793} = 0.498358$$

$$q' = 1 - p' = 0.501642$$

$$n = 9240$$

Since $np = 4604 > 5$

and $nq = 4635 > 5$

the normal approximation may be used.

$$\mu = np = 4604$$

$$\sigma = \sqrt{npq} = 48.0622$$

$$S_c = \mu + \sigma z = 4604 + (48.0622)(\pm 1.96)$$

$$S_c = 4604 \pm 94$$

$$S_c = 4510 \text{ and } 4698$$

After following the above procedure, the decision rule is to reject the null hypothesis if there are less than 4510 or more than 4698 clouds on points with $W \geq 0$. For the first case, 3070 clouds were a success therefore the null hypothesis is rejected. In this case, the bias is negative and suggests that RTNEPH clouds are less likely than random to occur on a grid point with $W \geq 0$. Tables 8.5 through 8.8 show how cloud distribution fared against the null hypothesis for each of the 12 data sets examined here.

Of the twelve cases evaluated, only one of them is not significantly different from what would be expected for randomly distributed clouds (14 September 2000/06-UTC, NOGAPS sampling resolution). Interestingly, only a few of the cases indicate clouds are more likely to be associated with ascent. When considering all cases combined, RTNEPH clouds appear to be more likely to be associated with synoptic scale subsidence than would be expected if the clouds were distributed randomly. This result is quite confusing and does not bode well for using RTNEPH clouds to initialize a mesoscale model dependent on synoptic scale wind patterns.

Table 8.5. Domain 3, 6-km resolution explicit cloud placement, null-hypothesis test results. Test is to determine whether RTNEPH clouds are randomly distributed to points with $W \geq 0$. Failure indicates 95% probability that RTNEPH clouds are not randomly distributed. A (-/+) indicates that RTNEPH clouds are less/more likely than random to occur on a grid point with $W \geq 0$. Data sampled in 6-hour increments for the period 13 September 2000 (00-UTC) to 15 September 2000 (18-UTC). Dates in bold are used to initialize MM5.

13/00: Fail (-)	**13/06**: Fail (-)	**13/12**: Fail (-)	**13/18**: Fail (-)	Total: Fail (-)
14/00: Fail (-)	14/06: Fail (-)	**14/12**: Fail (-)	**14/18**: Fail (-)	
15/00: Fail (-)	15/06: Fail (+)	15/12: Fail (-)	15/18: Fail (-)	

Table 8.6. Domain 2, 18-km resolution explicit cloud placement, null-hypothesis test results.

13/00: Fail (-)	13/06: Fail (-)	13/12: Fail (-)	13/18: Fail (-)	Total: Fail (-)
14/00: Fail (-)	14/06: Fail (+)	14/12: Fail (-)	14/18: Fail (-)	
15/00: Fail (-)	15/06: Fail (-)	15/12: Fail (-)	15/18: Fail (-)	

Table 8.7. Domain 2, RTNEPH 8th-mesh resolution (48-km at ≥ 25%) cloud placement, null-hypothesis test results.

13/00: Fail (-)	13/06: Fail (+)	13/12: Fail (-)	13/18: Fail (-)	Total: Fail (-)
14/00: Fail (-)	14/06: Fail (+)	14/12: Fail (-)	14/18: Fail (-)	
15/00: Fail (-)	15/06: Fail (-)	15/12: Fail (-)	15/18: Fail (-)	

Table 8.8. Domain 2, NOGAPS 2.5-degree latitude/longitude resolution (at ≥ 25% cloud coverage amount) cloud placement, null-hypothesis test results.

13/00: Fail (-)	13/06: Fail (+)	13/12: Fail (-)	13/18: Fail (-)	Total: Fail (-)
14/00: Fail (-)	14/06: PASS	14/12: Fail (-)	14/18: Fail (-)	
15/00: Fail (-)	15/06: Fail (-)	15/12: Fail (-)	15/18: Fail (-)	

This chapter has not attempted to remedy the apparent incompatibility in RTNEPH clouds occurring in regions of NOGAPS analyzed subsidence. It has, however served to identify a potentially great cloud maintenance problem in using these clouds and winds to initialize MM5. Chapters IX and X next present an analysis of cloud variables forecast by MM5 when initialized with these NOGAPS analyses and with clouds and precipitation diagnosed from RTNEPH using CIS.

CHAPTER IX
LARGE SCALE ANALYSIS

9.1. Introduction

An analysis of clouds and precipitation produced by mesoscale NWP models is difficult for two reasons. First, mesoscale NWP models do not globally conserve water mass. Inner regions of a modeled domain are subject to the vagaries of the initial boundary conditions, which are necessary to provide unique solutions to the model's differential equations. In MM5 for instance, cloud quantities are quasi-static on the boundaries. Clouds are considered zero on inflow and zero gradient on outflow. After initialization, clouds are either generated or destroyed within the model domain, never advected into the mother domain. These boundary conditions limit the ability of the model to simulate cloud changes due to advection at scales larger than the modeled domain. The second reason that clouds are difficult to analyze is that cloud and precipitation mass distribution has very large spatiotemporal variability particularly on cloud scales (< 10 km). The mesoscale models have difficulty capturing the magnitude of this variability (demonstrated in this chapter), and point-by-point correlation with analyzed cloud coverage is poor (demonstrated later in Chapter X). Mesoscale models also have a tendency to distribute clouds in a smooth and nearly continuous manner as directed by the continuous differential equations governing the model. It is generally expected that the correlation between modeled and analyzed cloud will decrease as analyzed cloud discreteness increases.

To get around these two problems, mixing ratios and masses representative of the entire domain are analyzed. Plots of total domain mass and domain averaged mixing ratio and coverage amount minimize the information related to local scale variability, and they allow comparison of predicted and analyzed cloud characteristics at greater spatial scales. In the analysis presented here, model output is compared to cloud variables diagnosed from RTNEPH using CIS. There is no direct comparison between model output and RTNEPH.

Two general classes of analyses are performed: Large-scale analysis (this chapter) and local-scale analysis (presented in Chapter X). To characterize large-scale predicted and analyzed cloud, two categories of plots are produced. In section 9.2, plots within the first category, or mass category, are used to evaluate the characteristics of domain cloud constituent mass. These plots include the vertical distribution of cloud constituent mass and the variation of total domain cloud constituent mass with time. In section 9.3, plots within the second category, or mixing ratio category, are used to evaluate the characteristics of water constituent mixing ratio. Among these are histograms of the cloud and precipitation constituents (mixing ratios of cloud liquid water - CLW, cloud ice - ICE, rain - RNW, and snow - SNOW) and plots to show how these mixing ratios vary in time. The plot types just described are presented next in detail along with some inferred model features.

9.2. Mass Analysis

a. Cloud insertion

Total cloud constituent mass is computed using equation 9.1.

$$T_\gamma = \sum_{i,j} \sum_k \frac{q_{\gamma_{i,j,k}} P_{i,j}^* \delta\sigma \delta x^2}{g} \tag{9.1}$$

The i and j coordinate indicates horizontal location, and the k coordinate indicates vertical location. The cloud constituents, q_γ, represent mixing ratios of water vapor, cloud liquid water, cloud ice, rain, and snow having units kg kg^{-1} at each grid point. P^* is the difference between the surface pressure and the model lid defined at 10^4 Pa. Acceleration of gravity is given as g, and the resulting total mass has units kg. The sigma layer depth ($\delta\sigma$) is 0.05, and q_γ is interpolated to the evenly spaced sigma layers when necessary. The grid spacing (δx) is 6 km for the finest model grid (domain 3) and is 18 km for domain 2. The total domain water constituent masses are listed in Tables 9.1a through 9.2c. These mass values are computed before cloud insertion and at cloud insertion times. Cloud insertion times are at forecast hours -06 and +00. Mass is also computed 18 minutes into the simulation after each cloud insertion time. Other mass calculations are summarized in Tables 9.3 through 9.6.

Before insertion, the only water constituent present is water vapor. After insertion, water vapor mass increases about 8% and total domain water mass increases about 10% (Table 9.3). This is because the water vapor mixing ratio at grid points identified to contain cloud is adjusted to saturation. Cloud insertion dramatically affects total water mass in domains 2 and 3. At cloud insertion times, domain 2 total water mass (Q+CLW+ICE+RNW+SNOW) averages 0.17 metric tera-tons, and domain 3 total water mass is about 5% of this value or 8.83 metric giga-tons. (One metric ton is equivalent to 10^3 kg.) Q (water vapor) represents the largest water constituent at more than 97% of the average domain total water mass (Table 9.4). Rain mass makes up the second largest constituent at roughly 1.5%.

Within minutes of cloud insertion times, the mesoscale model rapidly decreases total water mass. Mass values are sampled 18 minutes after each insertion time. After 18 minutes, water vapor makes up more than 99% of the total domain water mass (Table 9.5). The percent change in mass for each water constituent 18 minutes after the insertion times is listed in Table 9.6. Rain mass decreases more than 85%. "Rain-out" is a reasonable explanation for why the bulk of these mass changes occur in such a short time. Indeed, this magnitude of rainout is expected because rain is directly inserted without being coupled to cloud-scale circulations that can maintain the rain rate. Cloud liquid water mass decreases about 75%. The reduction of cloud liquid water mass is examined further in Chapter XI. Because the domains are open, there is no global mass conservation and it is not possible to accurately gauge where all the mass is going.

Table 9.1a. Total cloud constituent mass for domain 2 before cloud insertion.

Day/Hour	Vapor (x10^{14} kg)	Liquid water	Ice	Rain	Snow
13/00	1.59	0.00	0.00	0.00	0.00
14/12	1.63	0.00	0.00	0.00	0.00
Average	1.61	0.00	0.00	0.00	0.00

Table 9.1b. Total cloud constituent mass for domain 2 at cloud insertion time.

Day/Hour	Water vapor (x10^{14} kg)	Liquid water (x10^{12} kg)	Ice (x10^{11} kg)	Rain (x10^{12} kg)	Snow (x10^{11} kg)
13/00	1.66	0.90	2.86	3.37	6.81
13/06	1.67	0.61	1.30	1.48	3.48
14/12	1.79	1.11	2.19	2.83	6.69
14/18	1.78	1.05	0.82	1.91	5.06
Average	1.73	0.92	1.79	2.40	5.51

Table 9.1c. Total cloud constituent mass for domain 2, 18 minutes after cloud insertion time.

Day/Hour	Water vapor (x10^{14} kg)	Liquid water (x10^{11} kg)	Ice (x10^{11} kg)	Rain (x10^{11} kg)	Snow (x10^{11} kg)
13/00	1.57	0.99	1.26	4.07	7.45
13/06	1.57	1.74	0.45	1.76	2.24
14/12	1.69	1.88	0.99	3.23	6.00
14/18	1.68	3.59	0.70	4.35	5.09
Average	1.63	2.03	0.85	3.35	5.20

Table 9.2a. Total cloud constituent mass for domain 3 before cloud insertion.

Day/Hour	Water vapor (x10^{12} kg)	Liquid water	Ice	Rain	Snow
13/00	7.46	0.00	0.00	0.00	0.00
14/12	8.21	0.00	0.00	0.00	0.00
Average	7.84	0.00	0.00	0.00	0.00

Table 9.2b. Total cloud constituent mass for domain 3 at cloud insertion time.

Day/Hour	Water vapor (x10^{12} kg)	Liquid water (x10^{10} kg)	Ice (x10^{10} kg)	Rain (x10^{11} kg)	Snow (x10^{10} kg)
13/00	7.99	7.13	2.79	4.60	6.26
13/06	8.46	2.44	0.11	0.12	0.91
14/12	8.97	3.29	0.07	0.15	0.91
14/18	8.93	5.27	0.78	1.52	2.86
Average	8.59	4.53	0.94	1.60	2.74

Table 9.2c. Total cloud constituent mass for domain 3, 18 minutes after cloud insertion time.

Day/Hour	Water vapor (x10^{12} kg)	Liquid water (x10^{10} kg)	Ice (x10^{10} kg)	Rain (x10^{10} kg)	Snow (x10^{10} kg)
13/00	8.10	0.77	1.32	4.42	7.13
13/06	8.55	1.37	0.08	0.39	0.66
14/12	8.98	1.02	0.12	0.63	0.88
14/18	8.99	1.99	0.65	3.75	3.08
Average	8.66	1.29	0.54	2.30	2.94

Table 9.3. Change in water vapor mass and total water mass due to cloud insertion.

	Domain 2	Domain 3
Total mass before insertion	1.61 x 10^{14} kg	7.84 x 10^{12} kg
Total mass at insertion	1.77 x 10^{14} kg	8.83 x 10^{12} kg
% change in total mass	9.94 % increase	12.6 % increase
% change in water vapor mass	7.45 % increase	9.57 % increase

Table 9.4. Average fraction of total domain mass for each water constituent at cloud insertion time.

	Domain 2	Domain 3
Q	97.7 %	97.3 %
CLW	0.52 %	0.51 %
ICE	0.10 %	0.11 %
RNW	1.36 %	1.81 %
SNOW	0.31 %	0.31 %

Table 9.5. Average fraction of total domain mass for each water constituent 18 minutes after cloud insertion time.

	Domain 2	Domain 3
Q	99.4 %	99.2 %
CLW	0.12 %	0.15 %
ICE	0.01 %	0.06 %
RNW	0.20 %	0.26 %
SNOW	0.32 %	0.34 %

Table 9.6. Average percent change in mass 18 minutes after cloud insertion time.

	Domain 2	Domain 3
Total	7.34 % decrease	1.13 % decrease
Q	5.78 % decrease	0.81 % increase
CLW	77.9 % decrease	71.5 % decrease
ICE	53.7 % decrease	42.6 % decrease
RNW	86.0 % decrease	85.6 % decrease
SNOW	5.63 % decrease	7.30 % increase

b. Precipitable water

Precipitation mass is computed in CIS using parameterizations involving the mixing ratios of cloud liquid water and cloud ice, which are computed at less than adiabatic values. The link between water vapor and precipitation mass is indirect and possibly disconnected if these parameterizations produce more precipitation than is possible from the profile of water vapor. One validation check of the precipitation mass is to compare it to precipitable water computed from the water vapor in the cloudy column. Total column precipitation mass that exceeds total column precipitable water mass indicates that the model is not well "tuned" and that an adjustment must be made to the coefficients in the precipitation parameterizations. Model-diagnosed precipitable water (PW) is computed by integrating the vertical profile of q_v as follows:

$$PW = \frac{P*}{g\Delta x^2 \rho_w} \sum_{k=1}^{N} q_v(k)\Delta\sigma_k \qquad (9.2)$$

where $q_v(k)$ is the model specific humidity at the kth layer; $\Delta\sigma_k$ the layer thickness of the model at the kth layer; N is the total number of layers; ρ_w is the density of liquid water, Δx^2 is the grid area; g is gravity; $P*$ is defined as p_s - p_t, where p_s is the surface pressure and p_t is the pressure at the top of the model (100 hPa). Model diagnosed precipitation water is computed similarly following:

$$\text{Precip} = \frac{P*}{g\Delta x^2 \rho_w} \sum_{k=1}^{N} \left(q_r(k) + q_s(k)\right)\Delta\sigma_k \qquad (9.3)$$

where $q_r(k)$, and $q_s(k)$ are the mixing ratios of rain, and snow respectively. Units for equations 9.2 and 9.3 are equivalent depth of liquid water.

Figures 9.1 through 9.3 show the horizontal distribution of the ratio of precipitation to precipitable water (expressed in percent) computed above each surface grid point within the modeled domain (100% x Precip / PW) sampled at forecast hour +12 for the 13 September 2000 simulation. Maximum precipitable water values varied from 72 mm to 88 mm. Values less than 100% indicate precipitation is less than the theoretical limit of the precipitable water mass. Upward spikes in the plots locate positions with heavy precipitation. The analysis shows slightly greater spatial variability and more heavy precipitation on domain 2 than the model does. Both the analysis and the model show spikes indicating discretely distributed maximum precipitation shafts. The analysis is more likely to produce precipitation near the theoretical precipitable water limit on domain 2.
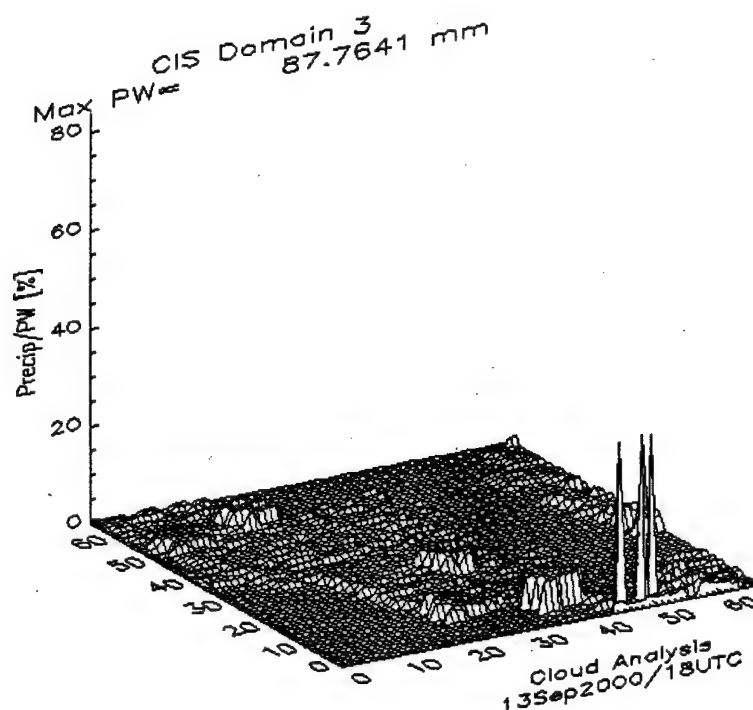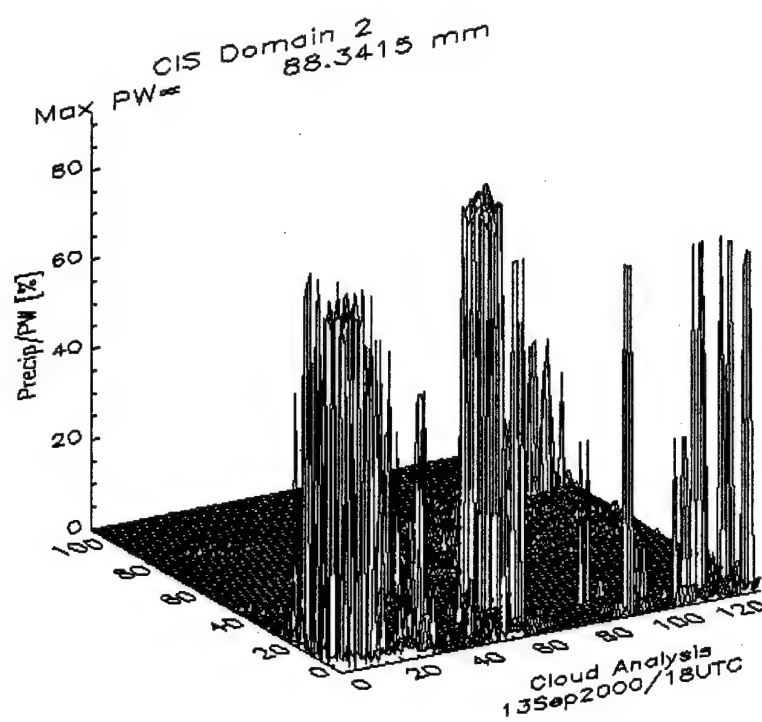
Figure 9.1. Horizontal distribution of the ratio of precipitation to precipitable water (expressed in percent) computed above each surface grid point within the modeled domain for 13 September 2000 / 18-UTC analysis on domains 2 and 3. Viewpoint is from the Southwest. The X and Y-axes indicate horizontal position and the Z-axis is the computed mass difference expressed in mm depth of water. Positive values indicate computed precipitation mass is less than the theoretical limit imposed by precipitable water.
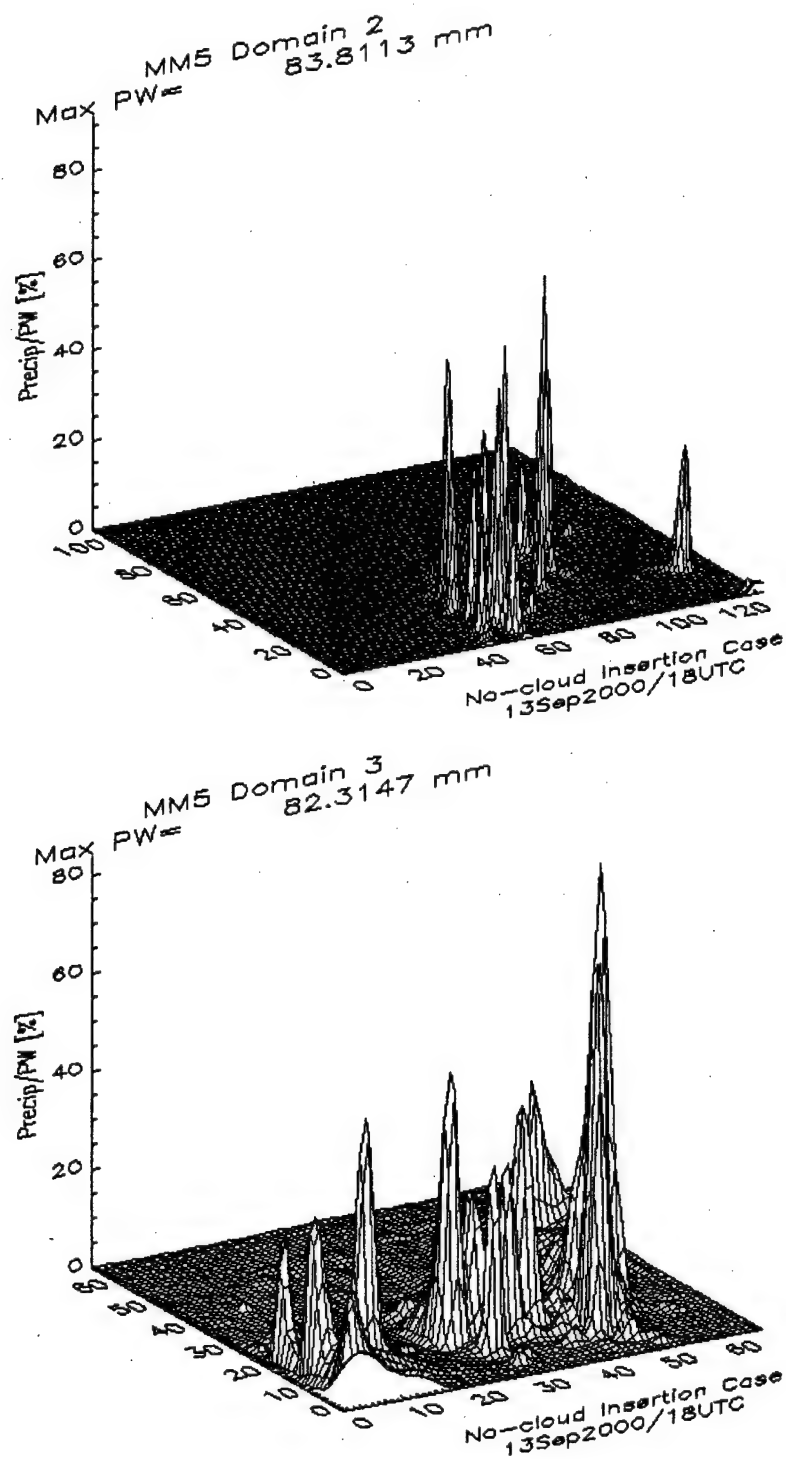
Figure 9.2. Horizontal distribution of the ratio of precipitation to precipitable water (expressed in percent) computed above each surface grid point within the modeled domain of the MM5 no-cloud simulation for 13 September 2000 (forecast hour +12) on domains 2 and 3. Viewpoint is from the Southwest. The X and Y-axes indicate horizontal position and the Z-axis is the computed mass difference expressed in mm depth of water. Positive values indicate computed precipitation mass is less than the theoretical limit imposed by precipitable water.
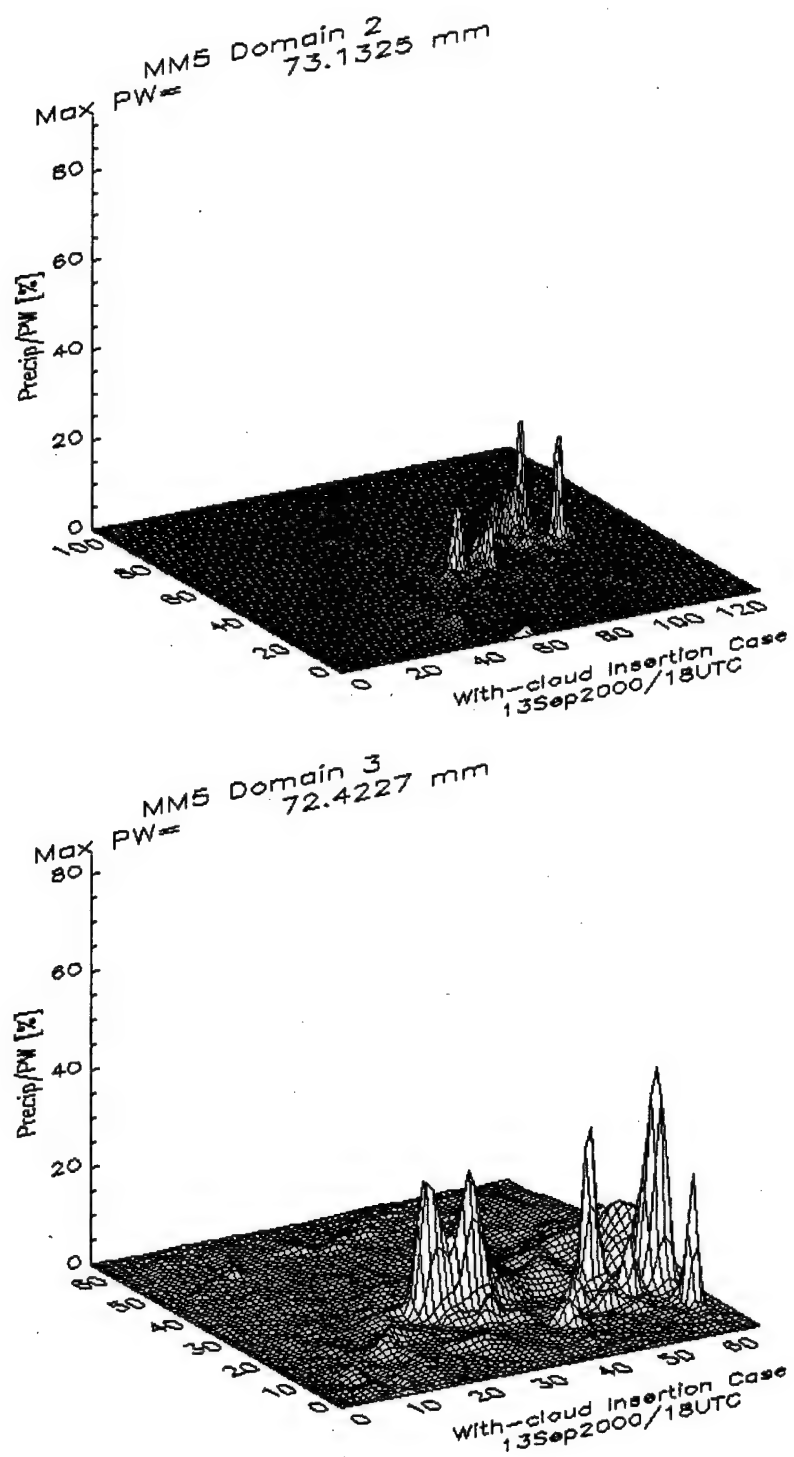
Figure 9.3. Horizontal distribution of the ratio of precipitation to precipitable water (expressed in percent) computed above each surface grid point within the modeled domain of the MM5 with-cloud simulation for 13 September 2000 (forecast hour +12) on domains 2 and 3. Viewpoint is from the Southwest. The X and Y-axes indicate horizontal position and the Z-axis is the computed mass difference expressed in mm depth of water. Positive values indicate computed precipitation mass is less than the theoretical limit imposed by precipitable water.

c. Vertical mass distribution

Figures 9.4 through 9.8 show the vertical mass distribution of water vapor, cloud liquid water, cloud ice, rain, and snow sampled at forecast hour +12 for the 13 September 2000 simulation. These plots are sensitive only to order-of-magnitude variation. There are no large differences in the vertical distribution of water vapor mass (Figure 9.4) between the simulations and the analysis, which indicates at forecast hour +12, water vapor depends much more on the NOGAPS analysis than on MM5. The following paragraphs present a subjective comparison of these mass profiles among the RTNEPH analysis (using CIS), the with-cloud insertion simulation, and the without-cloud insertion simulation in domains 2 and 3.
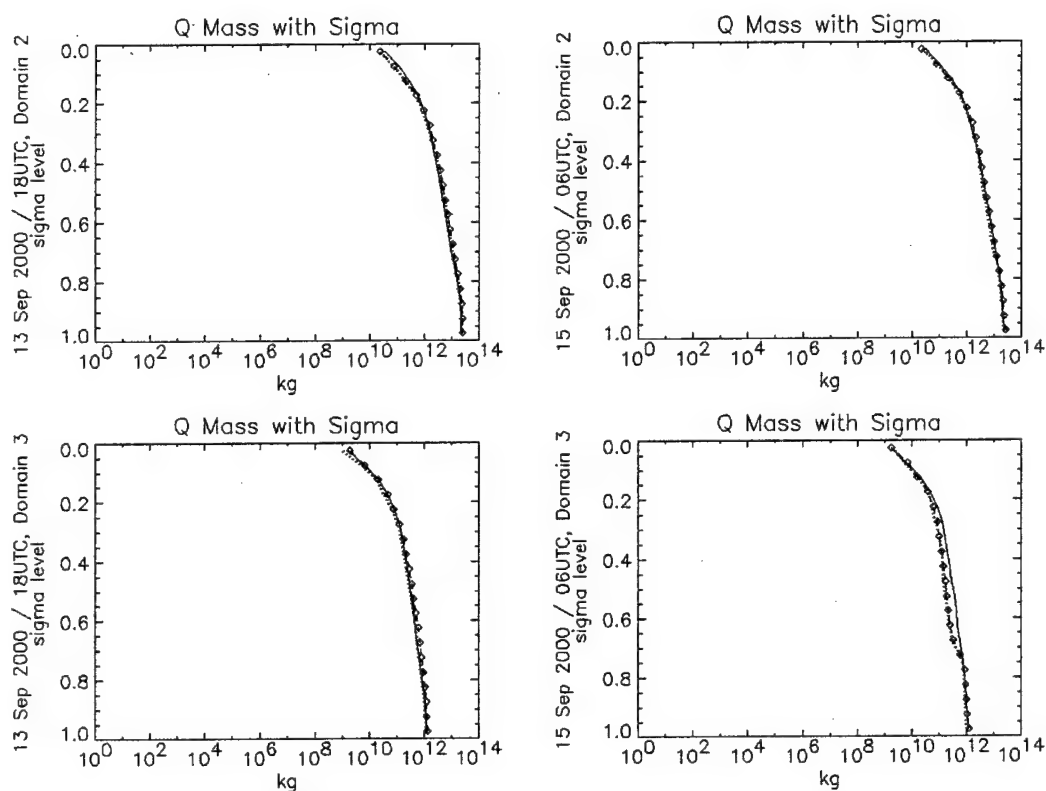
Figure 9.4. Typical water vapor mass vertical distribution in kg, domains 2 and 3, 13 and 14 September simulations. These mass profiles are sampled at forecast hour +12. Solid line indicates with-cloud insertion case, dotted line indicates no-cloud insertion case, dashed line indicates analysis. Diamonds on analysis line indicate sampled sigma levels.

1) CLOUD LIQUID WATER MASS VERTICAL DISTRIBUTION

(Figure 9.5). Among the profiles, there is generally good agreement in vertical distribution pattern. Most vertical distribution patterns exhibit a logarithmic increase in mass between the lowest sigma level and sigma level 0.8. Mass values then change little between sigma level 0.8 and 0.2 where an abrupt decrease occurs. Although there is small variation in mass magnitudes, this uni-modal vertical distribution pattern appears for most forecast times. There are exceptions: for example, the vertical distribution of mass for the domain-3 without-cloud initialization simulation is bimodal with maxima occurring at sigma levels 0.8 and 0.4. In domain 2, the vertical distribution of mass between the lowest level and sigma level 0.8 is nearly identical between the MM5 simulations regardless of cloud insertion. The analysis however, generally contains an order of magnitude more mass than the MM5 simulations at each level. In other words, for each sigma layer, the MM5 simulations produce 10% of the cloud liquid water mass analyzed by CIS. Mass drops abruptly with height above sigma level 0.2 for the analysis and the with-cloud insertion simulation, and above sigma level 0.1 for the without-cloud insertion simulation. This is indicative of the homogeneous freezing level at which all cloud water is converted to cloud ice. Domain 3 cloud liquid water shows larger variability in vertical mass distribution than domain 2 among the various forecast hours and simulation cases examined (not shown). Domain 3 CIS values also may not necessarily have larger mass than the MM5 simulations as is noted for domain 2. This larger variability on domain 3 may be due to the relatively smaller sample size. Smaller variability in domain 2 may also reflect slower changes in synoptic scale distributions of cloud liquid water mass. Among the cloud and precipitation variables considered, cloud liquid water has the highest 3-hourly variability in distribution pattern in domain 3.
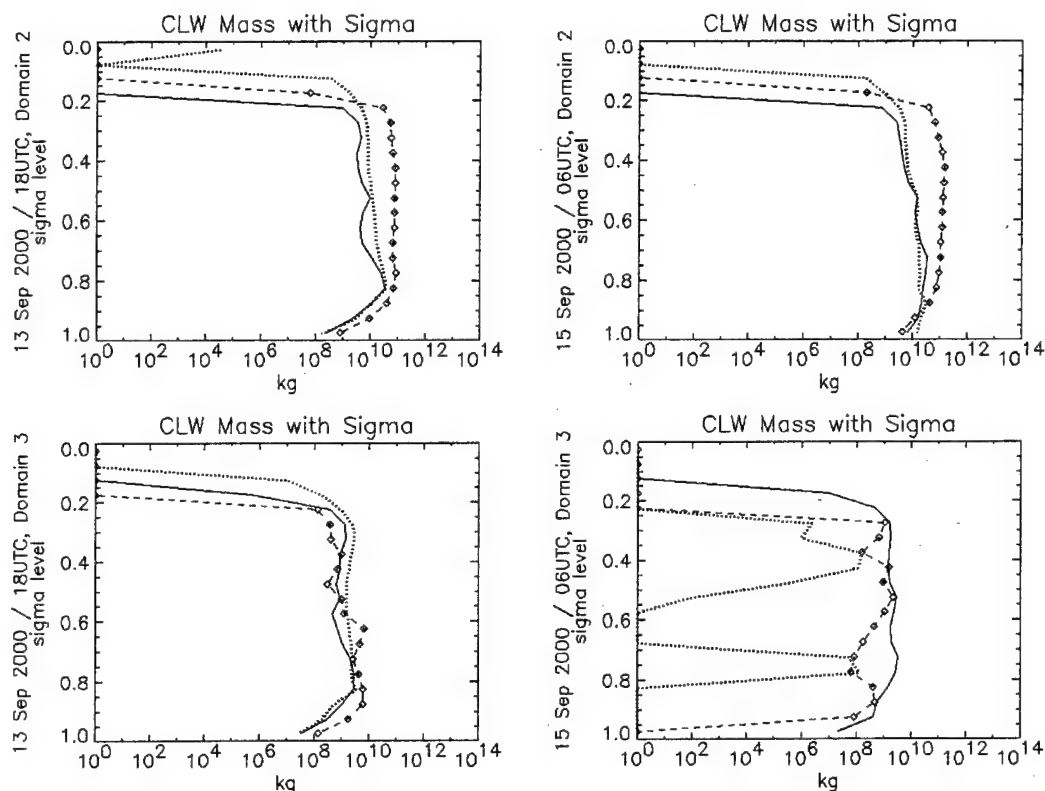
Figure 9.5. Typical cloud liquid water mass vertical distribution in kg, domains 2 and 3, 13 and 14 September simulations. These mass profiles are sampled at forecast hour +12. Solid line indicates with-cloud insertion case, dotted line indicates no-cloud insertion case, dashed line indicates analysis. Diamonds on analysis line indicate sampled sigma levels.

2) CLOUD ICE MASS VERTICAL DISTRIBUTION

(Figure 9.6). Among the profiles, CIS and MM5 simulated vertical distributions of ice mass show similar patterns. This pattern has three parts. The lower part of the pattern shows a rapid increase in cloud ice mass with height. This indicates variation in the height of the melting level within the domain. The second part of the pattern indicates an exponential increase of mass with height up to about sigma level 0.2. The third part of the pattern shows mass reaching a peak at the homogeneous freezing line then a slight decrease to represent variation in the maximum cloud heights within the domain. Analyzed ice mass values can be an order of magnitude larger than MM5 simulated values depending on the forecast hour being sampled. The vertical distribution pattern between the simulations is nearly identical regardless of cloud insertion. The vertical distribution pattern changes little with forecast hour reflecting slow changes expected for synoptic scale distributions of mass. Vertical distribution patterns between CIS and MM5 simulated ice mass show greater vertical variation in domain 3 than in domain 2. There is also less agreement between the simulations in domain 3. The hour-to-hour variation of ice mass in domain 3 is generally less than that for cloud liquid water.
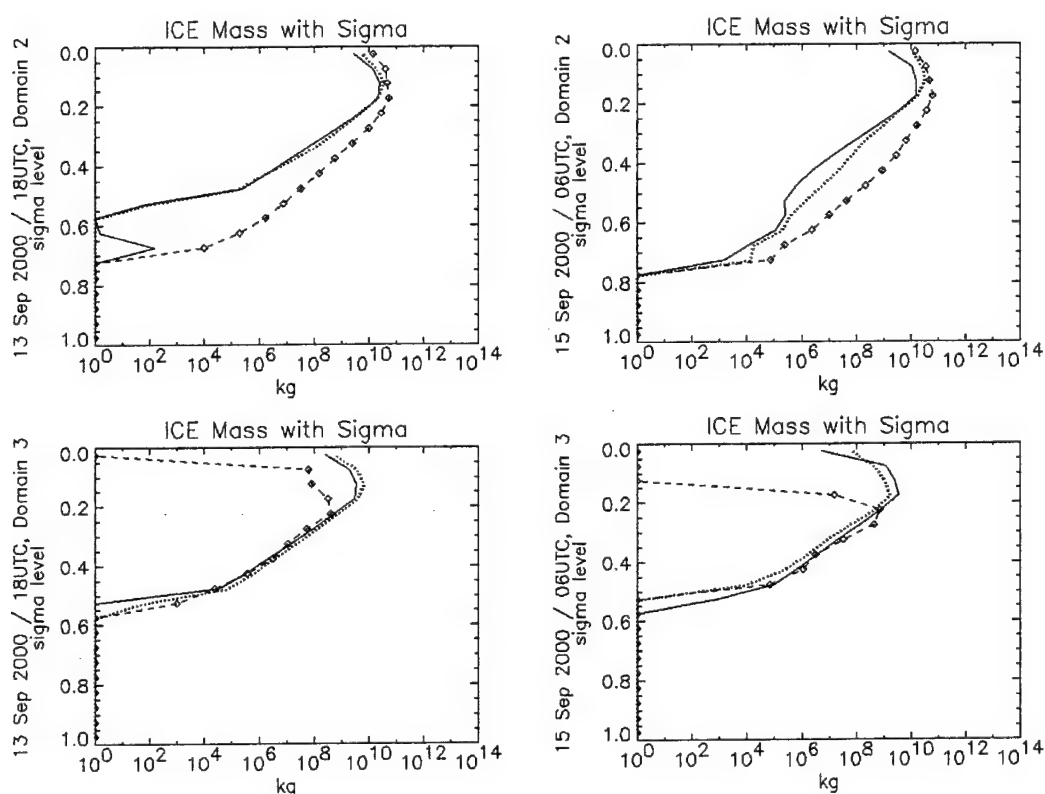
Figure 9.6. Typical cloud ice mass vertical distribution in kg, domains 2 and 3,
13 and 14 September 2000 simulations. These mass profiles are sampled at forecast hour +12.
Solid line indicates with-cloud insertion case, dotted line indicates no-cloud insertion case,
dashed line indicates analysis. Diamonds on analysis line indicate sampled sigma levels.

3) RAIN MASS VERTICAL DISTRIBUTION

(Figure 9.7). Both the analysis and the simulations show a nearly constant profile of rain mass
from the lowest level to about midlevel. The simulations show an exponential decrease in mass upward
from about mid-domain. In MM5, rain is permitted to mix throughout the vertical extent of the domain;
therefore, this pattern indicates variation of cloud top height within the modeled domain. The most
dramatic and consistent difference between the analysis and the simulations is the abrupt decrease of
rain mass in the upper third of the analysis. This is a result of three factors in CIS. First, CIS computes
rain mass only by integrating downward. There is no method in CIS to vertically transport rain upward.
Second, in cumuliform clouds, the cloud liquid water mixing ratio must exceed 0.5 g kg^{-1} before rain
becomes activated at upper levels while snow can become active with any concentration of cloud ice
present. Finally, the RTNEPH analysis can many times underestimate the horizontal distribution of
deep cumuliform clouds in regions of sparse surface observations particularly if the cloud field contains
a great deal of obstructing cirroform clouds.

Generally, domain 2 rain mass from the analysis is one to two orders-of-magnitude greater than the simulations. There is greater hour-to-hour variation among domain 3 rain mass profiles than among domain 2 rain mass profiles. Unlike domain 2, domain 3 analysis rain mass is not necessarily always larger than MM5 forecast rain mass.
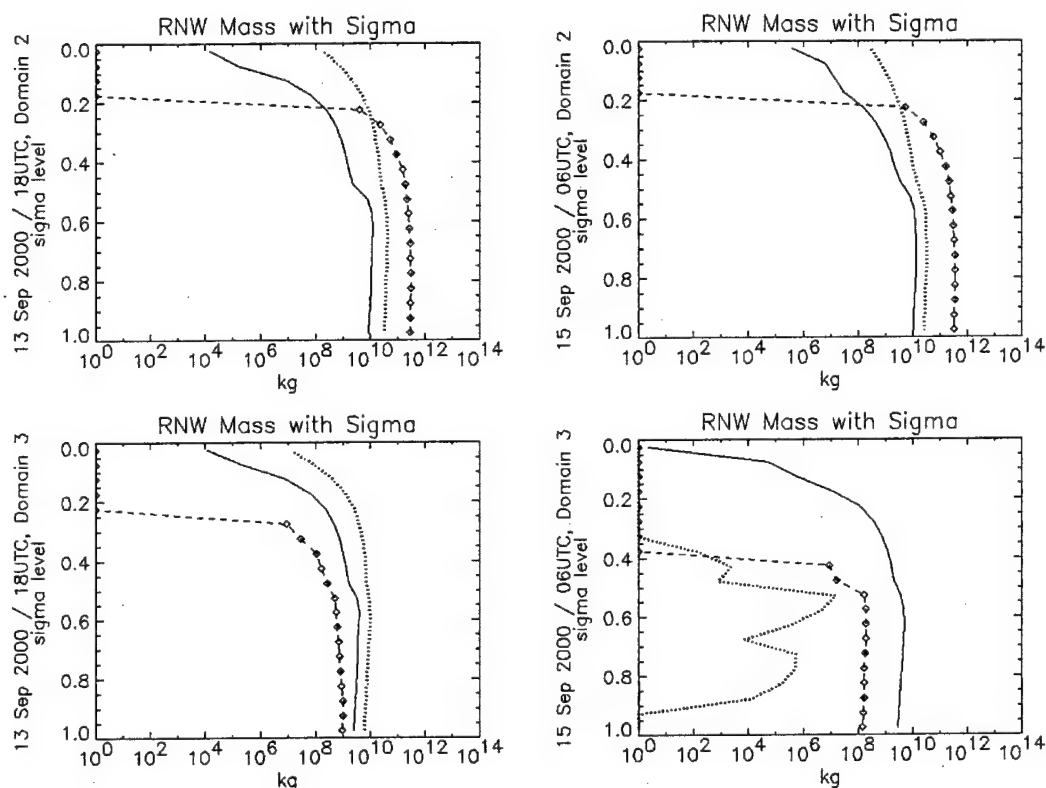
Figure 9.7. Typical rain mass vertical distribution in kg, domains 2 and 3, 13 and 14 September 2000 simulations. These mass profiles are sampled at forecast hour +12. Solid line indicates with-cloud insertion case, dotted line indicates no-cloud insertion case, dashed line indicates analysis. Diamonds on analysis line indicate sampled sigma levels.

4) SNOW MASS VERTICAL DISTRIBUTION

(Figure 9.8). Among the domain 2 simulation profiles, snow mass increases exponentially and continuously between the surface and sigma level 0.5. Between 0.5 and 0.2, the snow mass profile is nearly constant. This profile is due to the snow's source being at upper levels and decreasing downward through melting and sublimation below cloud base and by rain accumulation. The increase in rain mass produced by melting snow is not apparent on these plots because rain mass is several orders of magnitude larger than snow mass below sigma level 0.5. Snow mass decreases above sigma level 0.2 indicating the frequency distribution of deep precipitating clouds. Analyzed snow mass decreases abruptly as it falls below the height of the melting line. It is not clear whether CIS melts snow too

quickly or the MM5 simulations melt snow too slowly. CIS snow also decreases abruptly above sigma level 0.2 indicating snow may be under-analyzed just as rain is at higher sigma levels. MM5 is undoubtedly producing more snow at higher levels because of vertical transport, a process not accounted for in the analysis. Maximum analyzed snow values in domain 2 are roughly an order of magnitude larger than MM5 simulated snow mass values. Domain 3 maximum CIS snow mass values are not necessarily larger than MM5 simulated snow mass values.
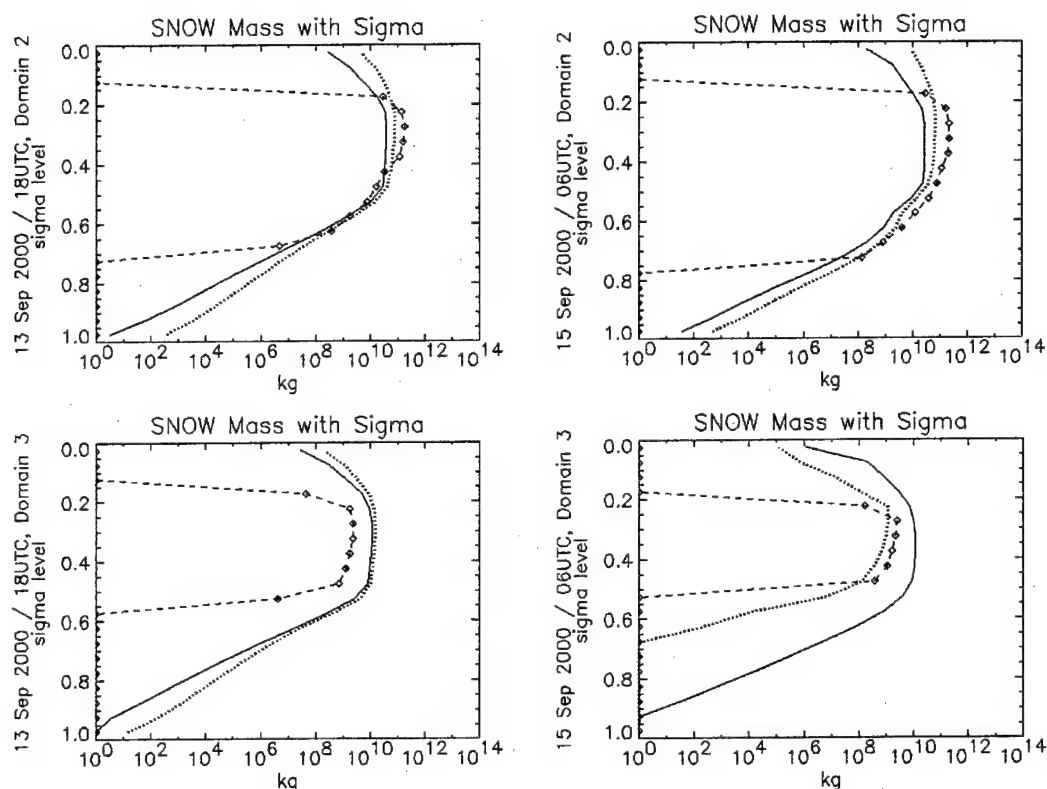
Figure 9.8. Typical snow mass vertical distribution in kg, domains 2 and 3, 13 and 14 September 2000 simulations. These mass profiles are sampled at forecast hour +12. Solid line indicates with-cloud insertion case, dotted line indicates no-cloud insertion case, dashed line indicates analysis. Diamonds on analysis line indicate sampled sigma levels.

d. Evolution of total domain water constituent mass

Figures 9.9 through 9.13 show the time evolution of total domain water constituent mass in domains 2 and 3. Data from both simulations are plotted for forecast hours -06 to +24. Analysis data is plotted at 3-hour intervals. Simulation data is plotted at six-minute intervals for forecast hours -06 to +06, then in 3-hour increments for the remainder of the forecast period. These plots are sensitive only to order-of-magnitude variation. The following paragraphs present a subjective comparison of these

mass profiles among the cloud analysis, the with-cloud insertion simulation, and the without-cloud insertion simulation in domains 2 and 3.

1) WATER VAPOR TOTAL DOMAIN MASS

(Figure 9.9). In both domains, total domain water vapor mass for the without-cloud simulation is consistently less than that of the with-cloud simulation and the analysis. The abrupt changes on the with-cloud simulation mass trace indicate changes due to direct insertion of water vapor at grid points identified to contain cloud. At those grid points, water vapor is adjusted upward to saturation. Generally, the with-cloud simulation mass trace departs from the analysis mass trace slowly. The additional water vapor added at direct insertion times does not rapidly equilibrate to another mass level. Beyond insertion times, the temporal variation of analyzed water vapor mass is larger than that of the simulations. The domain 3 water vapor analyses have greater variation in mass than the domain 2 analyses. The general mass trends for the simulations follow that of the analysis. This trend coherency is an indicator that mother domain (domain 1) forecasts of water vapor did well at setting boundary conditions for domains 2 and 3.

2) CLOUD LIQUID WATER AND RAIN TOTAL DOMAIN MASS

(Figures 9.10 and 9.11). The no-cloud simulations (dotted trace on Figure 9.10) begin with no cloud liquid water at forecast hour -06. Both domains 2 and 3 appear to spin-up domain mass by forecast hour +06. Beyond forecast hour +06, domain mass reaches a quasi-steady value of one giga-ton in domain 2 and of 0.01 to 0.1 giga-ton in domain 3. After spin-up, there is better agreement between the simulations than between a simulation and the analysis. The simulations using cloud insertion appear to reach these quasi-steady levels in domain mass immediately (solid line).

The model response to insertion appears as a spike in the mass trace diagram when the analysis mass is higher than the quasi-steady simulation mass. At each insertion time, cloud liquid water mass is immediately replaced by a larger analyzed mass (dashed line). Within minutes after insertion, modeled domain mass is adjusted to a smaller quasi-steady value which is only slightly larger than that from the no-cloud simulation. The with-cloud simulations do not show a slow spin-up in the equilibration of cloud liquid water, as do the no-cloud simulations. It is yet to be seen if the mass equilibrium level that the with-cloud insertion simulation adjusts to immediately after insertion is a result of diffusion to neighboring grid points. Plots of cloud liquid water mass for domain 3 occasionally show that analyzed mass is less than modeled mass. The model's response to cloud insertion in those cases is to increase cloud mass back up to the model's equilibrium level although at a slower rate.
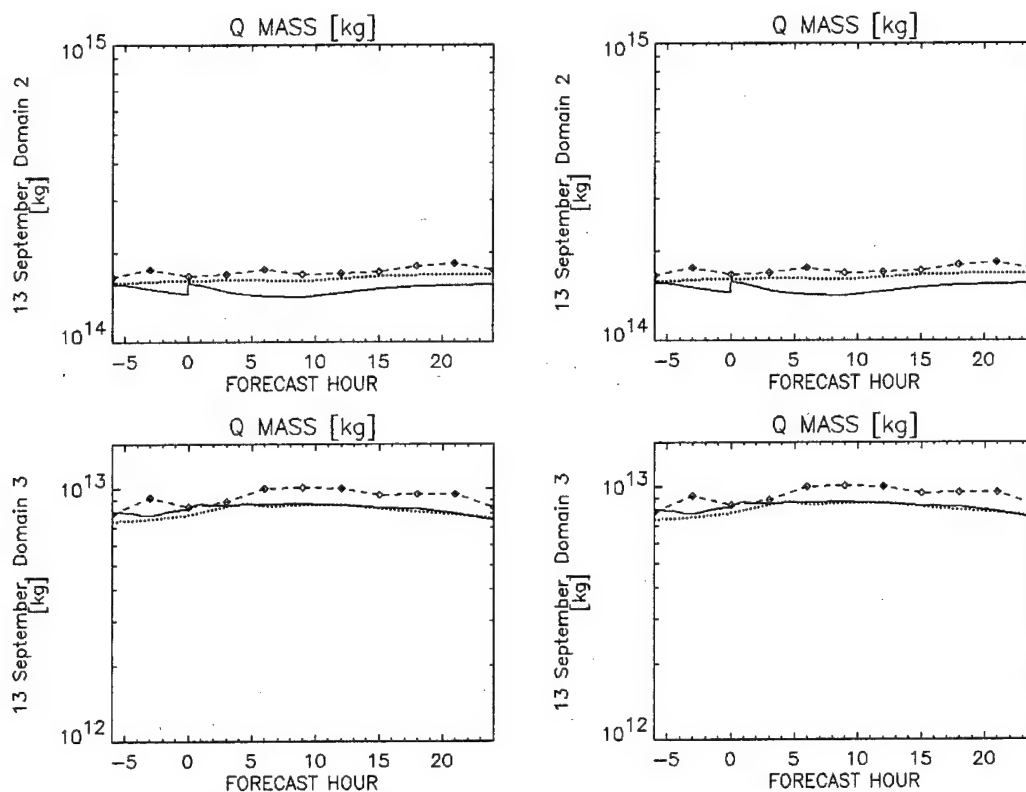
Figure 9.9. Total water vapor mass versus forecast hour, domains 2 and 3, 13 and 14 September 2000 simulations. Solid line indicates with-cloud insertion case, dotted line indicates no-cloud insertion case, and dashed line indicates analysis. Diamonds on analysis line indicate 3-hourly analysis interval.

Domain 3 analyzed mass is more variable than that of domain 2 and can be either greater than or less than modeled mass. Conversely, domain 2 analyzed mass is consistently greater than modeled mass by an order of magnitude. It is likely the differences in domain 2 mass between the analysis and the model are due to over-analyzing. Although domain 2 has larger grid spacing, the analysis on domain 2 is based on the same cloud process scales considered on domain 3 (i.e. adiabatic liquid water content retained, assumed time step in parameterization for cloud ice mixing ratio, etc.).

The convective scheme used in the model in domain 2 may also be contributing to under-forecasting cloud liquid water. The Grell (1993) scheme used in these simulations on domains 1 and 2 does not produce cloud liquid water but instead condenses water vapor and immediately converts it to rain water and deposits it into the next lower level. Any cloud liquid water forecast is produced by the model's explicit grid scale cloud physics.

The model appears insensitive to the initialization of cloud liquid water even though the water inserted may be far larger than the model's equilibrium value; the model rapidly adjusts back to the

equilibrium level. Because of the model's tendency to adjust cloud liquid water to some equilibrium level, direct insertion may only improve model performance during the early forecast hours it would otherwise be spinning up.
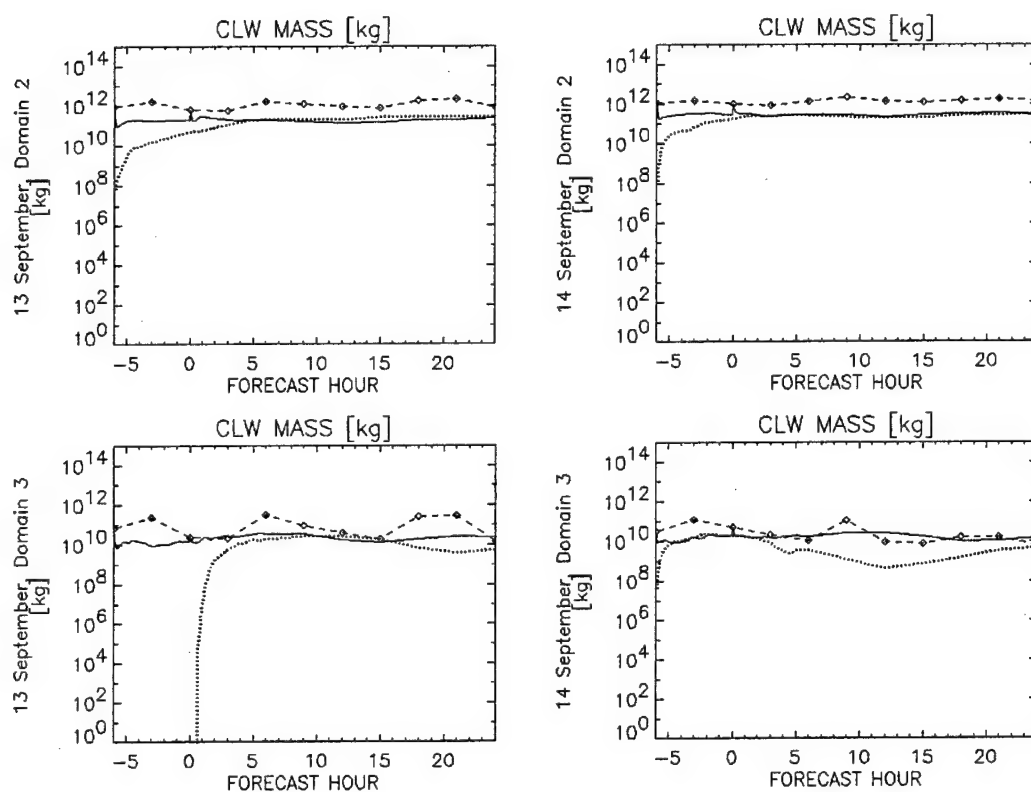
Figure 9.10. Total cloud liquid water mass versus forecast hour, domains 2 and 3, 13 and 14 September 2000 simulations. Solid line indicates with-cloud insertion case, dotted line indicates no-cloud insertion case, and dashed line indicates analysis. Diamonds on analysis line indicate 3-hourly analysis interval.

The rain trace (Figure 9.11) shows mass trends similar to that of cloud liquid water. This is because the principal formation mechanism of rain in both the analysis and the model is the accumulation of cloud liquid water. On domain 2, rain mass is analyzed one to two orders of magnitude higher than simulated mass. Rain spin-up time on the no-cloud simulations is also similar to that of cloud liquid water.
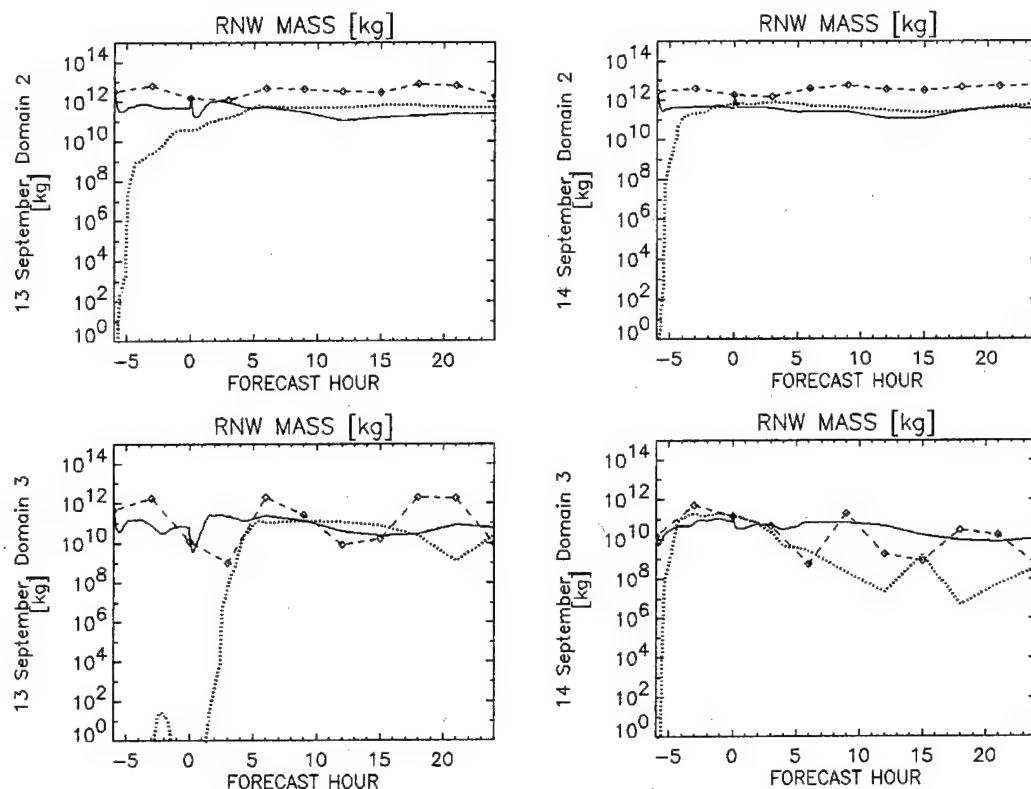
Figure 9.11. Total rain mass versus forecast hour, domains 2 and 3, 13 and 14 September 2000 simulations. Solid line indicates with-cloud insertion case, dotted line indicates no-cloud insertion case, and dashed line indicates analysis. Diamonds on analysis line indicate 3-hourly analysis interval.

3) CLOUD ICE AND SNOW TOTAL DOMAIN MASS

The no-cloud simulations (Figure 9.12) begin with no cloud ice at forecast hour -06. Ice mass spin-up time varies from 2 to 14 hours then reaches a quasi-steady equilibrium value. Domain ice mass is similar in magnitude to domain cloud liquid water mass. There is better agreement between the analysis and the simulations for ice mass than there is for cloud liquid water particularly on domain 2. Domain 3 analyzed ice mass is more variable than simulated ice mass. After spin-up, there is better agreement between the simulations than between a simulation and the analysis. Spikes in the with-cloud simulation mass trace after insertion show that the model adjusts domain mass back to an equilibrium level but not as quickly as it does for cloud liquid water.
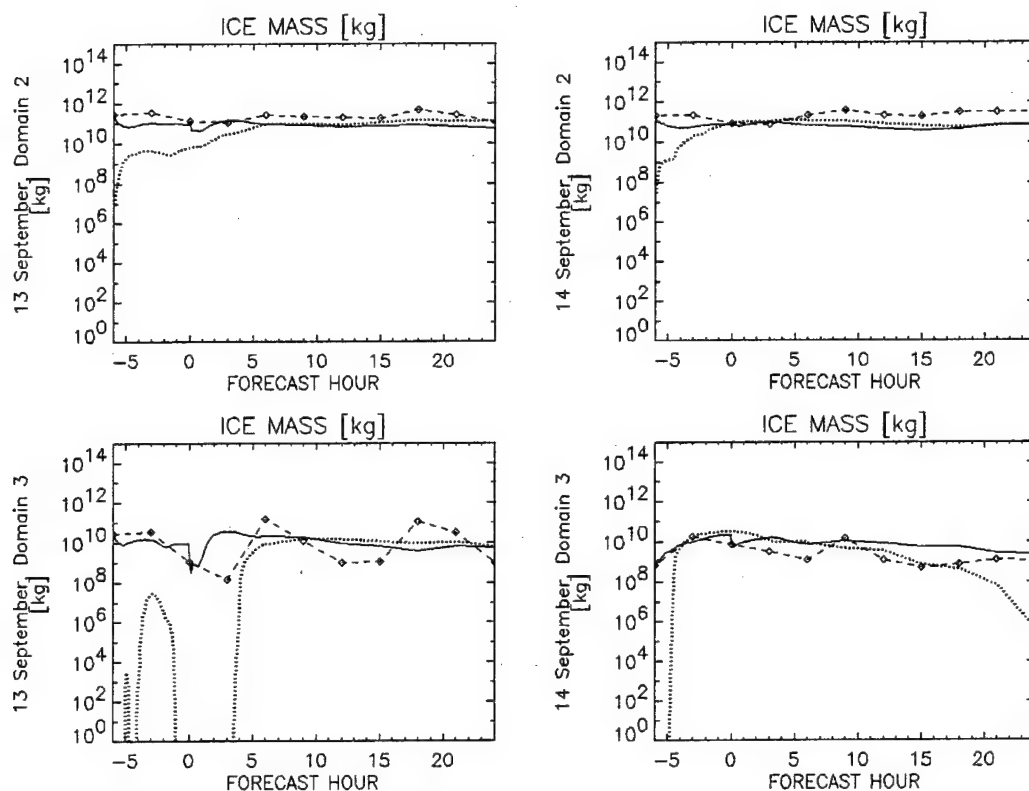
Figure 9.12. Total cloud ice mass versus forecast hour, domains 2 and 3, 13 and 14 September 2000 simulations. Solid line indicates with-cloud insertion case, dotted line indicates no-cloud insertion case, and dashed line indicates analysis. Diamonds on analysis line indicate 3-hourly analysis interval.

The snow trace (Figure 9.13) shows mass trends similar to that of cloud ice. Like cloud ice, snow mass is analyzed at nearly the same of magnitude as simulated snow mass on domain 2. Snow spin-up time on the no-cloud simulations is also similar to that of cloud ice. This is because the principal formation mechanism of snow in both the analysis and the model is the accumulation of cloud ice.
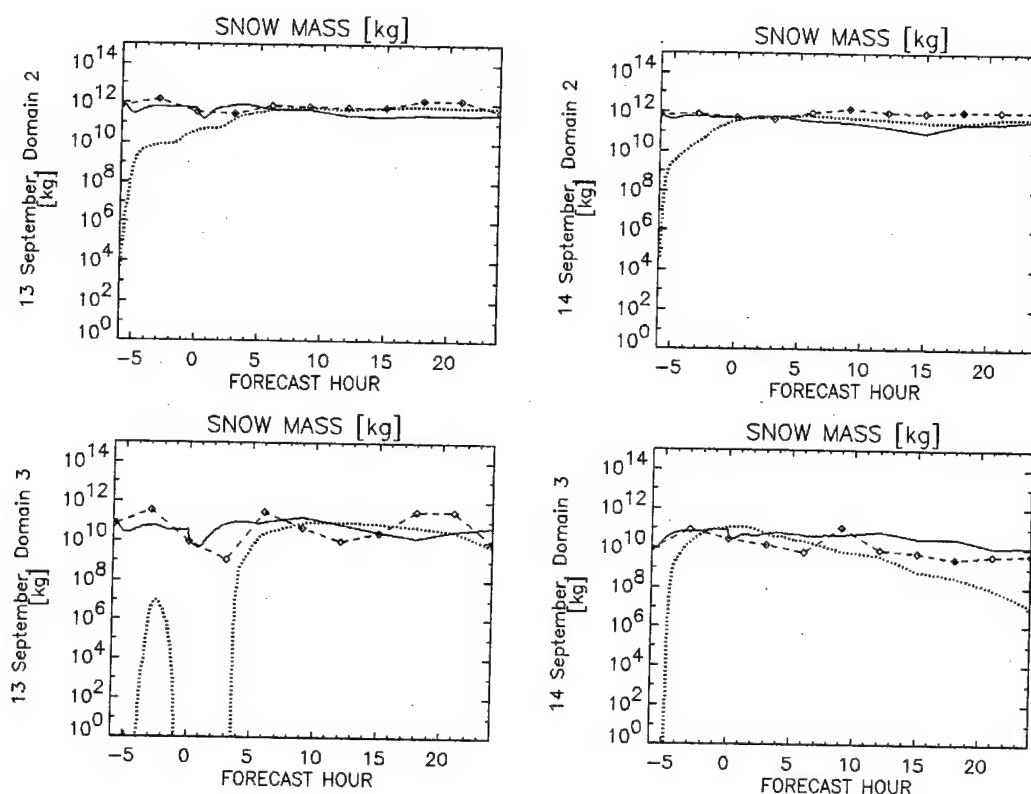
Figure 9.13. Total snow mass versus forecast hour, domains 2 and 3, 13 and 14 September 2000 simulations. Solid line indicates with-cloud insertion case, dotted line indicates no-cloud insertion case, and dashed line indicates analysis. Diamonds on analysis line indicate 3-hourly analysis interval.

9.3. Mixing Ratio Analysis

The previous section presented an analysis of cloud variables in terms of their total domain mass. This section evaluates the gross characteristics of water constituent mixing ratio. Mixing ratios of water vapor, cloud liquid water, cloud ice, rain, and snow are available from the CIS analysis and from MM5 model output. An examination of mixing ratios fulfills three objectives. First, it is the only way the model can fundamentally represent "cloud". MM5 output does not include cloud type, cloud base, or cloud top; it only produces 3-dimensional continuous distributions of mixing ratios. The second objective in examining mixing ratios is to evaluate the model's ability to represent the gross features of analyzed mixing ratios from clouds. Finally, if the gross characteristics of mixing ratio are dramatically different between model results and the analysis, we need to know how the model responds to these differences.

As will be presently shown in this section, large differences do indeed exist between the analysis and the model simulations. It is not known, however, whether these differences exist because the analysis produces an inaccurate picture of mixing ratio distribution or whether the model does. Such

comparisons are nevertheless constructive because the model is being used here to forecast variables that must be translated into information about the distribution of clouds. How that forecast cloud distribution compares to the cloud analysis is what matters most.

Four types of mixing ratio analyses are presented in this section: histograms, the temporal evolution of domain average mixing ratio, the temporal evolution of domain mixing ratio standard deviation, and the temporal evolution of cloud percent coverage. These four types of plots tell us the gross characteristics of cloud distribution in the analysis and in the model's output. In these analyses, we pay particular attention to differences between the analysis and the model's output and between the with-cloud and without-cloud insertion model output.

a. Histogram analysis

Histograms tell the frequency of occurrence for a given mixing ratio value, which can be interpreted here to tells us how often grid points with very low mixing ratios occur compared to how often grid points with very high mixing ratios occur. Histograms of cloud liquid water, cloud ice, rain, and snow mixing ratios are presented in Figures 9.14a through 9.17b. These histograms show the log-frequency of occurrence for the various mixing ratios composed from predictions and analyses at forecast hours +3 through +24 sampled at 3-hourly intervals for an entire domain.

1) CLOUD LIQUID WATER MIXING RATIO HISTOGRAMS

(Figures 9.14a and b). CIS frequency distribution has a pattern similar to MM5 frequency distribution. The log-frequency distribution produces decreasing and linear histograms with lowest frequency at highest mixing ratio. This pattern was consistent among the MM5 and CIS cloud liquid water mixing ratios for both domains studied (2 and 3). Both MM5 simulations consistently produce a histogram that can be approximated by a line function:

$$\log_{10}(Y) = -2 \log_{10}(X) + \log_{10}(4) \tag{9.4}$$

where Y is the number density and X is mixing ratio in g kg^{-1}. When this line function is plotted on the CIS histograms, there is significant area above the line indicating that CIS produces larger mixing ratios at more grid points than either of the MM5 simulations, with- or without-cloud insertion.

The range of maximum mixing ratio values is narrow, only 1.8 to 4.0 g kg^{-1}. From the mass analysis in Section 9.2, it was expected that maximum CIS mixing ratio values would be higher than maximum MM5 mixing ratio values, but this was not necessarily the case. An average of 3.4% of CIS grid points have mixing ratios larger than 0.1 g kg^{-1}. CIS produces higher mixing ratios on more grid points than MM5. For MM5 simulations without cloud insertion, only 1.5% of the grid points have these higher values. MM5 simulations with cloud insertion produce more, 1.9%, but still half as much as CIS. MM5 increases the frequency of higher mixing ratios after cloud insertion. CIS also produces mixing ratios larger than 1.0 g kg^{-1} more frequently than either MM5 simulation.

When comparing histograms for domain 2 and domain 3, no significant differences are found. This may imply cloud liquid water frequency distribution is insensitive to grid scale; however sampling variance has not been taken into account here to draw firm conclusions.

2) ICE MIXING RATIO HISTOGRAMS

(Figures 9.15a and b). The CIS frequency distribution pattern differs from both of the MM5 frequency distribution patterns (with and without cloud insertion). MM5's log-frequency distribution produces decreasing and linear histograms with lowest frequency at highest mixing ratio for model simulations with or without cloud insertion. CIS produces nearly flat distributions or distributions with a slight increase toward higher mixing ratios appearing bimodal with a peak at 1.8 g kg^{-1}. The MM5 simulations generally produce a histogram that can be approximated by a line function:

$$\log_{10}(Y) = -(8/3) \log_{10}(X) + \log_{10}(4) \tag{9.5}$$

where Y is the number density and X is mixing ratio in g kg^{-1}. When this line function is plotted on the CIS histograms, there is significant area above the line indicating that CIS produces larger mixing ratios at more grid points than either of the MM5 simulations, with- or without-cloud insertion.

CIS produces far more high ice mixing ratios than either MM5 simulation. The range of maximum mixing ratios are narrow, only 1.0 to 2.1 g kg^{-1}. Maximum CIS values are generally higher than maximum MM5 values. Approximately 0.8% of the CIS domain grid points have mixing ratios larger than 0.1 g kg^{-1}. The without-cloud simulations have half that amount or 0.4%, and the with-cloud simulations have only 0.5%.

When comparing frequency distributions between domain 2 and domain 3, there are no significant differences among the histograms; therefore, ice frequency distribution is possibly insensitive to grid scale. Because the Grell convection scheme used on domain 2 does not produce cloud liquid water or cloud ice, these two water species should not show significant differences in distribution pattern among the MM5 data sets except due to variation in sampling.

3) RAIN MIXING RATIO HISTOGRAMS

(Figures 9.16a and b). The MM5 log-frequency distributions produce decreasing and linear histograms with lowest frequency at highest rain mixing ratio. The analysis histograms are flatter and extend to mixing ratios nearly twice as high as do the MM5 histograms. There were no significant differences in histogram shape among the MM5 simulations with or without cloud insertion.

Maximum mixing ratios vary wildly among the data samples ranging from 4.3 to 19.2 g kg^{-1}. Maximum CIS values are always higher than maximum MM5 values. CIS rain occurs more frequently at higher mixing ratios than MM5 rain. An average of 6.2% of the CIS grid points have mixing ratios larger than 0.1 g kg^{-1}. For MM5 simulations without cloud insertion, only 1.7% has these higher values. MM5 simulations with cloud insertion produce nearly twice that fraction of large mixing ratios, 2.6%, but still less than half as much as CIS. Large differences in frequency distribution pattern are observed between domain 2 and domain 3 only for the analysis; however, large differences in frequency distribution between domains may be due to sampling variance instead of sensitivity to grid scale.

4) SNOW MIXING RATIO HISTOGRAMS

(Figures 9.17a and b). Similar to patterns for ice, there were generally two types of snow distribution pattern. The first type found for the MM5 simulations is a log-frequency distribution that produces decreasing and linear histograms with lowest frequency at highest snow mixing ratio. These distributions stretch out to snow mixing ratio values on the order of 5.0 g kg^{-1} on domain 2 and on the order of 3.0 g kg^{-1} on domain 3. The analysis histogram is not as smooth and continuous as the MM5 histograms, and it appears nearly bimodal with a peak at 4.0 g kg^{-1}. There is very good agreement in histogram shape among the MM5 simulations.

Maximum mixing ratios varied moderately among the simulations. The range of maximum mixing ratios ranged from 2.3 to 6.9 g kg^{-1}. Maximum CIS values were not necessarily higher than maximum MM5 values. Among the analysis histograms for the analysis and the MM5 simulations without-cloud insertion, an average of 2.3% of the grid points have mixing ratios larger than 0.1 g kg^{-1}. Among the histograms for the MM5 simulation with cloud insertion, an average of 2.9% of the grid points have mixing ratios larger than 0.1 g kg^{-1}. CIS snow occurs more frequently at higher mixing ratios than MM5 snow.
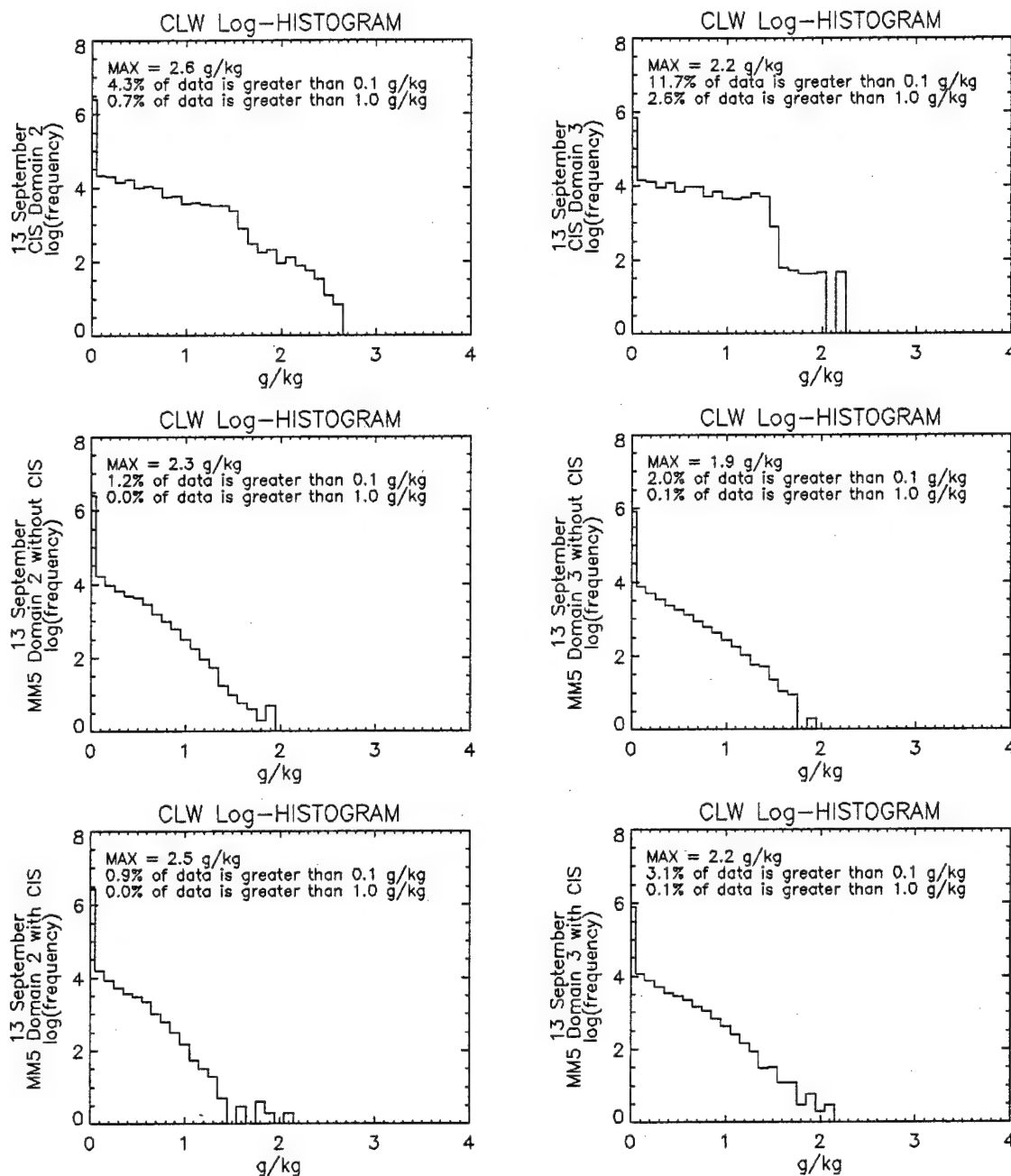
Figure 9.14a. Log-frequency histograms of cloud liquid water mixing ratio [g kg⁻¹] sampled from CIS, the MM5 simulation without cloud initialization, and the MM5 simulation with cloud initialization, at forecast hours +3 to +24 in 3-hourly intervals for the 13 September 2000 case. Domain 2 histograms are in the left column; domain 3 histograms are in the right column.
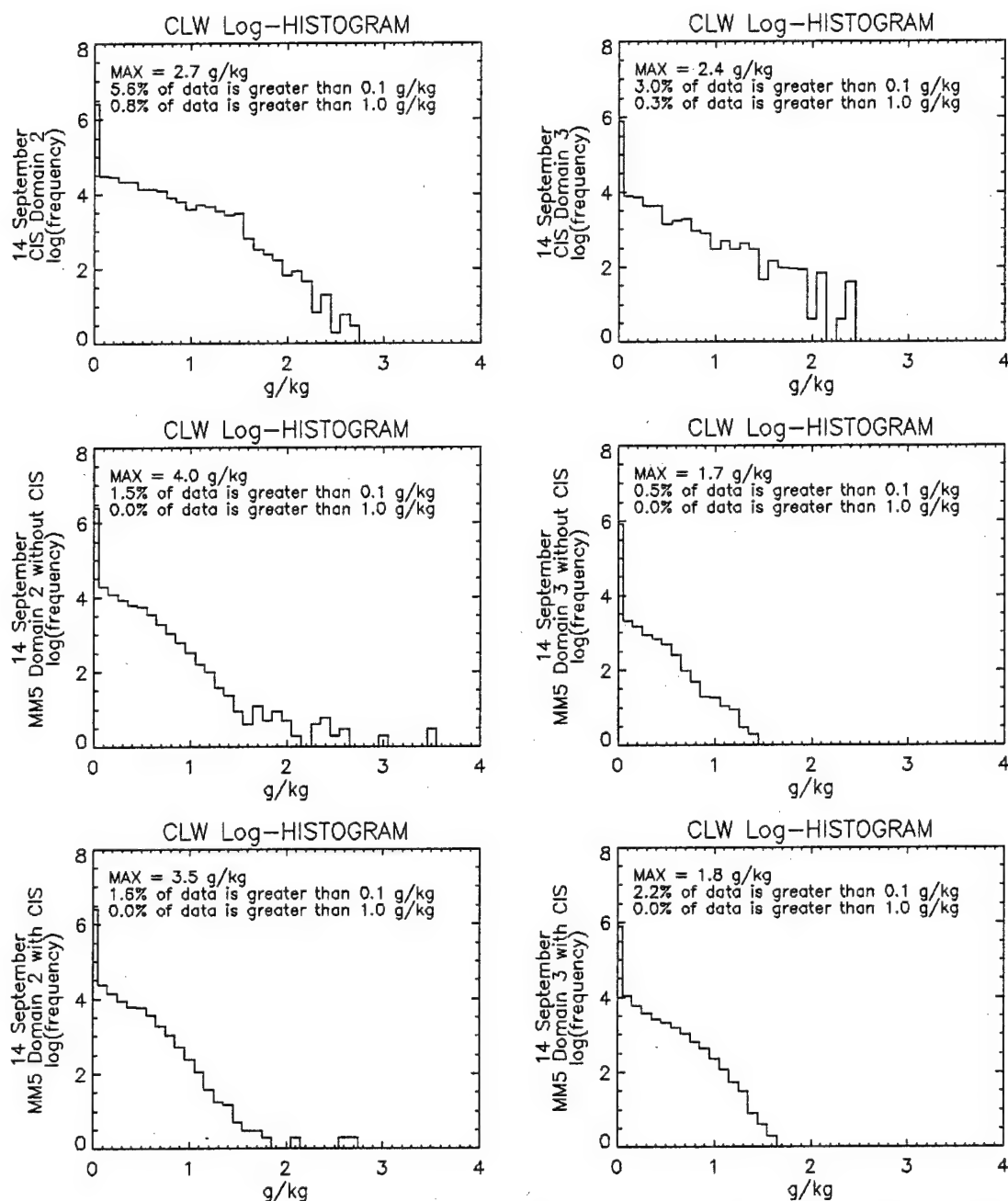
Figure 9.14b. Log-frequency histograms of cloud liquid water mixing ratio [g kg^{-1}] sampled from CIS, the MM5 simulation without cloud initialization, and the MM5 simulation with cloud initialization, at forecast hours +3 to +24 in 3-hourly intervals for the 14 September 2000 case. Domain 2 histograms are in the left column; domain 3 histograms are in the right column.
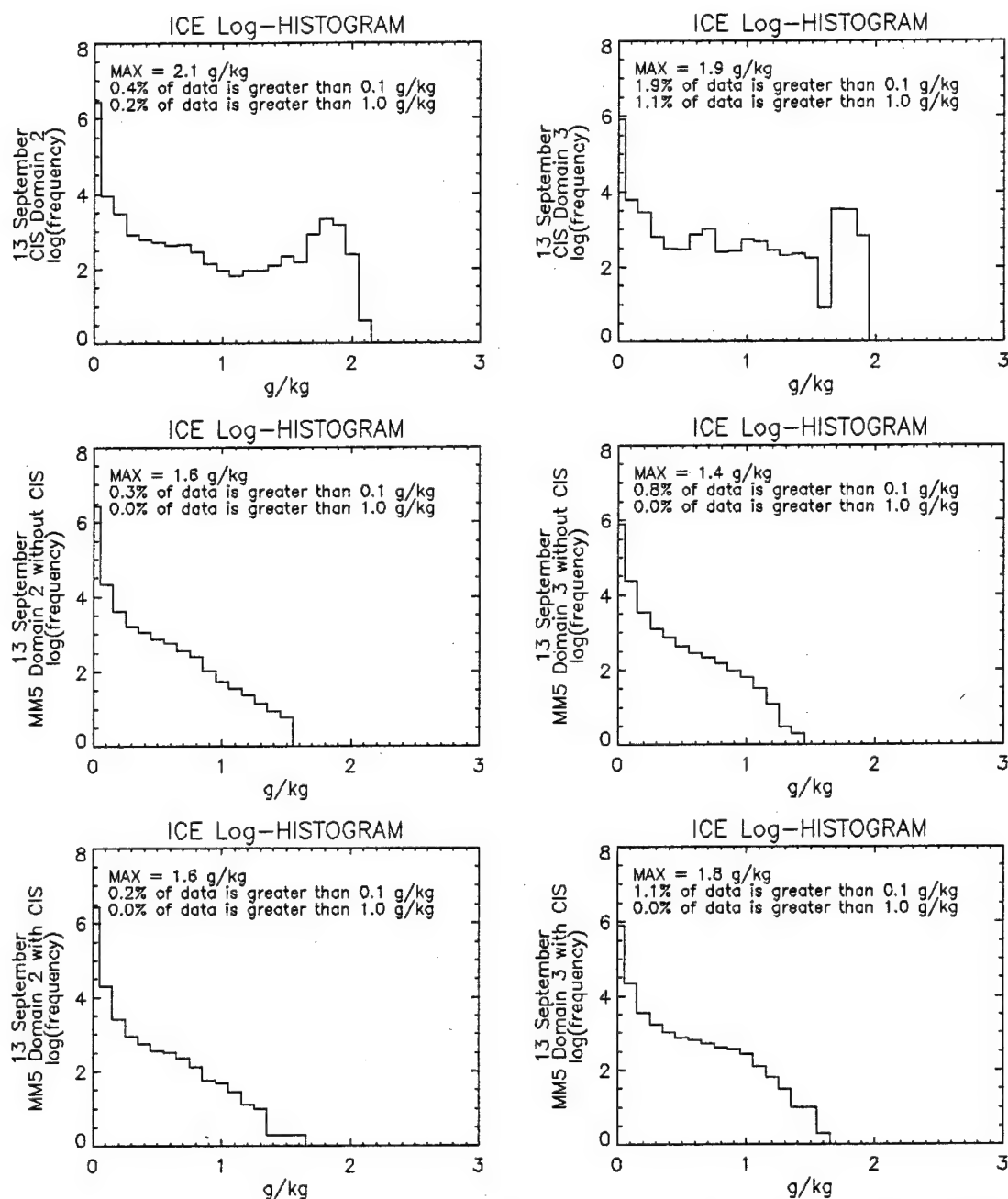
Figure 9.15a. Log-frequency histograms of cloud ice mixing ratio [g kg⁻¹] sampled from CIS, the MM5 simulation without cloud initialization, and the MM5 simulation with cloud initialization, at forecast hours +3 to +24 in 3-hourly intervals for the 13 September 2000 case. Domain 2 histograms are in the left column; domain 3 histograms are in the right column.
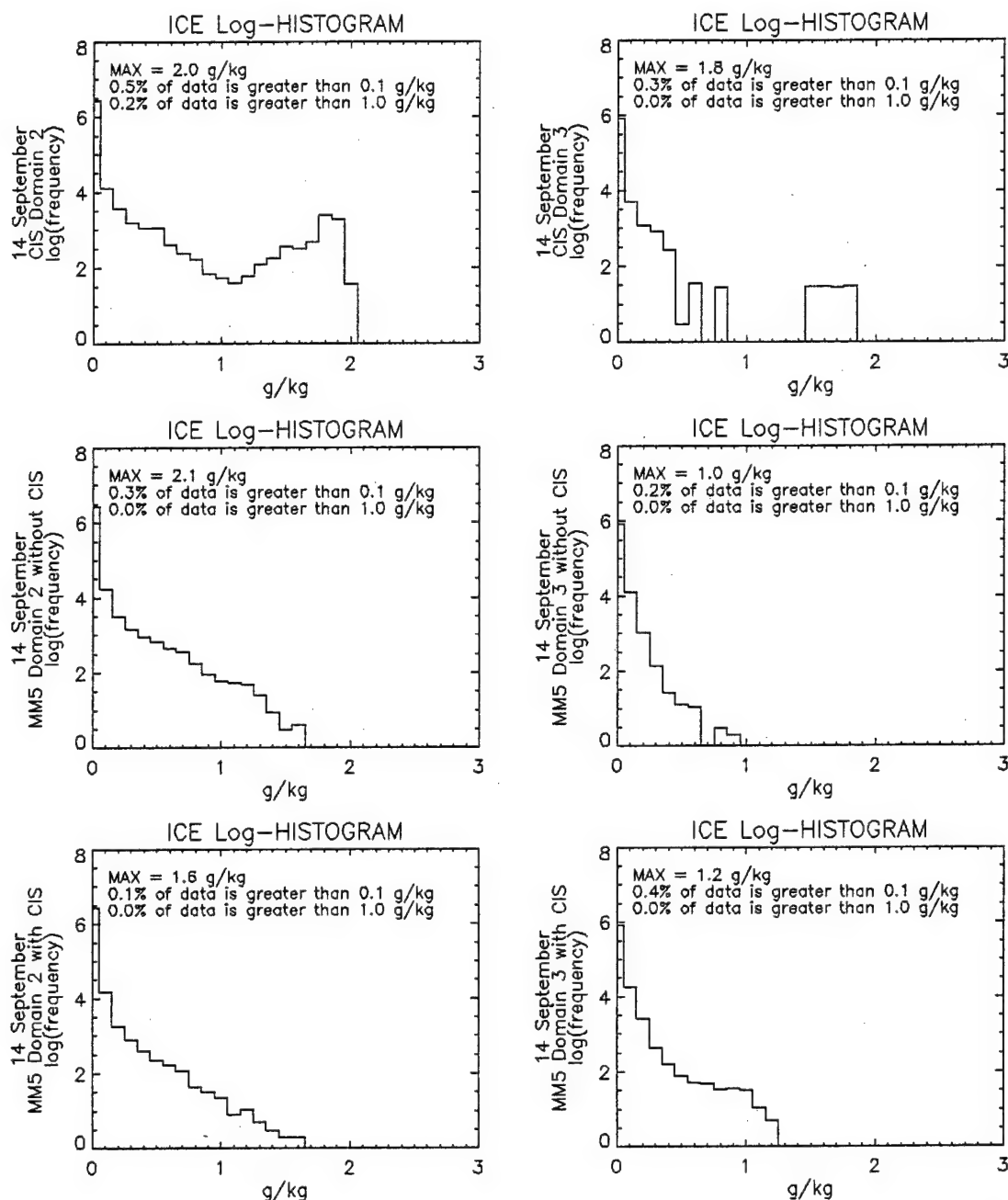
Figure 9.15b. Log-frequency histograms of cloud ice mixing ratio [g kg⁻¹] sampled from CIS, the MM5 simulation without cloud initialization, and the MM5 simulation with cloud initialization, at forecast hours +3 to +24 in 3-hourly intervals for the 14 September 2000 case. Domain 2 histograms are in the left column; domain 3 histograms are in the right column.
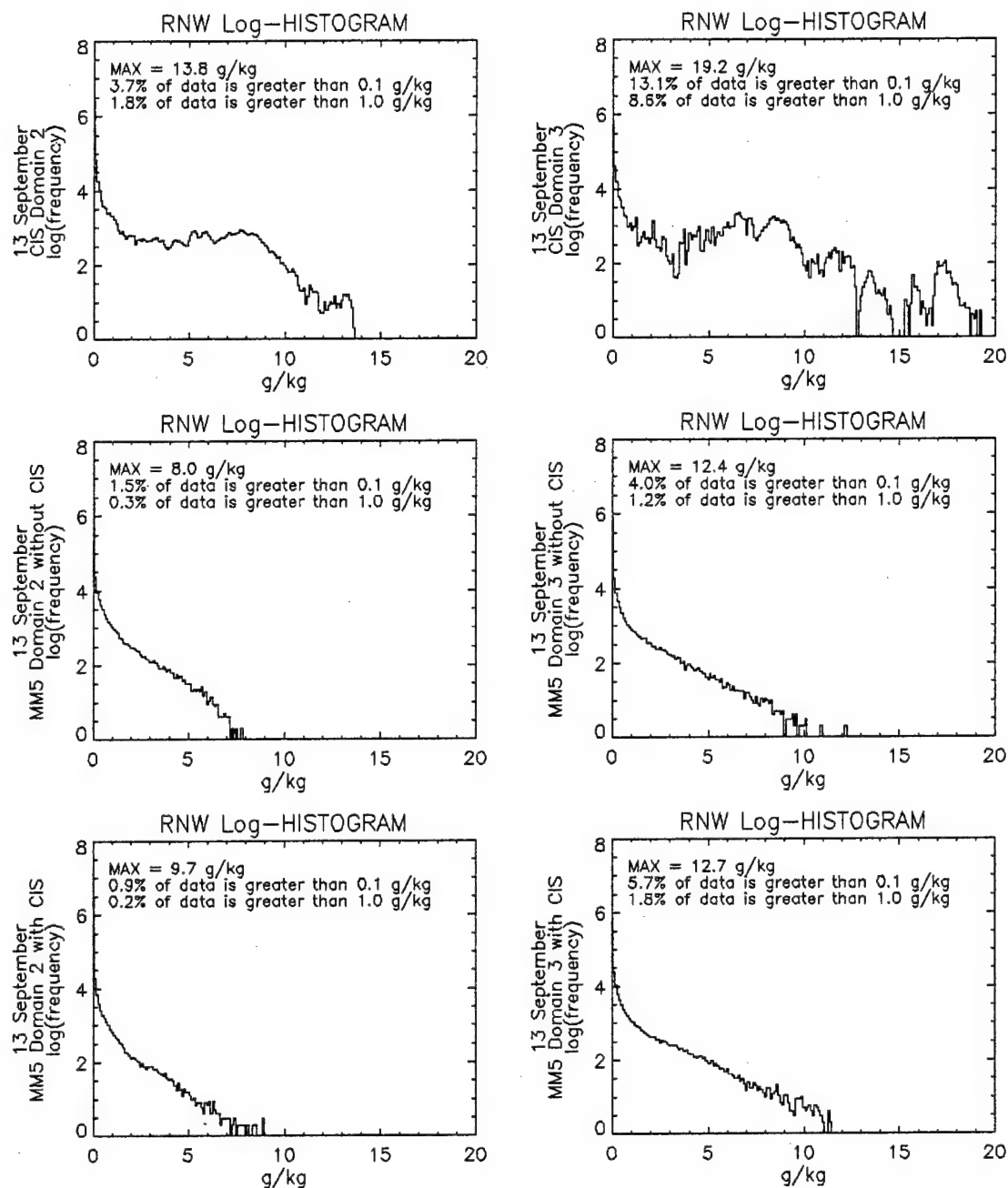
Figure 9.16a. Log-frequency histograms of rain mixing ratio [g kg⁻¹] sampled from CIS, the MM5 simulation without cloud initialization, and the MM5 simulation with cloud initialization, at forecast hours +3 to +24 in 3-hourly intervals for the 13 September 2000 case. Domain 2 histograms are in the left column; domain 3 histograms are in the right column.
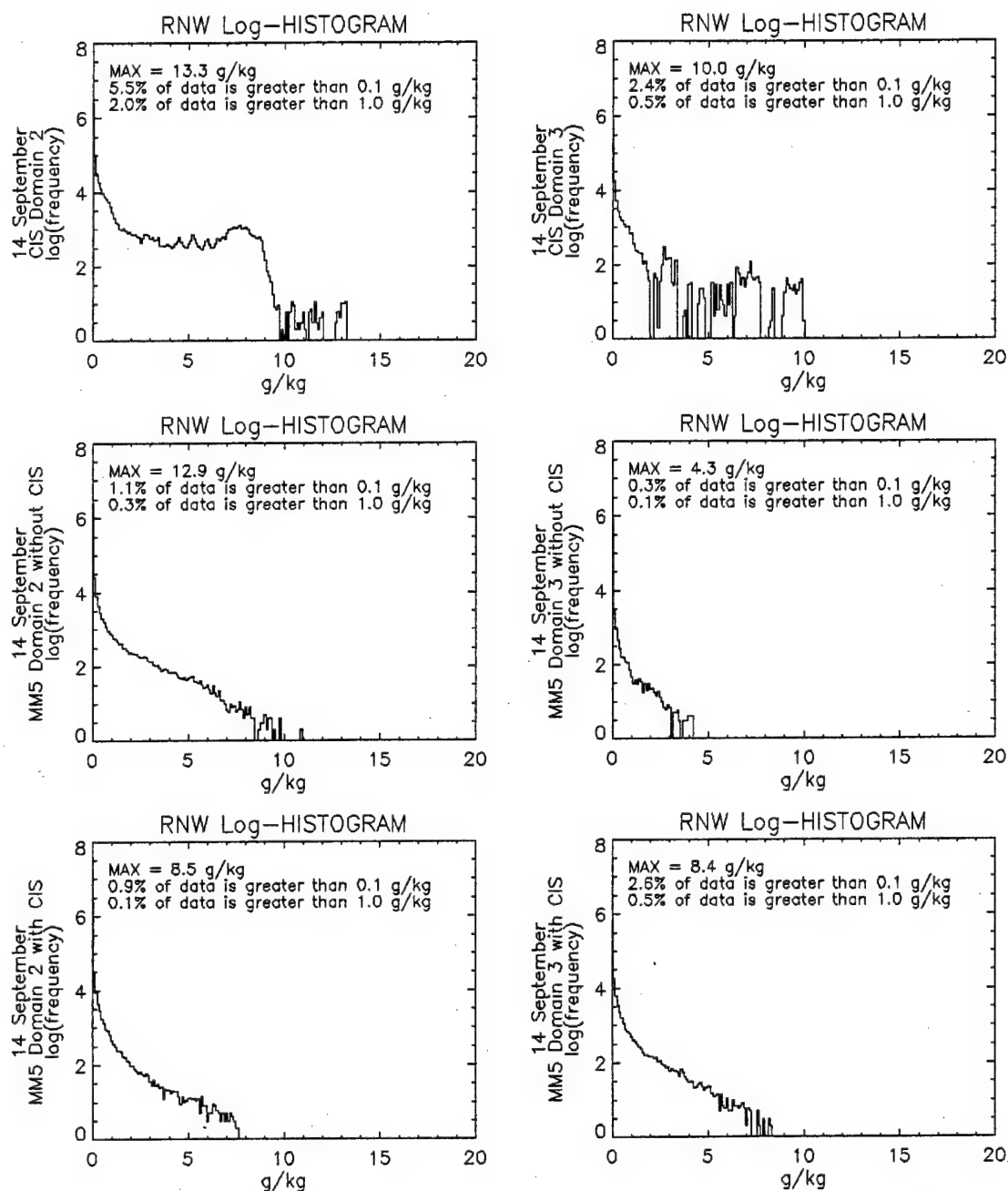
Figure 9.16b. Log-frequency histograms of rain mixing ratio [g kg^{-1}] sampled from CIS, the MM5 simulation without cloud initialization, and the MM5 simulation with cloud initialization, at forecast hours +3 to +24 in 3-hourly intervals for the 14 September 2000 case. Domain 2 histograms are in the left column; domain 3 histograms are in the right column.
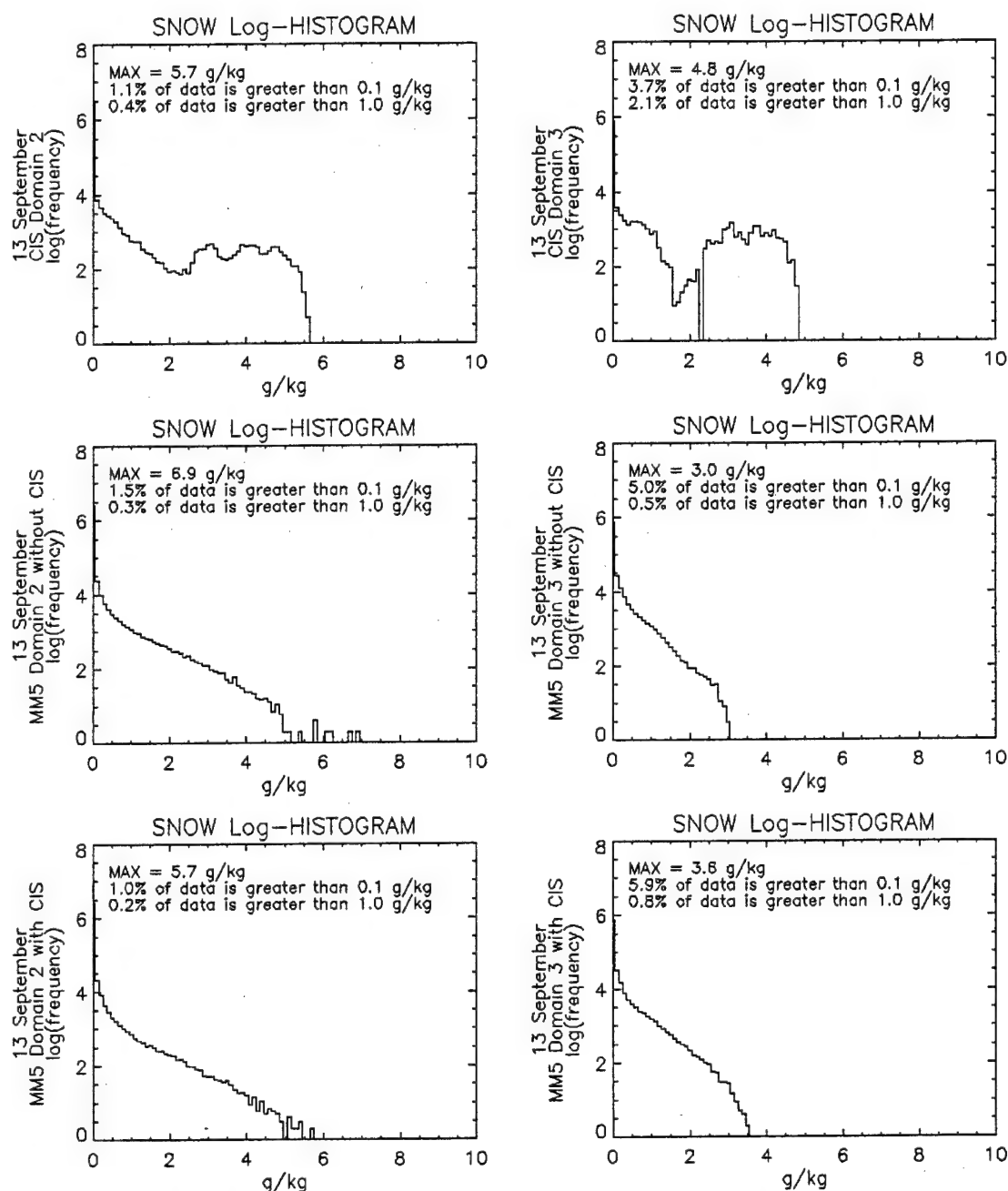
Figure 9.17a. Log-frequency histograms of snow mixing ratio [g kg⁻¹] sampled from CIS, the MM5 simulation without cloud initialization, and the MM5 simulation with cloud initialization, at forecast hours +3 to +24 in 3-hourly intervals for the 13 September 2000 case. Domain 2 histograms are in the left column; domain 3 histograms are in the right column.
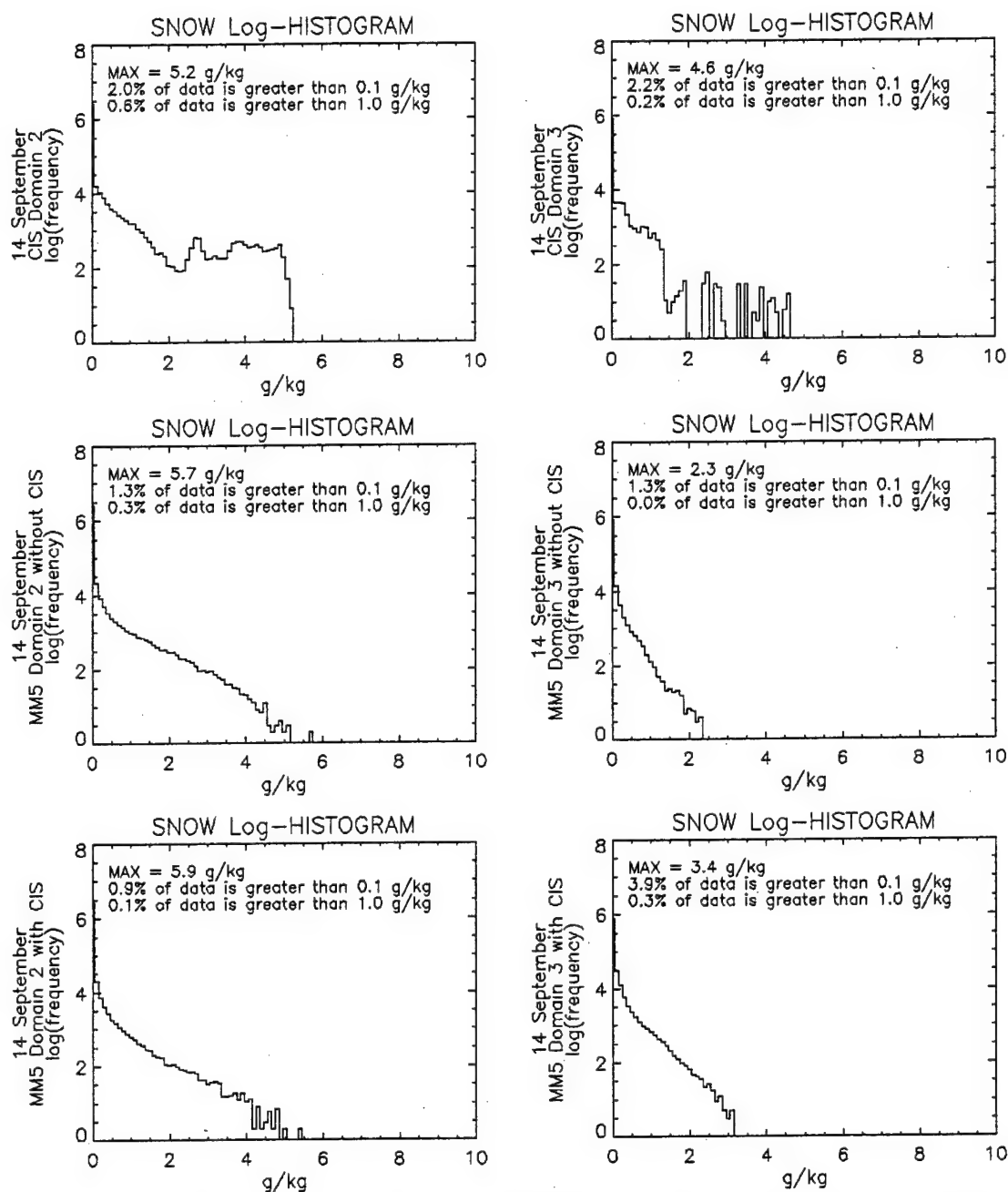
Figure 9.17b. Log-frequency histograms of snow mixing ratio [g kg^{-1}] sampled from CIS, the MM5 simulation without cloud initialization, and the MM5 simulation with cloud initialization, at forecast hours +3 to +24 in 3-hourly intervals for the 14 September 2000 case. Domain 2 histograms are in the left column; domain 3 histograms are in the right column.

b. Average domain mixing ratios

Another gross description of cloudiness is the average mixing ratio among all clouds in the domain. An examination of how average mixing ratio varies in time tells us how dramatically domain cloudiness changes during the evolution of weather. Average domain mixing ratios (Figures 9.18 through 9.21) are computed from only among those grid points containing a non-vapor water species having a non-zero mixing ratio. Average domain mixing ratios of cloud liquid water, cloud ice, rain, and snow from CIS are larger and vary substantially more with time than average domain mixing ratios produced by any of the MM5 simulations. Differences between CIS and MM5 average mixing ratios are larger for precipitation variables (rain and snow) than they are for cloud variables (cloud liquid water and cloud ice).

A significant feature of these plots is the tendency of the model to reach a quasi-static average mixing ratio value. During the dynamic initialization phase of the simulations (forecast hours -06 to +00), MM5 simulations without cloud insertion take longer to reach a quasi-static average mixing ratio. MM5 simulations with cloud insertion reach that level almost immediately. No similarly well-defined quasi-equilibrium value is obtained for the CIS average mixing ratios. Spikes in the with-cloud simulations show that although relatively very large average mixing ratios are inserted, the model equilibrates within minutes to the lower quasi-static level. Subsequent insertion at forecast hour +00 has little effect in altering the quasi-static level. This behavior is the same for all cloud and precipitation variables. It is not clear whether the greater temporal variability in average mixing ratios for domain 3 than for domain 2 indicates scale dependence or spatial sampling variability.
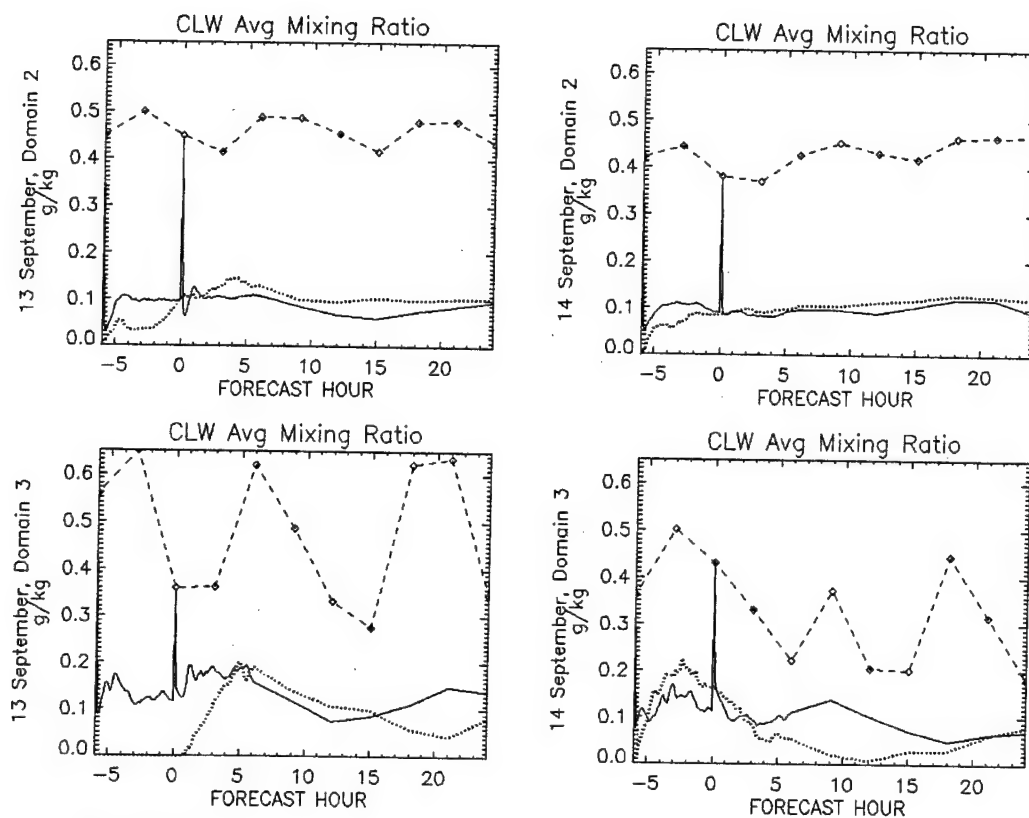
Figure 9.18. Cloud liquid water average mixing ratio, forecast hours -06 to +24, domains 2 and 3, 13 and 14 September 2000 simulations. Dashed line indicates cloud analysis, solid line indicates MM5 simulation with cloud insertion, and dotted line indicates MM5 simulation without cloud insertion. Diamonds indicate 3-hourly analysis times.
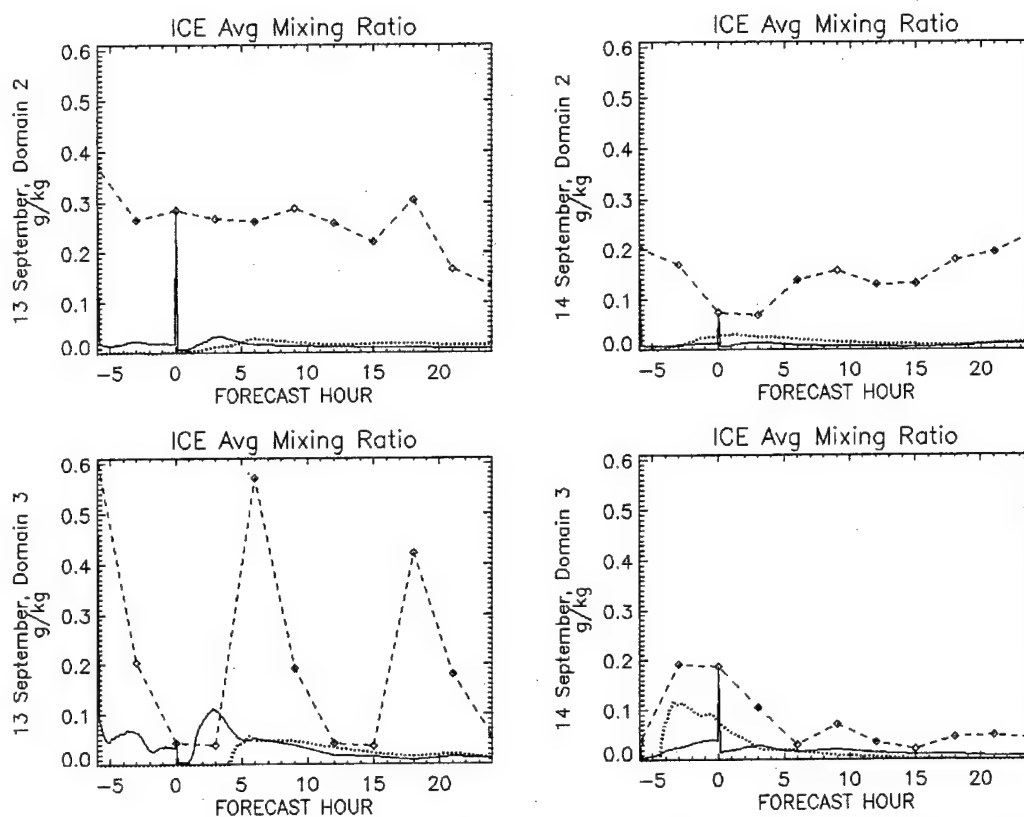
Figure 9.19. Cloud ice average mixing ratio, forecast hours -06 to +24, domains 2 and 3, 13 and 14 September 2000 simulations. Dashed line indicates cloud analysis, solid line indicates MM5 simulation with cloud insertion, and dotted line indicates MM5 simulation without cloud insertion. Diamonds indicate 3-hourly analysis times.
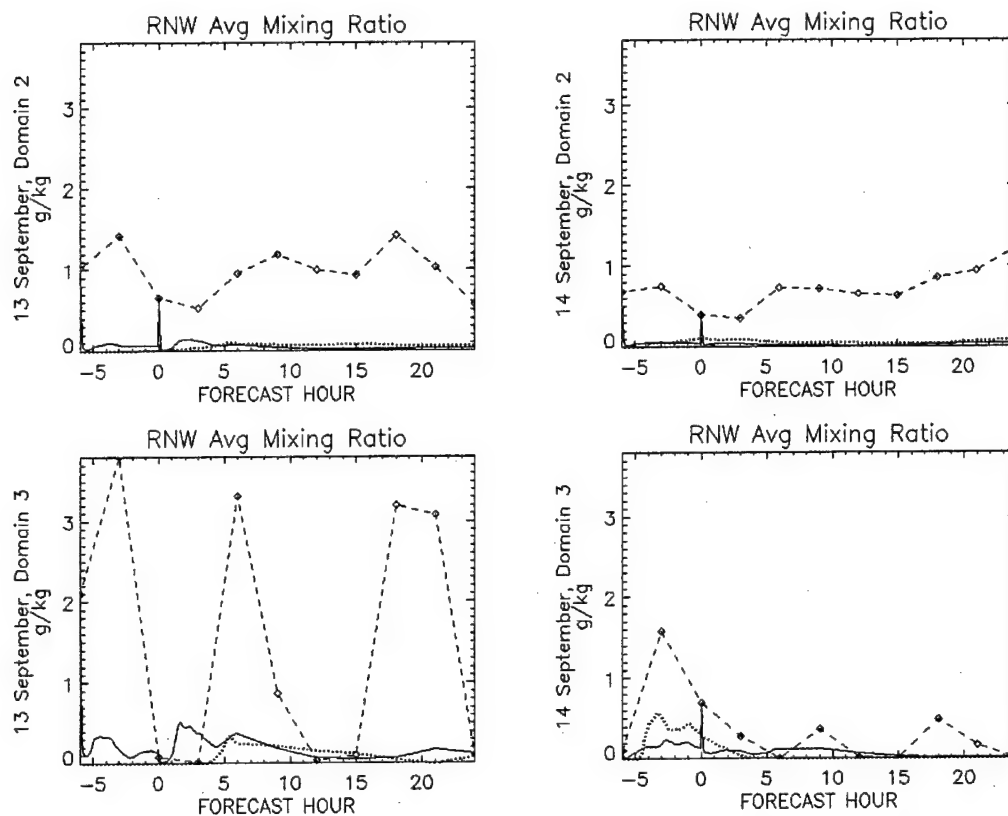
Figure 9.20. Rain average mixing ratio, forecast hours -06 to +24, domains 2 and 3, 13 and 14 September 2000 simulations. Dashed line indicates cloud analysis, solid line indicates MM5 simulation with cloud insertion, and dotted line indicates MM5 simulation without cloud insertion. Diamonds indicate 3-hourly analysis times.
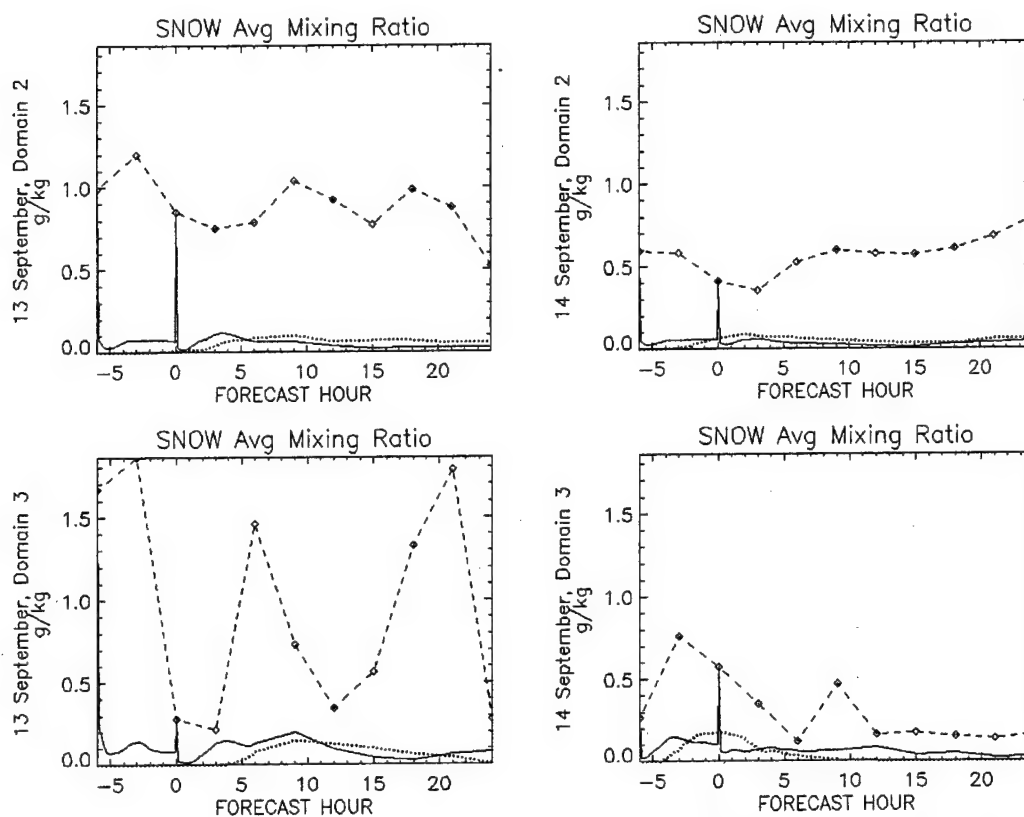
Figure 9.21. Snow average mixing ratio, forecast hours -06 to +24, domains 2 and 3, 13 and 14 September 2000 simulations. Dashed line indicates cloud analysis, solid line indicates MM5 simulation with cloud insertion, and dotted line indicates MM5 simulation without cloud insertion. Diamonds indicate 3-hourly analysis times.

Spin-up in average mixing ratio is apparent for the no-cloud simulations on both domains. The time to reach equilibration in average mixing ratio varied between 2 and 14 hours among the samples. The rapid equilibration of mixing ratio may be largely attributed to advection and diffusion of a discrete mixing ratio at a grid point to three of four of its neighboring grid points. Section 9.3.d later demonstrates the cloud analysis produces a cloud distribution that is more discrete than the distribution produced by MM5. This difference in discreteness is a likely cause of the rapid changes in average mixing ratio after direct insertion. Since the average mixing ratio is computed only among those points with a non-zero mixing ratio, the average value rapidly decreases as even the tiniest mixing ratio is distributed to neighboring grid points. Consider an initially cloudy grid point with some initial cloud liquid water mixing ratio surrounded by eight cloud-free grid points. The initial average mixing ratio computed among these nine grid points is the initial amount because the averaging method used here excludes non-cloudy grid points. If the cloud liquid water is slightly advected or diffused to three neighboring grid points in subsequent time steps, barring all other source or sink processes, the average mixing ratio becomes a fourth of the initial value.

c. Domain mixing ratio standard deviation

Another gross description of cloudiness is the mixing ratio standard deviation among all the clouds in the domain. Small standard deviations indicate homogeneity among the population of clouds, while large standard deviations indicate inhomogeneity. Just as average domain mixing ratio reaches a quasi-equilibrium value, so too does mixing ratio standard deviation. Mixing ratio standard deviation is computed only among those grid points containing a non-zero mixing ratio and plotted in Figures 9.22 through 9.25. For the without-cloud insertion simulations, spin-up times for the standard deviation of mixing ratio are the same as those for average mixing ratio. CIS mixing ratio standard deviations are larger and vary substantially more with time than MM5 values of mixing ratio standard deviation. During the dynamic initialization phase of the simulations (forecast hours -06 to +00), simulations without cloud insertion take longer to reach a quasi-static standard deviation. No similar well-defined quasi-equilibrium value is obtained for the analyzed standard deviations. Simulations with cloud insertion reach that level almost immediately. Spikes in the with-cloud simulations show that although relatively very large mixing ratio variances are inserted, the model equilibrates within minutes to the quasi-static level. Subsequent insertion at forecast hour +00 has little effect in altering the quasi-static level. This behavior is the same for all cloud and precipitation variables. Although the temporal variability in mixing ratio standard deviation is greater for domain 3 than for domain 2, it is not clear whether this indicates scale dependence or spatial sampling variability.
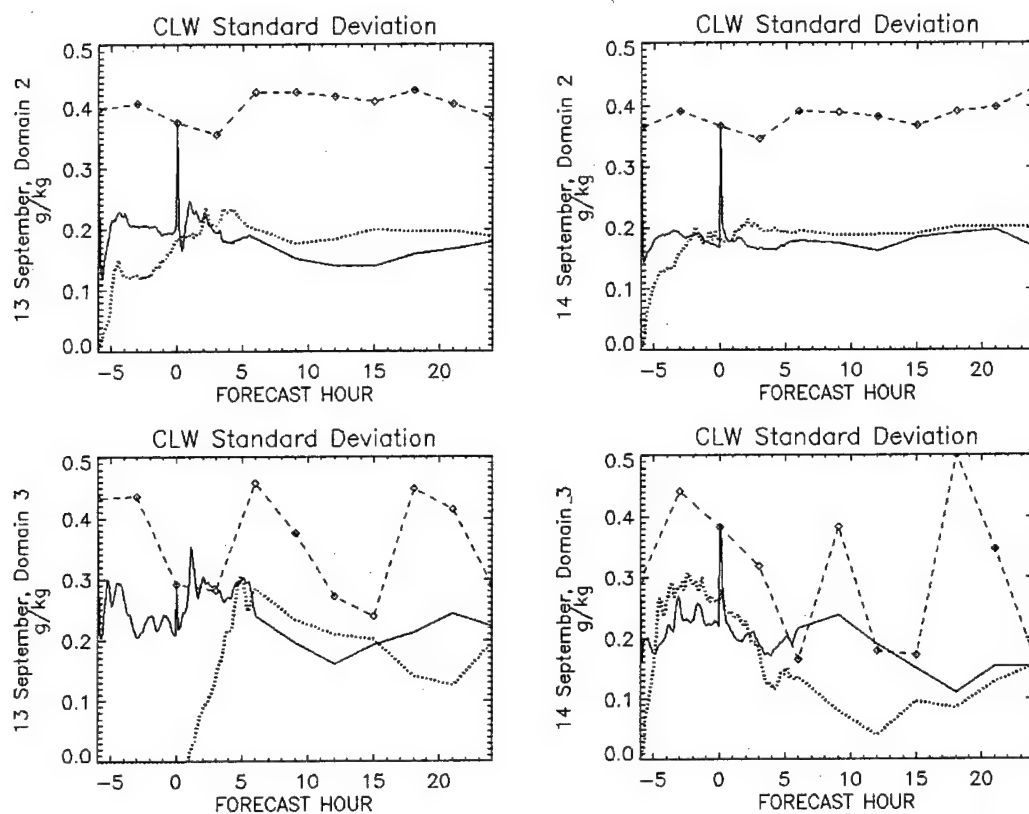
Figure 9.22. Cloud liquid water mixing ratio standard deviation, forecast hours -06 to +24, domains 2 and 3, 13 and 14 September 2000 simulations. Dashed line indicates cloud analysis, solid line indicates MM5 simulation with cloud insertion, and dotted line indicates MM5 simulation without cloud insertion. Diamonds indicate 3-hourly analysis times.
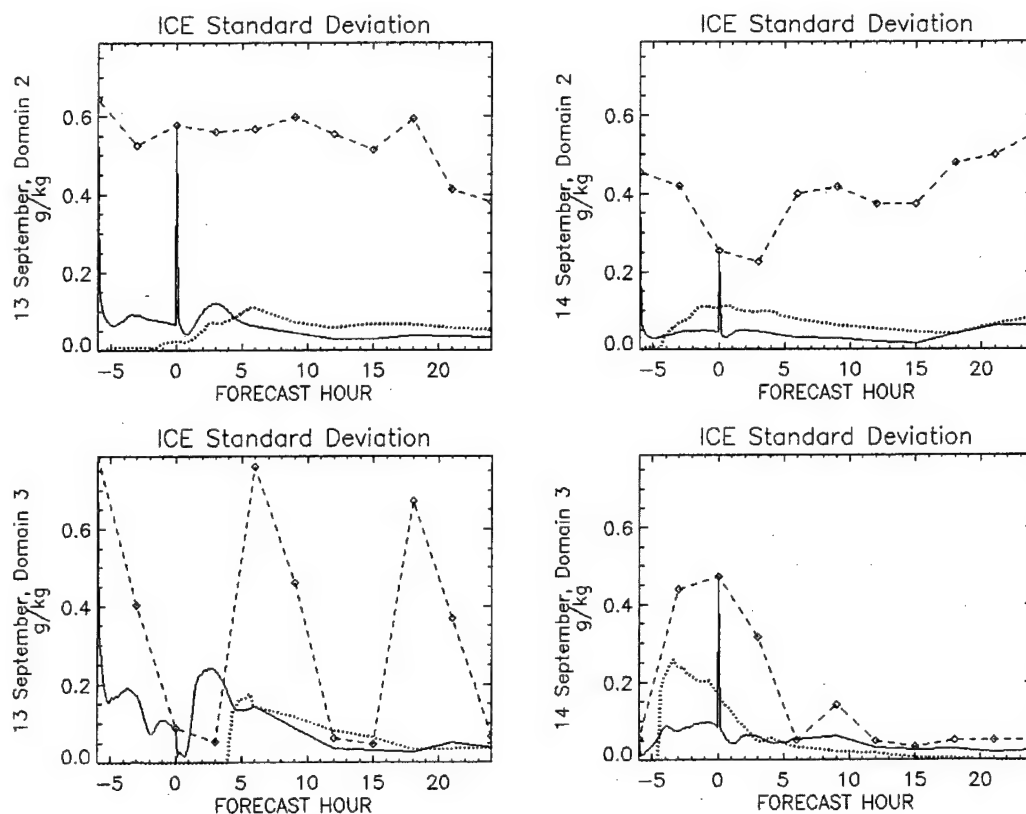
Figure 9.23. Cloud ice mixing ratio standard deviation, forecast hours -06 to +24, domains 2 and 3, 13 and 14 September 2000 simulations. Dashed line indicates cloud analysis, solid line indicates MM5 simulation with cloud insertion, and dotted line indicates MM5 simulation without cloud insertion. Diamonds indicate 3-hourly analysis times.
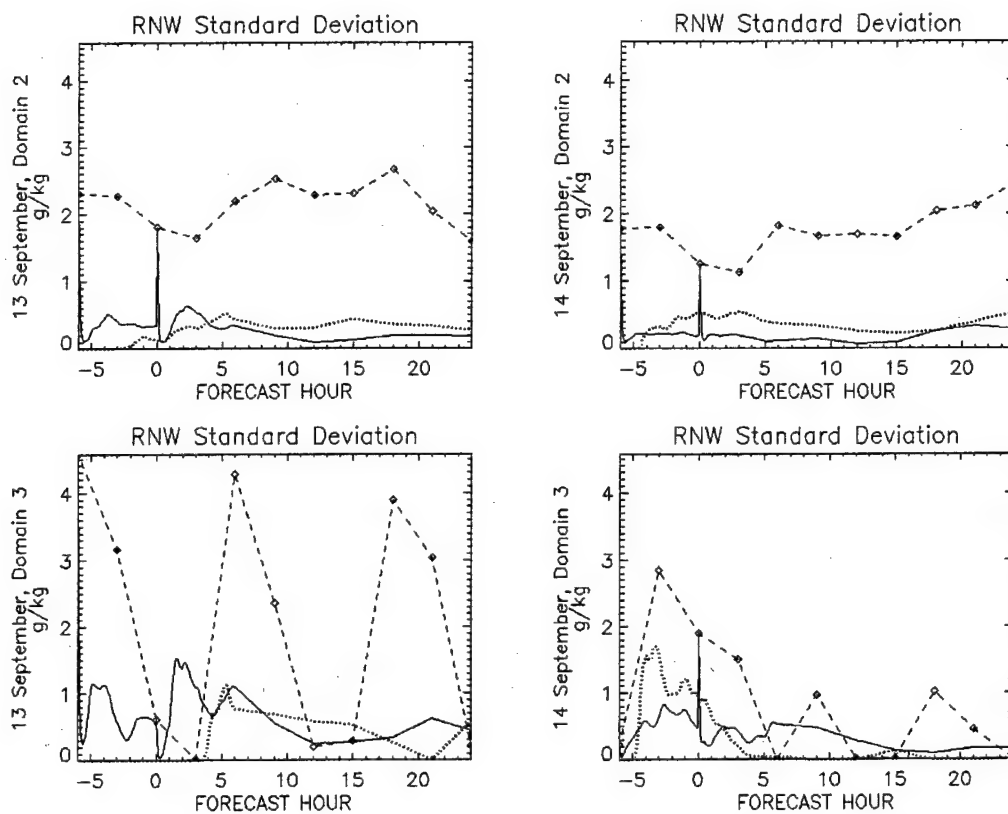
Figure 9.24. Rain mixing ratio standard deviation, forecast hours -06 to +24, domains 2 and 3, 13 and 14 September 2000 simulations. Dashed line indicates cloud analysis, solid line indicates MM5 simulation with cloud insertion, and dotted line indicates MM5 simulation without cloud insertion. Diamonds indicate 3-hourly analysis times.
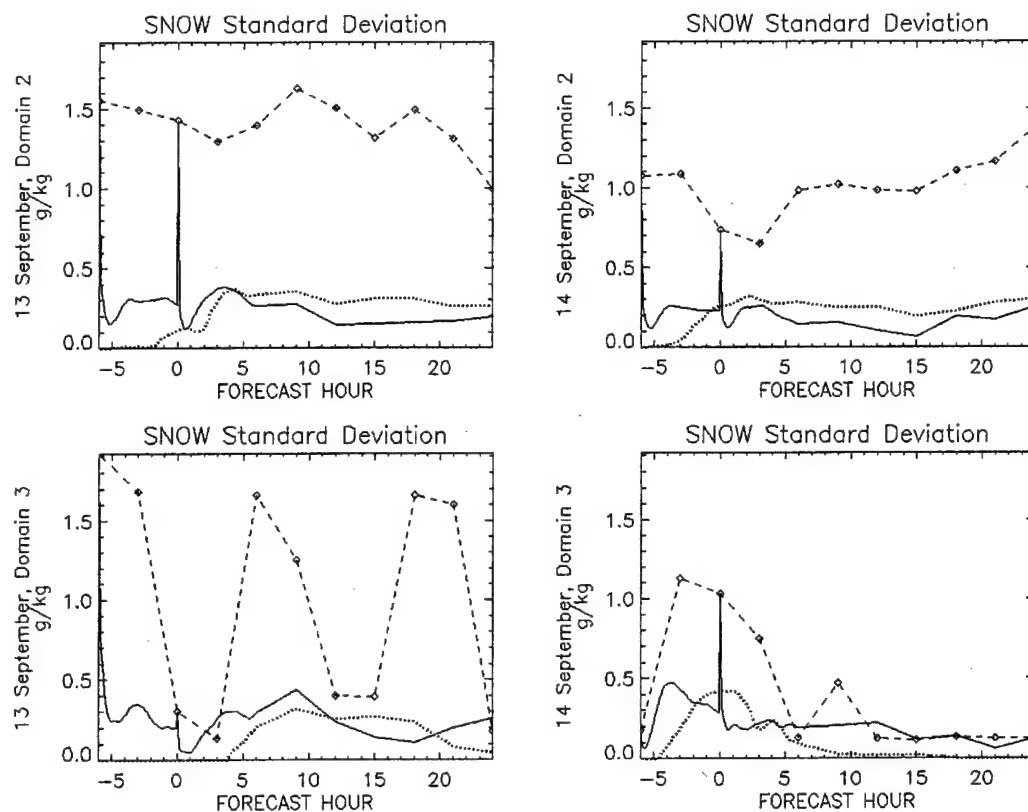
Figure 9.25. Snow mixing ratio standard deviation, forecast hours -06 to +24, domains 2 and 3, 13 and 14 September 2000 simulations. Dashed line indicates cloud analysis, solid line indicates MM5 simulation with cloud insertion, and dotted line indicates MM5 simulation without cloud insertion. Diamonds indicate 3-hourly analysis times.

d. Mixing ratio percent coverage

The final gross mixing ratio characteristic examined here is percent cloud coverage amount. The fraction of domain grid points containing a non-zero mixing ratio is plotted in Figures 9.26 through 9.29. Domain 2 contains 333,431 grid points and domain 3 contains 103,247 grid points. Quasi-steady values of percent coverage appear in the plots just as they did for average mixing ratio and standard deviation. Domain 2 cloud liquid water and rain have very similar quasi-steady percent coverage amounts among the analyses and the simulations. Domain 2 ice and snow simulated values vary slowly and are larger than the quasi-static analyzed values. Domain 3 percent coverage amounts are generally larger than domain 2 amounts. Percent coverage for the domain 3 simulations generally follows similar patterns with time regardless of cloud insertion, but the with-cloud insertion simulations usually have larger percent coverage. This is also apparent on domain 2. One reason for this is that the simulations produce rain and snow on more levels than they are analyzed by CIS (see Figures 9.7 and 9.8).

Initially, cloud insertion greatly alters the number of grid points containing cloud and precipitation. The model has two interesting but dramatic responses to cloud insertion shock. When cloud insertion results in a larger percent coverage, the simulation adopts the higher percent coverage as its new equilibrium level. Conversely, when cloud insertion results in a lower percent coverage, the simulation rapidly increases percent coverage, overshoots its equilibrium level, and then slowly drops back down. The increases in simulated percent coverage are roughly what would be expected by horizontal diffusion to three neighboring grid points from the position of a discrete cloud. It is not clear if spin-up time of the no-cloud insertion simulations can be determined using percent coverage. The spin-up signal was much more dramatic in plots of domain mass, average domain mixing ratio, and domain mixing ratio variance.
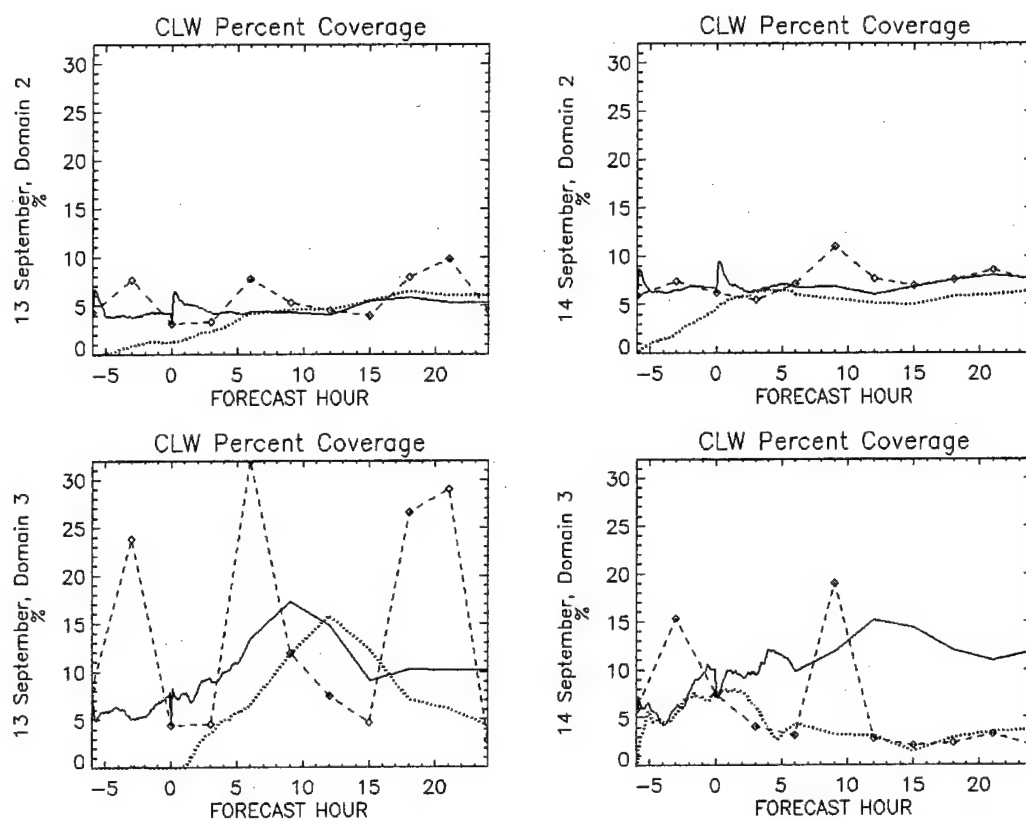
Figure 9.26. Cloud liquid water percent coverage, forecast hours -06 to +24, domains 2 and 3, 13 and 14 September 2000 simulations. Dashed line indicates cloud analysis, solid line indicates MM5 simulation with cloud insertion, and dotted line indicates MM5 simulation without cloud insertion. Diamonds indicate 3-hourly analysis times.
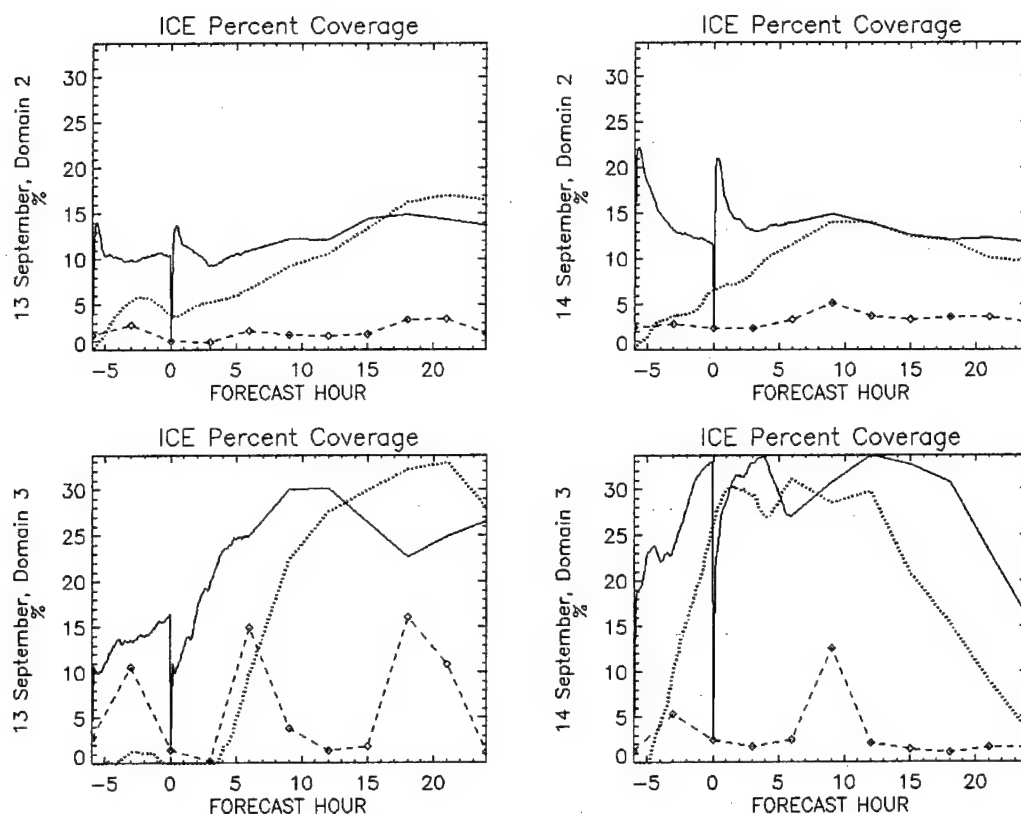
Figure 9.27. Cloud ice percent coverage, forecast hours -06 to +24, domains 2 and 3, 13 and 14 September 2000 simulations. Dashed line indicates cloud analysis, solid line indicates MM5 simulation with cloud insertion, and dotted line indicates MM5 simulation without cloud insertion. Diamonds indicate 3-hourly analysis times.
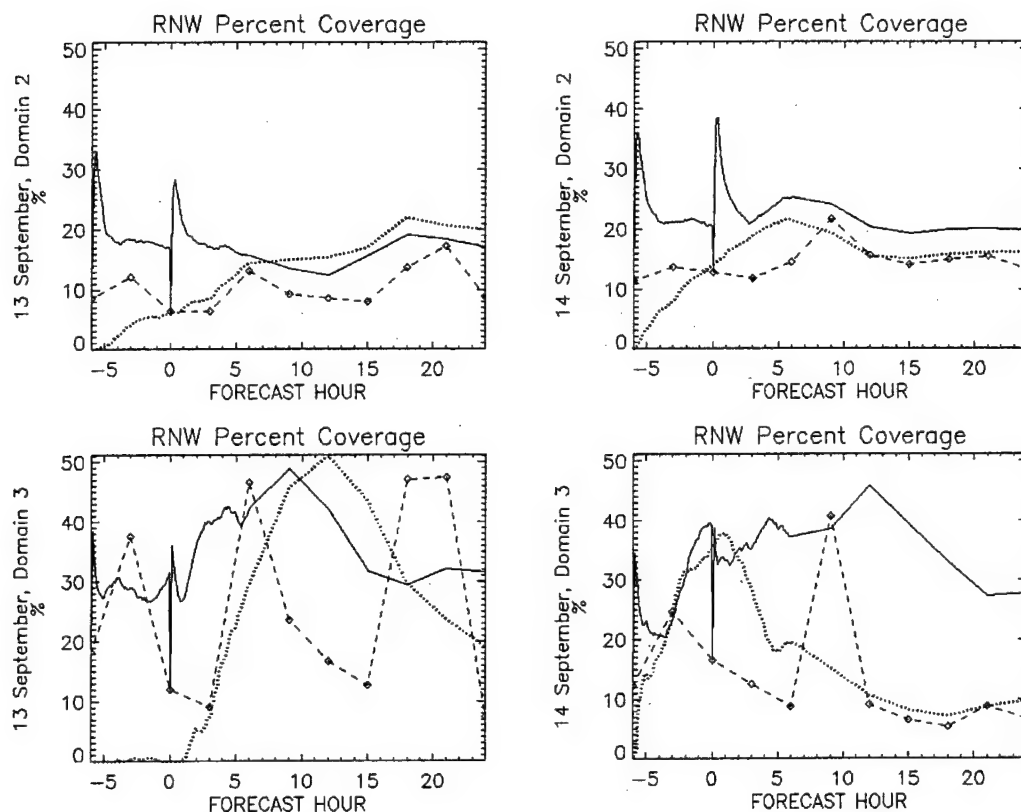
Figure 9.28. Rain percent coverage, forecast hours -06 to +24, domains 2 and 3, 13 and 14 September 2000 simulations. Dashed line indicates cloud analysis, solid line indicates MM5 simulation with cloud insertion, and dotted line indicates MM5 simulation without cloud insertion. Diamonds indicate 3-hourly analysis times.
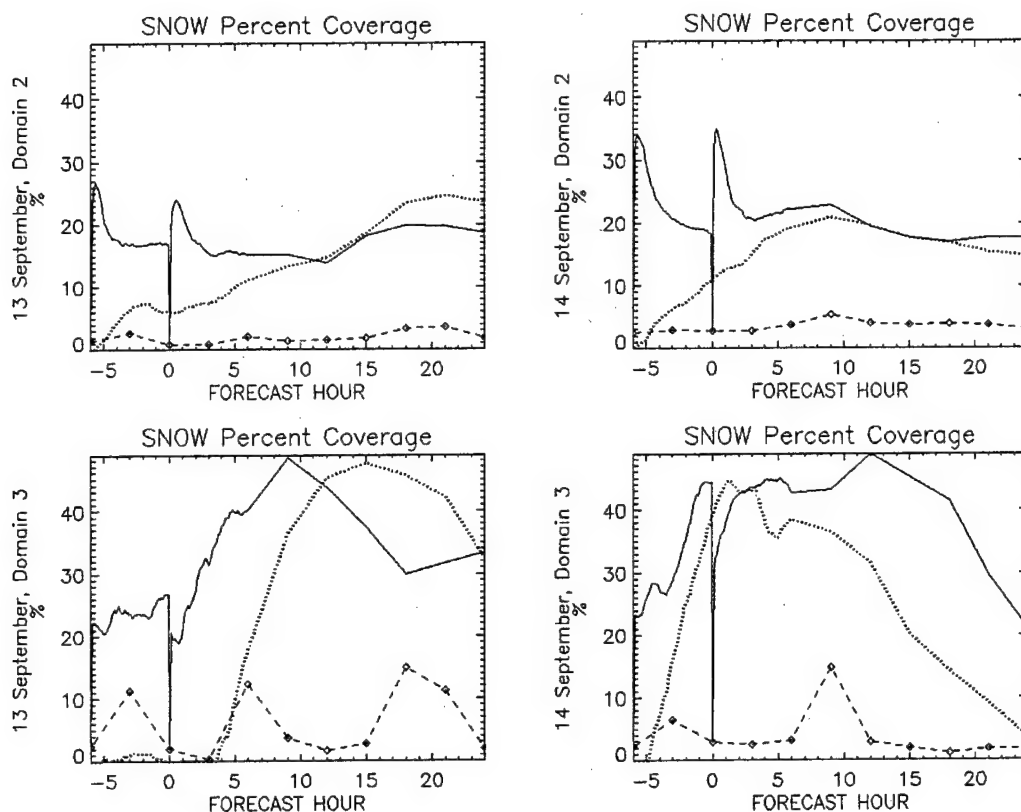
Figure 9.29. Snow percent coverage, forecast hours -06 to +24, domains 2 and 3, 13 and 14 September 2000 simulations. Dashed line indicates cloud analysis, solid line indicates MM5 simulation with cloud insertion, and dotted line indicates MM5 simulation without cloud insertion. Diamonds indicate 3-hourly analysis times.

In summary, the preceding paragraphs presented that CIS values of total domain mass, domain average mixing ratio, and domain mixing ratio standard deviation are larger than any of the MM5 simulation values regardless of whether the simulation had cloud insertion. Additionally, analyzed percent coverage is smaller than simulated percent coverage. From this we can only conclude that CIS mixing ratios have a larger measure of "discreteness" than MM5 mixing ratios. Additionally, CIS cloud and precipitation water is more likely to have higher mixing ratios at fewer grid points than MM5 cloud and precipitation water.

MM5 reduces the discrete characteristics of CIS cloud and precipitation after direct insertion. From this result, it is not clear whether the CIS analysis is overly discrete or whether the MM5 simulation results are not discrete enough. MM5 also appears to be relatively insensitive to the magnitude of cloud and precipitation mixing ratios inserted. At forecast hour +00, cloud insertion completely replaces model produced mixing ratios, yet minutes after cloud insertion, the equilibrium levels in average mixing ratio, standard deviation, and percent coverage equilibrate back to pre-insertion levels.

The main question still remaining is this: assuming the CIS cloud analysis represents the true distribution of clouds, how well does MM5 forecast clouds on a particular grid point? Point-level forecasting of clouds is of course the ultimate goal of cloud forecasting particularly for military operations. The following chapter attempts to answer that question with a local-scale validation analysis.

CHAPTER X
LOCAL ANALYSIS

10.1. Introduction

In the previous chapter, the first of two general classes of analyses was performed. The large-scale analysis examined metrics computed for an entire domain. Two categories of large-scale analyses were conducted: mass analysis and mixing ratio analysis. In this chapter, the second general class of analysis, or local-scale analysis, is presented. The local-scale analysis examines metrics computed on a grid point-to-grid point basis. Three categories of local-scale analyses are conducted: forecast skill scores, second moment statistics for various mixing ratios, and second moment statistics for cloud coverage amount. For each statistic, an index of improvement is also computed in an attempt to make an objective statement on whether cloud initialization improves the model's ability to match CIS-diagnosed cloud species mixing ratios. The following section describes how forecast skill scores are formulated and comments on their utility in classifying the skill of a cloud forecast. Section 10.3 describes the computation of second moment mixing ratio statistics, and section 10.4 describes the computation of second moment cloud coverage amount statistics. Finally, section 10.5 presents an analysis of results. Analysis data is too voluminous to be contained in the present chapter; however, a sample of the many tables analyzed in this study is included for illustrative purposes.

10.2. Forecast Skill Scores

Mixing ratios of cloud liquid water, cloud ice, rain, and snow produced from MM5 are compared to coincident mixing ratios analyzed from RTNEPH using the cloud initialization scheme (CIS). The comparison involves classifying model output as a dichotomous forecast in which mixing ratio is or is not forecast to exceed a stated threshold. Analysis of a dichotomous forecast requires the use of forecast contingency tables.

a. Contingency table

Following Doswell et al. 1990, Table 10.1 defines the elements of the basic 2-by-2 contingency table associated with dichotomous forecasts. The contingency table is constructed by comparing mixing ratios at each grid point and time. For evaluating a mixing ratio at a given model coordinate, an event is defined as the occurrence of a mixing ratio above a stated threshold. A non-event is defined as the occurrence of a mixing ratio at or below a stated threshold. An observed event is a mixing ratio analyzed from RTNEPH clouds to the model grid point using CIS. A forecasted event is a mixing ratio greater than a stated threshold value that is produced by MM5.

Table 10.1. Four-cell contingency table.

		FORECASTS		
		YES	NO	TOTAL
EVENTS	YES	X	Y	$X + Y$
	NO	Z	W	$W + Z$
	TOTAL	$X + Z$	$Y + W$	$N = W + X + Y + Z$

W: number of non-event forecasts validated by a non-event
X: number of event forecasts validated by an event
Y: number of non-event forecasts invalidated by an event
Z: number of event forecasts invalidated by a non-event
N: total number of cases

Although forecast skill scores were developed for evaluating severe weather forecasts, they have utility for evaluating clouds forecast by mesoscale NWP models. Contingency tables are constructed for each cloud variable (cloud liquid water, cloud ice, rain, and snow) at seven mixing ratio thresholds. These thresholds are 0.00, 0.05, 0.10, 0.25, 0.50, and 1.00 g kg^{-1}. The contingency tables consider every grid point in either domain 2 or domain 3 for forecast hours +03 to +24 in 3-hourly increments from a model simulation. Two model simulations (one with and one without cloud initialization) are evaluated over two different 24-hour forecast periods starting at 13 September 2000, 00-UTC and 14 September 2000, 12-UTC: four simulations combined. 1536 contingency tables are constructed among the forecast hours, simulation days, cases of cloud insertion, domains, and mixing ratio thresholds being considered. Contingency tables between forecast hours that use direct insertion of the analysis (-06 and +00) are not compiled. The following eight skill scores, presented in detail below, are used to evaluate the cloud forecast: probability of detection (*POD*), bias (*Bias*), critical success index (*CSI*), equitable threat score (*ETS*), false alarm rate (*FAR*), probability of false detection (*PoFD*), true skill score (*TSS*), and Heidke skill score (*HSS*).

b. Probability of Detection (POD)

The *POD* is the ratio of events correctly forecast to the total number of events (Jincai et al. 1992). It is the fraction of events that were forecasted. *POD* ∈ [0, 1] with a perfect score of 1. It is not defined if an event is never observed.

$$POD = X / (X + Y) \tag{10.1}$$

c. Bias (Bias)

Bias is a function of the ratio of the number of events forecast to occur to the number of events that did occur (Junker et al. 1992). It is similar to *POD* but includes incorrect event forecasts. This score indicates how well the model predicted the number of times a mixing ratio threshold was exceeded at a given grid point. *Bias* ∈ [0, π/2] with a perfect score of π/4. It is defined only if an event occurs. A *Bias* over π/4 indicates that a threshold is being predicted too often. A *Bias* under π/4 indicates that a

threshold is being under-predicted. This skill score has been transformed from its traditional form to polar coordinates to give it symmetrical properties when comparing equal under-forecasted and over-forecasted amounts.

$$Bias = \text{TAN}^{-1}[(X + Z) / (X + Y)] \qquad (10.2)$$

d. Critical Success Index (CSI)

The *CSI* is the ratio of successful event forecasts to the total number of event forecasts made or needed. Non-event forecasts are excluded from consideration. It is sometimes called Threat Score (e.g. Junker et al. 1992). It is an indicator of how accurately a threshold is being predicted. $CSI \in [0, 1]$ with a perfect score of 1. It is not defined if $W = N$. *CSI* is a biased estimation, or an overestimation of forecast skill. Schaefer (1990) stated that the magnitude of the overestimation increases as the frequency of the event being forecast increases. In the case of cloud forecasting, event-frequency is relatively high to begin with. Because *CSI* is dependent on event frequency, it will likely be biased toward model simulations that produce more clouds. The *CSI* is an appropriate tool to indicate the relative worth of different forecast techniques when they are applied to the same environment. It would not be appropriate to compare *CSI* scores among different observed environments. Use of the *CSI* also assumes that instances when an event was neither expected nor observed are of no consequences. An example would be cloud forecasting under tremendous large-scale subsidence. In that instance, clouds would not likely be observed nor forecast. The reader is reminded that when cloud forecasts are applied to many military applications, the occurrence of an unobscured surface (when looking down) or an unobscured sky (when looking up) is just as much of a concern as the occurrence of a cloud obscured surface or sky. Therefore, *CSI* is useful, but not as meaningful as other more balanced forecast skill scores.

$$CSI = X / (X + Y + Z) \qquad (10.3)$$

e. Equitable Threat Score (ETS)

The *ETS* is a modified *CSI* that gauges forecast skill relative to a random forecast (Schaefer 1990). This score is representative of real accuracy in situations where events are rare and where the frequency of events and non-events are nearly equal. It also has other advantages. It is not dominated by non-events, and it is sensitive to both false alarms and missed events. $ETS \in [-1/3, 1]$ with a perfect score of 1. Values ≤ 0 indicate no skill and generally occur for constant or random forecasts. It is undefined when $N = W$ (data sets composed only of un-forecasted non-events) or when $N = X$ (data sets composed only of forecasted events). The *ETS* is not well suited to situations where non-events are rare (i.e., a predominately overcast regime). Additionally, Hamill (1999) asserts that *ETS* is biased in favor of forecasts with higher *Bias* scores. This score is biased toward higher event frequencies making it a misleading indicator of forecast skill when comparing scores across different cloudiness regimes. The

ETS is widely used in precipitation forecast verification studies and has recently been used in a similar cloud forecast verification study conducted by Baylor et al. 2000. The cases studied here have very high cloud coverage frequency; therefore, we must be critical of this index because it is biased in favor of simulations that forecast greater cloud coverage amounts.

$$ETS = \frac{(WX - ZY)}{(Z + Y)N + (WX - ZY)} \tag{10.4}$$

f. False Alarm Rate (FAR)

FAR is the ratio of incorrect event forecasts to the total number of event forecasts (Jincai et al. 1992). The *FAR* is a measure of the failure of the forecast to exclude non-event cases. It is a measure of how much a model over-forecasted above a stated threshold. $FAR \in [0, 1]$ with a perfect score of 0. It is undefined if there are no events forecasted.

$$FAR = Z / (X + Z) \tag{10.5}$$

g. Probability of False Detection (PoFD)

PoFD is the ratio of incorrectly forecast events to the number of observed non-events (Jincai et al. 1992). *PoFD* is small for rare events because non-events will dominate in the denominator. It is a measure of how much a model under-forecasted below a stated threshold. $PoFD \in [0, 1]$ with a perfect score of 0. It is not defined if there are no observed non-events.

$$PoFD = Y / (Z + W) \tag{10.6}$$

h. True Skill Score (TSS)

TSS is the difference between *POD* and *PoFD*. *TSS* accounts for correctly forecast non-events (Jincai et al. 1992). It also compares the accuracy of forecasts to a standard random forecast. *TSS* will be negative if there is a greater tendency to under-forecast a non-event than to correctly forecast an event. Conversely, *TSS* will be positive if there is a greater tendency to correctly forecast an event than to under-forecast a non-event. Doswell et al. (1990) have shown that *TSS* does not work well in evaluating forecasts of rare events. It is likely to perform well for evaluating cloud forecasts because clouds are generally common. $TSS \in [-1, 1]$ with a perfect score of 1. It is undefined if there are no observed non-events or no observed events (all clear or all cloudy observations).

$$TSS = POD - PoFD \tag{10.7}$$

i. Heidke Skill Score (HSS)

HSS is similar to a correlation coefficient (Doswell et al. 1990). The numerator of this score is the departure of the number of correct forecasts (C) from the expected number of correct forecasts due purely to chance (E). Like *TSS*, *HSS* also accounts for correctly forecast non-events, and it compares

the accuracy of forecasts to a standard random forecast. $HSS \in [-1, 1]$ with a perfect score of 1. Unlike the other scores, HSS is always defined. HSS is a positive quantity if $XW > YZ$, i.e. positive values indicate the product of correct forecasts is larger than the product of incorrect forecasts.

$$HSS = \frac{C - E}{N - E}$$
$$C = X + W$$
$$N = W + X + Y + Z$$
$$E = \frac{(X + Z)(X + Y) + (Z + W)(Y + W)}{N}$$

(10.8)

j. Index of improvement

A sample of the cloud liquid water mixing ratio forecast skill scores for domains 2 and 3 for simulations with and without cloud insertion at forecast hour +12 are provided in Tables 10.2 and 10.3. Table 10.4 illustrates how these forecast skill scores vary with forecast hour. These forecast skill scores indicate how well the model forecasts a mixing ratio at a given grid point, and whether the model correctly predicted the period in which the mixing ratio was forecast. To determine if cloud insertion improves forecast skill scores, a comparison metric is also computed. This metric, the index-of-improvement for POD, CSI, ETS, TSS, and HSS, is defined as follows:

$$\text{Index of Improvement} = \frac{(Score)_{\text{with cloud}} - (Score)_{\text{no cloud}}}{(Score)_{\text{no cloud}}} x100\%$$

(10.9a)

for FAR and $PoFD$:

$$\text{Index of Improvement} = \frac{(Score)_{\text{no cloud}} - (Score)_{\text{with cloud}}}{(Score)_{\text{no cloud}}} x100\%$$

(10.9b)

and for $Bias$:

$$\text{Index of Improvement} = \frac{|BIAS - 45°|_{\text{no cloud}} - |BIAS - 45°|_{\text{with cloud}}}{|BIAS - 45°|_{\text{no cloud}}} x100\%$$

(10.9c)

The "no cloud" scores are those computed for the model simulations with no cloud insertion during the first six hours of integration. Index-of-improvement scores are also included in Tables 10.2 and 10.3.

Table 10.2. Cloud liquid water mixing ratio forecast skill scores for domains 2 and 3, with and without cloud insertion, valid 13 September 2000/18 UTC, forecast hour +12.

DOMAIN 2 CLW without RTNEPH

g/kg	BIAS	POD	FAR	CSI	PoFD	TSS	HSS	ETS
0.00	48.	0.12	0.89	0.059	0.041	0.075	0.067	0.035
0.05	22.	0.055	0.87	0.040	0.038	0.017	0.056	0.029
0.10	19.	0.044	0.87	0.034	0.035	0.0089	0.049	0.025
0.25	14.	0.024	0.90	0.020	0.026	-0.0021	0.028	0.014
0.50	9.2	0.0078	0.95	0.0068	0.016	-0.0081	0.0091	0.0046
1.00	1.7	0.0	1.0	0.0	0.0058	-0.0058	-0.00033	-0.00017

DOMAIN 2 CLW with RTNEPH

g/kg	BIAS	POD	FAR	CSI	PoFD	TSS	HSS	ETS
0.00	42.	0.091	0.90	0.050	0.042	0.049	0.055	0.028
0.05	16.	0.032	0.89	0.025	0.039	-0.0070	0.033	0.017
0.10	13.	0.024	0.90	0.019	0.036	-0.012	0.025	0.013
0.25	8.3	0.013	0.91	0.011	0.027	-0.014	0.016	0.0079
0.50	3.8	0.0021	0.97	0.0020	0.016	-0.014	0.0020	0.00098
1.00	0.18	0.0	1.0	0.0	0.0058	-0.0058	-3.3E-05	-1.8E-05

DOMAIN 2 CLW Index of Improvement (%)

g/kg	BIAS	POD	FAR	CSI	PoFD	TSS	HSS	ETS
0.00	0.0	-24.	-1.1	-15.	-2.4	-35.	-18.	-20.
0.05	-26.	-42.	-2.3	-37.	-2.6	-1.4E+02	-41.	-41.
0.10	-23.	-45.	-3.4	-44.	-2.9	-2.3E+02	-49.	-48.
0.25	-18.	-46.	-1.1	-45.	-3.8	5.7E+02	-43.	-44.
0.50	-15.	-73.	-2.1	-71.	0.0	73.	-78.	-79.
1.00	-3.5	NaN	0.0	NaN	0.0	0.0	-90.	-89.

DOMAIN 3 CLW without RTNEPH

g/kg	BIAS	POD	FAR	CSI	PoFD	TSS	HSS	ETS
0.00	66.	0.19	0.91	0.062	0.065	0.12	0.017	0.0085
0.05	40.	0.072	0.92	0.040	0.067	0.0053	0.017	0.0088
0.10	37.	0.060	0.92	0.035	0.059	0.0011	0.018	0.0090
0.25	33.	0.039	0.94	0.025	0.039	0.00063	0.018	0.0093
0.50	30.	0.0095	0.98	0.0061	0.019	-0.0091	-0.0012	-0.00062
1.00	27.	0.0073	0.99	0.0049	0.0027	0.0046	0.0079	0.0040

DOMAIN 3 CLW with RTNEPH

g/kg	BIAS	POD	FAR	CSI	PoFD	TSS	HSS	ETS
0.00	64.	0.20	0.91	0.068	0.064	0.13	0.030	0.015
0.05	33.	0.065	0.90	0.041	0.067	-0.0023	0.026	0.013
0.10	29.	0.050	0.91	0.033	0.060	-0.010	0.022	0.011
0.25	21.	0.022	0.94	0.016	0.039	-0.018	0.011	0.0054
0.50	17.	0.0037	0.99	0.0029	0.019	-0.015	-0.0027	-0.0014
1.00	9.7	0.0	1.0	0.0	0.0027	-0.0027	-0.00080	-0.00039

DOMAIN 3 CLW Index of Improvement (%)

g/kg	BIAS	POD	FAR	CSI	PoFD	TSS	HSS	ETS
0.00	9.5	5.3	0.0	9.7	1.5	8.3	76.	76.
0.05	-1.4E+02	-9.7	2.2	2.5	0.0	-1.4E+02	53.	48.
0.10	-1.0E+02	-17.	1.1	-5.7	-1.7	-1.0E+03	22.	22.
0.25	-1.0E+02	-44.	0.0	-36.	0.0	-3.0E+03	-39.	-42.
0.50	-87.	-61.	-1.0	-52.	0.0	65.	1.2E+02	1.3E+02
1.00	-96.	-1.0E+02	-1.0	-1.0E+02	0.0	-1.6E+02	-1.1E+02	-1.1E+02

Table 10.3. Cloud liquid water mixing ratio forecast skill scores for domains 2 and 3, with and without cloud insertion, valid 15 September 2000/00 UTC, forecast hour +12.

DOMAIN 2 CLW without RTNEPH

g/kg	BIAS	POD	FAR	CSI	PoFD	TSS	HSS	ETS
0.00	36.	0.15	0.79	0.095	0.070	0.080	0.12	0.063
0.05	17.	0.063	0.79	0.051	0.067	-0.0039	0.067	0.035
0.10	15.	0.052	0.81	0.043	0.061	-0.0090	0.058	0.030
0.25	12.	0.030	0.86	0.025	0.045	-0.015	0.034	0.017
0.50	7.8	0.017	0.87	0.015	0.026	-0.0082	0.024	0.012
1.00	1.1	0.00042	0.98	0.00041	0.0072	-0.0068	0.00056	0.00028

DOMAIN 2 CLW with RTNEPH

g/kg	BIAS	POD	FAR	CSI	PoFD	TSS	HSS	ETS
0.00	39.	0.10	0.87	0.061	0.074	0.030	0.051	0.026
0.05	17.	0.034	0.89	0.026	0.069	-0.035	0.020	0.010
0.10	15.	0.027	0.90	0.022	0.063	-0.036	0.018	0.0091
0.25	10.	0.016	0.91	0.014	0.046	-0.030	0.015	0.0073
0.50	6.0	0.0094	0.91	0.0085	0.026	-0.016	0.012	0.0061
1.00	0.29	0.0	1.0	0.0	0.0072	-0.0072	-7.8E-05	-3.6E-05

DOMAIN 2 CLW Index of Improvement (%)

g/kg	BIAS	POD	FAR	CSI	PoFD	TSS	HSS	ETS
0.00	33.	-33.	-10.	-36.	-5.7	-62.	-58.	-59.
0.05	0.0	-46.	-13.	-49.	-3.0	8.0E+02	-70.	-71.
0.10	0.0	-48.	-11.	-49.	-3.3	3.0E+02	-69.	-70.
0.25	-6.1	-47.	-5.8	-44.	-2.2	1.0E+02	-56.	-57.
0.50	-4.8	-45.	-4.6	-43.	0.0	95.	-50.	-49.
1.00	-1.8	-1.0E+02	-2.0	-1.0E+02	0.0	5.9	-1.1E+02	-1.1E+02

DOMAIN 3 CLW without RTNEPH

g/kg	BIAS	POD	FAR	CSI	PoFD	TSS	HSS	ETS
0.00	49.	0.19	0.84	0.097	0.023	0.17	0.15	0.081
0.05	4.6	0.0	1.0	0.0	0.021	-0.021	-0.0031	-0.0016
0.10	3.4	0.0	1.0	0.0	0.019	-0.019	-0.0021	-0.0010
0.25	1.4	0.0	1.0	0.0	0.0090	-0.0090	-0.00044	-0.00022
0.50	0.0	0.0	0.0	0.0	0.0023	-0.0023	0.0	0.0
1.00	90.	0.0	0.0	0.0	0.0	0.0	1.0	1.0E+03

DOMAIN 3 CLW with RTNEPH

g/kg	BIAS	POD	FAR	CSI	PoFD	TSS	HSS	ETS
0.00	80.	0.21	0.96	0.034	0.023	0.19	0.018	0.0092
0.05	68.	0.068	0.97	0.020	0.020	0.048	0.0099	0.0050
0.10	66.	0.054	0.98	0.017	0.018	0.036	0.0075	0.0038
0.25	69.	0.061	0.98	0.017	0.0085	0.052	0.021	0.010
0.50	76.	0.0	1.0	0.0	0.0023	-0.0023	-0.0038	-0.0019
1.00	90.	0.0	1.0	0.0	0.0	0.0	0.0	0.0

DOMAIN 3 CLW Index of Improvement (%)

g/kg	BIAS	POD	FAR	CSI	PoFD	TSS	HSS	ETS
0.00	-7.8E+02	11.	-14.	-65.	0.0	12.	-88.	-89.
0.05	43.	Inf	3.0	Inf	4.8	-3.3E+02	-4.2E+02	-4.1E+02
0.10	50.	Inf	2.0	Inf	5.3	-2.9E+02	-4.6E+02	-4.8E+02
0.25	45.	Inf	2.0	Inf	5.6	-6.8E+02	-4.9E+03	-4.6E+03
0.50	31.	NaN	-Inf	NaN	0.0	0.0	-Inf	-Inf
1.00	0.0	NaN	-Inf	NaN	NaN	NaN	-1.0E+02	-1.0E+02

Table 10.4. Cloud liquid water mixing ratio forecast skill scores for domains 2 and 3, with and without cloud insertion, valid for forecast hours +3 to +24 for the 13 September simulation at the 0.0 g kg^{-1} mixing ratio threshold.

hour	BIAS	POD	FAR	CSI	PoFD	TSS	HSS	ETS
DOMAIN 2 CLW without RTNEPH								
03	38.	0.071	0.91	0.042	0.032	0.040	0.053	0.027
06	30.	0.12	0.78	0.086	0.073	0.051	0.11	0.057
09	42.	0.17	0.82	0.096	0.047	0.12	0.13	0.070
12	48.	0.12	0.89	0.059	0.041	0.075	0.067	0.035
15	56.	0.16	0.89	0.068	0.035	0.12	0.084	0.044
18	41.	0.18	0.80	0.11	0.070	0.11	0.13	0.067
21	34.	0.14	0.79	0.094	0.093	0.049	0.10	0.053
24	55.	0.14	0.90	0.061	0.041	0.10	0.066	0.034
DOMAIN 2 CLW with RTNEPH								
03	53.	0.17	0.87	0.079	0.028	0.14	0.11	0.059
06	30.	0.16	0.73	0.11	0.070	0.086	0.15	0.081
09	39.	0.13	0.84	0.078	0.049	0.082	0.10	0.053
12	42.	0.091	0.90	0.050	0.042	0.049	0.055	0.028
15	55.	0.12	0.91	0.055	0.036	0.089	0.060	0.031
18	38.	0.17	0.78	0.11	0.071	0.099	0.13	0.070
21	29.	0.14	0.75	0.097	0.094	0.045	0.11	0.061
24	52.	0.098	0.92	0.045	0.043	0.055	0.038	0.019
DOMAIN 3 CLW without RTNEPH								
03	40.	0.091	0.89	0.052	0.043	0.047	0.060	0.031
06	12.	0.099	0.54	0.089	0.42	-0.32	0.056	0.029
09	46.	0.18	0.83	0.097	0.11	0.068	0.063	0.032
12	66.	0.19	0.91	0.062	0.065	0.12	0.017	0.0085
15	70.	0.18	0.93	0.051	0.040	0.14	0.030	0.015
18	16.	0.11	0.61	0.094	0.32	-0.21	0.062	0.032
21	13.	0.11	0.51	0.10	0.36	-0.25	0.083	0.043
24	58.	0.097	0.94	0.038	0.026	0.071	0.041	0.021
DOMAIN 3 CLW with RTNEPH								
03	64.	0.12	0.94	0.040	0.042	0.074	0.016	0.0081
06	24.	0.20	0.54	0.16	0.37	-0.17	0.11	0.058
09	56.	0.21	0.86	0.091	0.11	0.10	0.028	0.014
12	64.	0.20	0.91	0.068	0.064	0.13	0.030	0.015
15	64.	0.14	0.93	0.048	0.043	0.095	0.030	0.015
18	21.	0.15	0.63	0.12	0.31	-0.16	0.072	0.037
21	20.	0.15	0.57	0.13	0.34	-0.19	0.088	0.046
24	75.	0.11	0.97	0.023	0.025	0.083	0.0020	0.0010

10.3. Second Moment Mixing Ratio Statistics

a. Gross error and bias

A few second moment statistics are also used to characterize the mixing ratio forecasts. Normalized average absolute gross error (*NAAGE*) is used to indicate how much predicted mixing ratios depart from analyzed mixing ratios. In concert with *NAAGE*, normalized bias (NB) is used to characterize the degree to which the model over-predicts or under-predicts the mixing ratios. These two metrics are given in equations 10.10 and 10.11. *N* represents only those grid points containing analyzed cloud; therefore, these metrics are only measures of error and bias in forecasting the occurrence of a cloudy grid point, not in forecasting the occurrence of a clear grid point.

$$NAAGE = \frac{1}{N}\sum_{i=1}^{N} \frac{|P_i - A_i|}{A_i} \qquad (10.10)$$

$$NB = \frac{1}{N}\sum_{i=1}^{N} \frac{P_i - A_i}{A_i} \qquad (10.11)$$

If a mixing ratio is perfectly predicted, all predicted mixing ratios (P_i) equal all analyzed mixing ratios (A_i) and both metrics are zero. If a mixing ratio is absolutely under-predicted with all $P_i = 0$, *NAAGE* is 1 and *NB* is -1. If a mixing ratio is absolutely over-predicted with P_i twice or greater than A_i, both metrics are > 1. These metrics can be expressed as a percent. Unfortunately, both metrics are undefined at grid points that do not contain analyzed cloud mixing ratios. They therefore ignore those grid points with predicted clouds but no analyzed clouds and can underestimate the true over-prediction character of the model.

b. Correlation

To include grid points with no analyzed clouds, the correlation coefficient (*r*) is used. In this case, *N* is defined for all grid points regardless of whether analyzed cloud is present or not.

$$r = \frac{\sum_{i=1}^{N}(P_i - \overline{P})(A_i - \overline{A})}{\sqrt{\sum_{i=1}^{N}(P_i - \overline{P})^2}\sqrt{\sum_{i=1}^{N}(A_i - \overline{A})^2}} \qquad (10.12)$$

The correlation coefficient (r) measures the degree to which predicted and analyzed mixing ratios are linearly related. It varies from -1 to +1. A score of 0 indicates absolutely no correlation. A score of 1 is perfect correlation, and a score of -1 is perfect negative correlation. Tables 10.5a through 10.6b list *NAAGE, NB,* and correlation (r) for cloud liquid water mixing ratios from model simulations with and without cloud insertion.

Table 10.5a. NAAGE (%), NB (%), r, and improvement for cloud liquid water, domain 2, 13 Sep 2000/09 UTC - 14 Sep 2000/06 UTC.

		GROSS ERROR	BIAS	CORRELATION
2000091309	wo/RTNEPH	1.1	-0.89	0.042
	w/RTNEPH	1.2	-0.70	0.035
	improvement	-	+	-
2000091312	wo/RTNEPH	1.0	-0.93	0.036
	w/RTNEPH	1.2	-0.76	0.088
	improvement	-	+	+
2000091315	wo/RTNEPH	1.0	-0.87	0.080
	w/RTNEPH	1.0	-0.89	0.045
	improvement	0	-	-
2000091318	wo/RTNEPH	1.1	-0.85	0.025
	w/RTNEPH	1.0	-0.90	0.018
	improvement	+	-	-
2000091321	wo/RTNEPH	1.1	-0.83	0.055
	w/RTNEPH	1.0	-0.90	0.022
	improvement	+	-	-
2000091400	wo/RTNEPH	1.1	-0.78	0.051
	w/RTNEPH	1.1	-0.86	0.042
	improvement	0	-	+
2000091403	wo/RTNEPH	1.1	-0.86	0.023
	w/RTNEPH	1.1	-0.89	0.028
	improvement	0	-	+
2000091406	wo/RTNEPH	1.1	-0.81	0.041
	w/RTNEPH	1.1	-0.89	0.0011
	improvement	0	-	-
Average	wo/RTNEPH	1.1	-0.85	0.044
	w/RTNEPH	1.1	-0.85	0.035
	improvement	0	0	-
Lag-1 rho	wo/RTNEPH	0.042	-0.021	0.028
	w/RTNEPH	0.0032	0.042	0.050

Table 10.5b. NAAGE (%), NB (%), r, and improvement for cloud liquid water, domain 2, 14 Sep 2000/21 UTC - 15 Sep 2000/18 UTC.

		GROSS ERROR	BIAS	CORRELATION
2000091421	wo/RTNEPH	1.1	-0.79	0.061
	w/RTNEPH	1.1	-0.81	0.051
	improvement	0	-	-
2000091500	wo/RTNEPH	1.2	-0.68	0.062
	w/RTNEPH	1.2	-0.76	0.064
	improvement	0	-	+
2000091503	wo/RTNEPH	1.3	-0.65	0.046
	w/RTNEPH	1.2	-0.75	0.046
	improvement	+	-	0
2000091506	wo/RTNEPH	1.1	-0.75	0.060
	w/RTNEPH	1.1	-0.87	0.023
	improvement	0	-	-
2000091509	wo/RTNEPH	1.2	-0.71	0.026
	w/RTNEPH	1.2	-0.74	0.016
	improvement	0	-	-
2000091512	wo/RTNEPH	1.4	-0.43	0.046
	w/RTNEPH	1.3	-0.56	0.055
	improvement	+	-	+
2000091515	wo/RTNEPH	1.8	-0.012	0.053
	w/RTNEPH	1.4	-0.47	0.056
	improvement	+	-	+
2000091518	wo/RTNEPH	1.4	-0.43	0.073
	w/RTNEPH	1.4	-0.43	0.082
	improvement	0	0	+
Average	wo/RTNEPH	1.3	-0.56	0.053
	w/RTNEPH	1.2	-0.67	0.049
	improvement	+	-	-
Lag-1 rho	wo/RTNEPH	0.12	0.15	-0.0052
	w/RTNEPH	0.27	0.26	0.071

Table 10.6a. NAAGE (%), NB (%), r, and improvement for cloud liquid water, domain 3, 13 Sep 2000/09 UTC - 14 Sep 2000/06 UTC.

	GROSS ERROR	BIAS	CORRELATION
2000091309 wo/RTNEPH	1.0	-0.93	0.043
w/RTNEPH	1.1	-0.79	0.012
improvement	-	+	-
2000091312 wo/RTNEPH	1.0	-0.89	0.062
w/RTNEPH	1.1	-0.82	0.089
improvement	-	+	+
2000091315 wo/RTNEPH	1.1	-0.78	-0.00033
w/RTNEPH	1.1	-0.73	0.00071
improvement	0	+	+
2000091318 wo/RTNEPH	1.2	-0.70	0.016
w/RTNEPH	1.2	-0.69	0.017
improvement	0	+	+
2000091321 wo/RTNEPH	1.1	-0.74	0.068
w/RTNEPH	1.0	-0.86	0.016
improvement	+	-	-
2000091400 wo/RTNEPH	1.0	-0.93	-0.0089
w/RTNEPH	1.2	-0.75	0.030
improvement	-	+	+
2000091403 wo/RTNEPH	1.0	-0.94	0.012
w/RTNEPH	1.0	-0.88	0.080
improvement	0	+	+
2000091406 wo/RTNEPH	1.0	-0.99	-0.0080
w/RTNEPH	1.0	-0.92	-0.010
improvement	0	+	-
Average wo/RTNEPH	1.0	-0.86	0.023
w/RTNEPH	1.1	-0.81	0.029
improvement	-	+	+
Lag-1 rho wo/RTNEPH	0.062	0.12	0.051
w/RTNEPH	0.16	0.20	-0.22

Table 10.6b. NAAGE (%), NB (%), r, and improvement for cloud liquid water, domain 3, 14 Sep 2000/21 UTC - 15 Sep 2000/18 UTC.

	GROSS ERROR	BIAS	CORRELATION
2000091421 wo/RTNEPH	0.97	-0.92	0.15
w/RTNEPH	1.1	-0.86	0.022
improvement	-	+	-
2000091500 wo/RTNEPH	1.1	-0.84	0.016
w/RTNEPH	1.1	-0.87	-0.013
improvement	0	-	-
2000091503 wo/RTNEPH	1.0	-0.99	0.0028
w/RTNEPH	1.4	-0.41	0.043
improvement	-	+	+
2000091506 wo/RTNEPH	1.0	-0.92	0.0021
w/RTNEPH	1.2	-0.71	0.011
improvement	-	+	+
2000091509 wo/RTNEPH	1.0	-0.99	-0.0038
w/RTNEPH	1.2	-0.61	0.022
improvement	-	+	+
2000091512 wo/RTNEPH	1.0	-0.90	0.0030
w/RTNEPH	1.1	-0.78	-0.0073
improvement	-	+	-
2000091515 wo/RTNEPH	0.99	-0.99	0.035
w/RTNEPH	0.99	-0.92	0.0097
improvement	0	+	-
2000091518 wo/RTNEPH	0.99	-0.99	0.024
w/RTNEPH	0.99	-0.96	0.0052
improvement	0	+	-
Average wo/RTNEPH	1.0	-0.94	0.029
w/RTNEPH	1.1	-0.76	0.012
improvement	-	+	-
Lag-1 rho wo/RTNEPH	0.024	0.10	-0.0016
w/RTNEPH	0.17	0.13	0.0054

c. Index of improvement

In addition to the second moment statistics, an index-of-improvement is included in the tables. Improvement indices for *NAAGE, NB,* and correlation (r) are computed as follows:

$$\text{Index of Impr. for NAAGE} = \frac{(NAAGE)_{\text{no cloud}} - (NAAGE)_{\text{with cloud}}}{(NAAGE)_{\text{with cloud}}} \, x100\% \qquad (10.13a)$$

$$\text{Index of Improvement for NB} = \frac{|NB|_{\text{no cloud}} - |NB|_{\text{with cloud}}}{|NB|_{\text{with cloud}}} \, x100\% \qquad (10.13b)$$

$$\text{Index of Improvement for r} = \frac{(r)_{\text{with cloud}} - (r)_{\text{no cloud}}}{(r)_{\text{with cloud}}} \, x100\% \qquad (10.13c)$$

$$\text{If } (r)_{\text{with cloud}} < (r)_{\text{no cloud}} \text{ then index} < 0.$$

d. Lag-one autocorrelations

To detect whether there are trends in *NAAGE, NB,* and *r* with forecast hour, lag-one autocorrelations are also computed for these metrics. The formula for autocorrelation is from Newton (1996). Values are sampled in 3-hourly intervals between forecast hours +03 to +24.

$$\hat{\rho} = \frac{\sum_{t=1}^{n-1} (x(t) - \bar{x})(x(t+1) - \bar{x})}{\sum_{t=1}^{n} (x(t) - \bar{x})^2} \qquad (10.14)$$

Lag-one autocorrelations, and indices of improvement for cloud liquid water on domains 2 and 3 for each simulation with and without cloud insertion are also included in Tables 10.5 and 10.6. These metrics are also computed for water vapor, cloud ice, rain, and snow (tables not shown).

e. Significance of correlation

A final question pertains to the significance of correlation: Is the distribution of predicted mixing ratio any different from random distributions of mixing ratio? One way to answer this question is to treat the problem as a simple binomial distribution problem. If clouds are assigned to a grid point randomly, then the probability of a success (assigning the predicted mixing ratio > a threshold to a point with an analyzed mixing ratio > a threshold) on one trial is designated *p*. The probability of a failure (assigning the predicted mixing ratio > a threshold to a point with an analyzed mixing ratio ≤ a threshold) on one trial is designated *q*. Define M as a mixing ratio threshold to be evaluated [0.00, 0.10, 0.25, 0.50, and 1.00 g kg^{-1}].

$$p = \frac{\text{number of points with analyzed mixing ratio} > M}{\text{total number of points}}$$

$$q = \frac{\text{number of points with analyzed mixing ratio} \le M}{\text{total number of points}} \qquad (10.15)$$

If there are n points with a predicted mixing ratio > M in a sample, then for a normal noise distribution the theoretical mean number of successes and their standard deviation are given by the formulas (Naiman et al. 1972):

$$\mu_s = np$$
$$\sigma_s = \sqrt{npq} \tag{10.16}$$

A good rule of thumb that assures the binomial histogram is approximately normal is when both np and nq are greater than 5. The normal distribution is defined by a table of z scores and percentile ranks. For the sample above, the z score for achieving at least m successes is given by the formula:

$$z_m = \frac{m - \mu_s}{\sigma_s} \tag{10.17}$$

The null hypothesis in this case is that a predicted mixing ratio > M placed on a grid point with an analyzed mixing ratio > M occurs at random.

$$H_0 : p' = p \tag{10.18}$$

The motivated, or alternative, hypothesis is that the placement of a predicted mixing ratio > M is not random and is more likely to be placed on a grid point with analyzed mixing ratio > M.

$$H_a : p' > p \tag{10.19}$$

The object now is to test whether the motivated hypothesis is correct or incorrect. To do this, the null hypothesis will be tested at the 0.05 significance level (the probability of incorrectly claiming that the predicted mixing ratios > M are biased in being placed on a grid point with analyzed mixing ratio > M). The 0.05 significance level identifies the area under the normal curve as 0.025 on the left and 0.0975 on the right. The critical z scores are ± 1.96. The limits of success for the null hypothesis are then defined by the equation:

$$S_c = \mu + \sigma z_c \tag{10.20}$$

Consider, for example, the model domain 2 forecast of cloud liquid water valid at 13 September 2000, 09-UTC, without cloud initialization (see Table 10.6.a). There were 11,011 points with analyzed cloud mixing ratio greater than the threshold 0.0 g kg^{-1}, and 322,420 points with analyzed cloud mixing ratios equal to zero g kg^{-1}. Of the predicted 8544 non-zero mixing ratio points, 785 of them occurred on a point with non-zero cloud mixing ratio analyzed from RTNEPH data. To determine if this number is significantly different from what would be expected by a random distribution of cloud liquid water, we make the following calculations:

$$p' = \frac{11011}{11011 + 322420} = 0.0330233$$
$$q' = 1 - p' = 0.9669767$$
$$n = 8544$$

Since $np = 282 > 5$, and $nq = 8262 > 5$, the normal approximation may be used.

$$\mu = np = 282.15$$

$$\sigma = \sqrt{npq} = 16.52$$

$$S_c = \mu + \sigma z = 282.15 + (16.52)(\pm 1.96)$$

$$S_c = 282.15 \pm 32.38$$

$$S_c = 250 \text{ and } 315$$

In following the decision rule for the above example, we reject the null hypothesis if we get less than 250 or more than 315 points with predicted non-zero cloud mixing ratios on coincident points with non-zero RTNEPH analyzed cloud mixing ratios. In this case, 785 predicted cloud points were a success so the null hypothesis is rejected. In addition, the bias is positive and suggests that predicted clouds are more likely than random to occur on a grid point with non-zero analyzed cloud mixing ratios.

Tables 10.7a through 10.8b provide a sample of the null hypothesis test results. The test is used to determine whether model predicted clouds having mixing ratios > M are randomly distributed to points with RTNEPH clouds having mixing ratios > M. A "Failure" indicates a 95% probability that predicted clouds are not randomly distributed. A (- ,+) indicates that predicted clouds are less (-) or more (+) likely than random to occur on a grid point with analyzed cloud mixing ratio > M.

Table 10.7a. Values computed in tests for random mixing ratio distribution for cloud liquid water mixing ratio greater than 0.00 g kg^{-1} for domain 2, valid for the 13 September 2000 simulation without cloud insertion, forecast hours +03 to +24.

	>=M mean	<M sigma	p s-range		q observed	n P/F
13Sep/09	11011	322420	0.033		0.97	8544
	282	17	250 to	315	785	FAIL(+)
13Sep/12	25713	307718	0.077		0.92	14769
	1139	32	1075 to	1202	3192	FAIL(+)
13Sep/15	17763	315668	0.053		0.95	16252
	866	29	810 to	922	2979	FAIL(+)
13Sep/18	14891	318540	0.045		0.96	16255
	726	26	674 to	778	1727	FAIL(+)
13Sep/21	13231	320200	0.040		0.96	19258
	764	27	711 to	817	2071	FAIL(+)
14Sep/00	26280	307151	0.079		0.92	22898
	1805	41	1725 to	1885	4676	FAIL(+)
14Sep/03	32688	300743	0.098		0.90	21762
	2133	44	2047 to	2219	4663	FAIL(+)
14Sep/06	15041	318390	0.045		0.95	21855
	986	31	926 to	1046	2131	FAIL(+)
TOTAL	156618	2510830	0.059		0.94	141593
	8314	88	8140 to	8487	22224	FAIL(+)

Table 10.7b. Values computed in tests for random mixing ratio distribution for cloud liquid water mixing ratio greater than 0.00 g kg^{-1} for domain 2, valid for the 13 September 2000 simulation with cloud insertion, forecast hours +03 to +24.

	>=M mean	<M sigma	p s-range		q observed	n P/F
13Sep/09	11011	322420	0.033		0.97	14703
	486	22	443 to	528	1874	FAIL(+)
13Sep/12	25713	307718	0.077		0.92	15041
	1160	33	1096 to	1224	4034	FAIL(+)
13Sep/15	17763	315668	0.053		0.95	14489
	772	27	719 to	825	2323	FAIL(+)
13Sep/18	14891	318540	0.045		0.96	13570
	606	24	559 to	653	1358	FAIL(+)
13Sep/21	13231	320200	0.040		0.96	18691
	742	27	689 to	794	1653	FAIL(+)
14Sep/00	26280	307151	0.079		0.92	20503
	1616	39	1540 to	1692	4457	FAIL(+)
14Sep/03	32688	300743	0.098		0.90	18427
	1806	40	1727 to	1886	4536	FAIL(+)
14Sep/06	15041	318390	0.045		0.95	18915
	853	29	797 to	909	1467	FAIL(+)
TOTAL	156618	2510830	0.059		0.94	134339
	7888	86	7719 to	8057	21702	FAIL(+)

Table 10.8a. Values computed in tests for random mixing ratio distribution for cloud liquid water mixing ratio greater than 0.00 g kg^{-1} for domain 3, valid for the 13 September 2000 simulation without cloud insertion, forecast hours +03 to +24.

	>=M mean	<M sigma	p s-range		q observed	n P/F
13Sep/09	4682	98565	0.045		0.95	3898
	177	13	151 to	202	424	FAIL(+)
13Sep/12	33000	70247	0.32		0.68	7123
	2277	39	2200 to	2354	3267	FAIL(+)
13Sep/15	12301	90946	0.12		0.88	12707
	1514	37	1442 to	1586	2204	FAIL(+)
13Sep/18	7670	95577	0.074		0.93	16848
	1252	34	1185 to	1318	1438	FAIL(+)
13Sep/21	4850	98397	0.047		0.95	13364
	628	24	580 to	676	880	FAIL(+)
14Sep/00	27464	75783	0.27		0.73	7711
	2051	39	1975 to	2127	3008	FAIL(+)
14Sep/03	29895	73352	0.29		0.71	6752
	1955	37	1882 to	2028	3319	FAIL(+)
14Sep/06	2865	100382	0.028		0.97	4639
	129	11	107 to	151	277	FAIL(+)
TOTAL	122727	703249	0.15		0.85	73042
	10853	96	10664 to	11041	14817	FAIL(+)

Table 10.8b. Values computed in tests for random mixing ratio distribution for cloud liquid water mixing ratio greater than 0.00 g kg^{-1} for domain 3, valid for the 13 September 2000 simulation with cloud insertion, forecast hours +03 to +24.

	>=M mean	<M sigma	p s-range		q observed	n P/F
13Sep/09	4682	98565	0.045		0.95	9633
	437	20	397 to	477	545	FAIL(+)
13Sep/12	33000	70247	0.32		0.68	14379
	4596	56	4486 to	4705	6683	FAIL(+)
13Sep/15	12301	90946	0.12		0.88	18419
	2194	44	2108 to	2281	2564	FAIL(+)
13Sep/18	7670	95577	0.074		0.93	16045
	1192	33	1127 to	1257	1507	FAIL(+)
13Sep/21	4850	98397	0.047		0.95	9787
	460	21	419 to	501	666	FAIL(+)
14Sep/00	27464	75783	0.27		0.73	10736
	2856	46	2766 to	2946	4021	FAIL(+)
14Sep/03	29895	73352	0.29		0.71	10786
	3123	47	3031 to	3215	4631	FAIL(+)
14Sep/06	2865	100382	0.028		0.97	10772
	299	17	265 to	332	312	PASS
TOTAL	122727	703249	0.15		0.85	100557
	14941	113	14720 to	15162	20929	FAIL(+)

10.4. Second Moment Cloud Coverage Amount Statistics

Cloud coverage amount in the RTNEPH database is at 48-km resolution. In the mixing ratio analysis, cloud coverage amount is randomly distributed to 18-km and 6-km spacing grids to explicitly define cloud location. To remove this random signal, cloud coverage is computed from a local distribution of cloud liquid water and cloud ice mixing ratios in the analysis and model simulation results. Cloud coverage amount is defined using seven mixing ratio thresholds (0.00, 0.05, 0.10, 0.25, 0.50, and 1.00 g kg^{-1}). A grid point is considered cloudy if the mixing ratio of either cloud liquid water or cloud ice exceeds the threshold. Cloud coverage amount is computed at 48-km resolution from mixing ratio threshold on domains 2 and 3. Second moment statistics (*NAAGE*, *NB*, *r*) are then computed for total cloud coverage amount at low, middle, and high regions using equations 10.10 through 10.12. Low cloud amount is computed by sampling only from the lowest eight sigma levels, middle cloud amount is computed from the next highest eight sigma levels, and high cloud amount is computed from the seven remaining upper sigma levels. Total cloud amount is computed by sampling all sigma levels. According to equations 10.10 and 10.11, *NAAGE* and *NB* are undefined if the analysis is zero, or in this case "cloud free". Therefore, *NAAGE* and *NB* are computed only among those grid points that contain cloud in the analysis. A sample of these statistics are provided in Tables 10.9a through 10.9d for the total, high, middle, and low sigma layers on domain 2 valid during the 13 September 2000 simulations with and without cloud insertion.

Table 10.9a. NAAGE (%), NB (%), r, and improvement for total cloud coverage amount, domain 2, using 0.00 g kg^{-1} threshold. (13 Sep 2000/09 UTC - 14 Sep 2000/06 UTC)

		GROSS ERROR	BIAS	CORRELATION
2000091309	wo/RTNEPH	1.2	-0.47	0.012
TOTAL	w/RTNEPH	1.4	0.043	0.099
	improvement	-	+	+
2000091312	wo/RTNEPH	1.3	-0.15	0.13
TOTAL	w/RTNEPH	1.4	0.15	0.16
	improvement	-	0	+
2000091315	wo/RTNEPH	1.6	0.32	0.15
TOTAL	w/RTNEPH	1.7	0.57	0.12
	improvement	-	-	+
2000091318	wo/RTNEPH	1.6	0.36	0.096
TOTAL	w/RTNEPH	1.8	0.49	0.060
	improvement	-	-	-
2000091321	wo/RTNEPH	1.8	0.72	0.12
TOTAL	w/RTNEPH	1.8	0.72	0.090
	improvement	0	0	-
2000091400	wo/RTNEPH	1.6	0.59	0.18
TOTAL	w/RTNEPH	1.6	0.54	0.21
	improvement	0	+	+
2000091403	wo/RTNEPH	1.5	0.34	0.072
TOTAL	w/RTNEPH	1.5	0.27	0.12
	improvement	0	+	+
2000091406	wo/RTNEPH	1.7	0.48	0.025
TOTAL	w/RTNEPH	1.6	0.27	0.013
	improvement	+	+	-
Average	wo/RTNEPH	1.5	0.27	0.098
	w/RTNEPH	1.6	0.38	0.11
	improvement	-	-	+
Lag-1 rho	wo/RTNEPH	-0.022	0.013	0.078
	w/RTNEPH	6.6E-08	0.033	-0.042

Table 10.9b. NAAGE (%), NB (%), r, and improvement for high cloud coverage amount, domain 2, using 0.00 g kg^{-1} threshold. (13 Sep 2000/09 UTC - 14 Sep 2000/06 UTC)

		GROSS ERROR	BIAS	CORRELATION
2000091309	wo/RTNEPH	1.2	-0.43	0.042
HIGH	w/RTNEPH	1.7	0.59	0.080
	improvement	-	-	+
2000091312	wo/RTNEPH	2.0	1.0	0.23
HIGH	w/RTNEPH	2.5	1.9	0.23
	improvement	-	-	0
2000091315	wo/RTNEPH	2.3	1.5	0.20
HIGH	w/RTNEPH	2.8	2.3	0.19
	improvement	-	-	-
2000091318	wo/RTNEPH	2.4	1.6	0.16
HIGH	w/RTNEPH	2.7	2.0	0.11
	improvement	-	-	-
2000091321	wo/RTNEPH	2.7	2.1	0.17
HIGH	w/RTNEPH	2.6	2.0	0.14
	improvement	+	+	-
2000091400	wo/RTNEPH	2.3	1.8	0.26
HIGH	w/RTNEPH	2.2	1.8	0.30
	improvement	+	0	+
2000091403	wo/RTNEPH	2.5	2.0	0.20
HIGH	w/RTNEPH	2.3	1.7	0.22
	improvement	+	+	+
2000091406	wo/RTNEPH	3.0	2.3	0.061
HIGH	w/RTNEPH	2.7	1.9	0.053
	improvement	+	+	-
Average	wo/RTNEPH	2.3	1.5	0.17
	w/RTNEPH	2.4	1.8	0.17
	improvement	-	-	0
Lag-1 rho	wo/RTNEPH	0.070	0.079	-0.087
	w/RTNEPH	-0.039	-0.0051	-0.12

Table 10.9c. NAAGE (%), NB (%), r, and improvement for middle cloud coverage amount, domain 2, using 0.00 g kg^{-1} threshold. (13 Sep 2000/09 UTC - 14 Sep 2000/06 UTC)

		GROSS ERROR	BIAS	CORRELATION
2000091309	wo/RTNEPH	1.1	-0.65	0.028
MIDDLE	w/RTNEPH	1.4	0.18	0.19
	improvement	-	+	+
2000091312	wo/RTNEPH	1.2	-0.35	0.21
MIDDLE	w/RTNEPH	1.4	0.10	0.27
	improvement	-	+	+
2000091315	wo/RTNEPH	1.5	0.15	0.21
MIDDLE	w/RTNEPH	1.7	0.56	0.21
	improvement	-	-	0
2000091318	wo/RTNEPH	1.6	0.16	0.071
MIDDLE	w/RTNEPH	1.7	0.29	0.084
	improvement	-	-	+
2000091321	wo/RTNEPH	1.6	0.36	0.073
MIDDLE	w/RTNEPH	1.6	0.25	0.080
	improvement	0	+	+
2000091400	wo/RTNEPH	1.5	0.41	0.22
MIDDLE	w/RTNEPH	1.5	0.33	0.25
	improvement	0	+	+
2000091403	wo/RTNEPH	1.4	0.27	0.13
MIDDLE	w/RTNEPH	1.4	0.14	0.21
	improvement	0	+	+
2000091406	wo/RTNEPH	1.5	0.20	0.068
MIDDLE	w/RTNEPH	1.3	-0.10	0.043
	improvement	+	+	-
Average	wo/RTNEPH	1.4	0.069	0.13
	w/RTNEPH	1.5	0.22	0.17
	improvement	-	-	+
Lag-1 rho	wo/RTNEPH	-0.0080	0.027	-0.0052
	w/RTNEPH	0.12	0.097	-0.10

Table 10.9d. NAAGE (%), NB (%), r, and improvement for low cloud coverage amount, domain 2, using 0.00 g kg^{-1} threshold. (13 Sep 2000/09 UTC - 14 Sep 2000/06 UTC)

		GROSS ERROR	BIAS	CORRELATION
2000091309	wo/RTNEPH	1.3	-0.41	0.053
LOW	w/RTNEPH	1.3	-0.27	0.22
	improvement	0	+	+
2000091312	wo/RTNEPH	1.1	-0.45	0.17
LOW	w/RTNEPH	1.1	-0.44	0.26
	improvement	0	+	+
2000091315	wo/RTNEPH	1.3	-0.058	0.27
LOW	w/RTNEPH	1.3	-0.15	0.22
	improvement	0	-	-
2000091318	wo/RTNEPH	1.3	-0.065	0.22
LOW	w/RTNEPH	1.4	0.045	0.18
	improvement	-	+	-
2000091321	wo/RTNEPH	1.4	0.080	0.23
LOW	w/RTNEPH	1.6	0.34	0.17
	improvement	-	-	-
2000091400	wo/RTNEPH	1.3	-0.13	0.22
LOW	w/RTNEPH	1.3	-0.17	0.25
	improvement	0	-	+
2000091403	wo/RTNEPH	1.1	-0.50	0.19
LOW	w/RTNEPH	1.2	-0.36	0.23
	improvement	-	+	+
2000091406	wo/RTNEPH	1.3	-0.25	0.15
LOW	w/RTNEPH	1.3	-0.27	0.085
	improvement	0	-	-
Average	wo/RTNEPH	1.3	-0.22	0.19
	w/RTNEPH	1.3	-0.16	0.20
	improvement	0	+	+
Lag-1 rho	wo/RTNEPH	-0.077	0.024	-0.0026
	w/RTNEPH	0.0095	0.051	-0.15

10.5. Analysis of Results

a. Skill scores

Eight forecast skill scores are adapted to cloud and precipitation threshold forecasting (*Bias, POD, FAR, CSI, ETS, PoFD, TSS,* and *HSS*). Seven mixing ratio thresholds are used to compute the skill scores (0.00, 0.05, 0.10, 0.25, 0.50, and 1.00 g kg^{-1}). The skill scores are computed for forecast hours +03 through +24 for the two primary cases studied. Tables 10.2 and 10.3 only contain skill scores for forecast hour +12, an illustrative sample.

All skill scores except *PoFD* are best at the lowest two mixing ratio thresholds for all four cloud variables (cloud liquid water, cloud ice, rain, and snow). *PoFD* skill score is best at the highest mixing ratio threshold. *PoFD* is a measure of under-forecasting cloud-free or precipitation-free grid points. It excludes consideration of correct cloud and precipitation forecasts. *PoFD* scores are generally low. At the lowest mixing ratio threshold on domain 3, cloud liquid water has an average *PoFD* of 4%, ice and snow have the lowest at 1%, and rain has the largest at 9%. This skill score improves when mixing ratio threshold increases. Increasing the threshold mixing ratio effectively removes excess cloud and precipitation generated by the mesoscale model resulting in better cloud-free forecasts. It indicates the model may be producing low-mixing-ratio cloud and precipitation at too many grid points. Cloud insertion generally improves *PoFD* skill scores on domain 3 with percent improvement indices averaging 5% for cloud liquid water, 18% for ice, 20% for rain, and 19% for snow.

The *Bias* score indicates how well the model predicts the number of times a mixing ratio threshold is exceeded at a grid point. These scores are generally best at the lowest mixing ratio threshold. Increasing the threshold results in cloud and precipitation mixing ratios becoming increasingly under-predicted. Because *Bias* scores exclude analyzed cloud-free and precipitation-free grid points, it is expected that filtering low mixing ratios will increasingly show under-prediction. Cloud liquid water produces the best *Bias* scores at the lowest mixing ratio threshold. Except for cloud liquid water, cloud initialization consistently degrades *Bias* scores at the lowest mixing ratio threshold. Cloud insertion causes the model to increase the over-prediction of clouds and precipitation. At higher mixing ratio thresholds where *Bias* scores drop to under-prediction levels, cloud insertion results in improvement.

POD indicates the fraction of observed clouds and precipitation that are forecast correctly. *POD* decreases with increasing threshold indicating local maxima in analyzed mixing ratios are not well predicted by the models. At the lowest threshold on domain 3, cloud liquid water has the lowest *POD* with an average of only 15%, ice has the highest average at 65%, rain has 39%, and snow has 64%. Some of the lower *POD* scores for cloud liquid water and rain may be attributed to the tendency for the model to predict more cloud liquid water and rain at higher sigma levels where no cloud liquid water and rain are analyzed by CIS (refer to the domain 3 vertical mass distribution plots in Figures 9.5 and

9.7). Cloud insertion causes the model to produce more clouds and precipitation and consistently improves *POD* skill scores.

FAR is a measure of over-forecasting above the threshold. This skill score excludes all cloud-free and precipitation-free forecasts. All *FAR*'s are large indicating the model predicts all variables far more frequently than they are analyzed. At the lowest mixing ratio threshold on domain 3, cloud liquid water has an average *FAR* of 85%, ice has 88%, rain has the lowest at 76%, and snow has the largest at 91%. *FAR* generally increases with increasing threshold. This indicates little agreement in local maxima between analyzed and predicted mixing ratios. With cloud insertion, *FAR* scores generally worsen for all variables in domain 2. No clear score pattern is detected as a result of cloud insertion on domain 3.

CSI is a measure of how successful event forecasts are. All *CSI* scores were generally low. At the lowest mixing ratio threshold on domain 3, cloud liquid water and snow have an average *CSI* of 8%, ice has 11%, and rain has the highest at 17%. *CSI* generally decreases with increasing threshold. This may indicate the model does not do well at forecasting the placement of precipitation clouds that have very large mixing ratios; however, we must keep in mind that this score is biased toward situations in which an event occurs more frequently. Increasing mixing ratio threshold effectively decreases event frequency. With cloud insertion, *CSI* indices of improvement produce a mixed signal; they generally decrease except for rain and cloud liquid water on domain 3.

ETS is a measure of how forecast skill compares to a random forecast. All *ETS* scores are generally low and varied little among the cloud variables possibly indicating the forecast skill not much better than what would be expected of a random cloud forecast. At the lowest mixing ratio threshold on domain 3, cloud liquid water has an average *ETS* of 3%, ice has 7%, rain has 4%, and snow has 4%. *ETS* generally decreases with mixing ratio threshold. *ETS*, like *CSI*, is biased toward situations in which an event occurs more frequently. As mixing ratio threshold is increased, it is unknown if skill decreases because the model poorly forecasts the placement of high mixing ratio clouds, or if skill decreases because the event frequency decreases. With cloud insertion, *ETS* score changes varied greatly among the cloud variables and cases. No clear improvement or degradation signal is evident from *ETS* indices of improvement from cloud insertion. For example, cloud liquid water and rain showed degradation in the 13 September simulation but improvement in the 14 September simulation.

TSS compares a forecast to a standard random forecast and accounts for correctly forecast non-events. Almost all scores are > 0 indicating a greater tendency for the model to correctly forecast an event than to under-forecast a non-event. At the lowest mixing ratio threshold in domain 3, cloud liquid water has the worst average *TSS* at 5%, ice has the best at 63%, rain has 24%, and snow has 62%. *TSS* generally decreases with increasing threshold. The *TSS* is somewhat biased in favor of rare event forecasts. Because ice, rain and snow are rare relative to cloud liquid water, their *TSS*'s are expected to be higher. In domain 3, cloud insertion consistently improves *TSS*.

HSS is similar to *TSS*. Like *TSS*, almost all scores are > 0 indicating the product of correct forecasts is larger than the product of incorrect forecasts. At the lowest mixing ratio threshold on domain 3, there is less variability in *HSS*'s among the cloud variables. Cloud liquid water has an average *HSS* of 6%, ice has the best at 13%, rain has 7%, and snow has 8%. Except for snow, *HSS* generally decreases with cloud insertion. Values for snow show maxima at the 0.05 g kg^{-1} mixing ratio threshold. In domain 3, cloud insertion generally degrades *HSS* except for cloud liquid water and rain in the 14 September simulation.

b. Summary of skill score analysis

Skill scores: *Bias* skill scores are generally good. *POD* and *TSS* vary considerably among the cloud variables but are generally good. *CSI, ETS, FAR, PoFD* and *HSS* are generally bad. *Bias, POD,* and *TSS* may be best for evaluating cloud and precipitation forecasts where event frequency is high.

Inter-domain comparison: There is no detectable pattern of differences in skill scores between domain 2 and domain 3. This quite surprisingly may indicate that cloud forecast efficiency is generally not scale dependent.

Model performance: There is a greater tendency for the models to correctly forecast clouds and precipitation than to under-forecast cloud-free and precipitation-free grid points. The product of correct cloud and cloud-free forecasts is larger than the product of cloud and cloud-free incorrect forecasts. The model produces similar results for precipitation forecasts.

Varying mixing ratio threshold: Using a threshold mixing ratio of 0.0 g kg^{-1} produces better skill scores suggesting that analyzed mixing ratios are higher than modeled mixing ratios, and that there is little skill in forecasting local cloud and precipitation mixing ratio maxima.

Cloud insertion: Cloud insertion consistently improves *POD, PoFD,* and *TSS*. *HSS* improves only in domain 3. *Bias* scores improve with cloud insertion only at higher mixing ratio thresholds where *Bias* scores drop to under-prediction levels. Cloud insertion generally worsens *FAR* skill scores. This indicates a tendency for cloud insertion to cause the model to over-forecast clouds and precipitation. Cloud insertion causes the model to increase the over-prediction of clouds and precipitation. No trend in forecast skill score is noted with forecast hour (see Table 10.4) for any of the cloud variables.

c. Mixing ratio NAAGE, NB, and r

The normalized average absolute gross error, normalized bias, correlation, and percent improvement are computed for all four cloud variables and water vapor over forecast hours +03 to +24 in 3-hourly intervals in domains 2 and 3.

Normalized biases among the cloud variables show a detectable pattern. Cloud liquid water and cloud ice generally have negative biases while rain and snow all have positive biases. Negative biases indicate analyzed mixing ratios are generally larger than forecast mixing ratios. This pattern of biases

points toward the algorithm that produces mixing ratios from the RTNEPH data. Because analyzed precipitation is distributed more discretely than forecast precipitation, these biases may indicate the algorithm retrieves precipitation mixing ratios that are too high.

Correlations for all four cloud and precipitation variables are dismally low with averages generally less than 0.1. For any given forecast hour or cloud variable, cloud insertion improves about half of these scores possibly indicating a near random chance that cloud insertion has any impact.

For water vapor, the most important water-mass constituent, gross error averages about 32%, and biases average about +5% before cloud insertion. Gross error averages about 55% and biases average about +26% after cloud insertion. After cloud insertion, gross error nearly doubles and biases increase five-fold. Biases do not change sign indicating that before and after cloud insertion, the mesoscale model over-predicts water vapor mixing ratio. Bias and gross error tendencies are apparently scale-independent because there was no error pattern that distinguished domain 2 from domain 3 metrics. Correlations are generally high, usually above 0.95. Cloud insertion most frequently decreases correlation but by less than 1%.

In analyzing how forecast variables change with forecast length, it is usually found that most forecast errors grow with time. *NAAGE, NB* and *r* are expected to follow similar degradation patterns noted for most forecast variables. Absolute error and bias normally increase with forecast time and correlation normally decreases with forecast time. Unexpectedly, there is no discernable trend noted in these statistics for clouds and precipitation. The lag-one autocorrelations computed for each variable, case, and domain are dismally low as well. This may principally be due to the model's very poor forecast errors, biases, and correlations.

To determine if these low correlations indicate random placement of cloud variables, a significance test for randomness above the various mixing ratio thresholds are conducted for each cloud variable at each forecast time in each domain. Results indicate overwhelmingly that the frequency of occurrence and placement of forecast clouds and precipitation at the lowest mixing ratio threshold is not random. At the lowest mixing ratio threshold, the models generally forecast far more clouds and precipitation than would be expected for a random process. Out of 256 tests at the lowest mixing ratio threshold, only 6 pass the test for randomness at the 0.05 significance level. At higher mixing ratio thresholds, the test for randomness generally pass at the 0.5 or 1.0 g kg^{-1} mixing ratio for rain and cloud liquid water, and at the 0.05 g kg^{-1} mixing ratio for ice and snow.

In summary, for the mixing ratio *NAAGE, NB, r*, and significance, there is no trend in these statistics with forecast hour. Correlations between analyzed and predicted cloud variables are poor. Bias pattern may indicate the retrieval algorithm used in CIS over-estimates precipitation mixing ratios. The model forecast of cloud and precipitation is not random in spite of poor correlation and high biases. Generally, the model forecasts more clouds and precipitation than what is expected of a random process.

d. Cloud coverage amount NAAGE, NB, and r

NAAGE decreases with mixing ratio threshold. *NB* varies from large positive values at small mixing ratio thresholds to large negative values at large mixing ratio thresholds. A positive (negative) bias indicates predicted cloud coverage amounts are generally larger (smaller) than analyzed cloud coverage amounts. It is found in the large-scale analysis that analyzed mixing ratios are larger and have greater variance than predicted mixing ratios. Increasing threshold mixing ratio results in smaller predicted cloud coverage amounts while having little effect on analyzed cloud coverage amounts. Bias values indicate over prediction of cloud coverage amount at low mixing ratio thresholds, reach a minimum at intermediate mixing ratio thresholds, and indicate under prediction of cloud coverage amount at higher mixing ratio thresholds. This behavior is simply a reflection of the differences in data character between the analysis and the model output (e.g. average magnitude, discreteness, frequency of occurrence), and not a reflection of forecast skill.

Domain 3 *NAAGE* and *NB* values are always more positive than domain 2 values. In other words, at low mixing ratio thresholds, domain 3 over predicts clouds more than domain 2. At high mixing ratio thresholds, domain 3 under predicts clouds less than domain 2. The range of *NAAGE* and *NB* values computed among the sample data sets is larger for domain 3 than for domain 2. To produce this result, it is only necessary to predict clouds on a larger portion of domain 3 than on domain 2. This was accomplished by simply placing domain 3 in a region with great convective potential. In fact, the domain 3 study region was selected for its large convective potential. Had a small sub-region of domain 2 with little convective potential been selected for domain 3, then domain 3 *NAAGE* and *NB* values would likely be less positive than domain 2 values.

Correlation universally decreases as the mixing ratio threshold used to define a cloud increases. The best correlations between modeled cloud and analyzed cloud are found when using the lowest threshold. Domain 2 correlations are always better than domain 3 correlations.

At the lowest mixing ratio threshold, *NAAGE* and *NB* improvement indices for cloud coverage amount show universal deterioration after cloud insertion. Improvement indices on correlation are more confusing. For the 13 September 2000 case, cloud insertion improves correlation at all vertical levels on domain 2 and at all but the low level on domain 3. For the 14 September 2000 case, cloud insertion deteriorated correlation at all vertical levels on domain 2 and improved correlation at all vertical levels on domain 3. Among both domains and both simulation cases, correlation varies between -0.36 and +0.50. Such wide variation in correlation makes this metric suspect as a definitive forecast skill measure for clouds using a mixing ratio threshold. Statistics are also computed for the 0.0 g kg^{-1} mixing ratio threshold in the sub-region of domain 2 that contains domain 3 to facilitate comparison at different resolution. This comparison reveals that domain 2 *NAAGE* and *NB* values are consistently much smaller than domain 3 values. Predominately negative indices of improvement for *NAAGE* and *NB*

values imply skill degradation after cloud insertion, but this conclusion could not be corroborated with correlation values. No other grid-spacing conclusions could be reached because there was no consistency in correlation values. There are no discernable trends in *NAAGE*, *NB*, or in correlation with forecast hour.

In summary, for the cloud coverage amount *NAAGE*, *NB*, and *R*, these correlation scores do not provide adequate measurement of forecast skill. Selection of a mixing ratio threshold that produces the lowest cloud coverage bias metrics does not necessarily help to define cloud coverage forecast skill. *NAAGE* and *NB* cannot provide an objective measure of how forecast skill changes with grid spacing when comparing *NAAGE* and NB scores computed from all of domains 2 and 3. It is not possible to determine if forecast skill changes with forecast length using these metrics. It is not possible to determine if forecast skill changes with grid resolution.

This chapter presented a description of eight forecast skill scores, and three second moment statistics scores for the occurrence of a non-zero mixing ratio and a non-zero cloud coverage amount. It was found that cloud insertion slightly improves most forecast skill scores; however, it also demonstrated that the model has a tendency to over forecast clouds and precipitation when compared to the cloud analysis produced by CIS. Second moment statistics computed for cloud coverage amount using a threshold mixing ratio to define "cloudiness" proved useless. These preliminary results indicate that direct insertion of clouds is insufficient to significantly improve cloud forecasts. The following chapter next presents a discussion on how the mesoscale model responds to cloud insertion. It also explores why direct insertion of clouds is insufficient to improve cloud forecasts.

CHAPTER XI
DISCUSSION

11.1. Model Response to Cloud Insertion

Two questions are raised from the total domain mass traces (Figures 9.9 through 9.14); what causes the rapid adjustment in domain mass in the cloud insertion simulations at forecast hours -06 and +00, and why do all simulations tend toward a quasi-steady total domain mass regardless of whether there is cloud insertion? Tables 9.1a and b show that at cloud insertion times (forecast hours -06 and +00), an average of 9.2×10^{11} kg of cloud liquid water is inserted into domain 2. Figure 9.10 shows that within minutes of insertion, total domain cloud liquid water mass drops rapidly to roughly 10% of its insertion value. A decline in cloud liquid water mass will occur through conversion processes and through evaporation processes. Possible conversion processes include autoconversion to rain or ice and accumulation by rain and snow. Possible evaporation processes include diabatic subsidence, diffusion, and turbulent mixing of saturated water vapor and cloud liquid water to neighboring grid points that are cloud free and unsaturated. Before investigating these, the question of how cloud insertion affects the initial distribution of pressure is examined.

a. Hydrostatic initialization

Up to this point, the impact on vertical acceleration due to the direct insertion of cloud has not been addressed. When a grid point is identified as cloudy during direct insertion of clouds, the specific humidity (q_v) at that grid point is adjusted to saturation. Any grid points containing mixing ratios of cloud liquid water, cloud ice, rain, and snow are removed in lieu of the CIS parameterizations of these mixing ratios. CIS will also parameterize zero kg kg^{-1} mixing ratios on cloud-free grid points. No changes are made to the pressure or to the temperature during the insertion process. In an initially hydrostatically balanced air column, an increase in q_v results in an increase in virtual temperature (T_v) and an increase in buoyancy.

$$q_v = \frac{w}{1+w}, \quad q_{vs} = \frac{w_s}{1+w_s} \tag{11.1}$$

$$w = \frac{\varepsilon e}{p-e}, \quad w_s = \frac{\varepsilon e_s}{p-e_s} \tag{11.2}$$

$$e = e_{s0} \exp\left[\frac{L}{R_v}\left(\frac{1}{T_{00}} - \frac{1}{T_d}\right)\right], \quad e_s = e_{s0}\exp\left[\frac{L}{R_v}\left(\frac{1}{T_{00}} - \frac{1}{T}\right)\right] \tag{11.3}$$

$$p = \rho_d R_d T_v, \quad T_v = T(1+0.608q_v), \quad T_v' = T(1+0.608q_v) - T_0 \tag{11.4}$$

$$\underset{\text{decreased}}{\underbrace{\rho_d}} = \underset{\text{constant}}{\underbrace{\frac{p}{R_d T}}}\left(\frac{1}{1+0.608\underset{\text{increased}}{\underbrace{q_v}}}\right) \tag{11.5}$$

If the environment is initially in hydrostatic balance, a decrease in dry air density produces a non-hydrostatic distribution of pressure. If the lapse rate of the environment's temperature is conditionally unstable, an additional buoyancy term is immediately added to the vertical acceleration as liquid water condenses out of and heats the cloud layer that is rising to reach hydrostatic equilibrium. Cloud insertion also results in an increase in water loading from non-vapor cloud elements. Removing cloud-mixing ratios from grid points identified to be cloud-free during the direct-insertion process will eliminate water loading terms and increase buoyancy in the vertical acceleration equation.

The initialization of the non-hydrostatic model is described in Chapter 7 of the MM5 tutorial notes (Dudhia et al. 2000) and in Grell et al. 1994. The initial pressure distribution is described in terms of a basic state pressure (p_0) and a departure from the basic state pressure (p'). The total pressure (p) at a grid point, which remains unchanged during cloud insertion, is:

$$p^* = p_s - p_t$$
$$p_0 = p^* \sigma + p_t \tag{11.6}$$
$$p = p_0 + p'$$

The vertical pressure gradient ($\partial p / \partial \sigma$) is initialized in hydrostatic balance in the model preprocessor called INTERPF. The model's vertical velocity equation is used with the acceleration and advection terms set to zero (refer to equation 2.3.7, page 8 of Grell et al. 1994). This leaves a relation between virtual temperature perturbation [$T'_v(\sigma)$] and the vertical gradient of p'.

$$0 = \underbrace{p^* g \frac{\rho_0}{\rho} \left[\frac{1}{p^*} \frac{\partial p'}{\partial \sigma} + \frac{T'_v}{T} - \frac{c_v T_0 p'}{c_p T p_0} - \frac{R_d p' T_0}{c_p p_0 T} \right]}_{\text{various sources of buoyancy}} - \underbrace{p^* g [q_c + q_r]}_{\text{water loading}} \tag{11.7a}$$

$$0 = \frac{\rho_0}{\rho} \left[\frac{1}{p^*} \frac{\partial p'}{\partial \sigma} + \frac{T'_v}{T} - p' \left(\frac{c_v + R_d}{c_p} \right) \left(\frac{T_0}{p_0 T} \right) \right] - [q_c + q_r], \quad \frac{c_v + R_d}{c_p} = 1 \tag{11.7b}$$

$$0 = \frac{\rho_0 T_v R_d}{p_0 + p'} \left[\frac{1}{p^*} \frac{\partial p'}{\partial \sigma} + \frac{T'_v}{T} - p' \left(\frac{T_0}{p_0 T} \right) \right] - [q_c + q_r] \tag{11.7c}$$

$$0 = \rho_0 T_v R_d \left[\frac{1}{p^*} \frac{\partial p'}{\partial \sigma} + \frac{T'_v}{T} - p' \left(\frac{T_0}{p_0 T} \right) \right] - (p_0 + p')(q_c + q_r) \tag{11.7d}$$

$$0 = \rho_0 T_v R_d \left[\frac{1}{p^*} \frac{\partial p'}{\partial \sigma} - p' \left(\frac{T_0}{p_0 T} \right) \right] + \frac{\rho_0 T_v R_d T'_v}{T} - p_0 (q_c + q_r) - p'(q_c + q_r) \tag{11.7e}$$

$$\frac{\partial p'}{\partial \sigma} = \frac{p_0 (q_c + q_r) - \dfrac{\rho_0 T_v R_d T'_v}{T} + \dfrac{\rho_0 T_v R_d p' T_0}{p_0 T} + p'(q_c + q_r)}{\dfrac{\rho_0 T_v R_d}{p^*}} \tag{11.7f}$$

The variables q_c and q_r are the mixing ratios of cloud liquid water and rain included in the initialization fields prior to cloud insertion. According to Dudhia et al. 2000, given the sea-level pressure p_{s0}, p' at the lowest model sigma level can be estimated by using equation 11.7f while

assuming p' is constant below the lowest model sigma level. (Refer to Dudhia et al. 2000, Chapter 7 for a description of the basic state pressure profile.)

$$0 = \frac{p_0(q_c + q_r) - \dfrac{\rho_0 T_v R_d T_v'}{T} + \dfrac{\rho_0 T_v R_d p' T_0}{p_0 T} + p'(q_c + q_r)}{\dfrac{\rho_0 T_v R_d}{p^*}} \tag{11.8a}$$

$$0 = p_0(q_c + q_r) - \frac{\rho_0 T_v R_d T_v'}{T} + p'\left(\frac{\rho_0 T_v R_d T_0}{p_0 T} + (q_c + q_r)\right) \tag{11.8b}$$

$$p' = \frac{\left(\dfrac{\rho_0 T_v R_d T_v'}{T} - p_0(q_c + q_r)\right)}{\left(\dfrac{\rho_0 T_v R_d T_0}{p_0 T} + (q_c + q_r)\right)} \quad \text{at lowest sigma level} \tag{11.8c}$$

Given p' at the lowest sigma level, and given the profile of virtual temperature, vertical integration of equation 11.7f can estimate p' at the other levels.

$$p'_{\sigma_{k-1}} = \left[\frac{\left(\begin{array}{l} p_0(q_c + q_r) - \dfrac{\rho_0 T_v R_d T_v'}{T} \\ + \dfrac{\rho_0 T_v R_d p' T_0}{p_0 T} + p'(q_c + q_r) \end{array}\right)}{\dfrac{\rho_0 T_v R_d}{p^*}}\right]_{\sigma_k} (\sigma_{k-1} - \sigma_k) + p'_{\sigma_k} \tag{11.9}$$

This method of computing p' ensures that the initial vertical acceleration is zero in each model column in the INTERPF preprocessor. After cloud insertion, the initial vertical acceleration is no longer zero in a cloudy column because T_v' has been adjusted and initial values of q_c and q_r have been replaced by a new distribution of q_c and q_r. The vertical pressure gradient is no longer in hydrostatic balance with the new profiles of T_v', q_c, and q_r. The magnitude of the vertical acceleration that arises from direct insertion of cloud after the INTERPF preprocessor is then given by:

$$\frac{\partial p^* w}{\partial t} = \underbrace{p^* g \frac{\rho_0}{\rho} \frac{\delta T_v}{T}}_{\substack{\text{extra buoyancy} \\ \text{due to increase} \\ \text{in } q_v}} - \underbrace{p^* g [\delta q_c + \delta q_r]}_{\substack{\text{adjusted} \\ \text{water loading}}} \tag{11.10}$$

The variables δT_v, δq_c, and δq_r are the departures from the initial values of T_v', q_c and q_r respectively. The parameterization of q_c and q_r in CIS is always non-zero in clouds, therefore, equation 11.10 will not always produce positive vertical accelerations. In fact, positive vertical accelerations are more likely in thin stratiform clouds that produce little cloud liquid water and rain. Deeper cumuliform clouds with large cloud liquid water and rain mixing ratios will have negative vertical accelerations.

Grid points already near saturation would be affected more by adjusted water loading than by buoyancy as well.

At forecast hour -06 (initialization time), q_c and q_r mixing ratios are set to zero by the model before cloud insertion. Without cloud insertion, these mixing ratios spin-up with time as convection develops. The model is normally in hydrostatic balance only at initialization before cloud insertion. At subsequent forecast times, even when performing a restart, the vertical distribution of pressure is not constrained to be hydrostatic. The cloud insertion procedure inserts cloud at grid points identified to be cloudy and removes cloud mixing ratios at grid points identified to be cloud-free. When clouds are inserted at cloudy grid points, q_v is increased to saturation, and q_c and q_r values are enhanced. At subsequent insertion times on grid points where the cloud insertion procedure diminishes cloud, q_v is entirely replaced by the unsaturated analysis, which produces a negative vertical acceleration component in the hydrostatic balance equation. Additionally, q_c and q_r decreases, which produces a competing positive vertical acceleration component because the water loading term has been removed from the hydrostatic balance equation. Except in columns with strong precipitation before cloud removal, the vertical acceleration may likely change sign from positive to negative in those columns where clouds have been removed.

The question begs whether these non-hydrostatic initial vertical velocity perturbations due to cloud insertion contribute to the dramatic decrease in total domain cloud liquid water mass. To examine this, the post-direct-insertion input file, MMINPUT_DOMAINn, is adjusted to hydrostatic balance after the INTERPF preprocessor. Rain shafts were able to dramatically decrease the magnitude of the hydrostatically balanced pressure perturbation by water loading. This means they caused a positive non-hydrostatic pressure anomaly. The water-loading anomaly was as high as 266 Pa in heavy rain shafts (mixing ratios as high as 19.0 g kg^{-1}) within the domain 2, 13 September 2000, 00-UTC cloud insertion case. Clouds generally increased the hydrostatically balanced pressure perturbation. This means they caused a negative non-hydrostatic pressure anomaly. The buoyancy anomaly was measured as high as 245 Pa within the domain 2, 13 September 2000, 00-UTC cloud insertion case. Clearly, the insertion of clouds is likely to produce some small additional buoyancy, but insertion of heavy rain shafts can produce very large water loading anomalies.

Table 11.1 contains the range of pressure anomalies computed as the difference between the initially hydrostatically balanced pressure perturbations and the hydrostatically balanced pressure perturbations after the insertion of clouds for the 23 modeled sigma levels. Values are given in units of Pa. Positive values indicate hydrostatically balanced pressure perturbation after cloud insertion is less than original hydrostatically balanced pressure perturbation. A positive value indicates a dominant water-loading effect, and a negative value indicates a dominant vapor buoyancy effect.

180

Table 11.1. Range of pressure anomalies (p'$_{original}$ - p'$_{cloud\ insertion}$) versus sigma level for the domain 2, 13 September 2000 00-UTC cloud insertion case.

Sigma Level	Range of Pressure Anomalies (Pa)		Sigma Level	Range of Pressure Anomalies (Pa)	
	MIN	MAX		MIN	MAX
0.025	-233.31	0.13	0.625	-231.29	242.37
0.075	-229.69	52.88	0.675	-210.82	225.09
0.125	-215.28	131.92	0.725	-189.21	205.20
0.175	-215.80	195.77	0.775	-153.65	185.85
0.225	-232.27	219.79	0.825	-129.01	159.16
0.275	-235.93	242.85	0.870	-118.74	128.69
0.325	-237.30	252.03	0.910	-84.60	96.48
0.375	-239.99	259.86	0.945	-53.71	61.27
0.425	-239.07	**266.48**	0.970	-28.45	32.16
0.475	-242.68	266.33	0.985	-12.61	13.49
0.525	**-244.96**	262.01	0.995	0.00	0.00
0.575	-236.62	254.33			
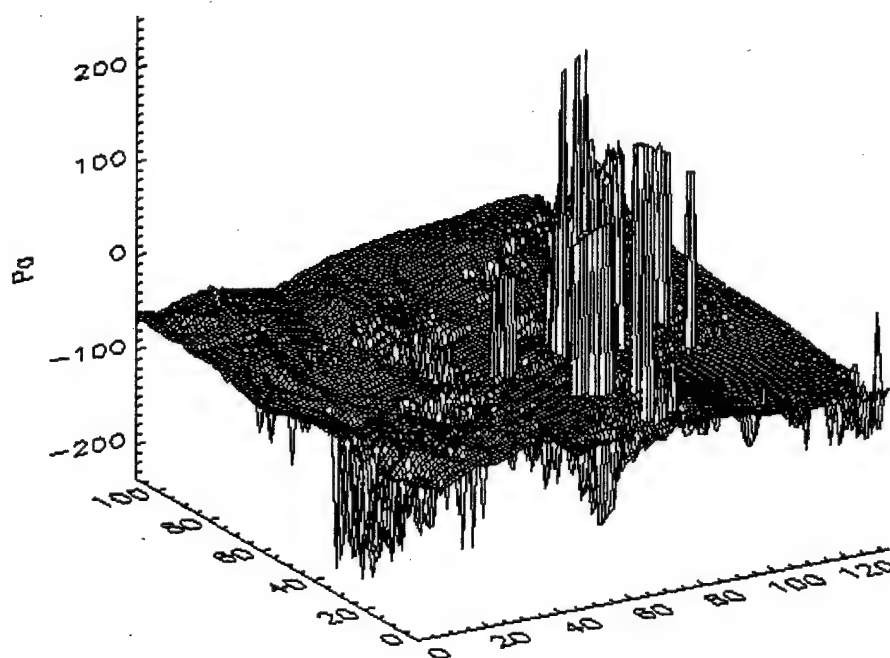
Figure 11.1. Difference between hydrostatic pressure perturbations computed before cloud insertion and after cloud insertion on sigma level 0.575. Horizontal axes identify grid point location; Z-axis indicates magnitude of pressure perturbation difference in Pa. Viewpoint is from the southwest of domain 2 at the 13 September 2000, 00-UTC model initialization time. Large positive peaks indicate horizontal position of large rain mixing ratios on this sigma level.

Figure 11.1 shows the horizontal distribution of the difference between pressure perturbations at the sigma level 0.575. Rain shafts are evident from the water loading effect as positive spikes in the figure. Negative spikes indicate buoyancy anomalies due to adjustment of water vapor to saturation. Large positive areas identically match the areas of heaviest rain mixing ratio (not shown).

MM5 is next initialized with the hydrostatically balanced cloud fields and compared to previous model simulations that are not in hydrostatic balance after cloud insertion. Specifically, the temporal evolution of total domain cloud liquid water is compared between with-cloud insertion cases that are and are not initially in hydrostatic balance between forecast hours -6.0 and -4.5. Figures 11.2a and 11.2b show how total domain cloud liquid water mass varies with time. The solid line represents the hydrostatically balanced full cloud insertion case, and the dotted line represents the non-hydrostatically initialized full cloud insertion case.

Figures 11.2a and 11.2b show that hydrostatic initialization after cloud insertion results in slightly increasing the rate at which cloud is reduced within the first six minutes of model integration. This is because the initially non-hydrostatic vertical distribution of pressure due to cloud insertion (increase of layer virtual temperature) increases buoyancy, possibly enough to initiate a small amount of convection that can maintain more cloud mass in the domain than would be possible otherwise. Therefore, direct insertion of clouds without resetting the vertical pressure distribution to hydrostatic equilibrium is not responsible for the dramatic loss of cloud soon after insertion and further indicates that a larger initial vertical acceleration term may be needed to maintain the clouds. Several other explanations for the initial cloud loss are now explored in the following sections.

b. Answer does not lie in convection scheme

In these simulations, the Grell (1993) convection scheme is used on domain 2. The Grell scheme does not produce cloud liquid water. When using the Grell scheme, cloud liquid water is produced solely by the model's explicit treatment of it. No convection scheme is used on domain 3. This eliminates the need to evaluate the convection scheme's part in producing the spikes at cloud initialization times in the domain mass traces.

Figure 11.2a. Total domain cloud liquid water mass versus forecast hour on domain 2, 13 September 2000 simulation, forecast hours -6.0 to -4.5 (hydrostatic test).

Figure 11.2b. Total domain cloud liquid water mass versus forecast hour on domain 3 (hydrostatic test).

c. Advection and mixing

Is advection responsible for the rapid decrease in cloud mass? To answer this question, we first look at the equations used to simulate the explicit treatment of cloud liquid water. The following equations are adapted from Grell, et al. (1994; chapters 2 and 5). Cloud liquid water is forecast using equation 11.11.

$$\frac{\partial p^* q_c}{\partial t} = -m^2 \left[\frac{\partial p^* u q_c / m}{\partial x} + \frac{\partial p^* u q_c / m}{\partial x} \right] \qquad \text{horizontal advection and divergence term}$$

$$-\frac{\partial p^* q_c \dot{\sigma}}{\partial \sigma} \qquad \text{vertical advection term} \qquad (11.11)$$

$$+ q_c DIV \qquad \text{non - hydrostatic divergence term}$$

$$+ p^* \left(P_{CON} - P_{RC} - P_{RA} \right) \qquad \text{phase conversion process term}$$

$$+ D_{q_c} \qquad \text{diffusion and vertical mixing term}$$

where,

q_c	Cloud liquid water mixing ratio
p^*	Difference between surface pressure and model lid pressure
m	Map scale factor
u, v	Components of horizontal wind
$\dot{\sigma}$	Vertical velocity in sigma coordinates
DIV	Non-hydrostatic divergence equation
D_{qc}	Diffusion and vertical mixing equations
P_{CON}	Release rate of cloud liquid water due to condensation
P_{RC}	Release rate of cloud liquid water due to autoconversion of cloud to rain
P_{RA}	Release rate of cloud liquid water due to collection of cloud liquid water by rain

Immediately after cloud insertion at forecast hours -06 and +00, domain 2 cloud liquid water mass is larger than the quasi-steady mass value preferred by the model, and dq_c/dt becomes strongly negative (see Figure 9.7a). It is not expected that the advection and divergence terms of equation 11.11 would be sufficiently large to result in such a rapid change in cloud water mass. Advection can decrease the mass of cloud liquid water in a domain but it doesn't explain why mass drops so abruptly and why mass stops at some quasi-steady level. The advective time scale (the ratio of domain length to domain average horizontal velocity) for domain 3 is on the order of 4×10^4 seconds (more than 10 hours). A similar 90% decrease in mass would take more than 9 hours instead of 18 minutes. Possible explanations that include advection are summarily dismissed.

Diffluence is also not likely to cause a rapid decrease in cloud mass after insertion. Large horizontal gradients in horizontal velocities have not had time to develop early on in the simulation. Initial horizontal wind fields are estimated from the large-scale wind field and are therefore smoothly distributed. Diffluence is therefore not likely to be large enough to be responsible for such large evaporations. This leaves us to consider the phase conversion processes and evaporation after subsidence and subgrid mixing or diffusion. The local rate of change in cloud liquid water, dq_c/dt, becomes strongly negative if P_{CON}, P_{RC}, P_{RA}, and diffusion become more efficient at large q_c mixing ratios. This is indeed the case.

d. Autoconversion to rain

Let us next consider the release rate due to autoconversion of rain from cloud liquid water. Grell et al. (1994) uses equation 11.12 to convert cloud liquid water to rain.

$$P_{RC} = \max[k_1(q_c - q_{critical}), \quad 0] \tag{11.12}$$

where $k_1 = 10^{-3}$ s^{-1}, and $q_{critical} = 0.5$ g kg^{-1}. In other words, P_{RC} is proportional to how much q_c is larger than 0.5 g kg^{-1}. Because $dq_c/dt \propto P_{RC}$, values of q_c significantly larger than 0.5 g kg^{-1} should result in a rapid decrease in q_c.

e. Collection by rain

The next factor to consider is the release rate due to collection of cloud liquid water by falling rain, P_{RA}. The accretion rate is given by equations 11.13 and 11.14.

$$P_{RA} = \frac{1}{4}\pi a q_c E N_0 \frac{\Gamma(3+b)}{\lambda^{3+b}} \tag{11.13}$$

$$\lambda = \left(\frac{\pi N_0 \rho_w}{\rho q_r}\right)^{1/4} \tag{11.14}$$

Γ is the gamma function, E is the collection efficiency (set to unity), and constants N_0, a, and b are set to 8×10^6 m^{-4}, 841.9967, and 0.8 respectively. In addition, q_r is the rain mixing ratio, ρ_w is the mean density of rain water (1000 kg m^{-3}), and ρ is air density. Just as $dq_c/dt \propto -P_{RC}$, so is $dq_r/dt \propto +P_{RC}$. A large autoconversion of cloud liquid water to rain will rapidly increase the rain mixing ratio. According to equations 11.13 and 11.14, P_{RA} is proportional to $q_c q_r^{1/4}$. Large values of q_c and q_r should therefore produce large values of P_{RA}. Since $dq_c/dt \propto -P_{RA}$, q_c should rapidly decrease if $[-P_{RA}]$ is large.

The mass analysis shows that the change in domain rain mass accounts for the bulk of the change in total domain water mass. It is further inferred that this occurs because of "rainout". To determine if rainout results in significant cloud liquid water accumulation and subsequently significant decreases in cloud liquid water mass, a test cloud insertion simulation is crafted which excludes rain and snow. In this test, only CIS cloud liquid water and ice are inserted into the initial fields valid at 13 September 2000, 00-UTC. The simulation is allowed to run 1.5 hours (from forecast hour -6.0 to -4.5). Figures 11.3a and 11.3b show how total domain cloud liquid water mass varies with time. The dotted line represents the full cloud insertion case, and the solid line represents the precipitation-free cloud insertion case. On both domains 2 and 3, both simulations show a similarly rapid decrease in mass over the first 6 to 18 minutes. This indicates no detectible impact from rainout and cloud water accumulation. The remaining conversion process, autoconversion to ice is temperature dependent and not likely to occur early on in the simulation because mesoscale vertical velocities have not developed

yet. The bulk of cloud liquid water mass, removed immediately after insertion, must therefore be a result of evaporation processes.
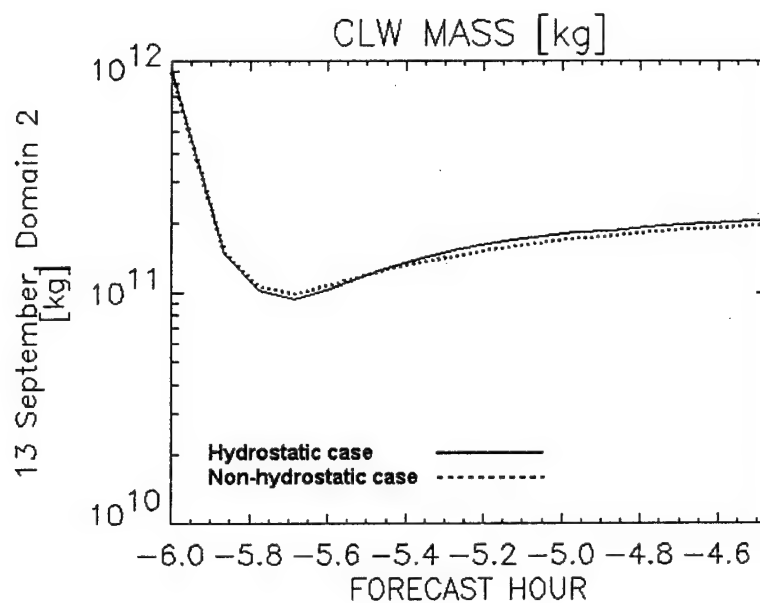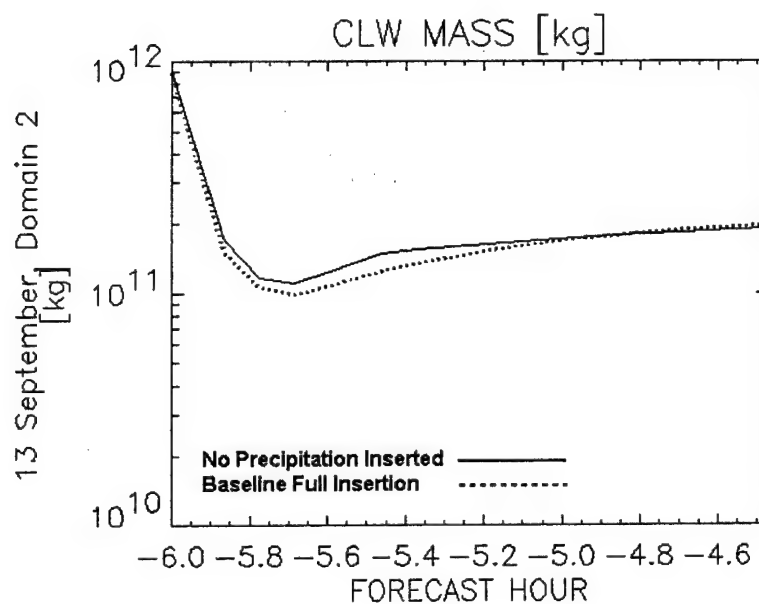

Figure 11.3a. Total domain cloud liquid water mass versus forecast hour on domain 2, 13 September 2000 simulation, forecast hours -6.0 to -4.5 (precipitation test).
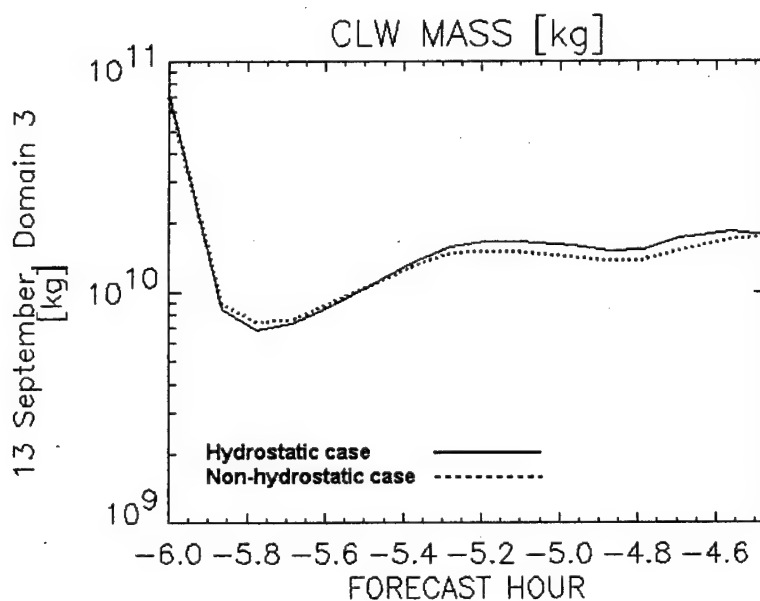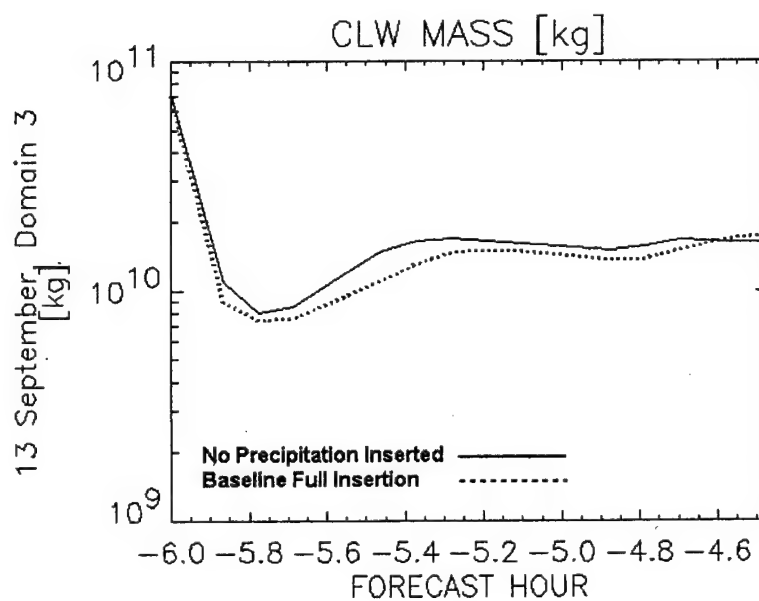

Figure 11.3b. Total domain cloud liquid water mass versus forecast hour on domain 3 (precipitation test).

f. Subsidence

Because mesoscale vertical velocities have not yet developed early on in the simulation, locally strong subsidence is not likely to occur. However, it is likely that large-scale diabatic subsidence is responsible for a large fraction of cloud liquid water evaporation. A test for compatibility between NOGAPS analyzed winds and RTNEPH cloud was conducted in Chapter VIII. It was found that 27% to 77% of the clouds inserted by CIS at any time during the simulation period would be associated with large-scale decent diagnosed from the NOGAPS winds. Evaporation of cloud liquid water is immediate in subsidence for two reasons. First, CIS analyzed cloud uses only a fraction of the adiabatic liquid water content. The adiabatic liquid water content is the maximum quantity of water that can be evaporated during adiabatic descent. Second, the water vapor mixing ratio is set to saturation at cloudy grid points. An air parcel can remain saturated during descent for a short distance only if the parcel was originally supersaturated. Evaporation occurs in unsaturated environments. Large-scale subsidence can account for more than half of the cloud liquid water loss observed only minutes after cloud insertion.

g. Diffusion of cloud liquid water and water vapor

Diffusion of cloud liquid water to neighboring grid points and subsequent evaporation is also a possible explanation for the rapid decrease in mass. Values of q_c directly inserted into a domain have a strongly discrete character and produce very steep gradients of water vapor between neighboring cloudy and cloud-free grid points. In MM5, horizontal diffusion is proportional to the fourth-order functions $\nabla_\sigma^4 q_c$ or $\nabla_\sigma^4 q_v$ and to the horizontal deformation. Such distributions produce large diffusion rates for water vapor and cloud liquid water. Neighboring grid points to cloudy grid points may also not necessarily be near saturation. Strong diffusion of water vapor and cloud liquid water to neighboring unsaturated grid points can redistribute water vapor out of a cloudy grid point and result in subsaturation. In addition to water vapor, diffusion also redistributes cloud liquid water to neighboring unsaturated grid points. If these diffusion rates are large, both diffusion processes will result in initially large evaporation rates and rapidly decrease total domain mass of cloud liquid water.

h. Evaporation after diffusion

The condensation release rate, *Pcon*, is determined as follows. Before cloud insertion, there are no saturated air parcels in the initialization field. Cloud insertion replaces unsaturated water vapor mixing ratios with saturated water vapor mixing ratios at all grid points identified to be cloudy ($q_v = q_{vs}$). No adjustment is made to neighboring cloud-free grid points when clouds are inserted. No grid points in the initialization field are supersaturated at cloud insertion time. Temperature, water vapor mixing ratio, and cloud liquid water are forecast first. The parameterization of cloud liquid water release rate

due to evaporation is then computed diagnostically using the following equation (equation 5.3.1.1.11b from Grell et al. 1994).

$$P_{CON} = -\min\left[-r_1 \frac{\delta M}{\Delta t}, \frac{q_c}{\Delta t}\right], \quad r_1 = \frac{1}{1 + \left(\dfrac{L_v^2 q_{vs}}{R_v c_{pm} T}\right)}, \quad \delta M = q_v - q_{vs} \tag{11.15}$$

At cloud insertion time, $\delta M = 0$, and $P_{CON} = 0$ at all cloudy grid points. No evaporation is occurring at the time of cloud insertion. Immediately following insertion, q_v^* values are not likely to be greater than q_{vs}^* because there are no vertical momentum or thermodynamic changes coordinated with the clouds just inserted. Assuming no diffusion, the magnitude of q_c will be dominated by its value in the previous time step. The magnitude of P_{CON} is computed by comparing the two terms in equation 11.15. Since air in the cloud layer is initially set to saturation, the first comparison term is initially near zero. The second comparison term is large. As diffusion of water vapor begins to decrease the cloudy grid point's water vapor mixing ratio, the first term in the comparison begins to grow to a value larger than zero. P_{CON} evaporation can only be governed by the magnitude of q_c when

$$q_c > r_1(q_v - q_{vs}) \tag{11.16}$$

If cloud liquid water is diffused to a very dry grid point, then P_{CON} will be a function of q_c, otherwise, it will be a function of specific humidity. Because $dq_c/dt \propto P_{CON}$, if the mass of cloud liquid water drops precipitously, P_{CON} must be greatly negative.

To determine if diffusion of water vapor and cloud liquid water is a significant factor in the initially great amounts of evaporation suspected, a test cloud insertion simulation is crafted which excludes rain and snow, and sets all diffusion coefficients to zero. In this test, only CIS cloud liquid water and ice are inserted into the initial fields valid at 13 September 2000, 00-UTC. The simulation is allowed to run 1.5 hours (from forecast hour -6.0 to -4.5). Figures 11.4a and 11.4b show how total domain cloud liquid water mass varies with time. The dotted line represents the full cloud insertion case, and the solid line represents the precipitation-free/diffusion-free cloud insertion case. Data for this case is only provided for the first 48 minutes of model simulation time because without diffusion, the model becomes unstable and fails.
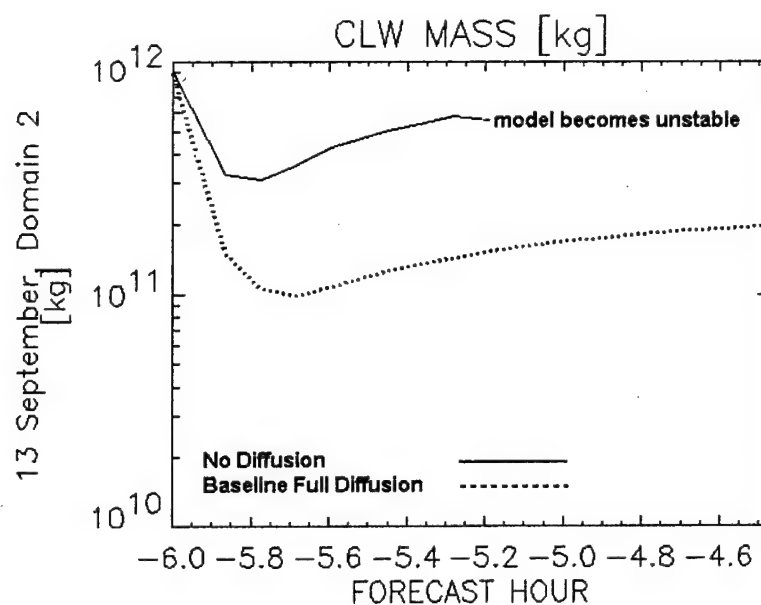
Figure 11.4a. Total domain cloud liquid water mass versus forecast hour on domain 2, 13 September 2000 simulation, forecast hours -6.0 to -4.5 (diffusion test).
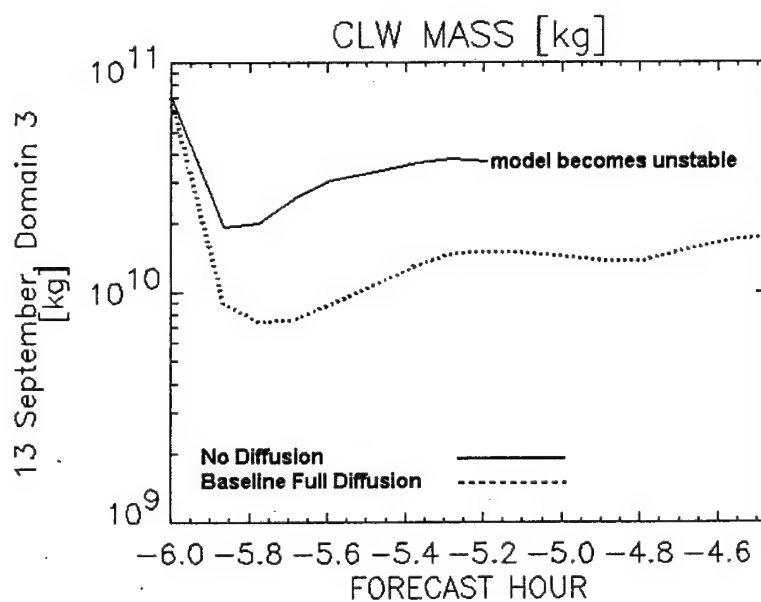
Figure 11.4b. Total domain cloud liquid water mass versus forecast hour on domain 3 (diffusion test).

With both initial precipitation and diffusion removed, total cloud liquid water mass on domain 2 decreases only 66% instead of 89% within the first few minutes of the simulation. On domain 3, total

cloud liquid water mass decreases only 71% instead of 89%. Large-scale subsidence most likely accounts for a large portion of the remaining decrease in mass. Subsidence evaporation is likely larger on domain 2 than on domain 3 because a larger fraction of domain 2 is in a subsidence regime.

These results lead to the conclusion that MM5 is not well suited to cloud initialization without two important changes. The first change must be in how MM5 handles subgrid scale mixing of discrete clouds. The model's diffusion equations must be adjusted to reduce the rapid diffusion of discrete cloud liquid water distributions. The model's tendency to produce smooth distributions of water vapor is contrary to maintaining realistic cloud distributions. This tendency also results in greater difficulty in defining cloud coverage amounts based on mixing ratios. The second change must be to the initialization wind fields that control subsidence evaporation. Clouds cannot persist long in subsidence. To reduce subsidence evaporation, the large-scale velocity field must have cloud-scale adjustments to account for the observed distribution of clouds. To reduce the effect of rainout, smooth initial vertical velocity distributions must have cloud scale adjustments to create circulations that will sustain cloud creation near initial precipitation. Without these changes, MM5 is a poor trajectory model for discretely introduced clouds.

11.2. A Method to Estimate Model Spin-Up

This section presents a method to objectively estimate how much total domain cloud liquid water mass MM5 will produce and when MM5 has spun-up. Cloud liquid water is the only cloud variable used here to estimate spin-up time. MM5's cloud physics package depends primarily on two factors to produce cloud liquid water -- vertical motion and supersaturation. Other processes such as vapor convergence, precipitation, and diffusion and evaporation are considered equal in importance. Vertical motion and supersaturation are easily diagnosed from the smooth and continuous fields of vertical velocity, temperature, water vapor and pressure. It is expected that cloud liquid water mass produced in each model time step will equilibrate well with vertical motion and diagnosed supersaturation.

An estimate of the spin-up total domain mass of cloud liquid water is computed using a simple lifting scheme to compute cloud condensation from supersaturation. Parcels are lifted from one sigma level (σ_k) to the next highest sigma level (σ_{k-1}). The condensation rate occurring because of supersaturation is computed using a formula similar to that used in the model (equation 5.3.1.1.11a, Grell et al. 1994).

$$P_{CON} = \frac{\left(\dfrac{q_v - q_{vs}}{\Delta t} \right)}{1 + \left(\dfrac{L_v^2 q_{vs}}{R_v c_{pm} T} \right)} F \approx \frac{\Delta q_c}{\Delta t} \qquad (11.17)$$

The supersaturation ($q_v - q_{vs}$) is computed using q_v, the mixing ratio at sigma level k, (σ_k), and q_{vs}, the saturation mixing ratio at the sigma level above, (σ_{k-1}). The condensation rate at the sigma level above,

P_{CON}, is weighted by the fraction (F) of the sigma layer that can be vertically advected in a unit model time step. This fraction is estimated as follows.

$$F = \left(\dot{\sigma} \frac{\Delta t}{\Delta \sigma} \right)$$
$$\Delta \sigma = \sigma_{k-1} - \sigma_k \tag{11.18}$$
$$\Delta t = \text{model time step}$$

Condensation of water vapor to cloud liquid water is assumed to occur only above melting temperature ($T > 0°C$), and only when lifting the parcel to the next sigma level results in supersaturation. Equation 11.17 is now reduced by multiplying through by the unit time step.

$$\frac{q_v - q_{vs}}{1 + \left(\dfrac{L_v^2 q_{vs}}{R_v c_{pm} T} \right)} \left(\dot{\sigma} \frac{\Delta t}{\Delta \sigma} \right) \approx \Delta q_c \tag{11.19}$$

Next, we integrate over the entire domain to estimate the spin-up mass of cloud liquid water that is equilibrated with the vertical motion field scaled by a factor of 10. This arbitrary scaling factor is akin to assigning a scale factor to an analog signal from an instrument to translate the meaning of the signal into a useful value. In this case, the "useful value" is an estimate of the total domain cloud liquid water mass that would exist in the model domain had the model been equilibrated with the humidity field (or spun up). It was selected based on several trials of spin up mass calculations computed as follows:

$$\text{Spinup Mass} \approx 10 \iiint_{x,y,\sigma} \frac{q_v - q_{vs}}{1 + \left(\dfrac{L_v^2 q_{vs}}{R_v c_{pm} T} \right)} \left(\dot{\sigma} \frac{\Delta t}{\Delta \sigma} \right) \frac{P^* d\sigma dx dy}{g} \tag{11.20}$$

Finally, to estimate when the model has reached spin-up, we simply calculate the mass of cloud liquid water present in the model at each time step, and then compare it to the estimated spin-up mass.

$$\iiint_{x,y,\sigma} \frac{q_c P^* d\sigma dx dy}{g} \approx 10 \iiint_{x,y,\sigma} \frac{q_v - q_{vs}}{1 + \left(\dfrac{L_v^2 q_{vs}}{R_v c_{pm} T} \right)} \left(\dot{\sigma} \frac{\Delta t}{\Delta \sigma} \right) \frac{P^* d\sigma dx dy}{g} \tag{11.21}$$

Because estimated spin-up mass is also computed at each time step using vertical velocities, cloud liquid water mass estimates should equilibrate with the upward motion producing clouds in a given time step. For example, if vertical motion throughout the domain is decreasing, the estimate of cloud liquid water mass should decrease as well. This will reduce the likelihood that model spin-up will be confused with developing circulations as compared to a model already equilibrated with the humidity field (see definition of spin-up in Section 2.2, or see Lee and Krishnamurti 1995).

Note that the estimate of total domain spin-up mass is one-tenth the amount of water estimated to arise in each time step due to lifting condensation. When the total domain spin-up mass is equivalent to the mass of cloud liquid water produced by the domain, and when the total domain mass of cloud liquid

water is quasi-steady, then a balance must occur between the 10% increase in cloud liquid water created by lifting condensation and an equal 10% decrease due to phase changes and to a lesser extent due to accumulation by precipitation. This method of estimating the quasi-steady total domain spin-up mass assumes that only 10% of the cloud mass is in some phase transition at any given time.

To test the effectiveness of this method at estimating when cloud liquid water has been "spun-up", cloud liquid water, water vapor, temperature, vertical velocity, and pressure data were sampled at 6-minute intervals between forecast hours -06 to +12 for both 13 September and 14 September model simulations. Only the without-cloud initialization simulations were studied because the with-cloud initialization simulations apparently have no cloud spin-up characteristics. Spin-up cloud liquid water mass is estimated then compared to the cloud liquid water mass output by the model. These comparisons are presented in Figures 11.5a through 11.5d. Spin-up time for cloud liquid water mass varied between 0.2 and 7.3 hours. After spin-up, estimated mass and modeled mass are reasonably close.

The question remains concerning the quasi-static character of q_c mass well beyond direct insertion times, even for the without-cloud initialization simulations. If the primary source and sink of q_c is PCON (either positive or negative values), then q_c is subject primarily to the fluctuations of water vapor, q_v, the largest and most continuous water constituent in the domain. Recall from equation 11.15 that when $\Delta q_c / \Delta t$ is large, evaporation will be dominated by the term

$$
\frac{\left(\dfrac{\delta M}{\Delta t} \right)}{1 + \left(\dfrac{L_v^2 q_{vs}^*}{R_v c_{pm} T^*} \right)}
\tag{11.22}
$$

This term is wholly controlled by forecast values of smooth and continuous variables, namely temperature, pressure and water vapor mixing ratio. Domain averaged values of q_v, p, and T do not change quickly and therefore result in only slowly changing totals of cloud liquid water.

Est Spinup and modeled CLW mass for domain 2

SPINUP TAKES ABOUT 1.6 HOURS

Forecast hour, 13 SEP 2000 Simulation
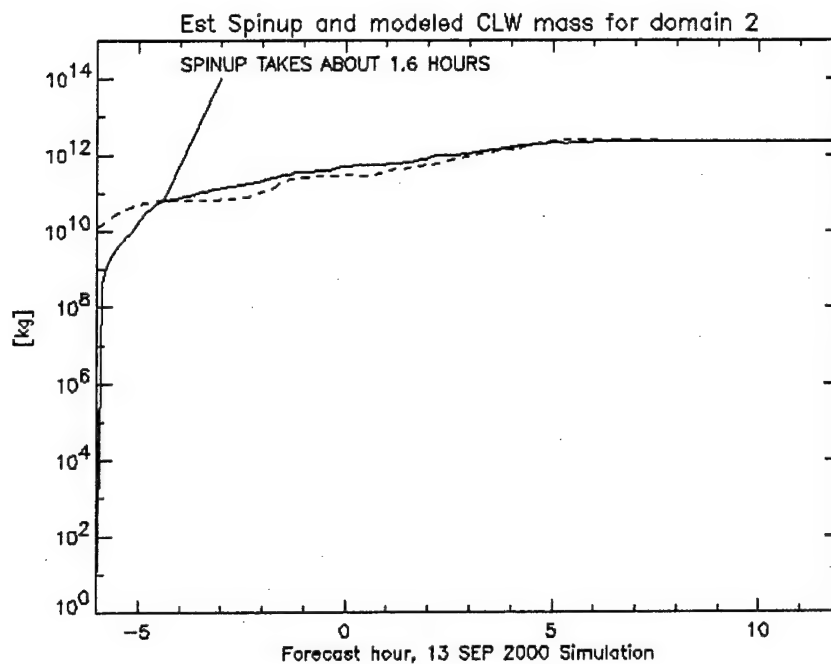
Figure 11.5a. Spin-up total domain cloud liquid water mass versus forecast hour on domain 2 for the 13 September 2000 simulation. Solid line indicates mass of cloud liquid water computed by model at each time step. Dashed line indicates estimation of spin-up mass of cloud liquid water.

Est Spinup and modeled CLW mass for domain 2

SPINUP TAKES ABOUT 0.5 HOURS

Forecast hour, 14 SEP 2000 Simulation
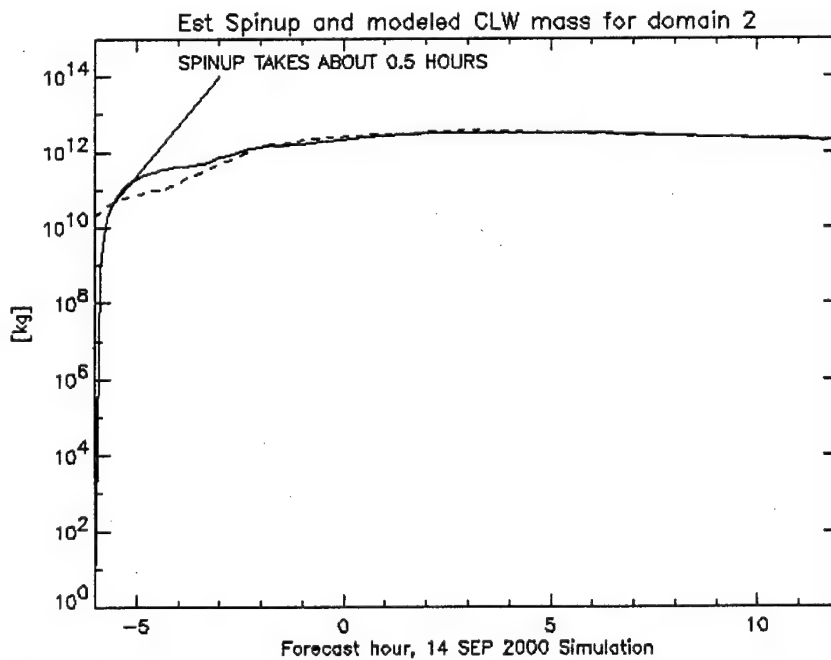
Figure 11.5b. Spin-up total domain cloud liquid water mass versus forecast hour on domain 2 for the 14 September 2000 simulation.
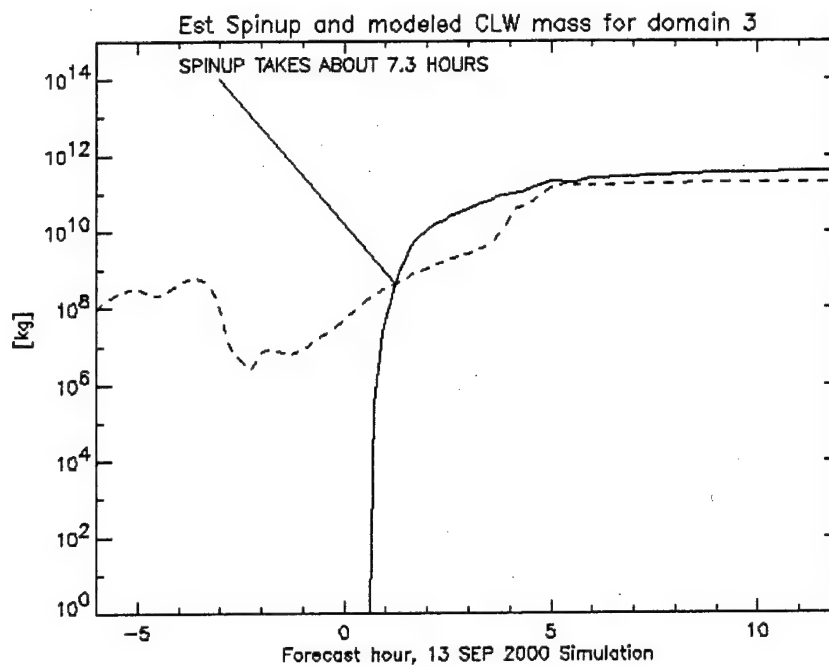
Figure 11.5c. Spin-up total domain cloud liquid water mass versus forecast hour on domain 3 for the 13 September 2000 simulation.
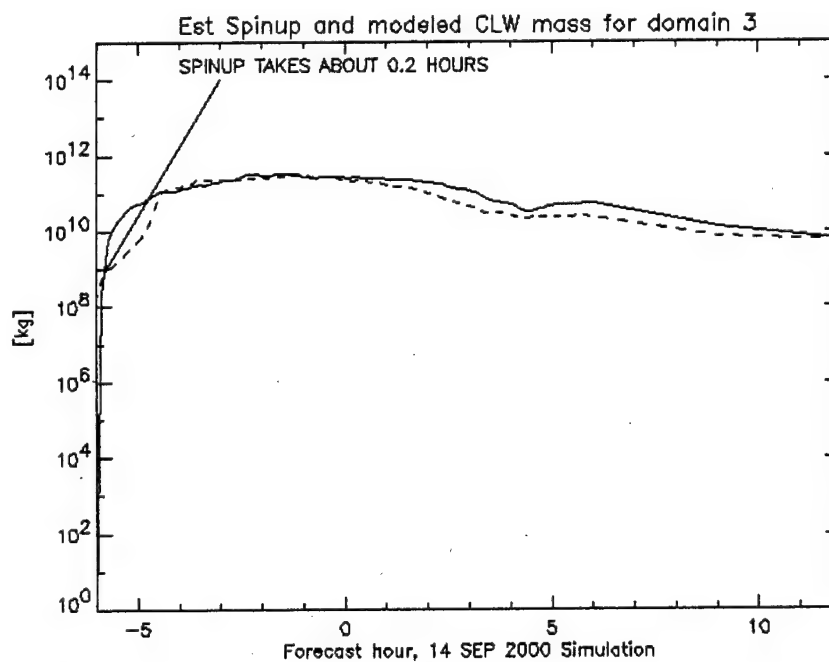
Figure 11.5d. Spin-up total domain cloud liquid water mass versus forecast hour on domain 3 for the 14 September 2000 simulation.

The argument for explaining the behavior of total domain cloud ice is nearly identical to that for cloud liquid water except process functions are with respect to ice instead of to water. Finally, because rain and snow are largely governed by the present concentrations of cloud liquid water and cloud ice, their domain mass totals will vary in a similar fashion.

Figures 11.5a through 11.5d show that after model spin-up, the estimated cloud liquid water mass is well coordinated with the model output of cloud liquid water mass. This coordination suggests that another way to initialize cloud variables may be to use the above estimation method independent of cloud observations. The cloud liquid water fields would then be immediately equilibrated with the distribution of vertical velocity. No cloud analysis would be necessary to eliminate cloud liquid water spin-up. To test this notion, a cloud liquid water mixing ratio is computed using equation 11.19. The distribution of cloud liquid water found using this equation is then directly inserted into MM5 initialization files for domains 2 and 3 for the 13 September 2000, 00-UTC case. Water vapor was also adjusted to saturation wherever clouds were inserted. The cloud insertion was performed only at forecast hour -06, and the model was integrated for 18 hours saving data every six minutes. Figures 11.6a and 11.6b are plots of the model produced and estimated spin-up total domain cloud liquid water masses. The domain-2 plot shows that spin-up is almost immediate (compare to the same case with no cloud insertion in Figure 11.5a). The domain-3 plot (Figure 11.6b), however, shows a dramatic drop in the cloud liquid water mass soon after insertion then nearly parallels the trace of Figure 11.5c. This may indicate some scale dependence on applying the method or it may indicate diffusion and evaporation was much stronger on this domain.
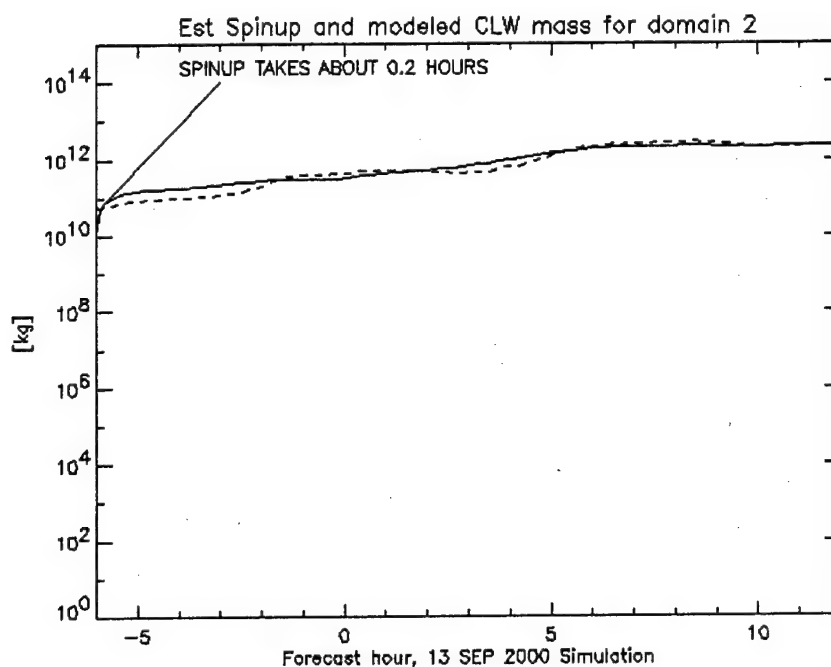
Figure 11.6a. Estimate of spin-up total domain cloud liquid water mass versus forecast hour on domain 2 for the 13 September 2000 simulation. Solid line indicates mass of cloud liquid water computed by model at each time step after cloud insertion at forecast hour -06. Dashed line indicates estimation of spin-up mass of cloud liquid water.
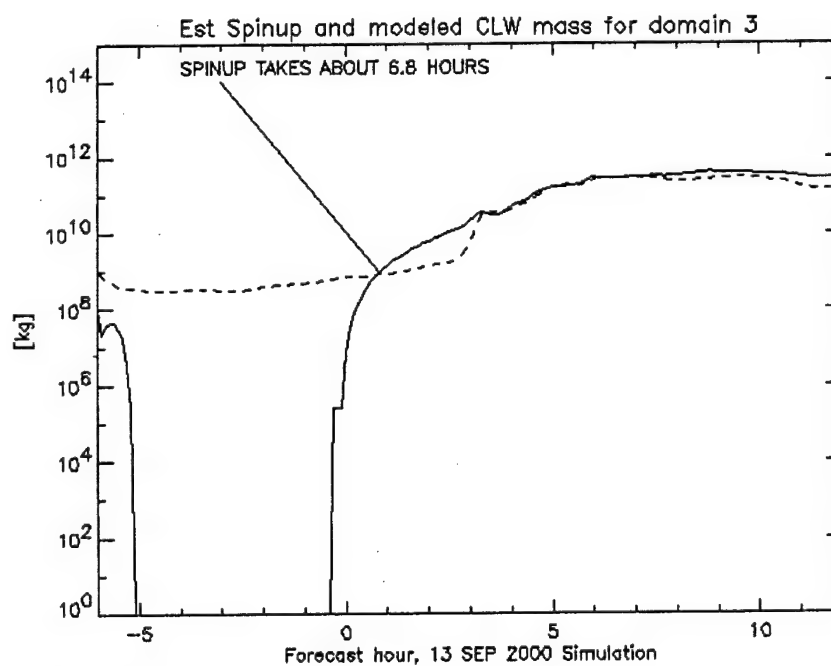
Figure 11.6b. Estimate of spin-up total domain cloud liquid water mass versus forecast hour on domain 3 for the 13 September 2000 simulation, with-cloud insertion case.

CHAPTER XII
CONCLUSION

12.1. Summary of Research

a. CIS

A method to convert the Air Force's Real-Time Nephanalysis, RTNEPH, to cloud variables, which can be used to initialize the PSU/NCAR MM5 mesoscale NWP model, has been presented. This method converts cloud amounts, types, top altitude, and base altitude to mixing ratios of cloud liquid water, cloud ice, rain and snow. The method also adjusts water vapor to saturation at cloud filled locations. The conversion process, called the Cloud Initialization Scheme (CIS), is performed in five steps:

1) RTNEPH DISTRIBUTION

Horizontally and vertically distribute the RTNEPH clouds to the mesoscale model grid (Chapter IV). Because up to four layers of cloud are possible over any one surface grid point, a unique scheme is developed to deconstruct cloud layer amounts into obscured and unobscured fractions. These fractions are then randomly distributed to model grid points that are horizontally spaced at roughly 1/9th and 1/64th of the original RTNEPH data resolution. Vertical distribution of cloud is done using a simple height intersection method. Cloud is placed on a model grid point at a given vertical level if that level occurs between a cloud's base and top.

2) CLOUD LIQUID WATER AND CLOUD ICE

Diagnose cloud liquid water mixing ratio using an adiabatic condensation method between the known cloud base and cloud top (Chapter V). The diagnostic method also includes entrainment factors based on cloud type. These entrainment factors comprise the most sensitive tuning parameters of the cloud initialization scheme. Once cloud liquid water mixing ratio is computed, parameterizations for homogeneous freezing and ice initiation are used to estimate cloud ice mixing ratio. These parameterizations are based on the physics package used in MM5.

3) RELEASE RATES

Diagnose the release rate of each cloud variable using parameterizations for several microphysical processes. Excluding the adiabatic estimate of cloud liquid water, 19 separate microphysical processes involving cloud liquid water, cloud ice, rain, and snow are estimated using bulk parameterizations in CIS. No graupel processes are included. Although CIS incorporates many release rate parameterizations found in the Reisner scheme, there are several distinct differences.

- Cloud locations are discrete and explicitly defined.
- Cloud liquid water and cloud ice mixing ratios are diagnosed instead of solved using prognostic equations.
- New parameterizations for the accumulation of snow by rain and for the accumulation of rain by snow are developed. The Reisner parameterizations were too unstable for the diagnostic downward vertical integrations used to compute rain and snow rates.
- Following the method of Zhao and Carr (1997), parameterizations for the accretion of cloud liquid water by snow, and for snow melt due to accumulation of cloud liquid water are added to CIS.

4) PRECIPITATION RATES

Diagnose rain and snow precipitation rates by integrating their release rates downward from the top of the modeled domain. The method used is fundamentally based on the work of Zhao and Carr (1997).

5) PRECIPITATION MIXING RATIOS

Parameterize rain and snow mixing ratios using precipitation rates. Time derivatives are removed by using idealized rain and snow size distributions that are functions of precipitation rates. These functions were developed by Sekhon and Srivastava (1970, 1971). The resulting equations to describe the rain and snow mixing ratios are purely diagnostic.

b. Tuning CIS

CIS was tested on six idealized vertical cloud profiles typical of what would be found in the RTNEPH database (Chapter VI). Those six profiles included multi-layered clouds (St/Ns, Cb/Cs, and Cu/As), single-layer clouds (St, Cb), and a clear column case. All the cases demonstrated reasonable vertical distribution of cloud species mixing ratio as a function of cloud type, cloud depth, and distance below cloud (if any). A special Cb test, which has cloud base at the melting level and saturated air below, was included. That test demonstrated reasonable phase conversion processes excluding evaporation below cloud base.

c. Source data

The mesoscale model used in this study was initialized with the Navy Operational Global and Regional Atmospheric Prediction System (NOGAPS) analysis and the Air Force's Surface Temperature Analysis (SFCTEMP). The NOGAPS analysis provides data at standard pressure levels while SFCTEMP provides data only at the surface. A data incompatibility between NOGAPS and SFCTEMP was revealed where NOGAPS temperatures on standard pressure levels intersected the surface

(Appendix E). To solve the data incompatibility problem, a non-linear vertical interpolation scheme for temperature was developed and presented. Temperatures were weighted in favor of SFCTEMP temperatures because they are updated more frequently and are archived at higher resolution. Air Force Weather Agency is encouraged to consider implementing this non-linear vertical interpolation scheme in order to make NOGAPS and SFCTEMP compatible for initialization of MM5.

A compatibility analysis was also performed between NOGAPS vertical winds and RTNEPH clouds (Chapter VIII). NOGAPS vertical winds were diagnosed assuming hydrostatic mass continuity. RTNEPH cloudy locations were compared to vertical motion diagnosed from NOGAPS winds. It was found that the distribution of clouds in regions of ascent generally differs from random placement. It was also found that on model initialization, half of the clouds would be dissipated by large-scale descent.

d. Experiment

A cloud variable analysis was produced using CIS at 3-hourly intervals. This analysis was compared to mesoscale model simulation output of the same variables. Some of the model simulations used CIS to initialize cloud variables. Because the mesoscale model does not output cloud type, cloud top, or cloud base information, no direct comparison with RTNEPH data was made. The purpose of the experiment was two-fold: to determine if model simulations initialized using CIS would spin-up faster than model simulations without initialization, and to determine if model simulations initialized using CIS would improve cloud variable forecasts over model simulations without cloud initialization.

Input data covered the period 13 September 2000, 00-UTC through 15 September 2000, 18-UTC. CIS cloud variables were diagnosed from RTNEPH, NOGAPS, and SFCTEMP, at 3-hourly intervals, on 18-km and 6-km grids. The PSU/NCAR MM5 mesoscale NWP model was used with three nested domains having grid spacing of 54 km (domain 1), 18 km (domain 2), and 6 km (domain 3). Domains 1 and 2 cover most of the United States. Domain 3 is roughly 400 km wide centered over the Houston Ship Channel. Among the physics packages selected for these simulations, the Reisner mixed-phase cloud physics scheme excluding graupel, the Grell convective scheme, and the MRF and Blackadar boundary layer schemes were used. FDDA was used to nudge initial temperatures and winds to analyzed temperatures and winds at forecast hours -06 and +00. All nesting was two-way.

Two simulation periods were examined in detail: a 24-hour forecast starting at 13 September 2000, 06-UTC, and a 24-hour forecast starting at 14 September 2000, 18-UTC. Both simulation periods also had 6 hours of dynamic initialization before forecast hour +00. Two types of simulations were performed -- with and without cloud initialization. Assimilation of cloud data was performed using direct insertion of CIS-diagnosed cloud species mixing ratios at forecast hours -06 and +00 into domains 2 and 3. Assimilation of clouds on domain 1 was performed using a Barnes analysis technique that analyzes cloud species mixing ratios from domain 2.

The weather situation for 13 through 15 September 2000 involved a stationary front that was positioned parallel to and just inland of the Gulf Coast along Texas and Louisiana. This front produced persistent clouds and scattered precipitation. A subjective analysis of the frontal system revealed that the presence of clouds and precipitation might have been a necessary pre-condition for the maintenance of the system. Midlevel advection of dry air north of the front would not have produced clouds if the drier air were not contributing to a mesoscale circulation that maintained a convective circulation oriented perpendicular to the front. Although randomly selected, such a scenario nevertheless proved useful in evaluating whether cloud initialization would contribute to accurately simulating clouds along the front (Chapter VII).

12.2. Inferences from Results

The large-scale analysis and local-scale analysis conducted in Chapters IX and X demonstrated that there are large differences between the CIS cloud species mixing ratio analysis and MM5's cloud species mixing ratio forecasts. The temporal variation of CIS total domain water species mass is larger than that of the simulations. Total domain cloud species mass from CIS can be one to two orders of magnitude larger than mass values produced by MM5. It is not clear whether the differences in total domain mass between the analysis and the model are due to over-analyzing or under-forecasting. CIS mixing ratios have a larger measure of "discreteness" than MM5 mixing ratios. Additionally, CIS cloud and precipitation water is more likely to have higher mixing ratios at fewer grid points than MM5 cloud and precipitation water. MM5 reduces the discrete characteristics of CIS cloud and precipitation after direct insertion. From this result, it is not clear whether the CIS analysis is overly discrete or whether the MM5 simulation results are not discrete enough.

Unfortunately, but not unexpectedly, direct insertion of clouds has little impact on cloud forecast skill beyond 6 to 12 hours after the start of dynamic initialization (Chapter X). Cloud insertion slightly improves most forecast skill scores but second moment statistics were dismally low or useless. It was also demonstrated that the model has a tendency to over forecast clouds and precipitation when compared to the cloud analysis produced by CIS. The results suggest that direct insertion of clouds is insufficient to significantly improve cloud forecasts.

Direct insertion of clouds resulted in nearly immediate equilibration of total domain cloud liquid water and cloud ice mass. As a measure of spin-up, this indicates that spin-up was immediate, within 12 minutes of model start time. Although CIS may have over-analyzed mixing ratios, the model was rather insensitive to the over-insertion of cloud water. Instead, the model rapidly adjusted mass quantities to quasi-stationary levels that appear independent of initial values. The model tended toward those quasi-stationary levels whether clouds were directly inserted or allowed to develop through dynamic initialization.

The model's insensitivity to over-cloud initialization was attributed to three distinct problems (Chapter XI). First, nearly half of the clouds inserted were diagnosed in regions of synoptic scale descent. Clouds in those regions are subsequently destroyed by drying subsidence. Second, the model's diffusion scheme assumes cloud species mixing ratios are smooth and continuous state variables. This makes it impossible to simulate the dramatically discrete characteristics of clouds we see in nature. The diffusion of clouds to neighboring grid points results in rapidly mixing and evaporating cloud elements. Diffusion and subsequent evaporation of discrete cloud species mixing ratios to neighboring cloud-free grid points was attributed to 35% of the rapid adjustment of cloud mass. Third, no cloud-scale vertical velocities were inserted with the clouds to maintain convection. As a result, nearly all of the precipitation inserted rained out within minutes.

Two of these problems may be solved by developing a parameterization for cloud-scale vertical velocities as a function of RTNEPH cloud distribution and then assimilating those vertical winds by dynamically adjusting the synoptic wind field. This will reduce the impact of synoptic scale descent on clouds, and this will help to maintain those circulations responsible for producing precipitation clouds. In addition to altering the initial data environment, changes must be made to the mesoscale model. The mesoscale model's diffusion scheme must be examined to determine if it can be reformulated to be "friendlier" to discrete cloud fields on initialization.

These results are not unique. Recently GOES analyzed optical depths were compared to MM5 forecasts of optical depth, which is a function of liquid water and ice water paths (Kelly et al. 2001). It was concluded in that study that forecast accuracy depends on the time of day in which the forecast was initialized because the model lacked a diurnal cycle of clouds as strong as that found in the GOES data. It was also found that forecast accuracy depends on the length of the forecast because the model under-forecasts clouds during the spin-up phase. Forecast accuracy was found to be highly accurate when dynamical forcing was strong. Kelly et al. (2001) tested several microphysical parameterization schemes available in MM5. They found that every scheme tested produced more clouds than observed. They suggest that more work is required to isolate the cause of the cloudy bias in MM5. The work heretofore presented has attempted to answer that question.

12.3. Variational Assimilation of RTNEPH

a. Discussion

Three-dimensional variational (3D-VAR) assimilation was considered as an alternative approach to direct insertion of clouds. This question was quite challenging. Useful introductions to variational techniques are given in Talagrand 1997, Cortier 1997, Lorenc 1986, and a book by Daley 1991.

Talagrand (1997) classifies the type of observations suitable for assimilation in NWP models as either "direct" or "indirect". Direct observations estimate the same physical quantities used in the

desired description of the flow (typically velocity, temperature, and humidity). Indirect observations are quantities that are functions of the quantities chosen for describing the flow. In the case of RTNEPH data this raises the question; "Are RTNEPH cloud quantities direct or indirect?" RTNEPH cloud quantities include cloud coverage amount (% coverage over a 48 km square area), cloud base and top altitudes, and cloud type. RTNEPH cloud quantities are clearly not direct observations as the definition applies to NWP.

The next question raised is then; "Can RTNEPH cloud quantities be described as complex functions of the quantities chosen to describe the flow?" The answer is no. Such observations are neither smooth nor continuous and have far more variability and discrete character than NWP prognostic variables. One thing to keep in mind is that RTNEPH quantities are the result of merging observations, satellite brightness temperatures, and even manual bogusing. Much of the RTNEPH algorithm is rules-based and therefore cannot be well approximated with integrating linear or non-linear functions of state variables. In fact, observations of water vapor or cloud liquid water contents do not go into RTNEPH at all. It is possible to define cloudy layers in NWP models by selecting threshold mixing ratios of water vapor and cloud liquid water; however, these fields are smooth and continuous and do not represent the discrete nature and high vertical resolution of the RTNEPH data very well. Two RTNEPH quantities viable for selection for assimilation are cloud coverage amount and maximum cloud top height. Vandenberghe (1999) recommends that these are the only RTNEPH variables that can be advantageously used in NWP but not necessarily via variational assimilation. Cloud coverage amount can be estimated from mixing ratios of water vapor and cloud liquid water and ice generated by the model. Similarly, maximum cloud height can be estimated from the model altitude of threshold mixing ratios of water vapor and cloud liquid water and ice. A comparison between MM5 forecast variables and RTNEPH clouds revealed there are no good combinations of MM5 variables that can diagnose forecast cloud patterns that match RTNEPH cloud patterns (Norquist 1999).

At the outset, RTNEPH data does not make good direct nor indirect observations viable for assimilation in MM5. There is some hope though. In the scheme presented here, RTNEPH quantities are used to produce mixing ratios of saturated water vapor, cloud liquid water, cloud ice, rain, and snow. Depending on the error covariances of the parameterized mixing ratios and on the error covariances of the model forecast mixing ratios, RTNEPH parameterized mixing ratios are strong candidates for assimilation.

Variational assimilation has two pitfalls. First, the dynamical balance present in the background is not well preserved in the analysis: the whole model state is subjected to the vagaries of imbalance introduced by the assimilation process (Andrews 1997). This is a problem if the model variables are not good predictors of the observations, which is especially true of RTNEPH clouds. Second, in order to extract the most information from an observation, we want to make the best possible model prediction of it; this is something that is not done well for clouds in MM5 (Norquist 1999).

RTNEPH observations are available at 30-m vertical resolution in the lowest 6 km then at 300-m vertical resolution. That translates to 255 levels of cloud information. MM5 works on roughly up to 30 or 40 levels and grossly parameterizes for the effects of clouds by partitioning them into low, medium or high regions and using subsaturated water vapor mixing ratios. There is little hope that MM5 can assimilate information from RTNEPH unless it is converted to variables that do not have such discrete characteristics.

In this research, cloud data is treated as horizontally independent, meaning they are treated as horizontally discrete variables, which are assumed independent of any horizontal gradients or that they have no horizontal correlation. For this reason a 3D-VAR approach has been discarded; however, an approach using 1D-VAR in the vertical has been earnestly considered. A direct 1D-VAR approach with RTNEPH cloud data may be beneficial because of the type of observations these data represent. The point of variational assimilation is to find the initial state variables that maximize a measure of the degree of fit between a first guess state and the observations. Clouds in RTNEPH vary dramatically in the vertical (meaning at a given level, clouds are either there or they are not) so there will likely be large unrealistic changes from the first guess after assimilation. Fillion and Errico (1997) stated that properly treating these types of discontinuities is a significant problem.

b. Challenges to variational assimilation of RTNEPH

Granted, the mixing ratios parameterized in the cloud initialization scheme (CIS) are treated like poor-quality soundings of water, ice, rain, and snow -- there is room for improvement already. Indirect assimilation of RTNEPH via these mixing ratios using 1D-VAR may improve forecast accuracy more than simply directly inserting mixing ratios from these "observations". Some of the problems that would need to be overcome are the following:

1) ESTIMATE BACKGROUND ERROR COVARIANCE MATRIX FOR MM5

Andrews (1997) recommends the so-called National Meteorological Center (NMC) method, which uses the difference between two forecasts valid for the same time but starting at different times and from different analyses. In this method, you compute the difference between 24-hour and 48-hour forecasts. This will balance errors introduced by the analysis, or even diurnal cycles in the atmosphere. In order to obtain reasonable, slowly time varying background error covariances, average the differences over a 2-week period. Then for each variable at each model level, average the differences over the horizontal domain and all cases. Finally, construct a vertical covariance matrix for each variable. (This would constitute a full study on its own in generating the statistics than analyzing them for tests against Gaussian assumptions, which are demanded in the assimilation step).

2) ESTIMATE ERROR COVARIANCE MATRIX FOR CIS MIXING RATIOS

Error covariances from CIS mixing ratios have not yet been estimated. These error metrics are a prerequisite to performing variational assimilation. It is also necessary to determine if a Gaussian error covariance matrix would be suitable to represent CIS mixing ratio error covariance. One way of estimating error in CIS mixing ratios would be to compare it to liquid water mixing ratios computed from coincident radar data.

3) DEVELOP ASSIMILATION ALGORITHM AND PROGRAM SOURCE CODE

The algorithm can be developed using those already provided in the literature to assimilate satellite brightness temperatures (e.g., Eyre et al. 1993, Fillion and Errico 1997). Using MM5's FDDA subroutines as a template or modifying them to process the desired mixing ratios are other ways to get this done quickly. FDDA currently does not deal with mixing ratios other than water vapor.

c. Benefits and goals of variational assimilation of RTNEPH

Other than simply improving the forecast of clouds, assimilation of RTNEPH data could have other indirect positive uses. Radiative flux (as measured by various spacecraft) can be estimated from complex functions of temperature and humidity profiles, cloud amount, cloud top pressure, and surface emissivity through a radiative transfer equation. By assimilating RTNEPH cloud-top-level pressure and amount, a better assimilation of radiative fluxes observed by satellites is possible. One-dimensional variational (1D-VAR) assimilation of RTNEPH mixing ratios can be accomplished and may even prove beneficial because it can provide coupling with dynamical processes in MM5.

The goal of the research presented herein was to first attack the simpler problem of the lack of observed values of water, ice, rain, and snow on model initialization. The only way to initialize models was to use previously forecast water content or to not use any at all and just wait for spin-up to give reasonable mixing ratios. The technique of cloud initialization presented here is an alternative to these two. Developing an assimilation technique is the next step. It has been established that the model forecast has some sensitivity to cloud initialization using mixing ratio profiles with direct insertion. Use of 1D-VAR could tune the process even further. A comparison of direct insertion with 1D-VAR would be most instructive in future work as well. If these additional steps were to be undertaken, a good research model would be to follow the example of Fillion and Errico (1997).

12.4. Other Future Research

a. Vertical velocity distribution

The most pressing problem with cloud initialization is that a way to estimate the vertical velocity distribution must be found which can be coupled with the cloud variable distribution. One method to

initialize a vertical velocity field coincident with a cloud analysis is summarized by McGinley and Smart (2001) for the Local Analysis and Prediction System (LAPS). After performing the cloud analysis portion of LAPS, a perturbation cloud omega value is determined using diagnosed cloud type, base altitude and top altitude. A constant perturbation vertical velocity value of 0.05 m s^{-1} is used in stratiform clouds. In cumuliform clouds, perturbation vertical velocity is computed from a parabolic function which has an amplitude proportional to cloud depth, reaches a peak one-third of the way up the base, and extends below the cloud base by one-third of the cloud depth. The parabolic function used to define vertical velocity in cumuliform clouds is estimated using Shultz and Albers (2001, Figure 1). It has the general form:

$$w(Z) = a(1 - h^2) \text{ where } a = 1.5\left[\frac{Z_{ct} - Z_{cb}}{3}\right], \text{ and Z is height in km.} \tag{12.1}$$

The coefficient a has units m s^{-1}, Z_{ct} and Z_{cb} are the cloud top and cloud base altitudes in km. The term h is a unitless height function given by

$$h = \frac{Z - m}{Z_{ct} - m}$$

$$m = Z_{ct} - \left\{\frac{Z_{ct} - \left[Z_{cb} - \left(\frac{Z_{ct} - Z_{cb}}{3}\right)\right]}{2}\right\}$$

where m is the height in km of the maximum vertical velocity within the cloud. In LAPS, cloud vertical motion is not assigned in the presence of precipitation since air parcels containing precipitation might be in downdrafts (Shultz and Albers 2001). When applying this vertical velocity profile in CIS, this rule must be ignored because all cloud profiles in CIS have some precipitation profile, all clouds are assumed to occur in the presence of large-scale vertical motion, and it's the only way to attack the problem of rainout. Figure 12.1 illustrates the assumed cloud vertical velocity profiles for cumuliform clouds of three depths (1 km, 3 km, and 5 km). The zero height indicates the height of the cloud base. No perturbation vertical velocity field is applied to clear grid points (Albers et al. 1996).

The introduction of this perturbation velocity must be dynamically adjusted to force the fundamental equations (thermodynamic, motion, and continuity) to be satisfied within the domain to a desired level of accuracy (McGinley and Smart 2001). The procedure to adjust the background field is based on a variational assimilation method.
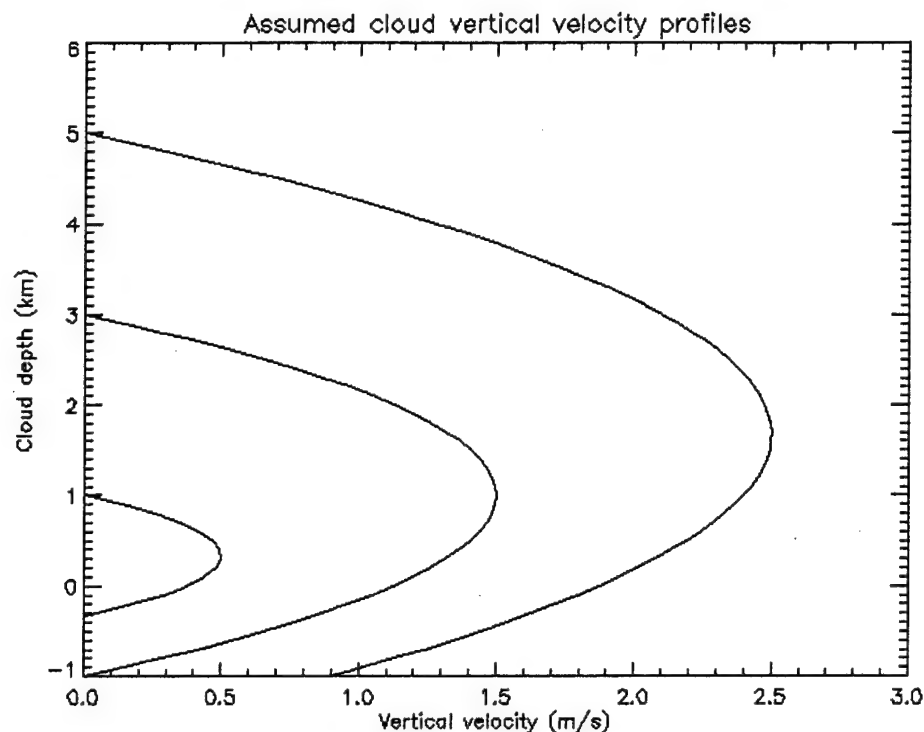
Figure 12.1. Cloud vertical motion profiles for cumuliform clouds of three depths (1 km, 3 km, and 5 km). This figure was constructed using equation 12.1.

A penalty function is defined using equation 12.2:

$$
\begin{aligned}
J = \sum_k \sum_j \sum_i O_V[(\hat{u} - u')^2 + (\hat{v} - v')^2] + O_w(\hat{w} - w'_c)^2 + O_\Phi(\hat{\Phi} - \Phi')^2 \\
+ \mu(\hat{u}_t{}^2 + \hat{v}_t{}^2) \\
+ \lambda(\hat{u}_x + \hat{v}_y + \hat{w}_z) \\
+ B_V(\hat{u}^2 + \hat{v}^2) + B_\Phi\hat{\Phi}^2 + B_w\hat{w}^2
\end{aligned}
\tag{12.2}
$$

The quantities with (^) above are solution residuals or differences between the solution and the background field, while primed quantities (') are observation residuals or differences between the observations and the background. State variables assimilated are geopotential height, horizontal wind components, and vertical velocity, which can be diagnosed from the NOGAPS horizontal wind field using the method described in Chapter VIII. The term w'_c represents the perturbation vertical velocity value for cloud. $O_V, O_w,$ and O_Φ represent user-defined weights for the observations, and $B_V, B_w,$ and B_Φ are defined from known error characteristics between observations and the background. The weight μ adjusts the solution residual u and v local tendencies. McGinley and Smart (2001) assert that this provides a balance among the mass and momentum fields. The weight λ is

unknown and must be solved to ensure that continuity is satisfied to the limits of computational accuracy. The residual local tendencies of u and v are computed following equation 12.3.

$$\hat{u}_t = -(u_b\hat{u}_x + \hat{u}u_{bx} + v_b\hat{u}_y + \hat{v}u_{by} + w_b\hat{u}_z + \hat{w}u_{bz}) - \hat{\Phi}_x + f\hat{v} - D(\hat{u})$$
$$\hat{v}_t = -(u_b\hat{v}_x + \hat{u}v_{bx} + v_b\hat{v}_y + \hat{v}v_{by} + w_b\hat{v}_z + \hat{w}v_{bz}) - \hat{\Phi}_y - f\hat{u} - D(\hat{v})$$

$$(12.3)$$

Terms subscripted with "b" indicate background values. Subscripts x, y, and z refer to horizontal and vertical derivatives. McGinley (1987) describes the three-dimensional variational (3D-VAR) approach used to minimize the penalty function J, how the weights for O and λ are computed, and how B is defined from known error characteristics.

As outlined in the previous paragraphs, the cloud assimilation portion of LAPS is composed of three steps: perform a cloud analysis that determines cloud type, base, and top; estimate a cloud omega field; then dynamically adjust the wind field using a 3D-VAR approach. RTNEPH clouds can satisfy the first step. The remaining two steps can then be applied using RTNEPH cloud and large scale analyzed winds from NOGAPS to provide a dynamically balanced three-dimensional wind field to initialize MM5 along with the water species analysis performed by CIS.

In addition to studies that use LAPS, other studies are underway now to initialize mesoscale NWP models with a cloud analysis. The Naval Research Laboratory (NRL) is researching ways to assimilate a cloud analysis from the Advanced Regional Prediction System / Data Assimilation System (ARPS/ADAS) to initialize COAMPS (Zhao, et al. 2001). The Cooperative Institute for Research in Environmental Sciences at the University of Colorado has been experimenting with initializing the MM5 with an analysis of Geostationary Operational Environmental Satellite (GOES) cloud-top pressures and an analysis of echo-top pressures from WSI Corp. national reflectivity data (Kim and Benjamin 2001).

b. CIS tuning

The large total domain cloud liquid water mass used to initialize MM5 is larger than the quasi-steady value to which the model converges. This is more apparent on domain 2 than on domain 3. This indicates that CIS must be tuned separately for each domain it is used to initialize. The most sensitive tuning parameter is the fraction of adiabatic cloud liquid water retained as a function of cloud type. More testing must be conducted to select the optimum cloud fraction that produces the best cloud forecast. One important physical process lacking in the CIS algorithm is the vertical transport of rain illustrated in Figure 9.7. In that figure, the vertical distribution of rain mass for the MM5 simulations with cloud insertion show a maximum in the middle layers instead of at the lowest layer as seen for the analysis. Although evaporation of rain below cloud base can account for a fraction of the decrease in rain mass, deep profiles of rain require equally deep clouds; therefore, the effect of evaporation may be restricted to only near-surface, cloud-free layers. Another possible explanation for this distribution of mass is net upward transport that shifts the maximum accumulation mass to higher levels. To simulate

this transport in the analysis, a vertical redistribution of the rain mass can be accomplished after its vertical profile is computed. The magnitude of the vertical redistribution should be proportional to the depth of the cloud layer that produces the rain and it should be proportional to the estimated vertical updraft velocity assumed for the cloud. Rain mass throughout the column should be conserved during the redistribution. This redistribution procedure would be designed to simulate larger vertical transports of rain because of a stronger updraft. A recommended procedure for the vertical redistribution of rain mass is as follows:

(1) Compute the cloud vertical velocity $w_c(\sigma)$ using equation 12.1.

(2) Compute the mass weighted mean terminal velocity V_T of the precipitation.

$$V_T(\sigma) = \frac{P_r}{LWC_r} \tag{12.4}$$

where P_r is the precipitation rate (expressed as a mass flux) and LWC_r is the rain liquid water content.

(3) Compute the fraction of the liquid water content on sigma level (σ) that must be displaced vertically to sigma level ($\sigma - \delta\sigma$) to simulate vertical transport of the precipitation mass.

$$\delta(LWC_r) = \left\langle \frac{V_T - w_c}{V_T} \right\rangle \langle q_r \rho \rangle, \quad \langle \ \rangle = (\delta\sigma)^{-1} \int_\sigma^{\sigma - \delta\sigma} (\ ) d\sigma \tag{12.5}$$

(4) Conserve LWC_r during the adjustment procedure.

$$\begin{aligned} LWC_r(\sigma) &= LWC_r(\sigma) - \delta(LWC_r) \\ LWC_r(\sigma - \delta\sigma) &= LWC_r(\sigma - \delta\sigma) + \delta(LWC_r) \end{aligned} \tag{12.6}$$

c. MM5's diffusion scheme

Adjustments must be made to MM5's diffusion scheme to permit clouds to keep their discrete characteristics longer. More research is needed on the frequency distribution of analyzed clouds and precipitation. MM5's diffusion scheme must then be adjusted to produce cloud and precipitation forecasts that simulate these frequency distributions. One possible approach is to eliminate diffusion of condensed mixing ratios and to use a conservative or positive definite advection scheme.

d. Sensitivity to random distribution of RTNEPH clouds

After cloud-scale vertical winds are assimilated with the cloud observations, and after MM5's diffusion scheme is modified to allow discrete clouds to persist longer, it must be determined how sensitive the model is to the horizontal distribution of clouds using a grid spacing that is finer than 8th mesh. In Chapter IV, RTNEPH cloud amounts were converted to discrete clouds by randomly identifying cloudy/cloud-free grid points within each 8th mesh box. To determine if forecast clouds are sensitive to the random placement, parallel simulations must be conducted which change only the random placement of clouds within each 8th mesh box.

e. Utilize improvements to RTNEPH

The next generation cloud analysis algorithm is nearly on line as part of the CDFS-II at Air Force Weather Agency (Sterling Software 1998). Some important changes to the RTNEPH database that will come from the new algorithm are increased resolution from 48 km to 6 km and inclusion of GOES hourly data. The CIS scheme could then be used to analyze three-dimensional precipitation data that can be better timed with surface radar observations. This comparison will permit better tuning of the CIS scheme. The RTNEPH database will also increase cloud top IR and visible gray-shades from 6-bit to 8-bit, which will increase cloud top temperature or cloud height resolution.

f. Diagnostic cloud scheme comparison studies

The efficacy of CIS in producing rain and snow mixing ratios must be compared to other methods that retrieve precipitation rate. Examples include spaceborne radar and rainfall retrievals from Tropical Rainfall Measuring Mission (TRMM) satellite data.

g. Adjustment for RTNEPH sampling error

One final point, RTNEPH cloud coverage amount sampling error has not been calculated. This sampling error should be taken into account when computing mesoscale model forecast error after the model is initialized with RTNEPH clouds. Sampling error in the RTNEPH cloud coverage amount analysis can arise for several reasons relating to input data availability and input data error.

A diurnal cycle likely exists in the sampling error in RTNEPH cloud coverage amounts. The RTNEPH algorithm, which computes cloud coverage amount, changes when visual satellite data is not available (i.e., at night). Sampling error should also vary with the availability of surface cloud observations that can be included in the RTNEPH (e.g., densely populated land areas vs. remote tropical ocean areas). Sampling error will also vary with spacecraft. Because these spacecraft are in sun-synchronous orbits, sampling error should vary in location and time according to which spacecraft provides the visual and IR data input into the RTNEPH process for that time and location. Finally, sampling error in RTNEPH could dramatically affect mesoscale forecast accuracy depending on where the forecast window was placed and when it was initialized (day or night).

REFERENCES

Albers, S. C., J. A. McGinley, D. L. Birkenheuer, and J. R. Smart, 1996: The Local Analysis and Prediction System (LAPS): Analyses of clouds, precipitation, and temperature. *Wea. Forecasting*, **11**, 273-287.

Andrews, P., 1997: NWP on-line Scientific Note No. 5, The Development of an Operational Variational Data Analysis Scheme at the UKMO. [2][Available on-line from http://www.met-office.gov.uk/sec5/NWP/NWP_ScienceNotes/No5/No5.html]

Arking, A., 1964: The latitudinal distribution of cloud cover from TIROS photographs. *Science*, **143**, 50-59.

Baylor, G. M., R. M. Aune, and W. H. Raymond, 2000: NWP cloud initialization using GOES sounder data and improved modeling of nonprecipitating clouds. *Mon. Wea. Rev.*, **128**, 3911-3920.

Baylor, G., and H. Lewit, 1992: The Navy Operational Global and Regional Atmospheric Prediction Systems at the Fleet Numerical Oceanography Center. *Wea. Forecasting*, **7**, 273-279.

Betts, A. K., and W. Ridgway, 1988: Coupling of the radiative convective and surface fluxes over the equatorial Pacific. *J. Atmos. Sci.*, **45**, 522-536.

_____, and R. Boers, 1990: A cloudiness transition in a marine boundary layer. *J. Atmos. Sci.*, **47**, 1480–1497.

Bigg, E. K., 1953: The supercooling of water. *Proc. Phys. Soc.*, **B 66**, 688-694.

Cahalan, R. F., and J. H. Joseph, 1989: Fractal statistics of cloud fields. *Mon. Wea. Rev.*, **117**, 261-272.

Carvalho, L. M. V., and M. A. F. Sliva Dias, 1998: An application of fractal box dimension to the recognition of mesoscale cloud patterns in infrared satellite images. *J. Appl. Meteor.*, **37**, 1265-1282.

Clapp, P. E., 1964: Global cloud cover for seasons using TIROS nephanalysis. *Mon. Wea. Rev.*, **92**, 147-159.

Coburn, A. R., 1970: Three dimensional nephanalysis. AFGWC Technical Manual 70-9, [1]Air Force Weather Technical Library, Asheville, NC, 49 pp.

Cortier, P., 1997: Variational methods. *J. Meteor. Soc. Japan*, **75**, 211-218.

Cortinas, J. V., Jr., and D. J. Stensrud, 1995: The importance of understanding mesoscale model parameterization schemes for weather forecasting. *Wea. Forecasting*, **10**, 716-740.

Cram, J. S., S. C. Albers, M. Jackson, and J. R. Smart, 1995: Three recent moisture-related analyses and modeling studies in LAPS. *WMO Itnl. Workshop on Imbalances of Slowly Varying Components of Predictable Atmospheric Motions*, Beijing, China, World Meteor. Org., WMO/TD-No. 652, 23-28.

Crook, N. A., 1996: Sensitivity of convection initiation to low-level thermodynamics fields. *Mon. Wea. Rev.*, **124**, 1767-1785.

Daley, R., 1991: *Atmospheric Data Analysis*. Cambridge Atmospheric and Space Science Series, Cambridge University Press, Cambridge, 457 pp.

Danard, M., 1985: On the use of satellite estimates of precipitation in initial analysis for numerical weather prediction. *Atmos.—Ocean*, **23**, 23-42.

Davies, R., 1984: Reflected solar radiances from broken cloud scenes and the interpretation of scanner measurements. *J. Geophys. Res.*, **89**, 1259-1266.

Doran, J. A., P. J. Roohr, D. J. Beberwyk, G. R. Brooks, G. A. Gayno, R. T. Williams, J. M. Lewis, and R. J. Lefevre, 1999: The MM5 at the Air Force Weather Agency - New products to support military operations. *Preprints, Eighth Conf. Aviation, Range, and Aerospace Meteorology*. Dallas, TX. Amer. Meteor. Soc. [2][Available on-line from http://www.confex2.com/ams/99annual/abstracts/1125.htm]

Doswell III, C. A., R. Davies-Jones, and D. L. Keller, 1990: On summary measures of skill in rare event forecasting based on contingency tables. *Wea. Forecasting*, **7**, 576-585.

Dudhia, J., D. Gill, Y.-R. Guo, D. Hanson, and K. Manning, 1999: PSU/NCAR mesoscale modeling system tutorial class notes and user's guide. [5]NCAR, Boulder, CO. [2][Available on-line from http://www.mmm.ucar.edu/mm5/mm5-home.html]

_____, D. Gill, Y.-R. Guo, K. Manning, and W. Wang, January, 2001. *PSU/NCAR Mesoscale Modeling System Tutorial Class Notes and User's Guide: MM5 Modeling System Version 3-4.* [5]NCAR, Boulder, CO. [2][Available on-line at http://www.mmm.ucar.edu/mm5/doc.html]

Eckmann, J., and D. Ruelle, 1985: Ergodic theory of chaos and strange attractors. *Reviews of Modern Physics*, **57**, 617-656.

Ellingson, R. G., 1982: On the effects of cumulus dimensions on longwave irradiance and heating rate calculations. *J. Atmos. Sci.*, **39**, 886-896.

Eyre, J. R., G. A. Kelly, A. P. McNally, E. Andersson, and A. Persson, 1993: Assimilation of TOVS radiance information through one-dimensional variational analysis. *Quart. J. Roy. Meteor. Soc.*, **119**, 1427-1463.

Fillion, L., and R. Errico, 1997: Variational assimilation of precipitation data using moist convective parameterization schemes: A 1D-VAR study. *Mon. Wea. Rev.*, **125**, 2917-2942.

Fletcher, N. H., 1962: *The Physics of Rain Clouds.* University of New England, CSIRO, Cambridge University Press, Cambridge, 386 pp.

Fritsch, J. M., and C. F. Chappell, 1981: Preliminary numerical tests of the modification of mesoscale convective systems. *J. Appl. Meteor.*, **20**, 910-921.

Fye, F. K., 1978: The AFGWC automated cloud analysis model. AFGWC/TN-78/002, [1]Air Force Weather Technical Library, Asheville, NC, 97 pp.

Gilmore, M. S., and L. J. Wicker, 1998: The influence of midtropospheric dryness on supercell morphology and evolution. *Mon. Wea. Rev.*, **126**, 943–958.

Grell, G. A., 1993: Prognostic evaluation of assumptions used by cumulus parameterizations. *Mon. Wea. Rev.*, **121**, 764-787

_____, J. Dudhia, and D. R. Stauffer, 1994: A description of the fifth-generation Penn State/NCAR mesoscale model (MM5). NCAR Technical Note NCAR/TN-398+STR, [5]NCAR, Boulder, CO, 122 pp.

Gotoh, K., and Y. Fujii, 1998: A fractal dimensional analysis on the cloud shape parameters of cumulus over land. *J. Appl. Meteor.*, **37**, 1283-1292.

Hamill, T. M., 1999: Hypothesis tests for evaluating numerical precipitation forecasts. *Wea. Forecasting*, **14**, 155–167.

_____, and S. J. Colucci, 1997: Verification of Eta–RSM short-range ensemble forecasts. *Mon. Wea. Rev.*, **125**, 1312–1327.

_____, R. P. D'Entremont, and J. T. Bunting, 1992: A description of the Air Force real time nephanalysis model. *Wea. Forecasting*, **7**, 288-306.

Hammarstrand, U., 1987: Prediction of cloudiness using a scheme for consistent treatment of stratiform and convective condensation and cloudiness in a limited area model. Short- and medium-range numerical weather prediction, suppl. to *J. Meteor. Soc. Japan*, T. Matsuno (Ed.), 187-197.

Han, D., and R. Ellingson, 1999: Cumulus cloud formulations for longwave radiation calculations. *J. Atmos. Sci.*, **56**, 837-851.

Harris, R., 1987: *Satellite Remote Sensing.* Routledge & Kegan Paul Ltd., London, 220 pp.

Harshvardhan, and J. A. Weinman, 1982: Infrared radiative transfer through a regular array of cuboidal clouds. *J. Atmos. Sci.*, **39**, 431-439.

Heckley, W. A., 1985: Systematic errors of the ECMWF operational forecasting model in tropical regions. *Quart. J. Roy. Meteor. Soc.*, **111**, 709-738.

Hoke, J. E., J. L. Hayes, and L. G. Renninger, 1979: Map projections and grid systems for meteorological applications. AFGWC Technical Note 79/003 (Rev March 1985). [1]Air Force Weather Technical Library, Asheville, NC, 87 pp.

Holton, J. R., 1992: *An Introduction to Dynamic Meteorology*, Third Edition. Academic Press, San Diego, 511 pp.

Hong, X., M. Leach, and S. Raman, 1995: A sensitivity study of convective cloud formation by vegetation forcing with different atmospheric conditions. *J. Appl. Meteor.*, **34**, 2008-2028.

Janjic, Z.I., 1994: The step-mountain eta coordinate model: Further developments of the convection, viscous sublayer, and turbulence closure schemes. *Mon. Wea. Rev.*, **122**, 927-945

Jensen, C. E., 1962: The forecasting of clouds and airframe icing, SS Technical Note 3, Hq 3 Weather Wing, [1]Air Force Weather Technical Library, Asheville, NC.

_____, 1963: Prediction of large-scale cloudiness and airframe icing conditions by machine methods. *J. Appl. Meteor.*, **2**, 337–344.

Jincai, D., C. A. Doswell III, and D. W. Burgess, 1992: Verification of mesoscale forecasts made during MAP '88 and MAP '89. *Wea. Forecasting*, **7**, 468-479.

Junker, N. W., J. E. Hoke, B. E. Sullivan, K. F. Brill, and F. J. Hughes, 1992: Seasonal and geographic variations in quantitative precipitation prediction by NMC's Nested-Grid Model and Medium Range Forecast Model. *Wea. Forecasting*, **7**, 410-429.

Kärner, O., and S. Keevallik, 1993: *Effective Cloud Cover Variations*. A. Deepak Publishing, Hampton, VA, 210 pp.

Kelly, M. A., R. J. Alliss, M. E. Craddock, and J. C. Lefever, 2001: A quantitative comparison of MM5 cloud forecasts and GOES cloud analyses. *14th Conf. on Numerical Weather Prediction*, Fort Lauderdale, FL, Amer. Meteor. Soc., J47-J49.

Kessler, E., 1969: *On the Distribution and Continuity of Water Substance in Atmospheric Circulations. Meteorological Monograph* 10 no. 32, Amer. Meteor. Soc., Boston, MA.

Kiess, R. B., and W. M. Cox, 1988: The AFGWC automated real-time cloud analysis model. AFGWC/TN - 88/001. [1]Air Force Weather Technical Library, Asheville, NC, 84 pp.

Kim, D., and G. Benjamin, 2001: Cloud/hydrometeor initialization for the 20-km RUC using satellite and radar data. *14th Conf. on Numerical Weather Prediction*, Fort Lauderdale, FL, Amer. Meteor. Soc., J113-J115.

Krishnamurti, T. N., J. Xue, H.S. Bedi, K. Ingles, and D. Oosterhof, 1991: Physical initialization for numerical weather prediction over the tropics. *Tellus*, **43AB**, 53-81.

_____, G. Rohaly, and H. S. Bedi, 1994: On the improvement of precipitation forecast skill from physical initialization. *Tellus*, **46A**, 598-614.

Kristjansson, J. E., 1992: Initialization of cloud water in a numerical weather prediction model. *Meteor. Atmos. Phys.*, **50**, 21-30.

Kopp, T. J., 1995: The Air Force Global Weather Central Surface Temperature Model. AFGWC/TN-95/004. [1]Air Force Weather Technical Library, Asheville, NC, 23 pp.

_____, M. M. Wonsick, L. E. Cantrell, and F. D. Bieker, 1997: ADVCLD: Air Force Global Weather Center's updated cloud forecast model. *Cloud Impacts on DOD Operations and Systems Conf.*, Newport, RI, Department of Defense, 107–110.

Lee, H. S., and T. N. Krishnamurti, 1995: Impact of physical initialization on cloud forecasts. *Meteor. Atmos. Phys.*, **56**, 261-273.

Lejenas, H., 1979: Initialization of moisture in primitive equation models. *Mon. Wea. Rev.*, **107**, 1299-1305.

Lewis, F. P., 1998: Concept of operations for reengineered Air Force weather. HQ USAF/XOW, 1490 Air Force Pentagon, Washington, D.C., 20330-1490.

Lipton, A. E., 1993: Cloud shading retrieval and assimilation in a satellite-model coupled mesoscale analysis system. *Mon. Wea. Rev.*, **121**, 3062-3081.

Lorenc, A., 1986: Analysis methods for numerical weather prediction. *Quart. J. Roy. Meteor. Soc.*, **112**, 1177-1194.

Lorenz, E. N., 1963: Deterministic nonperiodic flow. *J. Atmos. Sci.*, **20**, 130-141.

Lovejoy, S., 1982: Area perimeter relation for rain and cloud areas. *Science*, **216**, 185-187.

Mandelbrot, B., 1982: *The Fractal Geometry of Nature.* W. H. Freeman and Co., New York, NY, 461 pp.

Markowski, P. M., E. N. Rassmussen, J. M. Straka, and D. C. Dowell, 1998: Observations of low-level baroclinity generated by anvil shadows. *Mon. Wea. Rev.*, **126**, 2942-2958.

Marshall, J. S., and W. McK. Palmer, 1948: The distribution of raindrops with size. *J. Meteor.*, **5**, 165-166.

Mather, M. B., H. S. Bedi, T. N. Krishnamurti, M. Kanamitsu, and J. S. Wollen, 1992: Use of satellite-derived rainfall for improving tropical forecasts. *Mon. Wea. Rev.*, **120**, 2540-2560.

McAtee, M. D., 1999: Personal communication, June 1999, Aerospace Corporation, Air Force Weather Agency, Offutt AFB, NE.

McGinley, J. A., 1987: A variational objective analysis scheme for analysis of ALPEX data set. *Meteor. Atmos. Phys.* **36**, 5-23.

_____, and J. R. Smart, 2001: On providing a cloud-balanced initial condition for diabatic initialization. *14th Conf. on Numerical Weather Prediction*, Fort Lauderdale, FL, Amer. Meteor. Soc., 40-44.

_____, S. C. Albers, and P. Stamus, 1991: Local data assimilation and analysis for nowcasting. *Adv. Space Res.*, **12**, 179-188.

McNider, R. T., J. A. Song, and S. Q. Kidder, 1995: Assimilation of GOES-derived solar insolation into a mesoscale model for studies of cloud shading effects. *Int. J. Remote Sens.*, **16**, 2207-2231.

Mohanty U. C., A. Kasahara, and R. Errico, 1986: The impact of diabatic heating on initialization of divergent circulations in a global forecast model. *J. Meteor Soc. Japan*, **64**, 805-817.

Molinari, J., M. Dudek, 1992: Parameterization of convective precipitation in mesoscale numerical models: A critical review. *Mon. Wea. Rev.*, **120**, 326-344.

Murray, F. W., 1967: On the computation of saturation vapor pressure. *J. Appl. Meteor.*, **6**, 203-204.

Naber, P. S., and J. A. Weinman, 1984: The angular distribution of infrared radiances emerging from broken fields of cumulus clouds. *J. Geophys. Res.*, **89**, 1249-1257.

Naiman, A. R. Rosenfeld, and G. Zirkel, 1972: *Understanding Statistics*. McGraw-Hill, Inc., New York, NY, 235 pp.

Newton, H. J., 1995: *TIMESLAB: A Time Series Analysis Laboratory*. Wadsworth & Brooks/Cole Publishing Company, Pacific Grove, CA, 623 pp.

Norquist, D. C., 1999: Cloud predictions diagnosed from mesoscale weather model forecasts. *Mon. Wea. Rev.*, **127**, 2465-2483.

Park, S. K., 1999: Nonlinearity and predictability of convective rainfall associated with water vapor perturbations in a numerically simulated storm. *J. Geophys. Res.*, **104**, 31,575-31,587.

Perkey, D. J., 1976: A description and preliminary results from a fine-mesh model for forecasting quantitative precipitation. *Mon. Wea. Rev.*, **104**, 1513-1526.

Pielke, R. A., 1984: *Mesoscale Meteorological Modeling*. Academic Press Inc., London, 612 pp.

Pruppacher, H. R., and J. D. Klett, 1997: *Microphysics of Clouds and Precipitation*. Kluwer Academic Publishers, Boston, MA, 954 pp.

Reisner, J., R. M. Rasmussen, and R. T. Bruintjes, 1998: Explicit forecasting of supercooled liquid water in winter storms using the MM5 mesoscale model. *Quart. J. Roy. Meteor. Soc.,* **124,** 1071-1106.

Ritz, R. L., M. D. McAtee, and R. T. Swanson Jr., 2001: Data assimilation at the Air Force Weather Agency. *14th Conf. on Numerical Weather Prediction,* Fort Lauderdale, FL, Amer. Meteor. Soc., 19-21.

Rogers, R. R., and M. K. Yau, 1989: *A Short Course in Cloud Physics.* Pergamon Press, New York, NY, 293 pp.

Ruggiero, F. H., G. D. Modica, and A. E. Lipton, 1999: Assimilation of satellite imager data and surface observations to improve analysis of circulations forced by cloud shading contrasts. *Mon. Wea. Rev.,* **128,** 434-448.

Rutledge, S. A., and P. V. Hobbs, 1983: The mesoscale structure and organization of clouds and precipitation in midlatitude cyclones. VII: A model for the "seeder-feeder" process in warm-frontal rainbands. *J. Atmos. Sci.,* **40,** 1185-1206.

Rys, F. S., and A. Waldvogel, 1986: Fractal shape of hail clouds. *Phys. Rev. Lett.,* **56,** 784–787.

Schaefer, J. T., 1990: The critical success index as an indicator of warning skill. *Wea. Forecasting,* **5,** 570-575.

Schultz, P., and S. C. Albers, 2001: The use of three-dimensional analyses of cloud attributes for diabatic initialization of mesoscale models. *14th Conf. on Numerical Weather Prediction,* Fort Lauderdale, FL, Amer. Meteor. Soc., J122-J124.

Segal, M., J. F. W. Purdom, J. L. Song, R. A. Pielke, and Y. Mahrer, 1986: Evaluation of cloud shading effects on the generation and modification of mesoscale circulations. *Mon. Wea. Rev.,* **114,** 1201-1212.

Sekhon, R. S., and R. C. Srivastava, 1970: Snow size spectra and radar reflectivity. *J. Atmos. Sci.,* **27,** 299-307.

_____, and _____, 1971: Doppler radar observations of dropsize distributions in a thunderstorm. *J. Atmos. Sci.,* **28,** 983-994.

Sengupta, S. K., R. M. Welch, M. S. Navar, T. A. Berendes, and D. W. Chen, 1990: Cumulus cloud field morphology and spatial patterns derived from high spatial resolution Landsat imagery. *J. Appl. Meteor.,* **29,** 1245-1267.

Stensrud, D. J., and J. M. Fritsch, 1994: Mesoscale convective systems in weakly forced large-scale environments. Part II: Generation of mesoscale initial condition. *Mon. Wea. Rev.,* **122,** 2068-2083.

_____, J. V. Cortinas Jr., and H. E. Brooks, 1997: Discriminating between tornadic and nontornadic thunderstorms using mesoscale model output. *Wea. Forecasting,* **12,** 613-632.

Sterling Software, 1998: *Algorithm Description for the Cloud Depiction and Forecast System II.* Unpublished document prepared by [3]Sterling Software, Bellevue, NE, 361 pp. plus appendices.

Sundqvist, H., 1995: An approach to treatment of mixed phase hydrometeors in GCMs. Workshop on Cloud Microphysical Parameterizations in Global Atmospheric Circulation Models, WMO/TD-No. 713, 155-166.

_____, E. Berge, and J. E. Kristjansson, 1989: Condensation and cloud parameterization studies with a mesoscale numerical weather prediction model. *Mon. Wea. Rev.,* **117**, 1641-1657.

Swerdlin, S., L. Yubao, and T. Warner, 2001: Uses of high-resolution mesoscale modeling to support Army research and development, testing, and evaluation. *14th Conf. on Numerical Weather Prediction*, Fort Lauderdale, FL, Amer. Meteor. Soc., J55-J58.

Talagrand, O., 1997: Assimilation of observations, an introduction. *J. Meteor. Soc. Japan*, **75**, 191-209.

_____, and P. Courtier, 1987: Variational assimilation of meteorological observations with the adjoint vorticity equation. I: Theory. *Quart. J. Roy. Met. Soc.*, **113**, 1311-1328.

Tiedtke, M., 1993: Representation of clouds in large-scale models. *Mon. Wea. Rev.*, **121**, 3040-3061.

Turpeinen, O. M., L. Garand, R. Benoit, and M. Roch, 1990: Diabatic initialization of the Canadian regional finite-element (RFE) model using satellite data. Part I: Methodology and application to a winter storm. *Mon. Wea. Rev.*, **118**, 1381-1395.

Vandenberghe, F., 1999: Evaluation of 3D-VAR observations operators/adjoints. Submitted as deliverable for AFWA-NCAR FY99 Statement of Work Task # 2.02, NCAR Mesoscale Prediction Group, 28 pp. [2][Available on-line from http://www.mmm.ucar.edu/mm5/3dvar/docs/afwa_task_2.02.rev2.html]

Weger, R. C., J. Lee, T. Zhu, and R. M. Welch, 1992: Clustering, randomness and regularity in cloud fields. 2. Cumulus cloud fields. *J. Geophys. Res.*, **97**, 20,519-20,536.

Westphal, L. E. (Ed.), 1986: Surface temperature analysis: USAFETAC climatic database user's handbook no. 2. USAFETAC/UH-86/002, [1]Air Force Weather Technical Library, Asheville, NC, 15 pp.

Zamiska, A., and P. Giese, 1986: RTNEPH: USAFETAC climatic database user's handbook no. 1. USAFETAC/UH-86/001, [1]Air Force Weather Technical Library, Asheville, NC.

Zhao, Q., 1993: The incorporation and initialization of cloud water/ice in an operational forecast model. [4]Ph.D. dissertation, University of Oklahoma, 195 pp.

_____, and F. H. Carr, 1997: A prognostic cloud scheme for operational NWP models. *Mon. Wea. Rev.*, **125**, 1931-1953.

_____, K. A. Campana, and S. Moorthi, 1995: Prognostic clouds in NMC's global spectral model. Workshop on Cloud Microphysics Parameterizations in Global Atmospheric Circulation Models, WMO/TD-No. 713, 87-104.

_____, J. Cook, K. Sashegyi, Q. Xu, and L. Wei, 2001: A real-time, three-dimensional cloud analysis system at the Naval Research Laboratory. *14th Conf. on Numerical Weather Prediction*, Fort Lauderdale, FL, Amer. Meteor. Soc., J116-J117.

Zhu, T., J. Lee, R. Weger, and R. Welch, 1992: Clustering, randomness, and regularity in cloud fields: 2. Cumulus cloud fields. *J. Geophys. Res.*, **97**, 20 537-20 558.

Notes to References:

1. Requests for material from Air Force Weather Technical Library may be addressed to:
Air Force Weather Technical Library, 151 Patton Avenue, Room 120,
Asheville, NC 28801-5002.
Their customer service number is commercial 828-271-4270,
or email dorsvc@afccc.af.mil,
or visit http://afccc.af.mil and click "Air Force Weather Technical Library".

2. Web addresses valid at time of this writing.

3. Requests for material from Sterling Software may be addressed to:
Sterling Software, Information Technology Division
1404 Fort Crook Road South, Bellevue, NE 68005-2969
Their customer service number is commercial 402-291-8300.

4. Requests for a copy of dissertation may be addressed to:
School of Meteorology, University of Oklahoma
100 E. Boyd St., Energy Center, Room 1310, Norman, OK 73019

5. Requests for material from NCAR may be addressed to:
Mesoscale and Microscale Meteorology Division,
National Center for Atmospheric Research
P. O. Box 3000, Boulder, CO 80307

6. Journal abbreviations:

Adv. Space Res.	Advances in Space Research
Atmos.—Ocean	Atmosphere; Atmosphere—Ocean
Int. J. Remote Sens.	International Journal of Remote Sensing
J. Appl. Meteor.	Journal of Applied Meteorology
J. Atmos. Sci.	Journal of the Atmospheric Sciences
J. Geophys. Res.	Journal of Geophysical Research
J. Meteor.	Journal of Meteorology
J. Meteor. Soc. Japan	Journal of the Meteorological Society of Japan
Meteor. Atmos. Phys.	Meteorology and Atmospheric Physics
Mon. Wea. Rev.	Monthly Weather Review
Phys. Rev. Lett.	Physical Review Letters
Proc. Phys. Soc.	Proceedings of the Physical Society
Quart. J. Roy. Meteor. Soc.	Quarterly Journal of the Royal Meteorological Society
Wea. Forecasting	Weather and Forecasting

APPENDIX A

ACRONYMS

1D-VAR	One-Dimensional Variational Assimilation
3DNEPH	Three-Dimensional Nephanalysis Model
3D-VAR	Three-Dimensional Variational Assimilation
A&M	Agriculture and Mechanical
AFCCC	Air Force Combat Climatology Center
ADVCLD	Air Force Cloud Advection Model
AFWA	Air Force Weather Agency
ARPS/ADAS	Advanced Regional Prediction System / Data Assimilation System
As	Altostratus cloud type
ASCII	American Standard Code for Information Interchange
ATEC	Army Test and Evaluation Command
AVHRR	Advanced Very High Resolution Radiometer
Bias	Bias Skill Score
Cb	Cumulonimbus cloud type
CDFS	Cloud Depiction and Forecast System (versions I and II)
CIS	Cloud Initialization Scheme
CLW	Cloud liquid water variable
CPS	Condensation Pressure Spread
Cs	Cirrostratus cloud type
CSI	Critical Success Index Skill Score
Cu	Cumulus cloud type
DMSP	Defense Meteorological Satellite Program
ETS	Equitable Threat Score Skill Score
FAR	False Alarm Rate Skill Score
FDDA	Four-Dimensional Data Assimilation
FORTRAN-90	Formula Translation Language Version 90
FSL	Forecast Systems Laboratory
GCM	General Circulation Model
GOES	Geostationary Operational Environmental Satellite
HSS	Heidke Skill Score
ICE	Cloud ice variable
IDL	Interactive Data Language
IR	Infra-Red
LAPS	Local Analysis and Prediction System
MDA	Multiple Discriminate Analysis
MDAS/MVOI	Mesoscale Data Assimilation System / Multivariate Optimal Interpolation
MLR	Multiple Linear Regression
MM5	5th Generation Mesoscale Model
MMM	Mesoscale and Microscale Meteorology
MRF	Medium Range Forecast Model
MSL	Mean Sea Level
NAAGE	Normalized average absolute gross error
NB	Normalized bias
NCAR	National Centers for Atmospheric Research
NCEP	National Centers for Environmental Prediction
NMC	National Meteorological Center
NOAA	National Oceanic and Atmospheric Administration
NOGAPS	Navy Operational Global and Regional Atmospheric Prediction Systems
NRL	Naval Research Laboratory

Ns	Nimbostratus cloud type
NWP	Numerical Weather Prediction
NWS	National Weather Service
OLR SSM/I	Outgoing Longwave Radiometer Special Sensor Microwave Imager
POD	Probability of Detection Skill Score
PoFD	Probability of False Detection Skill Score
PRACS	Variable, release rate of rain due to accumulation of snow
PSACR	Variable, release rate of snow due to accumulation of rain
PSU	Pennsylvania State University
PDF	Probability Density Function
Q	Water vapor variable
r	Correlation coefficient
REGRID	MM5 preprocessor that horizontally distributes input data to MM5 grid
RH	Relative Humidity
RNW	Rain water variable
RTNEPH	Real-Time Nephanalysis
SFCTEMP	Surface temperature analysis
SGI	Silicon Graphics, Inc.
SNOW	Snow variable
SPD	Saturation Pressure Deficit
St	Stratus cloud type
TRMM	Tropical Rainfall Measuring Mission
TSS	True Skill Score
UTC	Universal Time Coordinates
	also known as Zulu Time (Z) or Greenwich Mean Time (GMT)

APPENDIX B

VARIABLE DEFINITIONS

$a_{r,s}$	Coefficient for rain and snow
a_l	Temperature dependent rate coefficient [s^{-1}]
$b_{r,s}$	Coefficients for rain and snow
A'	Coefficient 0.66 K^{-1}
B'	Coefficient 100 m^{-3} s^{-1}
C_b	Cloud base sigma level
c_p	Specific heat of dry air at constant pressure = 1004 J K^{-1} kg^{-1}
$c_{r,s}$	Coefficients for rain and snow
C_t	Cloud top sigma level
C_w	Specific heat of liquid water = 4218 J K^{-1} kg^{-1}
C_{ws}	Snowmelt rate factor [s^{-1}]
D	Droplet diameter [m]
D_i	Mean diameter of ice crystals [m]
E_r	Collection efficiency for rain = 1
E_{rr}	Release rate for evaporation of rain [s^{-1}]
E_{rs}	Release rate for sublimation of snow [s^{-1}]
E_{rsm}	Release rate for evaporation of melting snow [s^{-1}]
E_s	Collection efficiency for snow = 0.1
e_{sw}	Saturation vapor pressure with respect to liquid water [Pa]
e_{si}	Saturation vapor pressure with respect to ice [Pa]
F	Ventilation factor
f	Fraction of adiabatic liquid water content retained as a function of cloud type
f_1	Coefficient
f_2	Coefficient
g	Gravity = 9.8 m s^{-1}
k_1	Coefficient [s^{-1}]
K_a	Thermal conductivity of air [J m^{-1} s^{-1} K^{-1}]
L_c	Latent heat of condensation = 2.5 x 10^6 J kg^{-1}
L_f	Latent heat of fusion = 3.33 x 10^5 J kg^{-1}
L_s	Latent heat of sublimation = 2.833 x 10^6 J kg^{-1}
lwc_i	Equivalent liquid water content cloud ice [kg m^{-3}]
lwc'_c	Liquid water content cloud liquid water initial [kg m^{-3}]
lwc_c	Liquid water content cloud liquid water adjusted for ice [kg m^{-3}]
M_i	Mean mass of ice crystals [kg]
m_{i0}	Critical mixing rato [kg kg^{-1}]
M_{max}	Coefficient = 9.4 x 10^{-10} kg
M_0	coefficient = 10^{-12} kg
N_0	Marshall-Palmer raindrop size distribution intercept parameter = 8 x 10^6 m^{-4}
N_{0s}	Sekhon-Srivastava snow size distribution intercept parameter [m^{-4}]
n_c	number concentration of ice nuclei [kg^{-1}]
N_c	Number of cloud droplets per unit volume of air = 10^{10} m^{-3}
p	Pressure [Pa]
p_0	Reference pressure = 101325.0 Pa
P_{CI}	Release rate for heterogeneous freezing of cloud water to cloud ice [s^{-1}]
P_{ID}	Release rate for deposition of water vapor onto ice particles [s^{-1}]
P_{II}	release rate for cloud ice initiation [s^{-1}]
P_{racw}	Release rate of rain due to accumulation of cloud liquid water [s^{-1}]
P_{raut}	Release rate of rain due to autoconversion of cloud liquid water [s^{-1}]
P_{saci}	Release rate of snow due to accumulation of cloud ice [s^{-1}]
P_{sacw}	Release rate of snow due to accumulation of cloud liquid water [s^{-1}]

P_{saut}	Release rate of snow due to autoconversion of cloud ice [s^{-1}]
P_{sm1}	Release rate of snow melt due to increasing temperature [s^{-1}]
P_{sm2}	Release rate of snowmelt due to accumulation of cloud liquid water [s^{-1}]
P_{sm3}	Release rate of snowmelt due to being swept out by rain [s^{-1}]
q_c	Cloud liquid water mixing ratio adjusted for ice [kg kg^{-1}]
q'_c	Initial cloud liquid water mixing ratio [kg kg^{-1}]
$q'_c(\sigma)$	Initial cloud liquid water mixing ratio [kg kg^{-1}] at level σ
$q_{critical}$	Critical cloud liquid water mixing ratio [kg kg^{-1}]
q_r	Rain water mixing ratio [kg kg^{-1}]
q_s	Snow mixing ratio [kg kg^{-1}]
q_{sw}	Saturation mixing ratio with respect to liquid water [kg kg^{-1}]
q_{si}	Saturation mixing ratio with respect to ice [kg kg^{-1}]
q_v	Environmental water vapor mixing ratio [kg kg^{-1}]
q'_v	Saturation vapor pressure with respect to water in the cloud region [kg kg^{-1}]
Re	Reynolds number
R_d	Gas constant for dry air = 287 J K^{-1} kg^{-1}
R_v	Gas constant for water vapor = 461 J K^{-1} kg^{-1}
S_c	Schmidt number
S_i	Supersaturation with respect to ice
S_w	Supersaturation with respect to liquid water
T	Temperature [K]
T_0	Reference melting temperature = 273.15K
V	Droplet fall speed [ms^{-1}]
w_s	Saturation mixing ratio [kg kg^{-1}]
Δt	Characteristic time step [s]
Δx	Characteristic grid spacing [m]
ε	Ratio of molecular weights water to dry air = 0.622
λ_r,	Marshall-Palmer raindrop size distribution slope parameter [m^{-4}]
λ_s,	Sekhon-Srivastava snow size distribution slope parameter [m^{-1}]
μ	Dynamic viscosity of air [kg m^{-1} s^{-1}]
ρ	Air density [kg m^{-3}]
$\rho(\sigma)$	Air density [kg m^{-3}] at level σ
ρ_w	Density of water = 1000 kg m^{-3}
ρ_{ws}	Mean density of snow particles = 100 kg m^{-3}
Γ	Gamma function
Γ_m	Moist lapse rate [K m^{-1}]
Γ_d	Dry adiabatic lapse rate [K m^{-1}]
σ	Sigma model level
χ	Diffusivity of vapor in air [m^2 s^{-1}]
$\chi(\sigma)$	Adiabatic liquid water content [kg m^{-3}] at level σ

APPENDIX C

POTENTIAL ENERGY THOUGHT EXPERIMENT

Will initialization with saturated columns of water vapor (clouds) fundamentally change the available potential energy of the initial state? To answer that question, a thought experiment is constructed analogous to a thermally driven circulation experiment by Wallace and Hobbs (1977). Begin with a fictitious tank containing two different vertical distributions of density. The air in each profile is separated by an initially rigid vertical partition. Assume the profiles are in hydrostatic equilibrium, are dry, have the same base temperature (T_0), and have a constant dry adiabatic lapse rate of temperature (Γ_d).
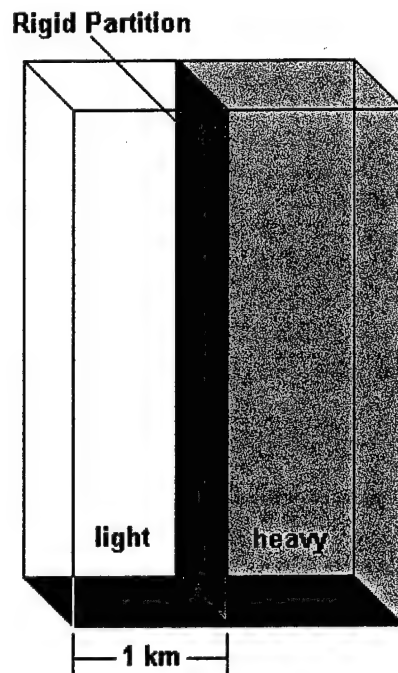
Figure C.1. Tank composed of two air columns separated by an initially rigid partition. Both air columns are dry. The column on the left contains lower density air than the column on the right. Hydrostatic assumption applies to the air columns.

The tank's walls are frictionless and non-conductive. The tank depth may stretch or shrink to accommodate changes in density (floating lid). Air in the left tank is designated double-prime. Air in the right tank is designated prime. The mean density and temperature are defined at the base as follows.

$$\overline{\rho}_0 = \frac{\rho_0'' + \rho_0'}{2} \tag{C.1}$$

$$T_0 = T_0'' = T_0' \qquad T_0 = 15°C(288K) \tag{C.2}$$

The tank width is assumed 2 km with a floating lid. The designation of other tank dimensions is not necessary. The following initial values are used:

$$\rho_0' = 1.1\overline{\rho}_0$$

$$\rho_0'' = 0.9\overline{\rho}_0$$

$$\overline{\rho}_0 = 1.0\,\text{kg m}^{-3}$$

The density profile in each half of the tank is estimated using an adiabatic form of the hydrostatic approximation.

$$dp = -\rho g dz \tag{C.3}$$

Rewrite equation C.3 using the ideal gas law.

$$dp = -\frac{p}{R_d T} g dz \tag{C.4}$$

$$d\ln(p) = -\frac{g}{R_d T} dz \tag{C.5}$$

The temperature at height z (T) in the tank is linearly estimated from the base temperature (T_0) assuming an adiabatic lapse rate.

$$\Gamma_d = -\frac{dT}{dZ} = -\frac{T - T_0}{Z - Z_0} \tag{C.6}$$

$$T = T_0 - \Gamma_d(Z - Z_0), \quad \Gamma_d = \frac{g}{c_p}, \quad Z_0 = 0 \tag{C.7}$$

Substitute equation C.7 into C.5

$$d\ln(p) = -\frac{g}{R_d(T_0 - \Gamma_d Z)} dz \tag{C.8}$$

Integrate both sides of the equation.

$$\int d\ln(p) = -\frac{g}{R_d} \int \frac{1}{T_0 - \Gamma_d Z} dz \tag{C.9}$$

Use the identity $\int \frac{dx}{a + bx} = \frac{1}{b} \ln|a + bx|$ and evaluate using limits of integration from the base of the

column to the level at which the mass above is equivalent to the mass below ($p_c = p_0 / 2$)

$$\int_{p_0}^{p_c} d\ln(p) = \ln(p)\Big|_{p_0}^{p_c} = \frac{g}{R_d} \frac{1}{\Gamma_d} \ln|T_0 - \Gamma_d Z|\Big|_{Z=0}^{Z=Z_c} \tag{C.9a}$$

Solve for the height of the center of mass for each column.

$$\ln\left(\frac{1}{2}\right) = \frac{1}{\kappa}\ln\left(\frac{|T_0 - \Gamma_d Z_c|}{|T_0|}\right), \quad p_c = \frac{p_0}{2}, \quad \frac{g}{R_d}\frac{1}{\Gamma_d} = \frac{c_p}{R_d} = \frac{1}{\kappa} \tag{C.10}$$

Take the exponent of both sides of the equation.

$$T_0\left(\frac{1}{2}\right)^{\kappa} = |T_0 - \Gamma_d Z_c| \tag{C.11}$$

$$\frac{T_0\left[1 - \left(\frac{1}{2}\right)^{\kappa}\right]}{\Gamma_d} = Z_c = 5303 \text{ m} \tag{C.12}$$

Notice that the height of the center of mass is independent of base density and identical for both columns if the surface temperature is identical. Next, compute the density at the vertical center of mass for each column. Again, the density profile in each half of the tank is estimated using an adiabatic form of the hydrostatic approximation beginning with equation C.3. Rewrite equation C.3 using the ideal gas law.

$$d(R_d T\rho) = R_d \rho dT + R_d T d\rho = -\rho g dz \tag{C.13}$$

$$R_d \rho \frac{dT}{dz} + R_d T \frac{d\rho}{dz} = -\rho g \tag{C.14}$$

$$-\frac{R_d}{g}\frac{dT}{dz} - \frac{R_d T}{g}\frac{d\ln\rho}{dz} = 1, \quad -\frac{dT}{dz} = \Gamma_d, \quad \frac{R_d}{g}\Gamma_d = \kappa \tag{C.15}$$

$$\int d\ln\rho = \int(\kappa - 1)\frac{g}{R_d T}dz \tag{C.16}$$

Substitute for T with equation C.7.

$$\int d\ln\rho = (\kappa - 1)\frac{g}{R_d}\int\frac{dz}{T_0 - \Gamma_d Z}dz \tag{C.17}$$

Evaluate equation C.17 using limits of integration from the base of the column to the level at which the mass above is equivalent to the mass below.

$$\ln\left(\frac{\rho_c}{\rho_0}\right) = \frac{g(1-\kappa)}{R_d\Gamma_d}\ln\left(\frac{|T_0 - \Gamma_d Z_c|}{|T_0|}\right) = \frac{(1-\kappa)}{\kappa}\ln\left(\frac{|T_0 - \Gamma_d Z_c|}{|T_0|}\right) \tag{C.18}$$

Take the exponent of both sides of the equation and solve for the density at the vertical center of gravity for each column.

$$\rho_c = \rho_0\left(\frac{|T_0 - \Gamma_d Z_c|}{|T_0|}\right)^{\frac{(1-\kappa)}{\kappa}} = 0.6096\rho_0 \tag{C.19}$$

$$\rho_c' = (0.6096)(1.1)\bar{\rho}_0 = 0.67056 \text{ kg m}^{-3} \tag{C.20}$$

$$\rho_c'' = (0.6096)(0.9)\bar{\rho}_0 = 0.54864 \text{ kg m}^{-3} \tag{C.21}$$

The initial center of gravity for the system is found by constructing a line connecting the vertical centers of mass between the two columns then locating the point on that line that produces a zero first moment.

$$\rho_c' \delta l_{right} = \rho_c'' \delta l_{left}, \quad \delta l_{left} + \delta l_{right} = 1\,\text{km} \tag{C.22}$$

$$\frac{\rho_c'}{\rho_c''} = \frac{\delta l_{left}}{\delta l_{right}} = \frac{0.67056}{0.54864} = 1.22 \tag{C.23}$$

$$\delta l_{left} = 1.22 \delta_{right}$$

$$\delta_{right} = \frac{1000\,\text{m}}{1+1.22} = 450\,\text{m} \tag{C.24}$$

$$\delta l_{left} = 550\,\text{m}$$
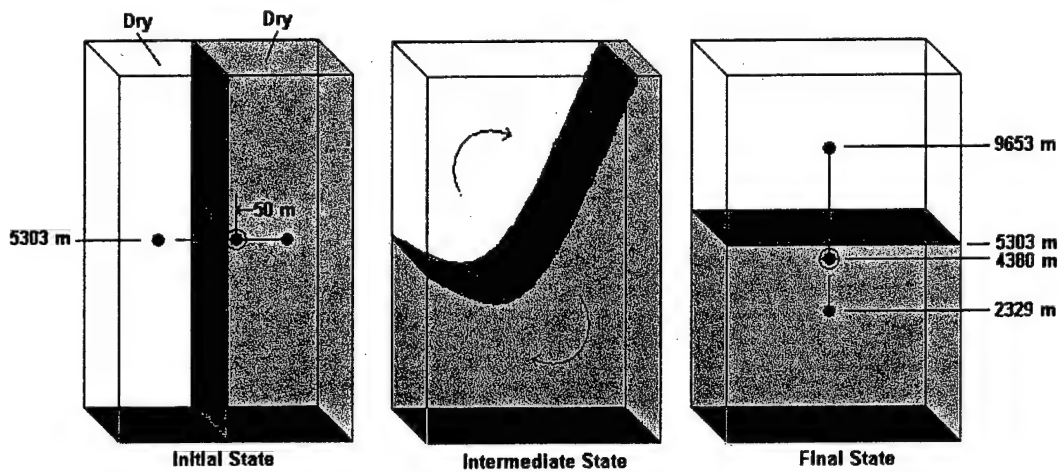
Figure C.2. Initial, intermediate and final states of the fluid system. The system center of gravity is designated by a circle around a point. Large dots designate the vertical centers of gravity for the light (left) and heavy (right) fluid respectively. The initial centers of gravity are located at the same geometric height for each column.

The horizontal center of the column at this level defines the initial center of gravity for the column. When the partition is relaxed, the system eventually settles into an equilibrium state. Assuming an adiabatic lapse rate when the fluid comes to rest, the new centers of gravity may be found. When the fluid comes to rest, half the mass of each column is distributed to another column. Because all of the denser fluid is denser at every level than the lighter fluid, it will all sink to the bottom. The interface height is found by computing the height immediately above half the mass. By definition, this height is the height of p_c and was found to be at 5303 m. It is now necessary to find the new centers of gravity for each of the fluid parcels. For the lower parcel, the center of gravity is found by integrating equation C.17 over the limits of p_0 to $3p_0/4$.

$$\int_{p_0}^{3p_0/4} d\ln(p) = \ln(p)\Big|_{p_0}^{3p_0/4} = \frac{g}{R_d}\frac{1}{\Gamma_d}\ln|T_0 - \Gamma_d Z|\Big|_{Z=0}^{Z=Z_{cl}} \tag{C.25}$$

Solve for the height of the center of mass of the lower parcel (Z_{cl}).

$$\ln\left(\frac{3}{4}\right) = \frac{1}{\kappa}\ln\left(\frac{|T_0 - \Gamma_d Z_{cl}|}{|T_0|}\right) \tag{C.26}$$

Take the exponent of both sides of the equation.

$$T_0\left(\frac{3}{4}\right)^{\kappa} = |T_0 - \Gamma_d Z_{cl}| \tag{C.27}$$

$$\frac{T_0\left[1-\left(\frac{3}{4}\right)^{\kappa}\right]}{\Gamma_d} = Z_{cl} = 2329\,\text{m} \tag{C.28}$$

Next, compute the temperature of the interface.

$$T_c = T_0 - \Gamma_d Z_c = 236.24\,\text{K} \tag{C.29}$$

The center of mass for the upper fluid is then

$$Z_{cu} = Z_c + \frac{T_c\left[1-\left(\frac{1}{2}\right)^{\kappa}\right]}{\Gamma_d} = 5303\,\text{m} + 4350\,\text{m} = 9653\,\text{m} \tag{C.30}$$

To estimate the new center of mass for the system, compute the densities at Z_{cu} and Z_{cl}.

$$\rho'_{cl} = \rho'_0\left(\frac{|T_0 - \Gamma_d Z_c|}{|T_0|}\right)^{\frac{(1-\kappa)}{\kappa}} = (1.1)\bar{\rho}_0(0.81431) = 0.85974\,\text{kg m}^{-3} \tag{C.31}$$

$$\rho''_{cu} = \rho''_c\left(\frac{|T_c - \Gamma_d Z_c|}{|T_c|}\right)^{\frac{(1-\kappa)}{\kappa}} = (0.54864)(0.60959) = 0.33445\,\text{kg m}^{-3} \tag{C.32}$$

To find a new system center of gravity, construct a vertical line passing through both centers of gravity and locate a point on the line that produces a zero first moment.

$$\rho'_c\delta z_{lower} = \rho''_c\delta z_{upper}\,,\quad \delta z_{lower} + \delta z_{upper} = Z_{cu} - Z_{cl} = 9653\,\text{m} - 2329\,\text{m} = 7324\,\text{m} \tag{C.33}$$

$$\frac{\rho'_c}{\rho''_c} = \frac{\delta z_{upper}}{\delta z_{lower}} = \frac{0.85974}{0.33445} = 2.57 \tag{C.34}$$

$$\delta z_{upper} = 2.57\delta z_{lower}$$
$$\delta z_{lower}(1+2.57) = 7324\,\text{m} \tag{C.35}$$
$$\delta z_{lower} = 2051\,\text{m}\,,\quad \delta z_{upper} = 5273\,\text{m}$$

The system center of gravity is therefore 4380 m, or 923 m below the interface (at 5303 m).

The initial and final states of the system are analogous to the initial and final states of a mesoscale NWP model with a cloud-resolving grid. Noting the change in altitude of the system's center of gravity

can approximate the root-mean-square maximum kinetic energy of this system. The vertical kinetic energy per unit mass (K.E.) is estimated by equation C.36.

$$K.E. = \frac{V^2}{2} = \delta z g \tag{C.36}$$

The system's center of gravity is found by computing the first moments about the center of gravity in each fluid column. A ring surrounding the dots in Figure C.2 denotes the system centers of gravity. For the case in which neither column becomes saturated, the system's center of gravity drops 923 m resulting in a maximum K.E. of 9,045 m^2 s^{-2} per unit mass. Lateral displacement of the system's center of gravity does not release vertical K.E.

We now consider the initial system with a lighter saturated column of air. In this column, assume simply that the lapse rate is constant as well over the column's depth such that $\Gamma_s = \Gamma_d / 2$ to approximate the influence of latent heating from a rising saturated column. It is readily seen that the centers of gravity differ from the dry case. The same method is used to locate centers of gravity for each parcel; however, the lapse rate Γ_s is used in the lighter column in place of Γ_d.

$$\int_{p_0}^{p_c} d\ln(p) = \ln(p)\Big|_{p_0}^{p_c} = \frac{g}{R_d}\frac{1}{\Gamma_s}\ln|T_0 - \Gamma_s Z|\Big|_{Z=0}^{Z=Z_c} \tag{C.37}$$

Solve for the height of the center of mass for each column.

$$\ln\left(\frac{1}{2}\right) = \frac{2}{\kappa}\ln\left(\frac{\left|T_0 - \frac{\Gamma_d Z_c}{2}\right|}{|T_0|}\right), \quad p_c = \frac{p_0}{2}, \quad \frac{g}{R_d}\frac{1}{\Gamma_s} = \frac{2c_p}{R_d} = \frac{2}{\kappa} \tag{C.38}$$

Take the exponent of both sides of the equation.

$$T_0\left(\frac{1}{2}\right)^{\kappa/2} = \left|T_0 - \frac{\Gamma_d Z_c}{2}\right| \tag{C.39}$$

$$\frac{2T_0\left[1 - \left(\frac{1}{2}\right)^{\kappa/2}\right]}{\Gamma_d} = Z_c = 5566\,\text{m} \tag{C.40}$$

The dry column on the right has $Z_c = 5303$ m. Next, compute the density at the vertical center of gravity for each column.

$$d(R_d T\rho) = R_d \rho dT + R_d T d\rho = -\rho g dz \tag{C.41}$$

$$R_d \rho \frac{dT}{dz} + R_d T \frac{d\rho}{dz} = -\rho g \tag{C.42}$$

$$-\frac{R_d}{g}\frac{dT}{dz} - \frac{R_d T}{g}\frac{d\ln\rho}{dz} = 1, \quad -\frac{dT}{dz} = \frac{\Gamma_d}{2}, \quad \frac{R_d \Gamma_d}{2g} = \frac{\kappa}{2} \tag{C.43}$$

$$\int d\ln\rho = \int\left(\frac{\kappa}{2}-1\right)\frac{g}{R_d T}dz \qquad (C.44)$$

Substitute for T.

$$\int d\ln\rho = \left(\frac{\kappa}{2}-1\right)\frac{g}{R_d}\int\frac{dz}{T_0 - \frac{\Gamma_d Z}{2}}dz \qquad (C.45)$$

Evaluate equation C.45 using limits of integration from the base of the column to the level at which the mass above is equivalent to the mass below.

$$\ln\left(\frac{\rho_c}{\rho_0}\right) = \frac{2g\left(1-\frac{\kappa}{2}\right)}{R_d\Gamma_d}\ln\left(\frac{\left|T_0 - \frac{\Gamma_d Z_c}{2}\right|}{|T_0|}\right) = \frac{(2-\kappa)}{\kappa}\ln\left(\frac{\left|T_0 - \frac{\Gamma_d Z_c}{2}\right|}{|T_0|}\right) \qquad (C.46)$$

$$\rho_c'' = (0.9)\bar{\rho}_0\left(\frac{\left|T_0 - \frac{\Gamma_d Z_c}{2}\right|}{|T_0|}\right)^{\frac{(2-\kappa)}{\kappa}} = (0.9)\bar{\rho}(0.55207) = 0.60728\,\text{kg m}^{-3} \qquad (C.47)$$

The density at the vertical center of gravity for the heavy column is unchanged from the previous example.

$$\rho_c' = (1.1)\bar{\rho}_0(0.6096) = 0.67056\,\text{kg m}^{-3} \qquad (C.48)$$

The geometric center of gravity is then found to be along an inclined line connecting the two vertical centers of gravity. Using simple trigonometry, the length of the line connecting the two column-centers of gravity is 1034 m, and the system center of gravity is located at elevation 5428 m on that line. The system center of gravity is horizontally displaced approximately 26 m into the heavy dry column. After the fluid comes to rest, the height of the lower fluid's center of gravity is unchanged from the previous example (Z_{cl} = 2329 m), and the density of the fluid at this height is the same as well (ρ'_{cl} = 0.67056 kg m^{-3}). Next, compute the height and density of the upper fluid's new center of gravity.

$$Z_{cu} = \frac{2T_c\left[1-\left(\frac{1}{2}\right)^{\kappa/2}\right]}{\Gamma_d} + Z_c = 9869\,\text{m} \qquad (C.49)$$

$$\rho_{cu}'' = (0.9)\bar{\rho}_0\underbrace{\left(\frac{\left|T_0 - \frac{\Gamma_d Z_c}{2}\right|}{|T_0|}\right)^{\frac{(2-\kappa)}{\kappa}}}_{\text{density of upper fluid at interface}}\left(\frac{\left|T_c - \frac{\Gamma_d(Z_{cu}-Z_c)}{2}\right|}{|T_c|}\right)^{\frac{(2-\kappa)}{\kappa}} \qquad (C.50)$$

$$\rho_{cu}'' = (0.9)\bar{\rho}_0(0.56856)(0.55204) = 0.28248\,\text{kg m}^{-3} \text{ at } 9869\,\text{m}$$

Finally, find the new system center of gravity by connecting a vertical line between the parcel's centers of gravity and locating the point on that line with a zero first moment.

During moist ascent, all of the condensed liquid water is assumed to remain suspended with the rising parcel (cloud). In this case, the new system center of gravity is located in the horizontal center of the domain at elevation 4194 m, a drop of 1234 m from its original position. This translates into a maximum K.E. of 12,093 m^2 s^{-2} per unit mass (see Figure C.3.)
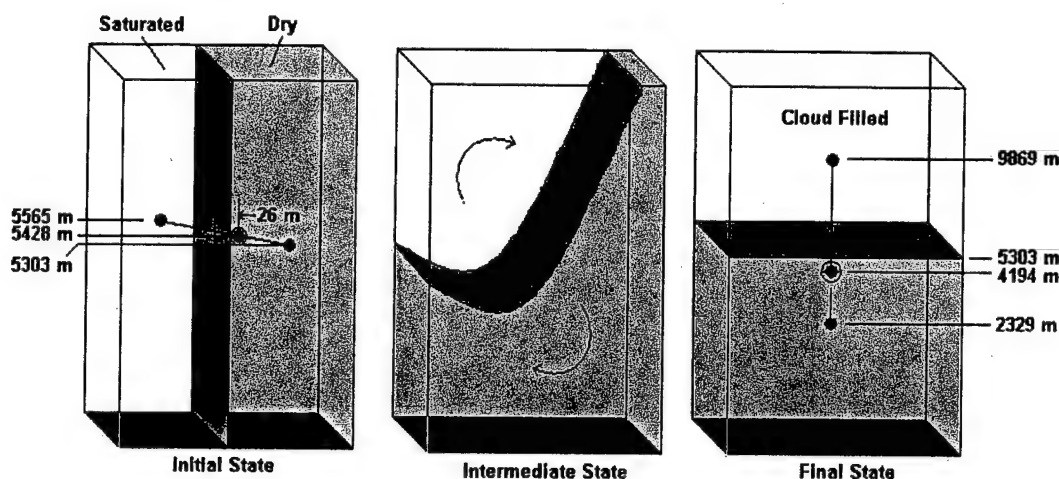
Figure C.3. System centers of gravity for initial and final saturated and dry states. A ring designates the system center of gravity. All condensed water is assumed to remain suspended in the air parcel.

In this thought experiment, the K.E. increased 34% by replacing the lighter dry column with a saturated one that demands a less steep lapse rate in temperature. If the light column had been partially saturated such that condensation would not begin immediately but rather sometime during the ascent, a continuous range of K.E. changes would occur. The K.E. change would depend on the amount of condensation occurring as the light column is lifted. It is concluded from this result that the potential energy of an initial model environment is underestimated if clouds are not included.

APPENDIX D

IDEALIZED ATMOSPHERIC PROFILES

Case 1. Ns/St (Surface RH = 95%)

Sigma	Height [m]	P [kPa]	T [C]	T_{dd} [C]	Q [kg/kg]
1.000	100.000	100.129	4.35	0.73	0.00493516
0.995	136.173	99.700	4.11	0.73	0.00487283
0.985	208.927	98.840	3.64	0.73	0.00475380
0.970	319.079	97.550	2.93	0.73	0.00457859
0.945	505.468	95.398	1.71	0.73	0.00428834
0.910	772.546	92.382	-0.02	0.73	0.00390395
0.870	1087.06	88.930	-2.07	16.34	0.00100034
0.825	1453.59	85.039	-4.45	18.98	0.000673919
0.775	1877.99	80.707	-7.21	22.02	0.000416136
0.725	2322.21	76.366	-10.09	22.98	0.000303640
0.675	2788.39	72.016	-13.12	24.18	0.000210601
0.625	3279.06	67.656	-16.31	25.46	0.000140311
0.575	3797.20	63.287	-19.69	26.98	8.75108e-05
0.525	4346.43	58.908	-23.25	28.42	5.26834e-05
0.475	4931.12	54.519	-27.05	30.00	2.94493e-05
0.425	5556.74	50.120	-31.12	30.00	1.89438e-05
0.375	6230.13	45.711	-35.50	30.00	1.14779e-05
0.325	6960.14	41.292	-40.24	30.00	6.45702e-06
0.275	7758.42	36.862	-45.43	30.00	3.29365e-06
0.225	8640.87	32.421	-51.17	30.00	1.47616e-06
0.175	9629.99	27.969	-57.59	30.00	5.55090e-07
0.125	10759.4	23.504	-64.94	30.00	1.60698e-07
0.075	12082.6	19.080	-68.50	30.00	9.45940e-08
0.025	13694.5	14.798	-68.50	30.00	1.21966e-07

Case 2. Cb/Cs (Surface RH = 95%)

Sigma	Height [m]	P [kPa]	T [C]	T_{dd} [C]	Q [kg/kg]
1.000	100.000	100.129	14.35	0.79	0.00971233
0.995	136.173	99.700	14.11	0.79	0.00960205
0.985	208.927	98.840	13.64	0.79	0.00939130
0.970	319.079	97.550	12.93	0.79	0.00908018
0.945	505.468	95.398	11.71	0.79	0.00856193
0.910	772.546	92.382	9.98	0.79	0.00787062
0.870	1087.06	88.930	7.93	16.40	0.00225805
0.825	1453.59	85.039	5.55	19.04	0.00157944
0.775	1877.99	80.707	2.79	22.08	0.00102203
0.725	2322.21	76.366	-0.09	23.04	0.000770921
0.675	2788.39	72.016	-3.12	24.24	0.000555851
0.625	3279.06	67.656	-6.31	25.52	0.000386879
0.575	3797.20	63.287	-9.69	27.04	0.000254027
0.525	4346.43	58.908	-13.25	28.48	0.000161842
0.475	4931.12	54.519	-17.05	30.00	9.73150e-05
0.425	5556.74	50.120	-21.12	30.00	6.60950e-05
0.375	6230.13	45.711	-25.50	30.00	4.26386e-05
0.325	6960.14	41.292	-30.24	30.00	2.58126c-05
0.275	7758.42	36.862	-35.43	30.00	1.43723e-05
0.225	8640.87	32.421	-41.17	30.00	7.16841e-06
0.175	9629.99	27.969	-47.59	30.00	3.08214e-06
0.125	10759.4	23.504	-54.94	30.00	1.06342e-06
0.075	12082.6	19.080	-58.50	30.00	6.88250e-07
0.025	13694.5	14.798	-58.50	30.00	8.87404e-07

Case 3. St (Surface RH = 80%)

Sigma	Height [m]	P [kPa]	T [C]	T_{dd} [C]	Q [kg/kg]
1.000	100.000	100.129	14.35	3.40	0.00817175
0.995	136.173	99.700	14.11	3.40	0.00807636
0.985	208.927	98.840	13.64	3.40	0.00789410
0.970	319.079	97.550	12.93	3.40	0.00762522
0.945	505.468	95.398	11.71	3.40	0.00717795
0.910	772.546	92.382	9.98	3.40	0.00658239
0.870	1087.06	88.930	7.93	19.01	0.00183600
0.825	1453.59	85.039	5.55	21.65	0.00127226
0.775	1877.99	80.707	2.79	24.69	0.000813713
0.725	2322.21	76.366	-0.09	25.65	0.000608735
0.675	2788.39	72.016	-3.12	26.85	0.000434697
0.625	3279.06	67.656	-6.31	28.13	0.000299287
0.575	3797.20	63.287	-9.69	29.65	0.000194022
0.525	4346.43	58.908	-13.25	30.00	0.000137337
0.475	4931.12	54.519	-17.05	30.00	9.73150e-05
0.425	5556.74	50.120	-21.12	30.00	6.60950e-05
0.375	6230.13	45.711	-25.50	30.00	4.26386e-05
0.325	6960.14	41.292	-30.24	30.00	2.58126e-05
0.275	7758.42	36.862	-35.43	30.00	1.43723e-05
0.225	8640.87	32.421	-41.17	30.00	7.16841e-06
0.175	9629.99	27.969	-47.59	30.00	3.08214e-06
0.125	10759.4	23.504	-54.94	30.00	1.06342e-06
0.075	12082.6	19.080	-58.50	30.00	6.88250e-07
0.025	13694.5	14.798	-58.50	30.00	8.87404e-07

Case 4. Cu/As (Surface RH = 70%)

Sigma	Height [m]	P [kPa]	T [C]	T_{dd} [C]	Q [kg/kg]
1.000	100.000	100.129	14.35	5.39	0.00714664
0.995	136.173	99.700	14.11	5.39	0.00706142
0.985	208.927	98.840	13.64	5.39	0.00689863
0.970	319.079	97.550	12.93	5.39	0.00665860
0.945	505.468	95.398	11.71	5.39	0.00625976
0.910	772.546	92.382	9.98	5.39	0.00572943
0.870	1087.06	88.930	7.93	21.00	0.00156302
0.825	1453.59	85.039	5.55	23.64	0.00107515
0.775	1877.99	80.707	2.79	26.68	0.000681359
0.725	2322.21	76.366	-0.09	27.64	0.000506412
0.675	2788.39	72.016	-3.12	28.84	0.000358889
0.625	3279.06	67.656	-6.31	30.00	0.000247989
0.575	3797.20	63.287	-9.69	30.00	0.000187035
0.525	4346.43	58.908	-13.25	30.00	0.000137337
0.475	4931.12	54.519	-17.05	30.00	9.73150e-05
0.425	5556.74	50.120	-21.12	30.00	6.60950e-05
0.375	6230.13	45.711	-25.50	30.00	4.26386e-05
0.325	6960.14	41.292	-30.24	30.00	2.58126e-05
0.275	7758.42	36.862	-35.43	30.00	1.43723e-05
0.225	8640.87	32.421	-41.17	30.00	7.16841e-06
0.175	9629.99	27.969	-47.59	30.00	3.08214e-06
0.125	10759.4	23.504	-54.94	30.00	1.06342e-06
0.075	12082.6	19.080	-58.50	30.00	6.88250e-07
0.025	13694.5	14.798	-58.50	30.00	8.87404e-07

Case 5. Cb (Surface RH = 100%)

Sigma	Height [m]	P [kPa]	T [C]	T_{dd} [C]	Q [kg/kg]
1.000	086.630	100.129	14.44	0.0	0.0102868
0.995	122.825	99.700	14.20	0.0	0.0101710
0.985	195.614	98.840	13.73	0.0	0.00994989
0.970	305.820	97.550	13.02	0.0	0.00962332
0.945	492.302	95.398	11.80	0.0	0.00907908
0.910	759.515	92.382	10.07	0.0	0.00835269
0.870	1074.19	88.930	8.02	0.0	0.00755130
0.825	1440.91	85.039	5.64	0.0	0.00670104
0.775	1865.53	80.707	2.88	0.0	0.00581321
0.725	2310.00	76.366	0.00	0.0	0.00499185
0.675	2776.45	72.016	-3.03	0.0	0.00423166
0.625	3267.40	67.656	-6.22	0.0	0.00353636
0.575	3785.86	63.287	-9.60	0.0	0.00290424
0.525	4335.42	58.908	-13.16	0.0	0.00234346
0.475	4920.50	54.519	-16.96	0.0	0.00184666
0.425	5546.54	50.120	-21.03	0.0	0.00141506
0.375	6220.42	45.711	-25.41	0.0	0.00104840
0.325	6950.97	41.292	-30.15	30.00	2.61179e-05
0.275	7749.90	36.862	-35.34	30.00	1.45528e-05
0.225	8633.11	32.421	-41.08	30.00	7.26482e-06
0.175	9623.17	27.969	-47.50	30.00	3.12700e-06
0.125	10753.7	23.504	-54.85	30.00	1.08044e-06
0.075	12078.6	19.080	-58.41	30.00	6.99805e-07
0.025	13692.9	14.798	-58.41	30.00	9.02303e-07

APPENDIX E

INCOMPATIBILITY BETWEEN NOGAPS AND SFCTEMP

E.1. Surface Temperature Problem

During this study, a problem was encountered that involves data incompatibility between the NOGAPS and SFCTEMP analyses. Specifically, NOGAPS 1000-mb temperatures did not match SFCTEMP surface temperatures at the surface locations where the 1000-mb pressure level intersected the surface. This problem produces an "edge" in estimates of temperature on a terrain following sigma level near the surface.

To illustrate the horizontal temperature discontinuity problem, temperature and pressure contours are presented in Figure E.1 (following page, upper half of figure) for the 0.995 sigma level produced by MM5's INTERPF preprocessor valid for 13 September 2000, 00UTC. The lower half of Figure E.1 shows surface temperatures and terrain elevation. The region depicted in these plots is roughly a 400-km wide box surrounding the Houston, Texas ship channel. As expected, surface pressure follows the terrain pattern because the 0.995 sigma level is a terrain following surface very near to the ground.

The problem identified here is the unrealistic temperature gradient on the terrain following sigma level. The gradient indicates an immediate drop of about 5 K. This temperature gradient is not apparent on the surface temperature plot (Figure E.1) or on the 1000-mb and 950-mb temperature plots (Figure E.2.) Such boundaries can cause unrealistic instabilities if they are used to initialize a mesoscale NWP model.

INTERPF linearly interpolates sigma level temperatures between NOGAPS pressure level temperatures (see Figure E.3.) When the sigma level is below the lowest NOGAPS pressure level, SFCTEMP surface temperatures are used in the interpolation. Surface temperature values are also used in the interpolation when a sigma level occurs between two pressure levels one of which is beneath terrain elevation. Such pressure distributions occur when a surface pressure is lower than a standard pressure level included in the NOGAPS analysis. The region where the 1000-mb pressure contour intersects the surface in Figure E.1 locates an anomalously high temperature gradient for the lowest sigma level.
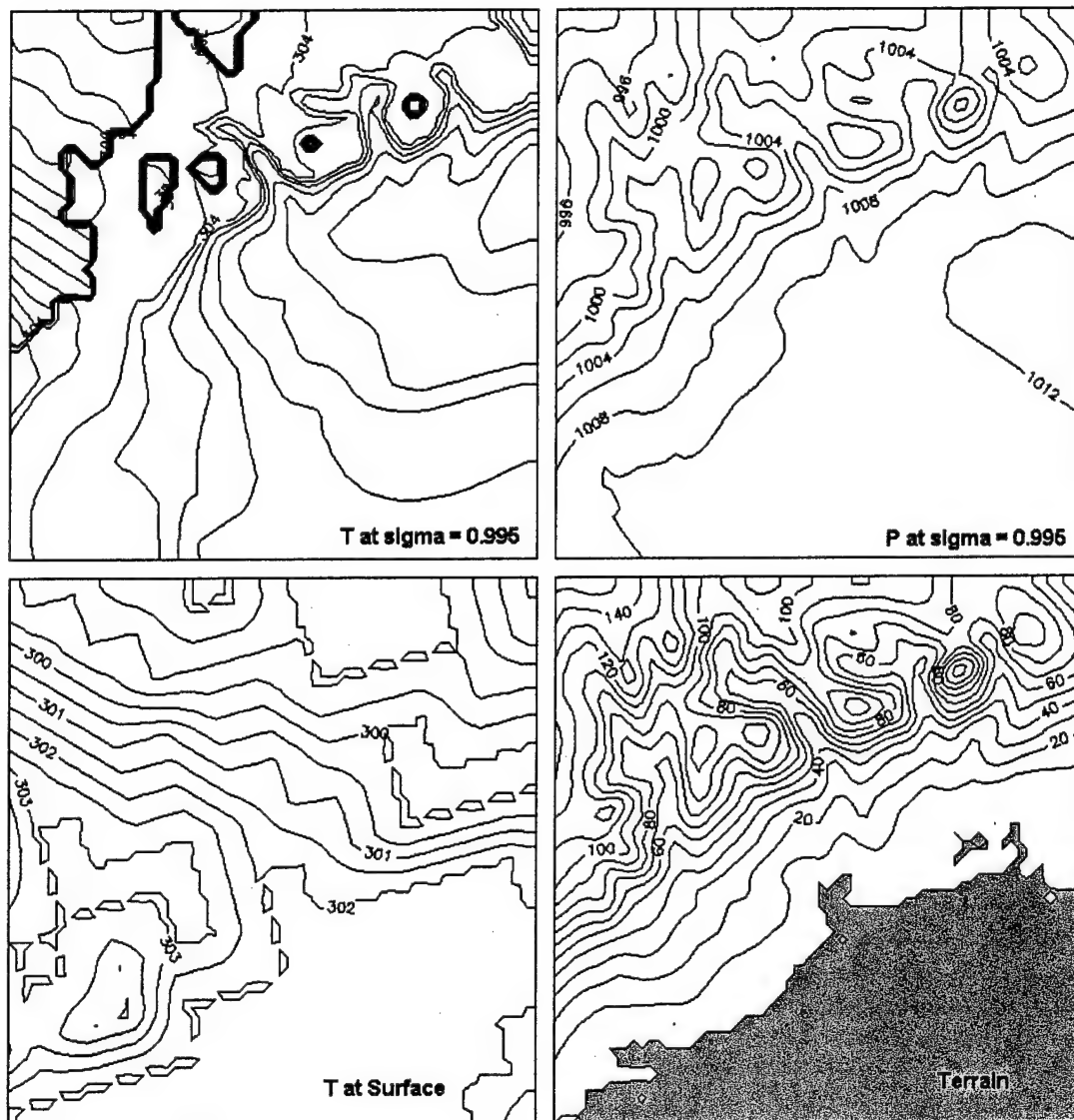
Figure E.1. Contours of temperature for the 0.995 sigma level (upper left, units of K, contour interval 0.5 K), pressure for the 0.995 sigma level (upper right, units of mb, contour interval 1 mb), temperature on surface (lower left, units of K, contour interval 0.5 K), and terrain elevation (lower right, units of m, contour interval of 10 m) surrounding the Houston Ship Channel.
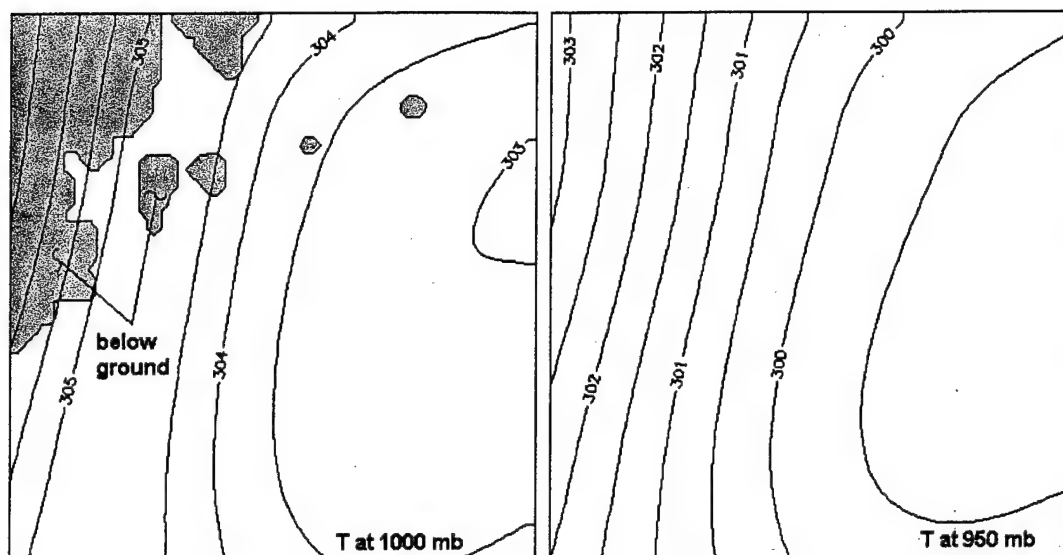
Figure E.2. 1000-mb and 950-mb temperature plots for same region depicted in Figure E.1. Units are in K and the contour interval is 0.5 K
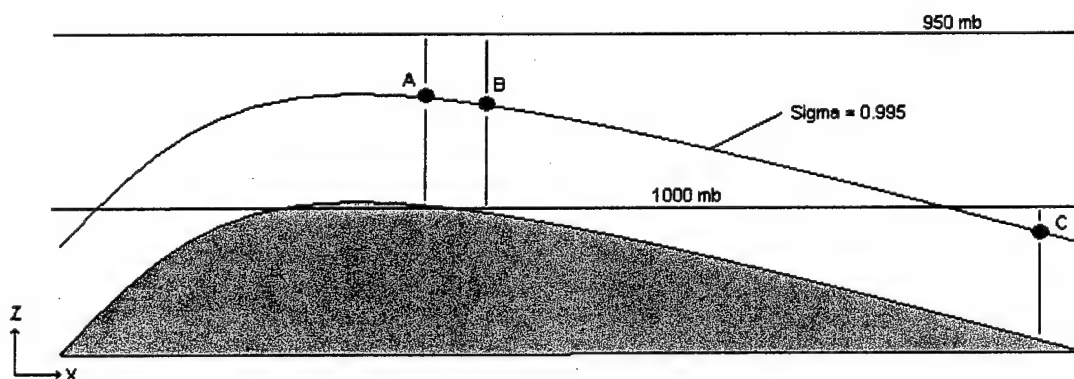

Figure E.3. Schematic of linear interpolation to a sigma level. Point **A** is interpolated between the surface and the 950-mb pressure level, point **B** is interpolated between the 950-mb and 1000-mb pressure levels, and point **C** is interpolated between the 1000-mb pressure level and the surface. If the 1000-mb temperature below point **B** departs significantly from the surface temperature below point **A**, that variation will translate into an unrealistically steep temperature gradient between points **A** and **B** along the sigma level. This occurs when the 1000-mb temperature value intersecting the surface departs significantly from the surface temperature value.

2. Vertical Adjustment Scheme

One solution to fix this problem is to use a simple vertical adjustment scheme to adjust the lower pressure level temperatures. This scheme makes the following assumptions:

- Surface temperatures are perfect.
- Upper pressure level temperatures are perfect.

- Lower pressure level temperatures are not perfect.
- Lower pressure level temperatures should be weighted more toward the surface temperatures the closer the surface is below the lower pressure level.

The crux of the scheme takes these four assumptions and computes appropriate weights for the temperature lapse rates between the upper pressure level and the lower pressure level (Γ_{ul}) and between the upper pressure level and the surface (Γ_{us}). Figure E.4 illustrates the process.
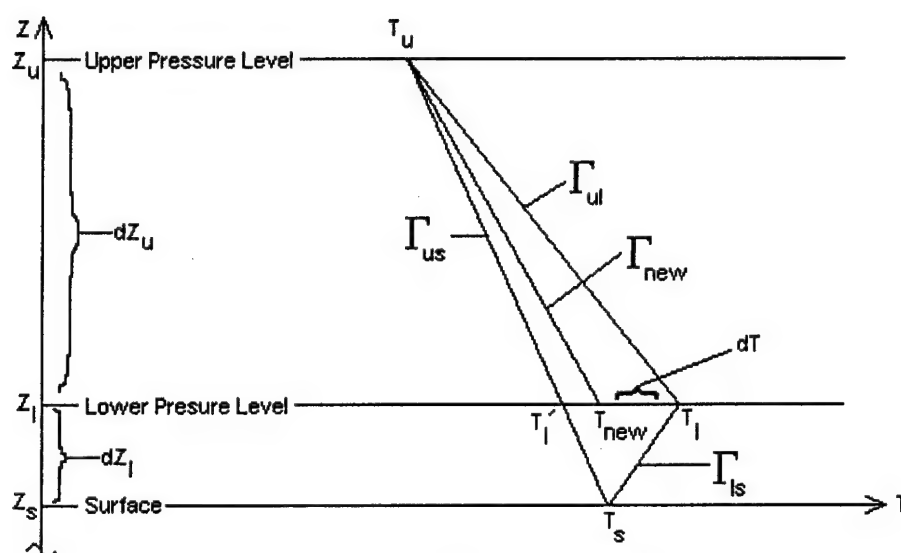

Figure E.4. Schematic of temperature profile adjustment method.

Variable Key:

Z_u	Height of upper pressure level (NOGAPS data)
Z_l	Height of lower pressure level (NOGAPS data)
Z_s	Height of surface (MM5 Terrain data)
T_u	Temperature of upper pressure level (NOGAPS data)
T_l	Temperature of lower pressure level (NOGAPS data)
T_l'	Temperature of lower pressure level if linearly interpolated between T_u and T_s
T_s	Temperature of surface (SFCTEMP data)
dZ_u	Height difference between upper and lower pressure levels (Z_u - Z_l)
dZ_l	Height difference between lower pressure level and surface (Z_l - Z_s)
Γ_{us}	Vertical lapse rate of temperature between upper pressure level and surface
Γ_{ul}	Vertical lapse rate of temperature between upper and lower pressure levels
Γ_{ls}	Vertical lapse rate of temperature between lower pressure level and surface
Γ_{new}	Vertical lapse rate computed using interpolation method
dT	Temperature adjustment to lower pressure level temperature (T_{new} - T_l)
T_{new}	Temperature of lower pressure level computed using interpolation method

One important characteristic of this scheme is that it is not linear. The interpolation method is only applied when $dZ_u \geq dZ_l$. This is to preserve the lower pressure level temperatures when they are sufficiently far above the surface. If a straight linear interpolation were applied, then when $dZ_u = dZ_l$,

T_{new} would immediately be adjusted to midway between T'_l and T_l. A more gradual method of adjusting the temperatures is required. Intuitively, one can think of the proposed scheme in the following manner:

- If dZ_u is equal to dZ_l, then dT is zero.
- If dZ_u is infinitely times dZ_l (i.e. the surface intersect the lower pressure level), then dT is equal to the value of $T'_l - T_l$.

The following constraints are placed on the "weights" given to the lapse rates Γ_{us} and Γ_{ul}:

(1) When $dZ_u \geq dZ_l$ (i.e. the surface is sufficiently below the lower pressure level), the weight for Γ_{us} is 0.
(2) When $dZ_u \geq dZ_l$ (i.e. the surface is sufficiently below the lower pressure level), the weight for Γ_{ul} is 1.
(3) When $dZ_l = 0$ (i.e. the surface intersect the lower pressure level), the weight for Γ_{us} is 1.
(4) When $dZ_l = 0$ (i.e. the surface intersect the lower pressure level), the weight for Γ_{ul} is 0.

The next step is to design a formula that will compute T_{new} given the available information and the constraints. To achieve constraints (1) and (3), the weight for Γ_{us} is formulated as follows:

$$w_{us} = \frac{dZ_u - dZ_l}{dZ_u + dZ_l} \tag{E.1}$$

Check constraint (1) $dZ_u = dZ_l$,   the weight = 0. $\checkmark$
Check constraint (3) $dZ_l = 0$,   the weight = 1. $\checkmark$

To achieve constraints (2) and (4), the weight for Γ_{ul} is formulated as follows:

$$w_{ul} = 1 - w_{us} \tag{E.2}$$

Check constraint (2) $dZ_u = dZ_l$,   the weight = 1. $\checkmark$
Check constraint (4) $dZ_l = 0$,   the weight = 0. $\checkmark$

The next step in creating the formula is to set the new lapse rate as a sum of the "weighted" lapse rates.

$$\Gamma_{new} = w_{us}\Gamma_{us} + (1 - w_{us})\Gamma_{ul} \tag{E.3}$$

The final step is to solve for T_{new}.

$$T_{new} = T_u - dZ_u\left[w_{us}\Gamma_{us} + (1 - w_{us})\Gamma_{ul}\right] \tag{E.4}$$

Figures E.5 and E.6 provide an example of how a 1000-mb pressure level temperature is adjusted depending on the distance the surface lies below the 1000-mb pressure level. A 950-mb temperature of 287.7 K is set at an elevation of 548.0 m mean sea level (MSL). A 1000-mb temperature of 291.9 K is set at an elevation of 112.7 m MSL. Temperatures are assumed constant along the pressure surface. The vertical temperature distribution is computed assuming a hydrostatically balanced atmosphere with a dry adiabatic lapse rate. The temperatures on the pressure surfaces are computed from a temperature of 293.0K at 1013.25 mb, 0 m MSL. The surface elevation slopes upward from 0 m MSL through the 1,000-mb pressure level. Surface temperatures are assumed 4-degrees cooler than the temperatures computed from the dry adiabatic lapse rate between the pressure levels. The surface temperature is 289.0 K at point **A** and 287.9 K at point **B**. This results in the surface temperature being 4-degrees cooler than the temperature of the 1000-mb pressure level intersecting the surface. Such errors are

possible if radiational cooling of the boundary is not reflected in the isobaric temperature analysis, or if there is a warm sampling bias in the isobaric temperature analysis.
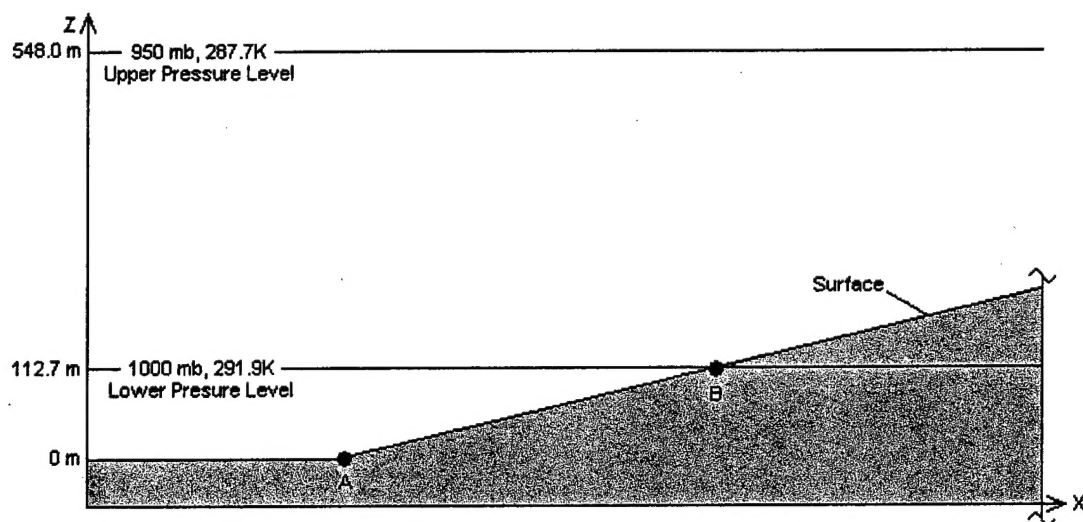

Figure E.5. Schematic of example surface intersecting 1000-mb pressure level.
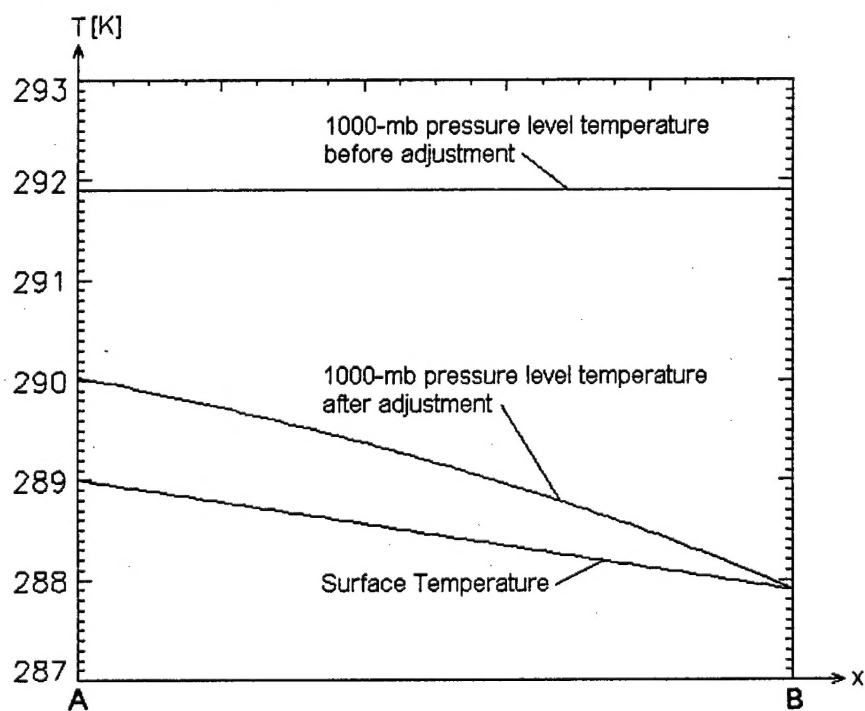

Figure E.6. Plots of temperature between points A and B for the surface, for the 1000-mb pressure level before adjustment, and for the 1000-mb pressure level after adjustment.

Another assumption must be made to adjust the lower pressure level temperatures if the lower pressure level is below the surface. Lower pressure level temperatures in this case, wherever they are below the surface, are replaced by values that linearly interpolate the surface temperature down to the estimated sea level temperature. See Dudhia et al. (1999, section 7.3) for a description of how sea level pressure and temperatures are estimated below the surface. Below ground, these temperatures are never used by the INTERPF preprocessor to MM5 in computing the sigma-level temperatures and only facilitate plotting a continuous horizontal temperature distribution on isobaric surfaces.

The above scheme is applied to all portions of the NOGAPS temperature profiles that require adjustment. No adjustment is made to the pressure level temperatures if $dZ_u \geq dZ_l$. No changes are made to SFCTEMP temperatures. The resulting temperature profiles are used to provide boundary conditions and to initialize MM5 in the INTERPF preprocessor. Figure E.7. illustrates the adjusted 1000-mb pressure level temperatures and the resulting sigma level 0.995 temperature distribution produced by the INTERPF preprocessor.
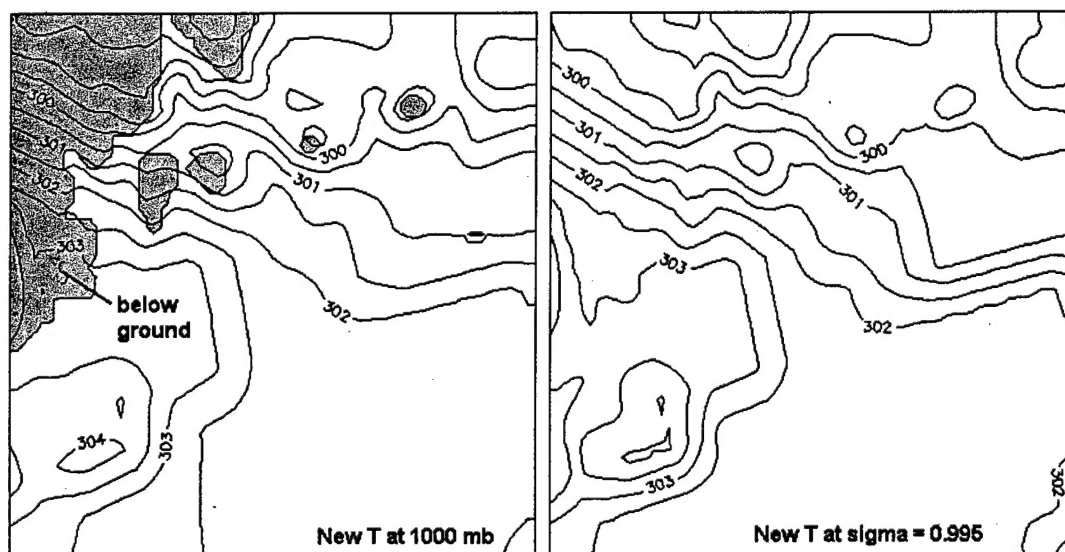

Figure E.7. Adjusted 1000-mb temperatures and resulting sigma level 0.995 temperatures.

APPENDIX F

EQUATIONS FOR HORIZONTAL DISTRIBUTION OF RTNEPH

Variable key:

L_i RTNEPH cloud coverage amount (as a fraction) for layer i

$_iU$ Unobscured portion of RTNEPH cloud coverage amount for layer i

$_iO_j$ Obscured portion of RTNEPH cloud coverage amount for layer i obscured by layers j

$_if_j$ Fraction of total 8th mesh area for layer i obscured by layers j

The left subscript i indicates the layer of the point of interest. The right subscripts indicate layers above that obscure the point of interest. A subscript of $j = 0$ indicates no obscuration from above.

Layer 1 equations:

$$_1U = L_1$$
$$_1f_1 = {_1U}$$
$$_1f_0 = 1 - {_1U}$$

Layer 2 equations:

$$_2O_1 = L_2\left(_1U\right)$$
$$_2U = L_2\left(1 - {_1U}\right)$$
$$_2f_{12} = {_2O_1}$$
$$_2f_1 = {_1U} - {_2O_1}$$
$$_2f_2 = {_2U}$$
$$_2f_0 = 1 - {_1U} - {_2U}$$

Layer 3 equations:

$$_3O_{12} = L_3\left(_2O_1\right)$$
$$_3O_1 = L_3\left(_1U - {_2O_1}\right)$$
$$_3O_2 = L_3\left(_2U\right)$$
$$_3U = L_3\left(1 - {_1U} - {_2U}\right)$$
$$_3f_{123} = {_3O_{12}}$$
$$_3f_{12} = {_2O_1} - {_3O_{12}}$$
$$_3f_{13} = {_3O_1}$$
$$_3f_1 = {_1U} - {_2O_1} - {_3O_1}$$
$$_3f_{23} = {_3O_2}$$
$$_3f_2 = {_2U} - {_3O_2}$$
$$_3f_3 = {_3U}$$
$$_3f_0 = 1 - {_1U} - {_2U} - {_3U}$$

Layer 4 equations:

$$_4O_{123} = L_4\left(_3O_{12}\right)$$
$$_4O_{12} = L_4\left(_2O_1 - {_3O_{12}}\right)$$
$$_4O_{13} = L_4\left(_3O_1\right)$$
$$_4O_1 = L_4\left(_1U - {_2O_1} - {_3O_1}\right)$$
$$_4O_{23} = L_4\left(_3O_2\right)$$
$$_4O_2 = L_4\left(_2U - {_3O_2}\right)$$
$$_4O_3 = L_4\left(_3U\right)$$
$$_4U = L_4\left(1 - {_1U} - {_2U} - {_3U}\right)$$
$$_4f_{1234} = {_4O_{123}}$$
$$_4f_{123} = {_3O_{12}} - {_4O_{123}}$$
$$_4f_{124} = {_4O_{12}}$$
$$_4f_{12} = {_2O_1} - {_3O_{12}} - {_4O_{12}}$$
$$_4f_{134} = {_4O_{13}}$$
$$_4f_{13} = {_3O_1} - {_4O_{13}}$$
$$_4f_{14} = {_4O_1}$$
$$_4f_1 = {_1U} - {_2O_1} - {_3O_1} - {_4O_1}$$
$$_4f_{234} = {_4O_{23}}$$
$$_4f_{23} = {_3O_2} - {_4O_{23}}$$
$$_4f_{24} = {_4O_2}$$
$$_4f_2 = {_2U} - {_3O_2} - {_4O_2}$$
$$_4f_{34} = {_4O_3}$$
$$_4f_3 = {_3U} - {_4O_3}$$
$$_4f_4 = {_4U}$$
$$_4f_0 = 1 - {_1U} - {_2U} - {_3U} - {_4U}$$